UNIVERSITY OF CALIFORNIA, SAN DIEGO

Seismic Behavior, Modeling, and Design of Deep Wide-Flange Steel Columns for Special Moment Frames

A Dissertation submitted in partial satisfaction of the requirements for the degree Doctor of Philosophy

in

Structural Engineering

by

Gulen Ozkula

Committee in charge:

Professor Chia-Ming Uang, Chair
Professor Li-Tien Cheng
Professor Francesco Lanza Di Scalea
Professor Gilberto Mosqueda
Professor Pui-Shum Benson Shing

2017

The dissertation of Gulen Ozkula is approved, and it is acceptable in quality and form for publication on microfilm:

Chair

University of California, San Diego

2017

DEDICATION

To my parents,

EPIGRAPH

Your need for acceptance can make you invisible in this word.
Risk being seen in all of your glory.
Jim Carey

TABLE OF CONTENTS

LIST OF FIGURES

LIST OF TABLES

ACKNOWLEDGEMENTS

I would like to express my deep appreciation to my advisor, Professor Chia-Ming Uang, for his encouragement and tireless dedication to support my Ph.D. research at the University of California, San Diego (UCSD). It was an honor to research under his supervision. I truly appreciate his time, patience and direction during all these years. I have been extremely lucky to have a supervisor who cared about my professional growth, and gave me opportunity to have a substantial teaching experience at UCSD.

I would also like to express my appreciation to my committee members, Professor Li-Tien Cheng, Professor Francesco Lanza Di Scalea, Professor Gilberto Mosqueda, and Professor Pui-Shum Benson Shing for the contribution of their time and help in my research efforts. My special thanks go to Professor G. Mosqueda and his Ph.D. student Alireza Sarebanha for assisting in developing a close-loop control algorithm for the Seismic Response Modification Device (SRMD) test facility for column testing. It would be impossible to finish our testing on time without their support.

Technical assistance from Danny Innamorato and Edward Stovin at the SRMD was greatly appreciated. Dr. Kikuo Ikarashi provided much appreciated assistance with testing.

I would like to express my gratitude to my team-mate Piyachai Chansuk for his help on proof reading my dissertation and his friendship. I would like to extend my special thanks to my dearest friends, Michelle Go, Ayse Okesli-Armlovich, and Selin Esener for their friendship and support in every step of my life.

Finally, all my accomplishments would be impossible without the guidance of my loving parents. I am extremely grateful for their influence that led me to become the person I am today.

Funding for this research was provided by the NEHRP Consultants Joint Venture Earthquake, Structural, and Engineering Research for the National Institute of Standards and Technology through Applied Technology Council. AISC donated steel materials and the Herrick Corporation donated the fabrication service. I also would like to acknowledge Ministry of National Education of Turkish Republic for their gracious support and the fellowship program.

Chapter 3 of this dissertation is based on material published by University of California, San Diego, titled “ATC-106: Seismic behavior and design of deep, slender wide-flange structural steel seam-column members.” with co-author Uang, C.-M. (2016). In this chapter, materials currently being prepared for submission for publication by University of California, San Diego, titled “ATC-106 Phase 2A: Seismic behavior and design of deep, slender wide-flange structural steel beam-column members” with co-authors Chansuk, P., Uang, C.-M. (2017). The dissertation author is the first author of these reports.

Chapter 4 of this dissertation is based on material published by University of California, San Diego, titled “ATC-106: Seismic behavior and design of deep, slender wide-flange structural steel seam-column members” with co-author Uang, C.-M. (2016). In this chapter, materials currently being prepared for submission for publication by University of California, San Diego, titled “ATC-106 Phase 2A: Seismic behavior and design of deep, slender wide-flange structural steel beam-column members” with co-authors Chansuk, P., Uang, C.-M. (2017). These materials were also published by Engineering Journal, titled “Observations from cyclic tests on deep, wide-flange beam-

columns” with co-authors Harris, J., and Uang, C.-M. (2017). The dissertation author is the first author of these reports and paper.

Additionally, these materials published by Structural Stability Research Council, titled “Observations from cyclic tests on deep, slender wide-flange structural steel beam-column members”, with co-authors Uang, C., and Harris, J. (2015). The dissertation author is the second author of these paper.

Chapter 5 of this dissertation is based on material published by Structures Congress, titled “Classifying cyclic buckling modes of steel wide-flange columns under cyclic loading” with co-authors Harris, J., and Uang, C. (2015). Materials were also submitted for publication by EuroSteel Conference, titled “Cyclic backbone curves for steel wide-flange columns: A numerical study” with co-authors Harris J.L., and Uang C.-M. (2017). The dissertation author is the first author of these papers.

Chapter 6 of this dissertation is based on material published by Structures Congress, titled “Classifying cyclic buckling modes of steel wide-flange columns under cyclic loading” with co-authors Harris, J., and Uang, C. (2015). Materials were also submitted for publication by EuroSteel Conference, titled “Cyclic backbone curves for steel wide-flange columns: A numerical study” with co-authors Harris J.L., and Uang C.-M. (2017). The dissertation author is the first author of these papers.

VITA

2007	Bachelor of Science, Celal Bayar University, Turkey
2009-2011	Research Assistant, University of Illinois at Urbana Champaign
2011	Master of Science, University of Illinois at Urbana Champaign
2011-2015	Research Assistant, University of California, San Diego
2015	Doctor of Philosophy, University of California, San Diego

PUBLICATIONS

Referred Technical Journals

Ozkula, G., Harris, J., and Uang, C.-M. (2017). "Observations from cyclic tests on deep, wide-flange beam-columns." *Engineering Journal*, 54(1), 45-59.

Conference Proceedings

Lee, P., Garai, R., **Ozkula** G., Uang, C.M., Sarkisian, M. (2014) "Issues on Using Welded Built-Up Box Columns in Steel Special Moment Frames", *Proc. 10th US National Conference on Earthquake Engineering Frontiers of Earthquake Engineering*, Alaska.

Sarkisian M., Lee, P., Garai, R., **Ozkula**, G., Uang, C.M., (2013) "Effect of Built-up Box Column Electroslag Welding on Cyclic Performance of Welded Steel Moment Connections", *Proc., SEAOC*, San Diego.

Uang C.M., **Ozkula** G., Harris J.L. (2015). "Cyclic performance of deep wide-flange steel columns." *Proc., ICASS*, Lisbon, Portugal.

Uang, C., **Ozkula**, G., and Harris, J. (2015). "Observations from cyclic tests on deep ,

slender wide-flange structural steel beam-column members." *Proc., Structural Stability Research Council*, Nashville, TN.

Ozkula G., Harris J.L., and Uang C.-M. (2017). "Classifying cyclic buckling modes of steel wide-flange columns under cyclic loading." *Proc., Structures Congress, ASCE*, Denver, CO, 254-263.

Ozkula G., Harris J.L., and Uang C.-M. (2017). "Cyclic backbone curves for steel wide-flange columns: A numerical study." *Proc., EuroSteel Conference*, Copenhagen, Denmark.

Technical Reports

Ozkula, G., Kim, D.-W., Uang, C.-M. "Swaged Bulkhead Analysis Verification: Phase 1 Study on Full-Scale Testing of Swaged and Bulb Stiffened Bulkheads." *Report No. SSRP-12/02*, University of California at San Diego, La Jolla, CA.

Ozkula, G., Uang, C.-M. "Swaged Bulkhead Analysis Verification: Phase 2A Study on Full-Scale Testing of Steel Swaged Bulkheads." *Report No. SSRP-13/15*, University of California at San Diego, La Jolla, CA.

Ozkula, G., Mashayekh, A., Uang, C.-M. "Swaged Bulkhead Analysis Verification: Phase 3 Study on Full-Scale Testing of Swaged and Bulb Stiffened Bulkheads." *Report No. SSRP-12/02*, University of California at San Diego, La Jolla, CA.

Ozkula, G. and Uang, C.M. (2013), "Cyclic Testing of Steel RBS Moment Connections with Built-up Box Column for the San Diego Central Court House", *Report No. TR-*

13/01, Department of Structural Engineering, University California, San Diego, La Jolla, CA.

Ozkula, G. and Uang, C.M. (2015), "Seismic Behavior and Design of Deep, Slender Wide-Flange Structural Steel Beam-Column Members", *Report No. SSRP-15/06*, Department of Structural Engineering, University California, San Diego, La Jolla, CA.

Ozkula, G., Chansuk, P., Uang, C.-M. (2017). "Seismic behavior and design of wide-flange structural steel beam-columns: Numerical simulations." *Report No. SSRP-17/02*, University of California, San Diego, La Jolla, CA.

Ozkula, G., Chansuk, P., Uang, C.-M. (2017). "ATC-106 Phase 2A: Seismic behavior and design of deep, slender wide-flange structural steel beam-column members." *Report No. SSRP-17/04*, University of California, San Diego, La Jolla, CA.

ABSTRACT OF THE DISSERTATION

Seismic Behavior, Modeling and Design of Deep Wide-Flange Steel Columns for Special Moment Frames

by

Gulen Ozkula

Doctor of Philosophy in Structural Engineering

University of California, San Diego, 2017

Professor Chia-Ming Uang, Chair

Steel Special Moment Frame (SMF) is a preferred seismic force-resisting system for its architectural flexibility and high ductility. To achieve economy in design and construction, there is a growing trend to use deeper columns (e.g., with a section depth larger than 14 in.) to limit the code-enforced story drift requirements in recent years. A deep column has larger slenderness ratios and is more vulnerable to both local and global buckling. Since AISC *Seismic Provisions* assume that plastic hinging will occur at not only beam ends but also column bases, little research was available on the deep column hinging behavior under axial compression and cyclic drift.

A full-scale test program with thirty-seven deep columns subjected to both axial compression and cyclic drift was conducted. Test variables included sectional and member slenderness ratios for local and global buckling controls, axial force level, axial force type (constant versus variable), boundary condition (fixed-fixed versus fixed-flexible), transvers loading type (monotonic, cyclic, or near-faulty), axis of bending (strong-axis versus weak-axis) and bending type (uniaxial versus biaxial). From the database of this test program and a prior one with shallow (W14) stocky columns, three buckling modes were identified. Significant shortening was common to two buckling modes that were typical in deep columns, but not in shallow and stocky columns.

While the observed buckling modes could be properly simulated by nonlinear finite element simulation, a practical procedure to predict the governing buckling mode was needed for both cyclic modeling and design purposes. One procedure which considered the interaction between flange and web local buckling was first proposed; the accuracy of the procedure was verified by results from both tested columns and a large number of numerically simulated columns. Second, the combined experimental and numerically simulated database was then used in a multi-variate regression analysis to establish expressions for the cyclic backbone curves; these curves are needed for ASCE 41-type performance-based nonlinear response analysis of SMF. Finally, the same database was used to establish the limiting width-thickness ratios for potential adoption by AISC Seismic Provisions. A novel approach which considered the axial shortening as the limit state was proposed to establish these limiting width-thickness ratios for column design.

1 INTRODUCTION

1.1 General

Columns are one of the most critical elements in the building systems. They support the self-weight of the structure and occupancy loads (i.e., dead and live loads). Failure of only few columns may lead to a collapse of the structure. Columns in the lateral resisting systems also need to resist horizontal forces caused by wind or earthquake forces. These members are called beam-columns since they subject to both axial and flexural forces. This dissertation focuses on column members that are a part of the seismic force-resisting system and are subjected to both axial load and flexural forces. In this dissertation, the term column generally refers to beam-column for simplicity.

1.2 Steel Seismic Force-Resisting Systems

In the current design, members are selected so that the sections remain elastic under an expected demand. However, under extreme loading such as an earthquake, buildings are designed for a lower seismic force level by relying on ductility of structural members to dissipate the energy. The concept of “structural fuse” is applied in a manner similar to circuit breakers in electrical systems. The overall forces in the structure are limited by the capacity of structural fuses and the remaining members of the system are designed to remain elastic under the maximum demand that can be delivered by the structural fuses.

Seismic force resisting systems can be categorized into moment and braced frame systems. Braced frame systems act like a vertical cantilevered truss to resist lateral loading. Braced frames have different structural fuses based on their bracing type. Tension yielding and compression buckling of the diagonal braces is the structural fuse mechanism for

concentrically braced frames (CBF). For the eccentrically braced frame (EBF) systems, ductile behavior is provided by shear yielding or a combination of shear and flexural yielding of specially detailed link beams located between the diagonal braces. Another type of braced frame system is buckling-restrained braced frames (BRBs), which are designed such that the global brace buckling is prevented. Tension and compression yielding of the BRB steel core provides the ductile structural fuse behavior.

On the other hand, moment-resisting frames (MRF) resist the lateral loading through flexural action. Therefore, bending strength of the columns is one of the most important parameters for MRFs. The structural fuse mechanism in MRFs is yielding or plastic hinging at the end of beams. Columns are designed to remain elastic except for the first-story columns, which are expected to inevitably form plastic hinges at the bottom ends.

1.3 Statement of Problem

Moment-resisting frames are one of the most common frame systems that are used in highly seismic regions due to their high energy dissipation capacity and architectural versatility. Unexpected non-ductile failure of seismically designed steel moment connections that was observed after the Northridge, California Earthquake in 1994 had triggered extensive studies on the behavior of these Special Moment Frames (SMF). Extensive studies, including those by the SAC Joint Venture (FEMA 2000), have been conducted to evaluate the cyclic behavior and design of beam-to-column connections. Since plastic hinging in the beams is expected in SMF design, cyclic behavior of beams, but not columns have been researched as part of the moment connection studies.

Before the Northridge earthquake, shallow wide-flange columns (e.g., W14 or W12 sections) were commonly used in moment-resisting frames because of their comparable strong- and weak-axis radii of gyration. However, it was challenging to continue to design columns using shallow sections since the lateral flexibility feature of moment frames requires a large moment of inertia in the plane of the frames to satisfy the code-enforced story drift requirement (ASCE 2010). To bypass this problem, engineers turned to deeper steel columns. For example, Figure 1.1 and Table 1.1 show one shallow and one deep sections with the same strong-axis moment of inertia. The benefit of using the deep W27×258 section is obvious; the weight of the column is reduced from 605 to 258 lb/ft. But the width-to-thickness ratios ($b_f/2t_f$ and h/t_w) for flange local buckling (FLB) and web local buckling (WLB) control are much larger for the deep section. Because the radius of gyration about the weak-axis (r_y) is smaller, the deep column is also prone to out-of-plane global-type buckling like flexural buckling (FB) or lateral-torsional buckling (LTB).

Most of the available experimental data on deep steel wide-flange sections is related to beam members (Krawinkler et al. 1983, Uang and Fan 2006, Lignos et al., 2005, Okazaki et al., 2006). In testing of moment connections with deep columns without the presence of an axial load in the column, Chi and Uang (2002) showed that columns were prone to LTB. For applications in braced frames, Newell and Uang (2006) conducted full-scale testing of W14 columns (W14×132 to W14×370) subjected to various levels of axial load and cyclic drift. It was concluded that this type of shallow columns, even under high axial load, had a ductility capacity much higher than that specified in ASCE 41 (ASCE 2013), mainly due to the highly compact sections commonly found among the shallow columns.

When deep columns (e.g., depth > 14 in.) are used, local buckling is a concern because the width-thickness ratios for both flanges and web are much larger. Note that AISC specifications treat both FLB and WLB of rolled wide-flange sections as independent limit states and no interaction between them is considered. Also, global buckling including LTB and FB may be a concern. Unfortunately, minimal experimental research on columns was available to extensively support the seismic design or assessment provisions in AISC 341 (AISC 2010b) and ASCE 41 (ASCE 2013). To fill this gap, NIST developed a comprehensive research plan to study the seismic behavior and design of deep, slender wide-flange structural steel beam-column members (NIST 2011). The plan included studies at the member, subassemblage, and system levels.

1.4 Research Objective and Scope

The objective of this research was to experimentally study the cyclic response of deep-section steel columns for use in SMFs. The data generated from this test program was be used to (1) calibrate analytical models, (2) develop extensive database on deep columns, (3) categorize sections based on their buckling modes, (4) evaluate the adequacy of design provisions for seismic design of new construction in AISC 341, and (5) evaluate the adequacy of design provisions for seismic evaluation of existing construction in ASCE 41.

A total of thirty-seven deep columns were tested under cyclic lateral drifts and different levels of constant axial compression forces (C_a = 0.2, 0.3, 0.4, and 0.6 where $C_a = P_u/\phi_c P_y$). Three W30, five W24 and three W18 different sections covering a wide range of slenderness ratios for both local buckling and global buckling were evaluated. The majority of specimens were subjected to strong-axis bending with AISC loading protocol,

while the remaining specimens were tested with either monotonic loading, near-fault loading, weak-axis bending, or bi-axial bending. To mimic more realistic column top rotation, boundary condition effects were examined. Tensile coupon tests, cyclic coupon tests, and residual stress measurements were also conducted to characterize the material structural characteristics.

1.5 Dissertation Outline and Chapter Summary

A brief summary of each chapter follows.

1.5.1 Chapter 1

This chapter introduces the steel seismic force- resisting systems along with the concept of a structural fuse. The problem statement was provided and the outline of each chapter listed.

1.5.2 Chapter 2

A review of the current state of the practice for seismic design of steel beam-columns is presented. The results of previous research and their limitations are discussed.

1.5.3 Chapter 3

The experimental testing program, test setup, instrumentation plan, and loading sequences are described. Tensile and cyclic coupon tests were conducted and the results were used in finite element simulations. To examine the effect of residual stresses on the overall behavior of the columns, experimental techniques to measure residual stresses are described in this chapter.

1.5.4 Chapter 4

The results of thirty-seven full-scale deep columns (W30, W24 and W18) are presented. A wide range of slenderness limits were investigated. To examine the loading history effect, AISC cyclic loading, SAC near-fault loading, and monotonic loading were applied to specimens with four different axial load levels (C_a = 0.2, 0.3, 0.4 and 0.6). Majority of the sections were loaded in the strong-axis direction, however some specimens were subjected to weak-axis bending and biaxial bending. The boundary condition effect as well as the varying axial load effect were also investigated.

1.5.5 Chapter 5

This chapter describes finite element simulation used to populate a database for further analytical investigation. Finite element models were calibrated using the experimental test results discussed in Chapter 4. The numerical database included a total of 1,100 computer runs with one hundred-ten different column sections. Analysis results confirmed that there are mainly three buckling failure modes for AISC W-shapes. The definition of deep versus shallow column is also presented.

1.5.6 Chapter 6

Both experimental and numerical results showed in previous chapters that the failure modes of the columns are (1) symmetric flange buckling (SFB), (2) antisymmetric local buckling (ALB), and (3) coupled buckling (CB). The buckling modes of the columns are categorized in this chapter and a novel equation is proposed to classify the governing buckling mode.

1.5.7 Chapter 7

Nonlinear structural analysis approaches are discussed and the ASCE 41 predicted plastic rotation is introduced in this chapter. Backbone curve parameters based on their buckling modes are proposed for ASCE 41.

1.5.8 Chapter 8

Current slenderness limits of AISC *Seismic Provisions* are discussed and new limits based on the experimental and numerical simulations are proposed for W-shape columns. These web slenderness limits are intended to prevent excessive axial shortening.

1.5.9 Chapter 9

This chapter provides a summary of the experimental and analytical work presented in this dissertation and highlights original contributions made on the design and modelling of steel wide-flange section columns. Conclusions are presented.

Table 1.1 Comparison of Two Sample Column Sections

Section	Weight (lb/ft)	r_x (in.)	r_y (in.)	I_x (in.^{4})	I_y (in.^{4})
W14×605	605	7.8	4.55	10800	3680
W27×258	258	11.9	3.36	10800	859

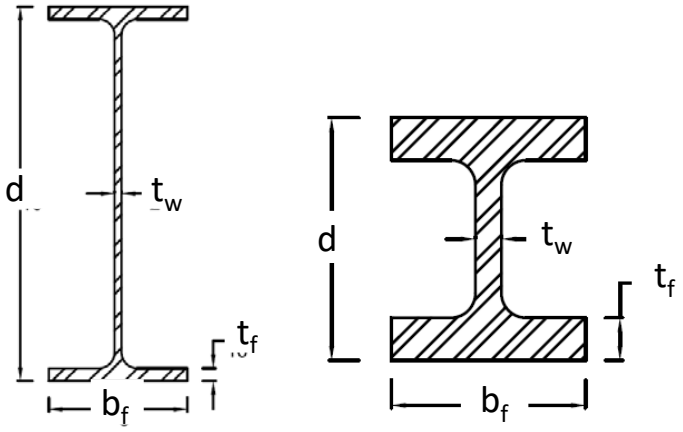

Figure 1.1 Deep Column vs. Shallow Column

2 LITERATURE REVIEW AND AISC DESIGN PRACTICE

2.1 Introduction

The primary function of columns in a building is to carry gravity loads. In a seismic event, columns in a moment frame are subjected to both axial force and bending moment due to lateral drift. To meet the story drift limitation specified in the building code (ASCE 2010), deep columns are frequently used by the designers in high seismic regions due to their high in-plane flexural stiffness. However, deep columns are vulnerable to local buckling and out-of-plane buckling. This chapter discusses previous research and the current design practice regarding the strength and deformation capacity of steel wide-flange columns under the combined axial and flexural loading.

2.2 Previous Research on Steel Wide-Flange Columns

Cyclic behavior of steel columns were investigated by many researchers for several decades. Popov et al. (1971 and 1973) tested eight small-size specimens, emphasizing the inelastic action in the columns of steel beam-column sub-assemblages. Later, Popov et al. (1975) tested another six specimens (W8×48 and W8×28) to study the behavior of column plastic hinges subjected to cyclic loading. Results indicated that flexural strength deterioration in the columns became severe when members were subjected to a compressive axial load larger than 50% of the axial yield strength, P_y. Additionally, considerable axial shortening occurred in the column plastic hinges under high axial loads. Therefore, it was suggested that the application of cyclic moment to an axially loaded column with a P/P_y ratio higher than 0.5 be avoided. For seismic rehabilitation, ASCE 41 (ASCE 2013) adopts this limit to distinguish between force-controlled and deformation-controlled columns.

Development of beam-column strength interaction equations has been based on numerous tests of relatively small size, wide-flange beam-columns of ASTM A7 and A36 steel subjected to a constant axial load (Galambos 1964; Bjorhovde et al. 1978). A database of small-scale beam-column tests (237 beam-columns of A36 steel subjected to monotonic loading) reported in Japanese literature was compiled by Nakashima et al. (1991). A good agreement was observed between the measured strength and the strength predicted by the design specification; the strength from tests was an average 16% higher than that predicted by the interaction equations.

MacRae et al. (1990) studied seismic behavior of moment-resisting frames and eccentrically braced frames. Eight column specimens were tested and the results showed excellent hysteretic behavior under cyclic loading. However, the negative effect of increased axial compressive loads on the column performance was documented. It was also reported that the amount of axial shortening depended on the magnitude of the axial load, yielded length of the member, stress-strain characteristics of the material, number of cyclic cycles being applied, and the displacement magnitude of those cycles. Nakashima et al. (1990) examined the behavior of steel beam-columns subjected to sideway. Forty-two beam-columns were tested under monotonic loading with axial forces, slenderness, geometrical and material properties as the major variables.

Schneider et al. (1993) tested five half-scale beam-column subassemblies. The test results indicated that weak-column strong-beam frames had sufficient ductility to sustain the inelastic demand induced by a major seismic event if the base shear strength exceeded that required by the code. They observed that column slenderness and axial load ratios affected the hysteretic behavior. But an over-strength base shear capacity had the largest

influence on the performance of weak-column strong-beam frames. It was also shown that an increase in axial load significantly degraded the column hysteretic behavior. This led to a concern about ductility of the columns subject to a combination of high axial load and flexural demand.

To predict nonlinear behavior of the structure under earthquake loading for performance-based design, concentrated plastic hinge models were developed and proposed in several standards (e.g., ASCE 41). The accuracy of these and their applicability to columns in both moment frames and braced frames were examined by Peng et al. (2008). Using an analytical procedure developed from first principles considering the reduction in member stiffness from axial force due to geometric and material nonlinearity, it was shown that the existing code equations were conservative. The research developed less conservative empirical equations based on the results. These models were applicable to frames with braced connection but not suitable for moment connection into the column. The analysis also showed that yielding often did not occur in the bottom-story columns during an earthquake excitation. A simple check was proposed to relate the axial force limit and the design drift to flexural yielding of columns, which could be used in conjunction with the proposed equations.

Wide-flange sections are routinely used for the construction of seismic force-resisting systems in the U.S. For braced frames, shallow and stocky sections (e.g., W14 section) are commonly used. However, deep sections (e.g., W27 section) are used nowadays in order to achieve economy when designing moment frames. Recent cyclic testing of deep, slender steel columns under varying degrees of axial compression showed that the overall behavior of the columns can be very different between shallow and deep

sections. Columns with a deep section are more prone to weak-axis buckling such as flexural buckling (FB) and lateral torsional buckling (LTB). In addition, their high width-to-thickness ratios (slenderness ratios) make them more susceptible to local buckling—either flange local buckling (FLB) or web local buckling (WLB).

Newell and Uang (2006) tested nine full-scale W14 columns for applications in braced frames. It was shown that these stocky columns had a very large inelastic story drift capacity even under a very high axial load ($0.75P_y$). But they demonstrated through numerical simulation that cyclic behavior of deep W27 columns subjected to high axial loads was characterized by a rapid strength degradation due to simultaneous flange and web local buckling.

Elkady and Lignos (2012) investigated the behavior of deep beam-columns through finite element simulation. Both axial shortening as well as severe strength degradation due to local buckling were reported.

Lamarche and Temblay (2011) performed full-scale compression buckling tests on steel columns subjected to monotonically and cyclically applied concentric as well as eccentric axial loading; no lateral drift was applied to the specimens. Experimental results were compared with a model created in the OpenSees framework. Analysis showed that the inclusion of residual stresses could reduce the compressive strength of the column by 30%. Local buckling in concentrically loaded columns did not significantly impact the column post-buckling axial strength based on the quasi-static cyclic test of a W12 section. However, local flange buckling did not occur before global buckling when the column was subjected to an eccentric axial load.

Cheng et al. (2013) subjected nine wide-flange cantilever members with large width-thickness ratios to a constant axial load coupled with a cyclic lateral displacement for weak-axis bending. The failure mechanism for each member was attributed to local instabilities. The authors concluded that the section classification rules in the current design specifications are not suitable for wide-flange sections bent about their weak-axis.

Fogarty and El-Tawil (2015) used detailed finite element models to evaluate the deep column response. It was observed that many deep columns that met the AISC high ductile requirement cannot reach 4% lateral drift under axial loads between $0.2P_y$ and $0.4P_y$. The width-thickness ratio of the web has a more significant effect than that of the flange.

Suzuki and Lignos (2015) tested lighter W14 cantilever columns with several loading protocols and concluded that realistic loading histories for the calibration of component deterioration models were essential and such protocols should capture the ratcheting effect of the member prior to failure. Using finite element simulation, Wu et. al (2017) also pointed out that selecting a proper loading history is critical for assessing the collapse of deep columns.

Based on the findings from available experimental results, National Institute of Standards and Technology (NIST) proposed an extensive research plan in 2011 (NIST 2011) to develop a nationally accepted guidelines for the design and assessment of deep, slender wide-flange beam-column members in seismic applications. The plan included studies at the member, subassemblage, and system levels. The first step in implementing this plan was to evaluate experimentally the cyclic behavior of deep columns at the member level. Test results will then be used by NIST to validate computational models and to

improve seismic design provisions. This research is the first step of this NIST research plan.

2.3 AISC Slenderness Requirements

To prevent premature local buckling in plate elements and lateral-torsional buckling of the member, AISC 360 (2010c) mandates certain limits on web and flange width-to-thickness ratios as well as member slenderness ratio, which are discussed in this section.

2.3.1 Flange Local Buckling

AISC 360 defines the flange local buckling criterion in terms of limiting width-to-thickness ratios. For an element of width, *b*, and thickness, *t*, the width-to-thickness ratio is

$$\lambda_f = \frac{b}{t} \tag{2.1}$$

where $b = b_f/2$ and $t = t_f$ is the flange thickness.

When local buckling governs the column capacity, the classical plate theory can be utilized to determine the plate strength. In general, plate compression elements can be classified into two categories: (1) stiffened elements, which are supported along both edges parallel to the compressive stress (i.e., web in a W-shape) and (2) unstiffened elements, which are supported along one edge and free on the other edge (i.e., flange in a W-shape). The elastic buckling stress of a plate element is

$$F_{cr} = k\frac{\pi^2 E}{12(1-\mu^2)}\left(\frac{t}{b}\right)^2 = k\frac{\pi^2 E}{12(1-\mu^2)}\left(\frac{1}{\lambda}\right)^2 \tag{2.2}$$

where *k* is the plate local buckling coefficient, which varies based on boundary and loading conditions as shown in Figure 2.1.

Plate elements with low *b/t* values can achieve yielding and strain hardening without experiencing local buckling, while buckling of slender plates with large *b/t* ratios is governed by Eq. (2.2) (Salmon et al. 2009). The actual strength for plates that buckle in the elastic range can also exceed the theoretical values as the plates develop additional post-buckling strength. Buckling curve of plate elements is illustrated in a dimensionless form in Figure 2.2. For elements with moderate slenderness ratios, residual stress and plate imperfections give rise to inelastic buckling represented by a transition curve shown in the figure.

To allow an axially loaded column to develop its full strength based on its overall slenderness ratio *KL/r*, local buckling in the plate elements must be avoided by satisfying the following expression:

$$F_{cr,component} \geq F_{cr,column} \tag{2.3}$$

Solving this equation for the limiting *b/t* ratio gives the ratio as a function of the column overall slenderness ratio, which is impractical. Design limits are generally simplified to assure that compression plate elements will reach yield stress F_y without an occurrence of local buckling even though the slenderness ratio of the column may prevent the elements from reaching yield stress. The width-to-thickness (*b/t*) ratios to prevent local buckling until the yield stress is reached are the λ_r values listed in Table B4.1 of AISC 360.

To ensure plate yielding without local buckling, the following expression must be satisfied:

$$F_{cr} = k\frac{\pi^2 E}{12(1-\nu^2)(b/t)^2} \geq F_y \tag{2.4}$$

Using $\nu = 0.3$, and E = 29,000 ksi, solving for the limiting *b/t* ratio gives

$$\frac{b}{t} \leq 0.951\sqrt{\frac{kE}{F_y}} \tag{2.5}$$

which is represented by point A ($\lambda_c = 1.0$) in Figure 2.2. Members subject to flexure have to tolerate larger plastic strain. Therefore, AISC proposes more stringent criteria for the limiting width-to-thickness ratios for members under flexure to ensure sufficient ductility before plate buckling occurs. Haaijer and Thurlimann (1960) compared the column and plate buckling curves as shown in Figure 2.3 and observed that plates achieved a strain hardening condition at relatively higher values of λ_c. Values of λ_o, a dimensionless constant indicating an onset of strain hardening, for columns and plates under uniform edge compression for F_y = 36 ksi were proposed as shown in Table 2.3. Plates can reach strain hardening without local buckling and provide higher rotation capacity if λ_c is smaller than λ_o. Setting λ_c equal to λ_o for fixed flanges (= 0.46), the limiting *b*/*t* ratios becomes

$$\frac{b}{t} \leq 0.437\sqrt{\frac{kE}{F_y}} \tag{2.6}$$

with k = 0.425 (the minimum value), the above equation is reduced to

$$\frac{b}{t} \leq 0.284\sqrt{\frac{E}{F_y}} \tag{2.7}$$

Since residual stress becomes irrelevant in the plastic range and material imperfections have negligible effect, AISC 360 relaxes the slenderness limit and suggest Eq. (2.8) for the flange slenderness

$$\frac{b}{t} \leq 0.38\sqrt{\frac{E}{F_y}} \tag{2.8}$$

AISC 341 (2010b) adopt this slenderness ratio in Table D1.1 for moderately ductile members and made it more stringent for highly ductile members as shown in Eq. (2.9).

$$\frac{b}{t} \leq 0.30\sqrt{\frac{E}{F_y}} \tag{2.9}$$

This limiting *b/t* ratio is defined as λ_{hd}.

2.3.2 Web Local Buckling

Web element of a W-shape is more sensitive to axial force than flange elements, making web slenderness limits more complicated to derive than flange slenderness limits. In addition, plates under a uniform edge compression in the longitudinal direction will develop a nonuniform stress profile after buckling occurs; this is due to loss of stiffness in the elements, which results in a stress redistribution. Accordingly, an effective width concept as a semi-empirical method is used to simplify the calculation of plate maximum strength. Utilizing this approach, the limiting width-to-thickness ratios for web elements were derived and implemented in AISC 360. The AISC code provisions for local and lateral buckling originated in the research by White (1956) and Lay and Galambos (1965, 1967). Yura et al. (1978) also indicated that AISC compact sections can provide a plastic rotation capacity of at least three to be used in plastic analysis. In the 1968 and later editions of the AISI specification for cold-formed steel members, the following equation was proposed.

$$\frac{b}{t} = 0.95\sqrt{\frac{kE}{\sigma_e}}\left(1 - 0.209\sqrt{\frac{kE}{\sigma_e}}\frac{t}{b}\right) \tag{2.10}$$

AISC 341 adopted Eq. (2.10) and modified it based on the available experimental test results over the years. Currently, Eq. (2.11b) has been used by AISC specification for highly ductile sections.

for $C_a \leq 0.125$

$$\lambda_{hd} = 2.45\sqrt{E/F_y}\,(1 - 0.93C_a) \tag{2.11a}$$

for $C_a > 0.125$

$$\lambda_{hd} = 0.77\sqrt{E/F_y}\,(2.93 - C_a) \geq 1.49\sqrt{E/F_y} \tag{2.11b}$$

2.3.3 Global Buckling (Member Slenderness)

AISC 341 (2010b) mandates a maximum unbraced length for highly ductile beams according to Eq. (2.12). However, there is no specific requirement for column slenderness.

$$L_b = 0.086 r_y E/F_y \tag{2.12}$$

To achieve a desirable rotation capacity in the plastic hinges, Kemp (1984) proposed that the member slenderness be limited according to Eq. (2.13) for members subjected to limited axial force in the regions of moment gradient:

$$\frac{L}{r_y} \leq \sqrt{\frac{\pi^2 E}{\sigma_y}}(0.6 - 0.4\beta)\left(\frac{1 - P/P_y}{1.5\,P/P_y}\right) \tag{2.13}$$

where β is the moment ratio at the position of lateral restraint.

Table 2.1 AISC 360 Limiting Width-to-Thickness Ratios for W-shapes

Width-to Thickness Ratio	Axial Compression	Flexure (Table B4.1b)	
	λ_r	λ_p	λ_r
$b_f/2t_f$	$0.56\sqrt{E/F_y}$	$0.38\sqrt{E/F_y}$	$1.0\sqrt{E/F_y}$
h/t_w	$1.49\sqrt{E/F_y}$	$3.76\sqrt{E/F_y}$	$5.70\sqrt{E/F_y}$

Table 2.2 AISC 341 Width-to-Thickness Ratios for W-shapes

Width-to Thickness Ratio	Axial Compression	
	λ_{hd}	λ_{md}
$b_f/2t_f$	$0.30\sqrt{E/F_y}$	$0.38\sqrt{E/F_y}$
h/t_w	for $C_a \leq 0.125$ $2.45\sqrt{E/F_y}(1-0.93C_a)$ for $C_a > 0.125$ $0.77\sqrt{E/F_y}(2.93-C_a) \geq 1.49\sqrt{E/F_y}$ where $C_a = \frac{P_u}{\phi P_n}$	for $C_a \leq 0.125$ $3.76\sqrt{E/F_y}(1-2.75C_a)$ for $C_a > 0.125$ $1.12\sqrt{E/F_y}(2.33-C_a) \geq 1.49\sqrt{E/F_y}$

Table 2.3 Slenderness for the Strain-hardening Range Based on Test Results (Haaijer and Thurlimann 1960)

Element	λ_0
Column	0.173
Long hinged flange	0.455
Fixed flange	0.461
Hinged web	0.588
Fixed web	0.579

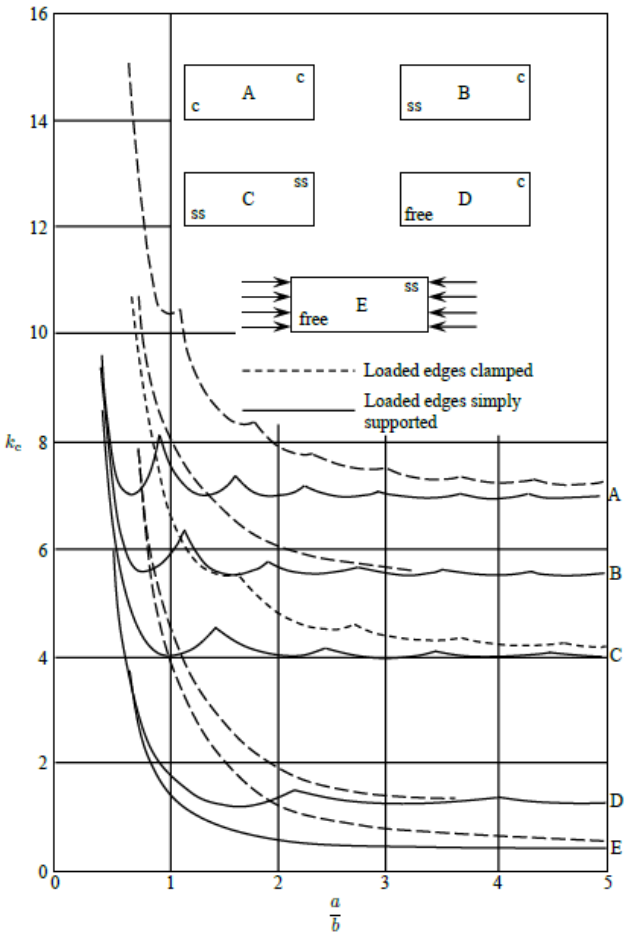

Figure 2.1 Elastic Buckling Coefficients (Salmon et al. 2009)

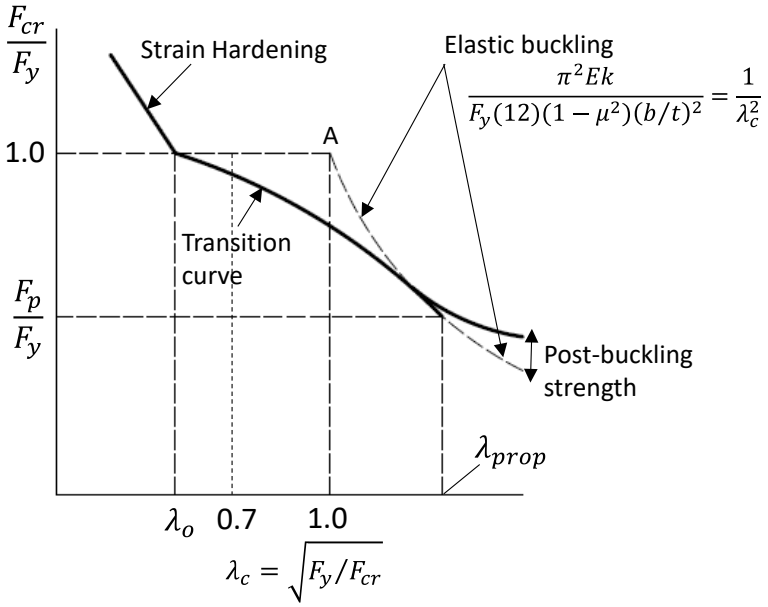

Figure 2.2 Dimensionless Representation of Plate Strength in Edge Compression (Salmon et al. 2009)

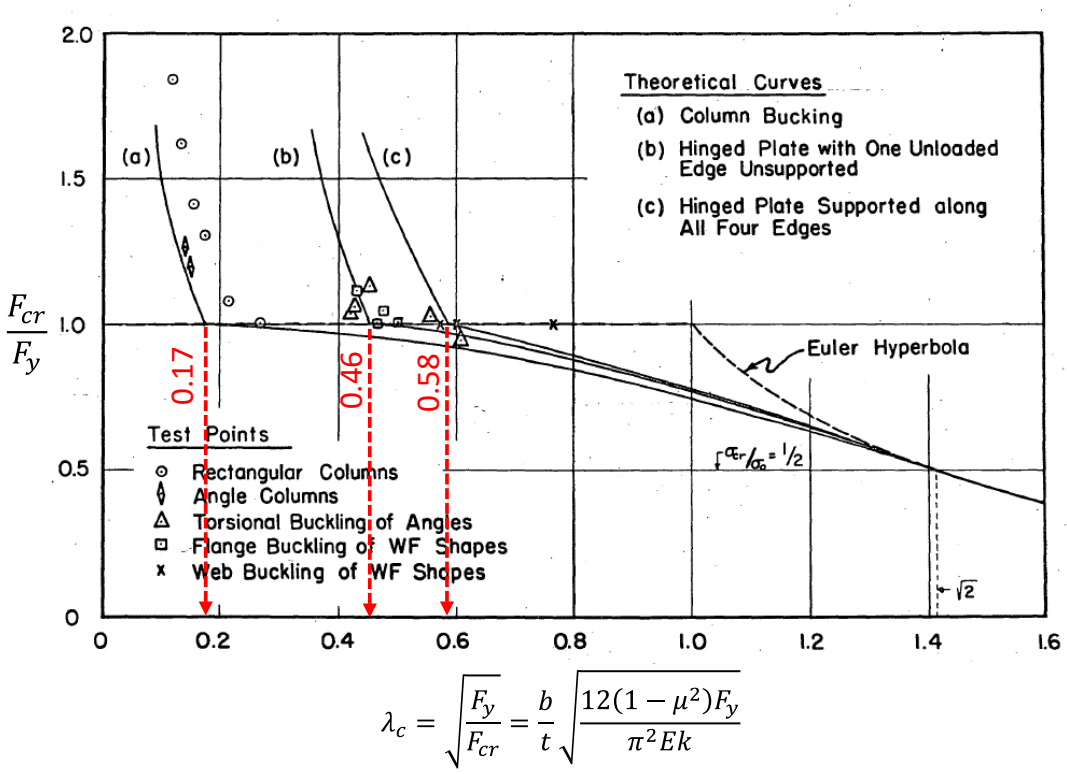

Figure 2.3 Plate Buckling Compared with Column Buckling (Haaijer and Thurlimann. 1960)

3 TESTING PROGRAM

3.1 Introduction

Thirty-seven full-scale deep column specimens were subjected to cyclic loading. Twenty-five specimens were tested in 2014 during Phase 1 of this project, while the other twelve specimens were tested in 2016 during Phase 2A. Phase 1 test matrix included five W24 sections (W24×55 to W24×176) in order to generate a database that covered a wide range of section slenderness ratios regarding FLB and WLB as well as member slenderness ratios concerning LTB and weak-axis FB. These columns were 18 ft long, simulating first-story columns under constant axial compression measured by a normalized parameter C_a (AISC 2010c):

$$C_a = \frac{P_u}{\phi_c P_n} \tag{3.1}$$

where P_u = applied axial compression, $P_n = A_g F_{yn}$, A_g = gross area, F_{yn} = nominal yield stress, and ϕ_c= resistance factor (0.9). With a few exceptions, three levels of axial compression (C_a=0.2, 0.4, and 0.6) were utilized in Phase 1 testing. A fixed-fixed boundary condition was simulated such that the specimens were subjected to bending in reverse curvature. All specimens were subjected to strong-axis bending, except for three and one specimens that were subjected to weak-axis bending and bidirectional bending, respectively. Table 3.1 summarizes the Phase 1 test matrix.

In Phase 2A, all except one were tested with constant axial compression. Since interior columns of SMFs experienced constant axial force while exterior columns were subjected to varying axial loads as a result of the overturning moment effect, a varying axial loading protocol was developed and implemented in one specimen to simulate the

exterior column response. In addition, since top ends of first-story columns would actually rotate, three specimens were subjected to fixed-flexible boundary condition. W30 and W18 sections with similar flange and web slenderness to Group 1 specimens of Phase 1 were also tested in Phase 2A to verify if the observed coupled buckling failure mode would also occur in columns of deeper and shallower sections. Phase 2A test matrix is summarized in Table 3.2.

3.2 Test Setup

The overall geometry of the test setup is shown in Figure 3.1. Testing was conducted in the Seismic Response Modification Device (SRMD) Test Facility at the University of California, San Diego. Specimens were tested in a horizontal position with one end (west end) connected to a reaction fixture fixed to a strong wall. The other end of the column (east end) was connected to a reaction fixture on the SRMD shake table platen. The platen has six degrees of freedom. Longitudinal movement of the platen imposed an axial force to the test specimen. A force-control algorithm was developed and employed to maintain a constant axial force or vary the axial load. Displacing the platen transversely in the horizontal plane and vertically out of the plane imposed strong-axis and weak-axis bending to the specimens, respectively. For boundary condition effect tests, the platen also rotated in the plane of strong-axis bending of the column. Displacement-control method was used for transverse, vertical, and rotational movements.

3.3 Test Specimens

Figure 3.2 and Figure 3.3 show the geometry of test specimens. The clear length of the column is 18 ft. End plates of 2-1/2 in. thick (or 3-1/2 in. thick for Groups 11, 12, and

13 specimens) were welded to each specimen. Another test variable in this program is L/r_y, where L is the column clear length, and r_y is the radius of gyration about the weak axis. To achieve a range of interest for L/r_y, it was decided to keep the column clear length constant and select different column sections (see Table 3.1). The weld access hole profile specified in AISC 360 (AISC 2010c) was used for welding the column to the end plates.

Figure 3.4 illustrates the range of specimen flange and web slenderness with dotted lines indicating compactness limits specified in AISC 341 (AISC 2010b) as discussed in Chapter 2.

Regarding specimen designation, letters "L", "M", and "H" represent low ($C_a =$ 0.2), medium ($C_a = 0.4$), and high ($C_a = 0.6$) axial load level, respectively. Group 12 (W30×261) is the heaviest and most compact section tested in this program. The shaking table at its operational maximum capacity could only apply an axial load equal to 30% of the section's yield strength. Therefore, Group 12 was tested with C_a equal to 0.3 and was designated as "LM" to indicate that level of axial load. Only Specimen 2Z was tested without any axial load. In Phase 1, Specimens 2L-P and 6L-P ("P" stands for pushover) were tested monotonically in strong-axis and weak-axis bending, respectively. In Phase 2A, Specimen 12LM-P was tested monotonically in strong-axis bending. Specimen 7M was subjected to bi-axial bending. A near-field loading protocol was implemented in testing of Specimen 8M.

In Phase 2A, the applied constant axial force was initially set to $C_a = 0.2$. However, due to limitations of test facility, some groups were subjected to higher axial load levels; a higher axial load would reduce the flexural strength of the column, and, hence, the transverse load requirement to the test facility. In Phase 1, an "unusual" coupled buckling

occurred during testing of Group 1 columns with a W24×176 section. Therefore, it was decided to test the same section in Phase 2A, designated as Group 11, to confirm if the same failure mode would be reproduced. In addition, W30×261 and W18×130 sections with similar flange and web slenderness ratios to Group 1 specimens were tested in Phase 2A to determine whether the knowledge about coupled buckling mode observed in Group 1 specimens could be applied to deeper (W30) and shallower (W18) sections.

In Phase 1 testing, Group 5 specimens failed due to elastic lateral-torsional buckling with no plastic hinge formation because the L/r_y ratio was much larger (= 161.2) compared to other specimens. Consequently, inelastic cyclic response data representing this section's slenderness characteristics was missing. To produce that data sample, Group 14 (W30×90) with similar section slenderness but a lower L/r_y ratio than Group 5 specimens was selected for testing in Phase 2A.

All the column specimens were tested with a fixed-fixed boundary condition in Phase 1 research. Since the top ends of the columns in SMFs actually will rotate with the beams, three specimens (11H-BC, 13M-BC, and 16M-BC) were subjected to fixed-flexible boundary condition in Phase 2A testing to investigate such effect. Specimen 11H-VA was tested with a varying axial force loading protocol to examine the behavior of exterior columns. In addition, it was decided to extend the database range to include sections more compact than Group 1; thus, section W18×192 was assigned to Group 15.

3.4 Testing Sequence and Loading Protocol

Newell and Uang (2006) developed a loading protocol for testing columns in braced frames. Since the objective of this research was to evaluate the cyclic response of columns

in steel moment frames, it was decided to use the AISC loading protocol both in Phases 1 and 2A testing. The AISC loading protocol was originally developed by Krawinkler et al. (2000) for the SAC Joint Venture to simulate the effect of far-field ground motions. AISC 341 (AISC 2010b) specifies a standard loading protocol for qualifying cyclic tests of beam-to-column moment connections of Special and Intermediate Moment Frames. The test is typically conducted by imposing a story drift ratio (SDR) to the moment connection specimen as shown in Figure 3.5(a). The AISC loading protocol mentioned above was used for testing most specimens in this research.

Reversed AISC loading protocol is shown in Figure 3.5(b). This loading scheme was implemented in two specimens (2L-P and 6L-P) following a monotonic test to a certain drift level. As shown in the figure, loading from *O* to *A* generates a monotonic response up to 4% SDR, which can be used to compare with the cyclic backbone curve of another nominally identical specimen subjected to cyclic test. Once the specimen was loaded to point *A*, testing continued to point *B*. The effect of loading sequence can be investigated by comparing the entire response of the reversed AISC loading protocol from points *O* to *B* with the response generated from the standard AISC loading protocol.

Specimen 7M was tested with biaxial bending. Since AISC 341 does not provide any guidance on biaxial testing, it was decided to use the AISC standard loading protocol for strong-axis bending coupled with the same protocol but was scaled by a factor 0.3 for the amplitude in the weak-axis direction as illustrated in Figure 3.5(c). Krawinkler et al. (2000) also developed a loading protocol as shown in Figure 3.5(d) to simulate the near-fault ground motion effect; this protocol is not required by the AISC Seismic Provisions. This was utilized in testing of Specimen 8M.

In this research, a constant axial compressive load was applied to the column specimens before a cyclic story drift protocol was imposed on the moving end of the column; the axial compression was intended to simulate mainly the gravity load effect because the seismic axial load in the interior columns was limited. To evaluate the exterior column behavior, one specimen (11H-VA) was tested with varying axial load as shown in Figure 3.6(b). The compressive force fluctuates about the gravity load of C_a = 0.45. The amplitude of axial force variation grows proportionally to the levels of lateral drift, simulating increasing overturning moment as the structure undergoes larger lateral displacement. At a certain drift level, say 1.5% drift, plastification in member level will occur, stiffness of the frame will decrease, and the overturning moment will stabilize as the frame approaches its ultimate strength. Accordingly, the variation of C_a was bounded between 0.3 and 0.6 at 1.5% drift and beyond.

All the column specimens were tested with a fixed-fixed boundary condition in Phase 1 research. Since top ends of columns in an SMF actually will rotate, the effect of fixed-flexible boundary condition was also included in Phase 2A testing. To evaluate the end rotation to be applied to these specimens, a three-bay, four-story SMF building designed by Harris and Speicher (2015) was analyzed. Results from nonlinear time-history analysis with 14 ground motions, scaled to match the Design Earthquake per ASCE 7 (ASCE 2010), showed that rotation at the column top and first-story drift angle are very similar in magnitude. Thus, the same amount of rotation as the story drift angle of the AISC loading protocol was imposed on one end of the specimens in fixed-flexible boundary condition tests. A complete loading scheme for fixed-flexible test is demonstrated in Figure 3.6(c).

3.5 Instrumentation

A combination of displacement transducers, inclinometers, strain gauge rosettes, and uniaxial strain gauges was used to measure the global and local responses. Figure 3.7 and Figure 3.8 show the displacement transducer and strain gauge locations, respectively. The movement and the associated force in each of the six degrees of freedom of the platen were also recorded.

3.6 Steel Mechanical Characteristics

3.6.1 Tensile Coupon Test

ASTM A992 was specified for all column specimens, and A572 Gr. 50 steel was specified for the end plates. Table 3.3 summarizes the mechanical characteristics of the materials used in Phases 1 and 2A. Coupons were taken from both flanges and webs of specimens. The table shows that web yield stresses is generally higher than flange yield stresses. The engineering stress versus strain relationships are shown in Figure 3.9.

3.6.2 Cyclic Coupon Test

Four round coupons (see Figure 3.10) were obtained from a W24×131 column in accordance with ASTM E606 (ASTM 1980). Each 3/8-in. diameter round coupon was instrumented with strain gages in order to control the cyclic test. Each of the four coupons was tested with the following strain ranges: 0.02 in./in., 0.04 in./in., 0.08 in./in., and 0.12 in./in.

Figure 3.11 shows the test results. The first three coupons were cycled 10 times, while the last coupon was cycled only 5 times before buckling occurred. A composite plot of all four constant-amplitude test data is presents in Figure 3.12.

For Coupon 1, after completing 10 cycles at the target strain range of 0.02 in./in., testing continued for 5 cycles at 0.04 in./in. strain range and another 5 cycles at the strain range of 0.06 in./in. before the coupon buckled; see Figure 3.13(a) for the complete response. Similarly, Coupon 2 was subjected to 5 additional cycles at the strain range of 0.06 in./in. and 2 additional cycles at the strain range of 0.08 in./in. before the coupon buckled. The measured response is shown in Figure 3.13(b).

3.7 Residual Stresses

Residual stresses play an important role on the buckling strength and stiffness of steel structural members subjected to compressive, flexural, and torsional loading (Ziemian 2010). Various studies have been completed in the past half century to determine residual stress profiles for various steel structural members based on their manufacturing, fabrication, and cross-sectional geometries. Examples of experimental studies include cold-formed channels (Weng and Pekoz 1990) welded flame-cut high strength H-sections (Wang et al. 2012), cold-bent wide flange sections (Spoorenberg et al., 2010), and cold-rolled I-sections (Jez-Gala 1963). In this study, W24×131 and W14×176 sections were examined to evaluate the residual stress profiles in the sections. For numerical modeling purposes (see Chapter 5), residual stress measurements were also conducted on a deep column section.

Experimental techniques to measure residual stresses can be classified as destructive (sectioning), semi-destructive (partial sectioning, hole-drilling), and nondestructive (ultrasonic testing). In this study, the sectioning method, originally developed by Luxion and Johnson in 1948 (Ziemian 2010), was used. Tebedge et al (1973) further elaborated on a step-by-step procedure of sectioning and hole-drilling. In the sectioning method, portions of a member are instrumented and cut into sections and slices (see Figure 3.14). Instruments such as Whittemore gages, linear variable displacement transducers (LVDTs), and electrical strain gages can be used to measure the initial and final strains of the specimens before and after cutting, respectively. The strains are then converted to stresses according to Hooke's Law.

Following Technical Memorandum No. 6 of SSRC (Ziemian 2010), measurements were made on a W24×131 member. For comparison purposes, a W14×176 member was also included in the study. Figure 3.15 shows the sectioning of the W24×131 member. The change in length was then measured by a Whittemore gage (see Figure 3.16). See Ozkula and Uang (2015) for the details of the measurement process including data reduction. The resulting residual stresses for both sections are presented in Figure 3.17 and Figure 3.18.

3.8 Data Reduction

3.8.1 Fixed-fixed Boundary Condition

The story drift ratio (SDR) is defined as the imposed lateral displacement, Δ, divided by the column length, L.

$$SDR = \frac{\Delta}{L} \tag{3.2}$$

Assuming an inflection point at mid-length of the column for a fixed-fixed boundary condition, the end moment can be computed as

$$M = \frac{1}{2}(VL + P\Delta) \tag{3.3}$$

where V is the lateral load (i.e., column shear) and P is the measured axial load with compression as positive. The first term on the right side is the primary moment, and the second term is due to the P-Δ effect. In the following chapters, sometimes it is more convenient to present the moment in a normalize form, where the moment is normalized by the reduced plastic moment, M_{pc} (ASCE-WRC 1971):

when $P/P_y \geq 0.2$,

$$M_{pc} = \frac{9}{8} M_p \left(1 - \frac{P}{P_y}\right) \tag{3.4a}$$

when $P/P_y < 0.2$,

$$M_{pc} = M_p \left(1 - \frac{P}{2P_y}\right) \tag{3.4b}$$

Figure 3.2(b) and Figure 3.3(b) shows the bolted connection at both ends of each specimen. Despite that 1 ¾ -in. diameter bolts were used to fasten each end to the fixed fixture, end rotation was unavoidable due to the flexibility of the end plate and elongation of the bolts. Such flexibility contributed to the elastic component of the lateral drift, Δ, in Eq .(3.5). The measured drift was composed of the following three components:

$$\Delta_m = \Delta_e + \Delta_c + \Delta_p \tag{3.5}$$

where Δ_e and Δ_p represent the elastic and plastic component of the column deformation, and Δ_c is the component due to connection flexibility. The following procedure was used to remove the Δ_c component.

Assuming that the Δ_c component remained elastic throughout the testing, (Δ_e+Δ_c) would collectively represent the elastic component of the measured Δ_m. The plastic component was extracted as follows:

$$\Delta_p = \Delta_m - \frac{V}{K_{em}} \tag{3.6}$$

where V is the measured column shear, and K_{em} is the measured elastic stiffness (or slope) computed from the initial (elastic) part of the Δ_m versus V response.

Then a theoretical Δ_e was added to the experimentally determined Δ_p for the corrected story drift:

$$\Delta = \Delta_e + \Delta_p \tag{3.7a}$$

where

$$\Delta_e = \frac{V}{K_e} \tag{3.7b}$$

For a fixed-fixed boundary condition without an axial compression, the theoretical elastic stiffness is

$$K_e = \frac{12EI_x}{L^3} \tag{3.8}$$

When an axial compression, P, exists, the elastic stiffness can be computed by assuming a sine-wave deflected shape shown in Figure 3.19. By using the moment-area method, the reduced elastic stiffness can be derived (Salmon et al. 2009):

$$K'_e = K_e\left(1 - \frac{P}{P_e}\right) = K_e - \frac{12}{\pi^2}\left(\frac{P}{L}\right) \tag{3.9}$$

where

$$P_e = \frac{\pi^2 EI}{L^2} \tag{3.10}$$

An example correction for the response of Specimen 2H subjected to strong-axis bending is shown in Figure 3.20. For this specimen, the values of K_{eam}, K_e, and K'_e are 87.8, 138.8, 133 kip/in., respectively.

3.8.2 Fixed-flexible Boundary Condition

The shake table's recorded data including the forces, moments, displacements, and rotations in all three directions of primary axes measured at the center of the table's platen. This reference point is 25 in. away from the east end plate connecting the column to the shake table fixture. In fixed-fixed boundary condition tests, the measured lateral displacement data obtained from the shake table's data acquisition system reflects the exact lateral displacement experienced by the columns. However, in fixed-flexible experiment, lateral displacement at the column end is no longer equal to the lateral displacement measured at the table's reference point due to the applied rotation to simulate flexible boundary condition. The following relationship is used to obtain the actual lateral displacement at the column's loading end:

$$\Delta = \Delta_T - \theta_{EAST} L_T \tag{3.11}$$

where Δ_T is the measured lateral displacement of the shake table, θ_{EAST} is the applied rotation at the east end of the column (defined positive in the counter-clockwise direction), and L_T is the distance between the table's reference point and the column end (27 in. and 28 in. for 2 in. and 3 in. thick end plates, respectively).

For fix-flexible boundary condition, east end moment of the column is smaller than west end moment. The measured moment of the shake table does not represent the east end moment in the column because it is affected by the shear and axial force transferred from the deformed column to the table fixture and their eccentricities relative to the table platen's center. Considering the moment equilibrium of the shake table, the following relationship was derived to calculate the actual east end moment of the column (see Figure 3.21):

$$M_{EAST} = M_T - V_T L_T \cos(\theta_{EAST}) - P_T L_T \sin(\theta_{EAST}) \quad (3.12)$$

where M_T, V_T, and P_T are the measured strong-axis moment, lateral force, and axial force obtained from the table with the same sign convention used for the column (see Figure 3.19)

Considering the moment equilibrium of the column and sum the moment about the west end, the following equation calculates west end moment:

$$M_{WEST} = V_T L + P_T \Delta - M_{EAST} \quad (3.13)$$

The calculated moment based on Eq. (3.13) was verified with the moment obtained from strain gauge readings when the columns remained in the elastic range.

3.9 Acknowledgements

The text below is reproduced verbatim as it appears in the acknowledgments section on page xvii per the UCSD Office of Graduate Studies Formatting Requirements.

Chapter 3 of this dissertation is based on material published by University of California, San Diego, titled "ATC-106: Seismic behavior and design of deep, slender wide-flange structural steel seam-column members." with co-author Uang, C.-M. (2016). In this chapter, materials currently being prepared for submission for publication by

University of California, San Diego, titled “ATC-106 Phase 2A: Seismic behavior and design of deep, slender wide-flange structural steel beam-column members” with co-authors Chansuk, P., Uang, C.-M. (2017). The dissertation author is the first author of these reports.

Table 3.1 Phase 1 Test Matrix

Group No.	Shape	Specimen Designation	Normalized Slenderness			Column Axial Load		Bending Direction
			λ_f	λ_w	λ_L	C_a	P (kips)	
1	W24×176	1L	0.67	0.57	1.42	0.2	465	Strong-axis
		1M		0.61		0.4	931	
		1H		0.66		0.6	1396	
2	W24×131	2Z	0.93	0.66	1.46	0.0	0	
		2L		0.70		0.2	347	
		2L-P		0.70		0.2	347	
		2M		0.76		0.4	693	
		2H		0.82		0.6	1040	
3	W24×104	3L	1.18	0.85	1.49	0.2	276	
		3M		0.91		0.4	551	
		3H		1.00		0.6	826	
4	W24×84	4L	0.81	0.91	2.22	0.2	222	
		4M		0.98		0.4	445	
5	W24×55	5L	0.81	1.08	3.23	0.2	146	
		5LM		1.12		0.3	219	
		5M		1.26		0.4	292	
6	W24×131	6L	0.93	0.70	1.46	0.2	347	Weak-axis
		6L-P		0.70		0.2	1040	
		6H		0.82		0.6	1040	
7	W24×131	7M	0.93	0.76	1.46	0.4	693	Biaxial
8	W24×131	8M	0.93	0.76	1.46	0.4	693	Strong-axis, Near Field

Table 3.2 Phase 2A Test Matrix

Group No.	Shape	Specimen Designation	Slenderness			Column Axial Load		Justification	Expected Behavior
			$b_f/2t_f$	h/t_w	L/r_y	$C_a = \frac{P_u}{\phi_c P_y}$	P (kips)		
11	W24×176	11M	4.81	28.7	71.05	0.4	930	1L Retest	Coupled Buckling
		11H-VA				0.6	Varies	Varying Axial Force Effect	
		11H-BC					1396	Boundary Condition Effect	
12	W30×261	12LM	4.59	28.7	61.19	0.3	1040	Similar to Group 1 (Section Depth Effect)	Coupled Buckling
		12LM-P						Monotonic Loading	
13	W30×173	13M	7.04	40.8	63.16	0.4	916	Similar to Group 2	In-plane Plastic Hinging
		13M-BC						Boundary Condition Effect	
14	W30×90	14L	8.52	57.5	103.35	0.2	237	More Slender than Group 5	In-plane Plastic Hinging
15	W18×192	15L	3.27	16.7	77.42	0.2	506	More Compact than Group 1	Coupled Buckling
16	W18×130	16M	4.65	23.9	80.0	0.4	690	Similar to Group 1 (Section Depth Effect)	
		16M-BC						Boundary Condition Effect	
17	W18×76	17L	8.11	37.8	82.76	0.4	201	Similar to Group 3	In-plane Plastic Hinging

Table 3.3 Steel Mechanical Properties

Shape	Coupon Name	Group No.	Yield Stress[a,c] (ksi)	Tensile Strength[a,c] (ksi)	Elong.[a,b,c] (%)
W24×176	1-F	GR.1	52.5	81.8	38.1
	1-W		58.5	82.5	38.0
W24×131	2-F	GR.2	50.8	75.9	38.4
	2-W		55.4	77.7	35.4
W24×104	3-F	GR.3	51.5	78	36.5
	3-W		58.1	80.6	31.3
W24×84	4-F	GR.4	51.3	77.6	36.2
	4-W		58.8	80.2	31.0
W24×55	5-F	GR.5	53.7	71.5	38.0
	5-W		59.8	74.3	32.4
W24×176	11-F	GR.11	52.11	83.53	33.20
	11-W		51.42	82.67	36.07
W30×261	12-F	GR.12	54.61	75.64	38.33
	12-W		59.61	74.44	41.04
W30×173	13-F	GR.13	57.30	73.59	41.73
	13-W		67.15	79.73	37.01
W30×90	14-F	GR.14	58.30	73.73	37.08
	14-W		62.65	75.90	38.10
W18×192	15-F	GR.15	55.27	77.44	36.31
	15-W		60.80	77.07	39.56
W18×130	16a-F	GR.16	49.92	78.97	34.51
	16a-W		53.27	78.79	34.83
	16b-F		52.11	71.19	40.92
	16b-W		56.61	71.93	40.11
W18×76	17-F	GR.17	57.30	75.26	38.46
	17-W		54.77	66.10	32.25

[a] Average values are based on tensile coupon testing.

[b] Elongations are based on a 2-in gage length.

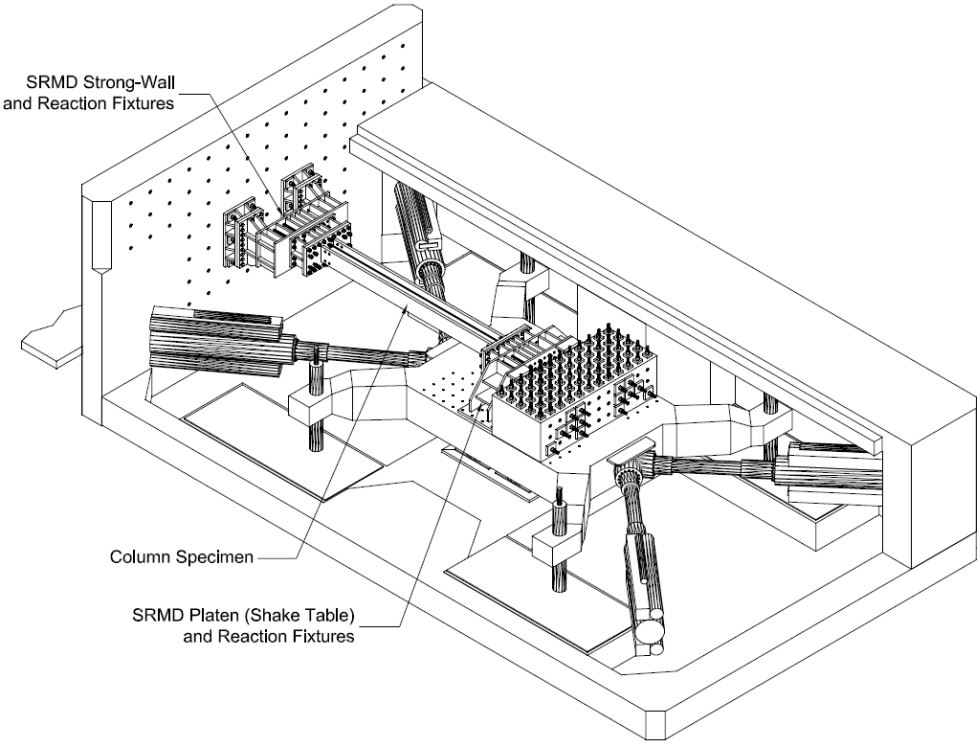

(a) Schematic View

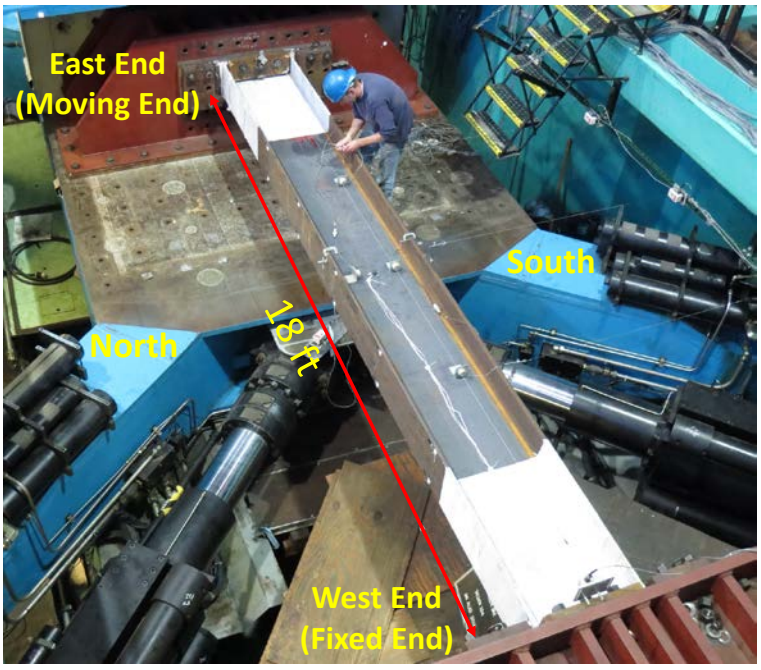

(b) Overview of Specimen

Figure 3.1 Test Setup

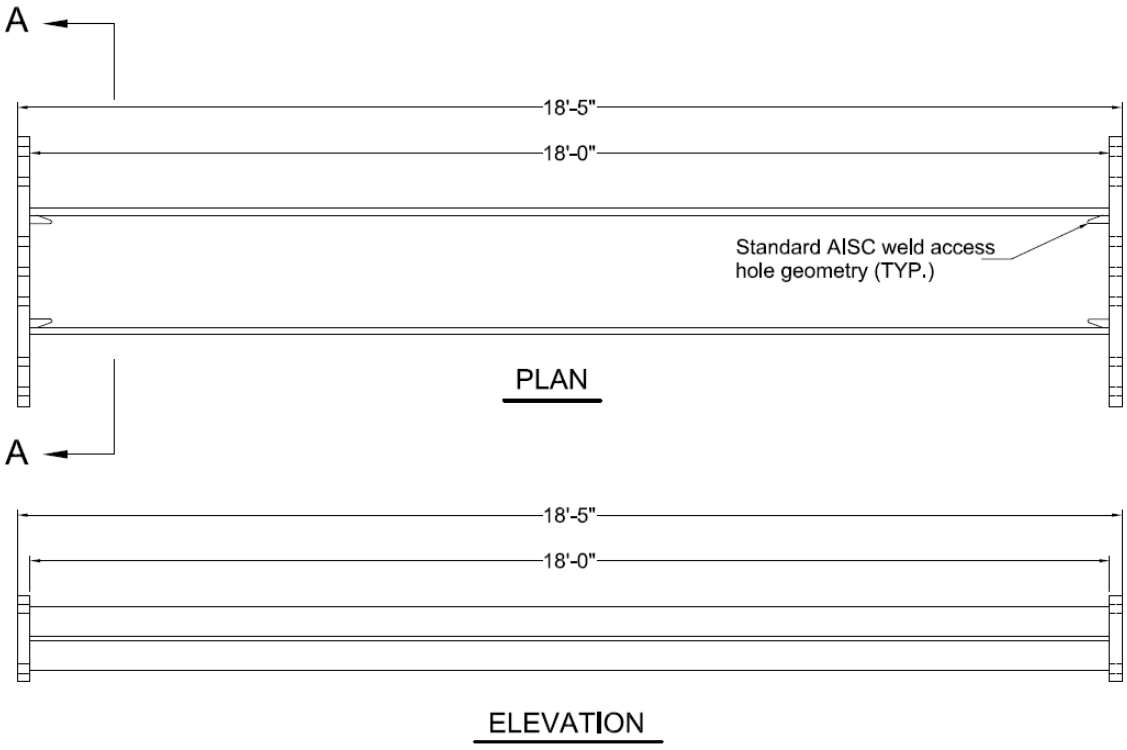

(a) Overall Dimentions

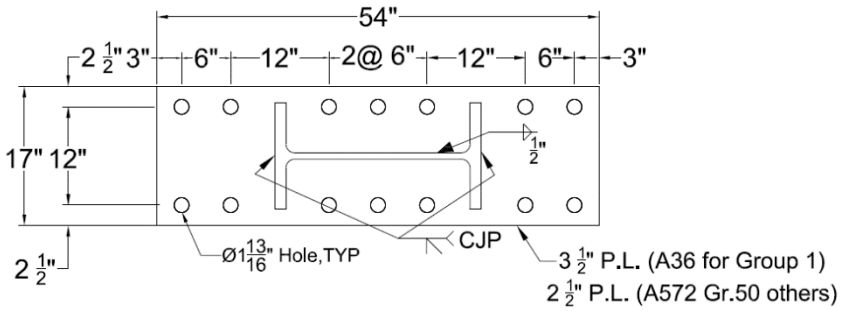

(b) Base Plate

Figure 3.2 Specimen Geometry and End Details (Strong-axis)

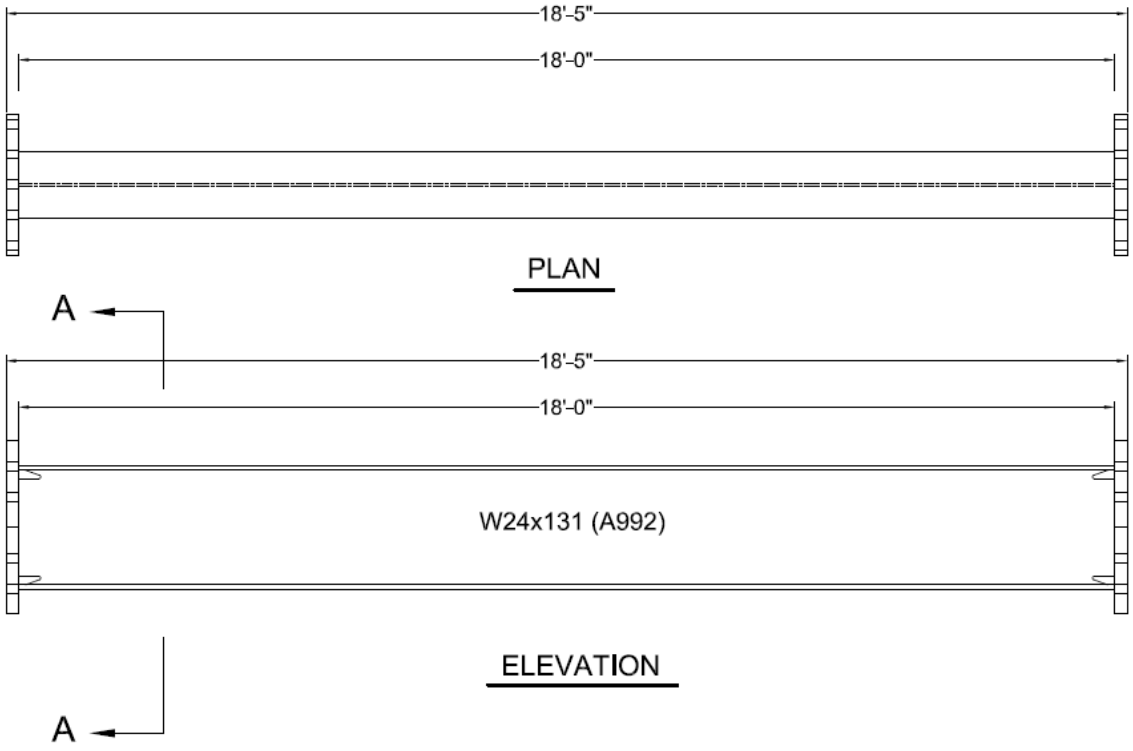

(a) Overall Dimentions

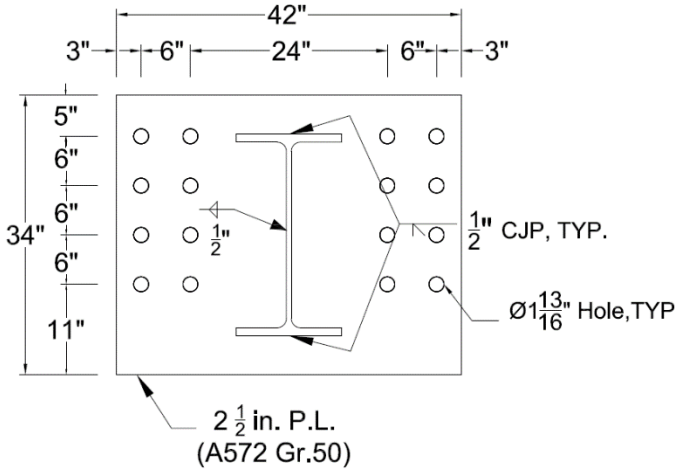

(b) Base Plate

Figure 3.3 Specimen Geometry and End Details (Weak-axis)

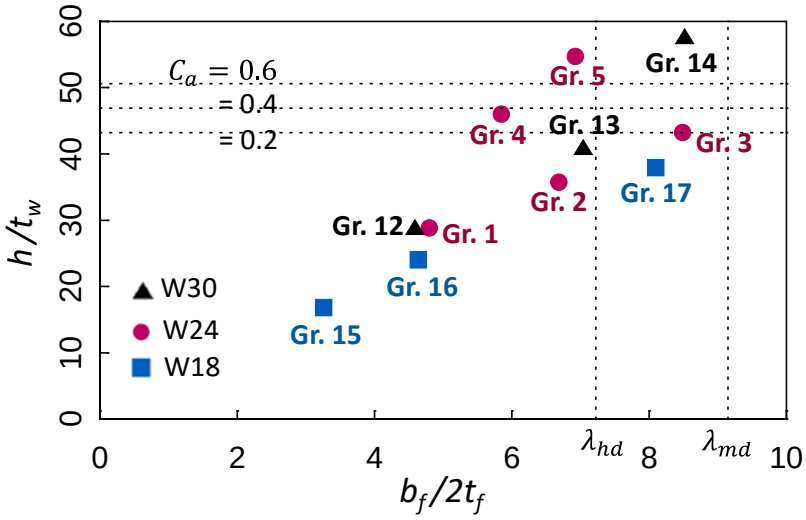

Figure 3.4 Comparison of width-to-thickness ratios

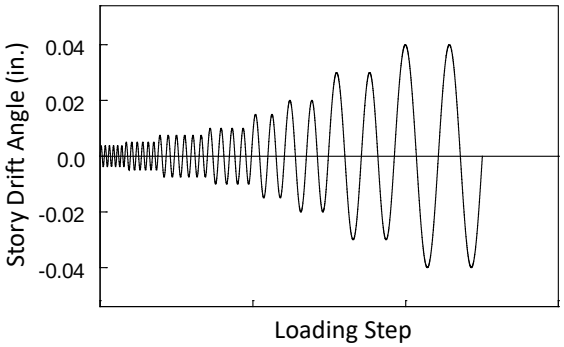

(a) Loading Scheme A: AISC Loading Protocol

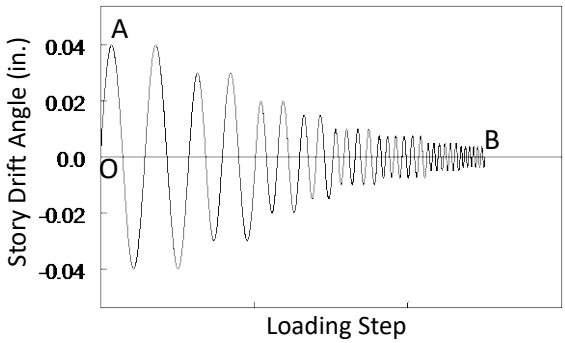

(b) Loading Scheme B: Reversed AISC Loading Protocol

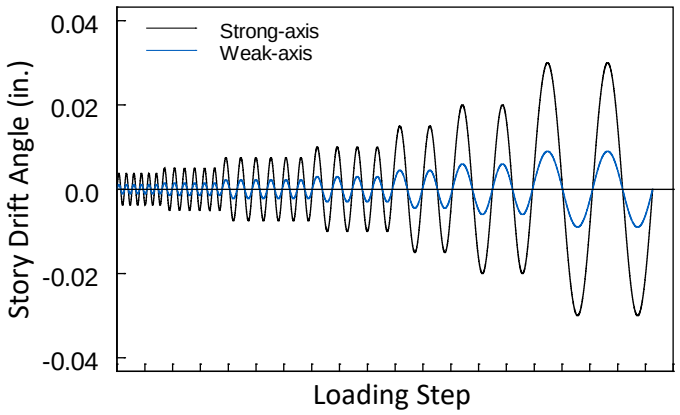

(c) Loading Scheme C: Biaxial Loading Protocol

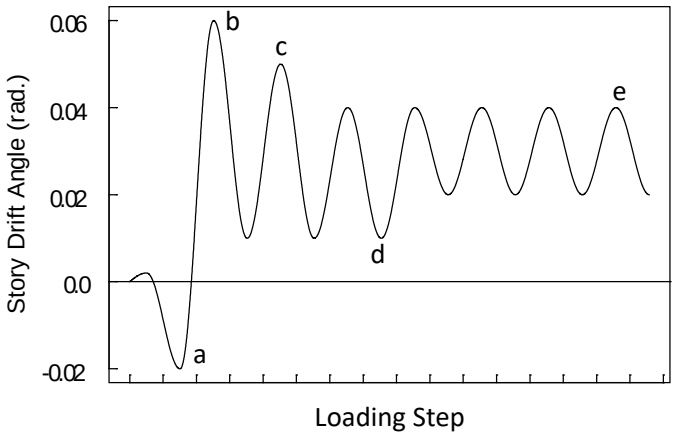

(d) Loading Scheme D: SAC Near-fault Loading Protocol

Figure 3.5 Phase 1: Cyclic Loading Schemes

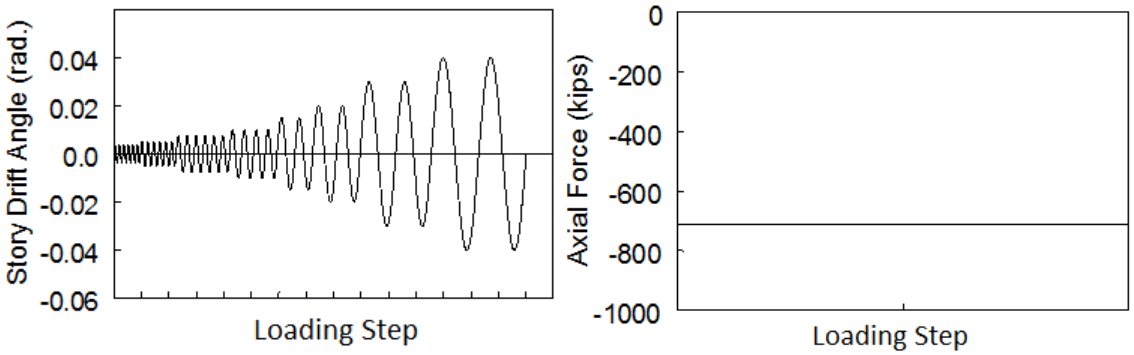

(a) Loading Scheme A: AISC Loading Protocol with Constant Axial Load

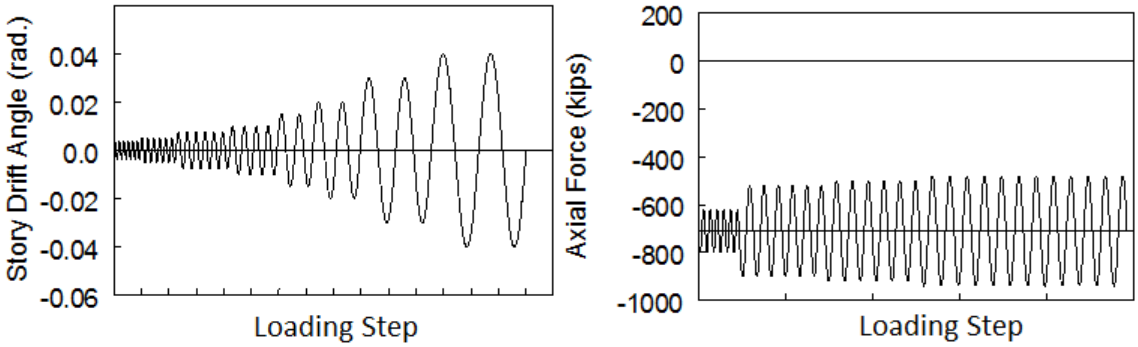

(b) Loading Scheme B: AISC Loading Protocol with Varying Axial Load

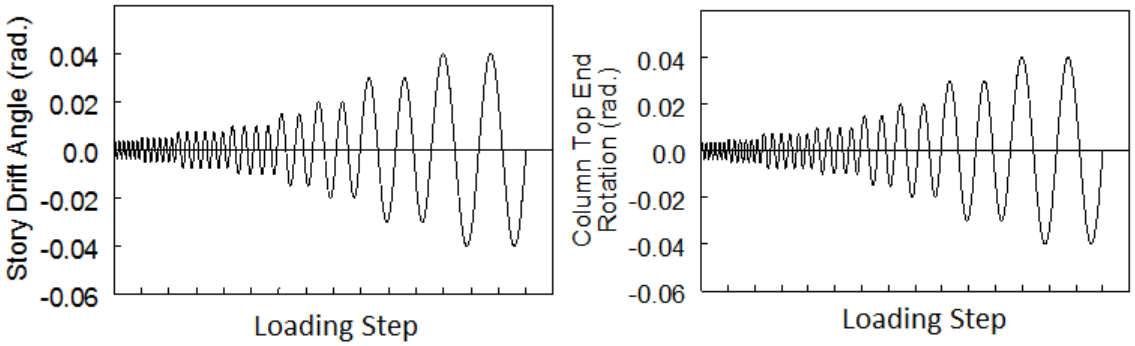

(c) Loading Scheme C: AISC Loading Protocol with Column Top End Rotation

Figure 3.6 Phase 2A: Cyclic Loading Schemes

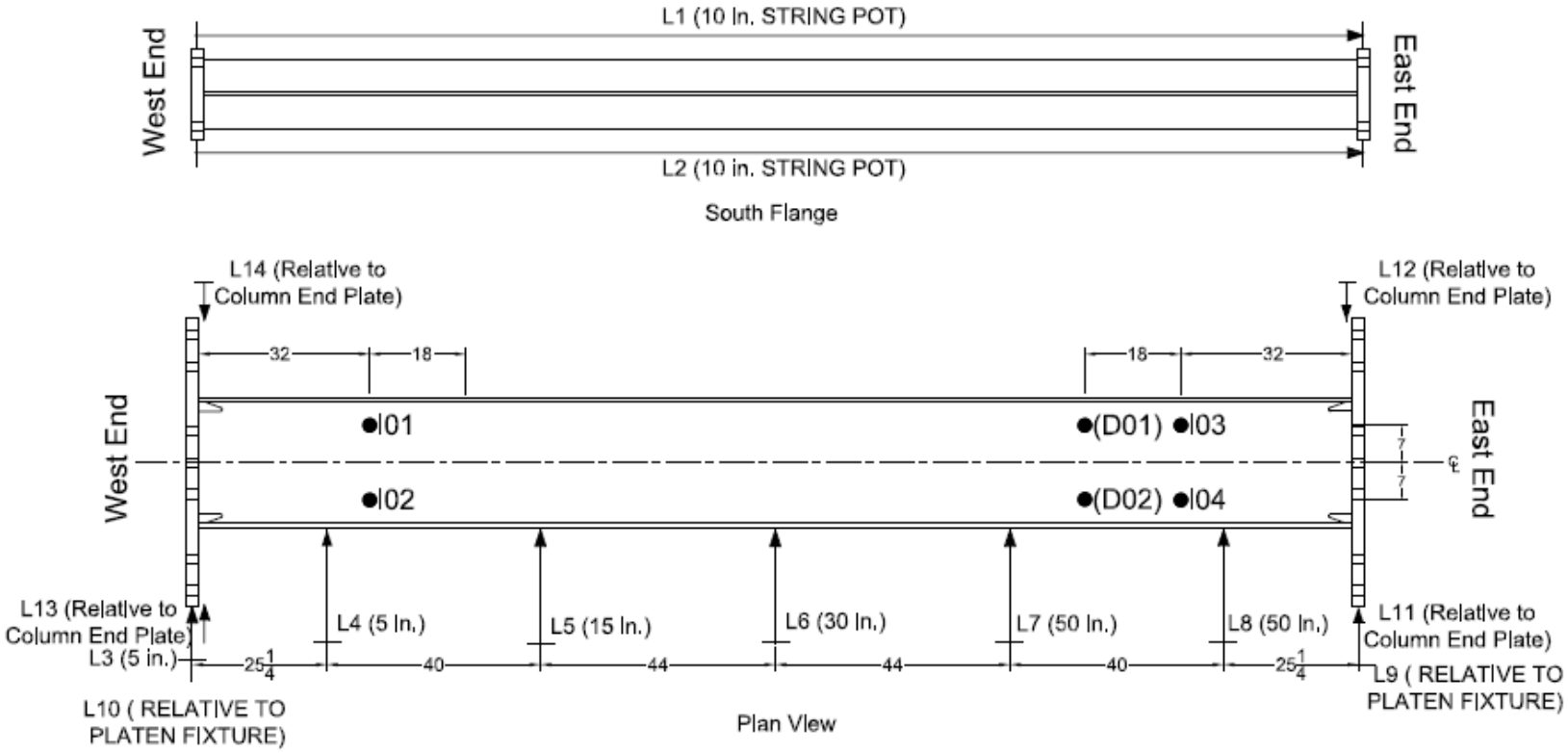

Figure 3.7 Displacement Transducer Layout

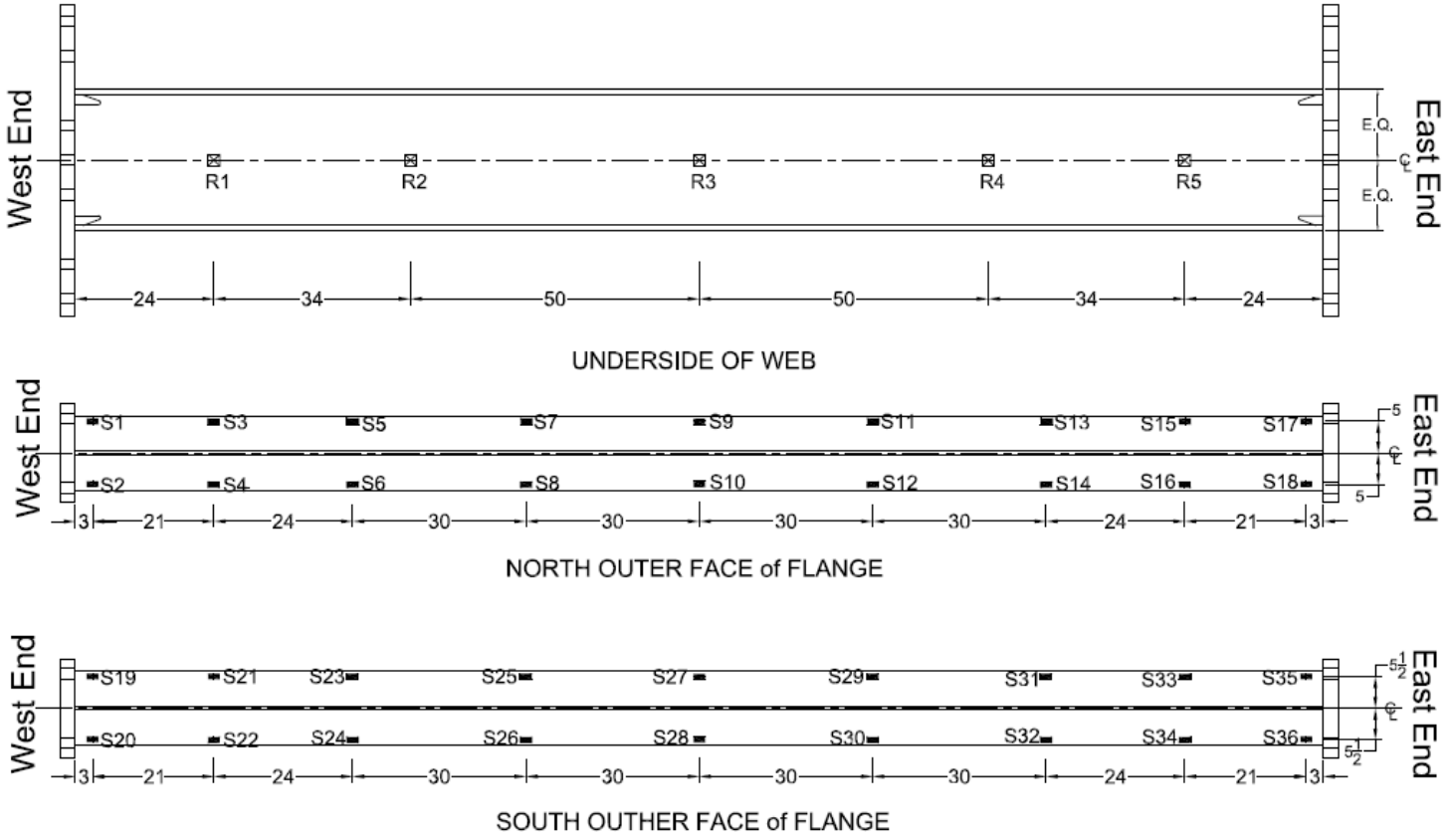

Figure 3.8 Strain Gages and Rosette Layout

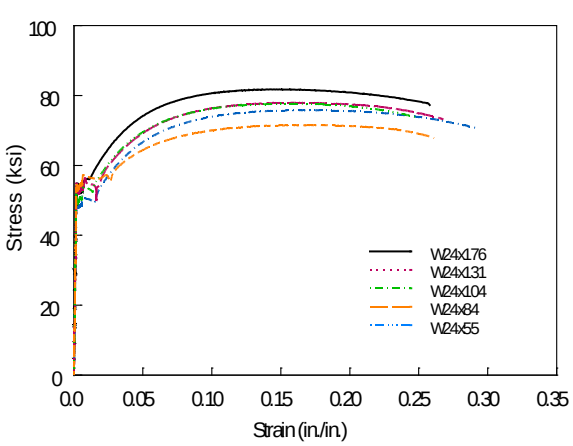

(a) Phase 1: Flanges

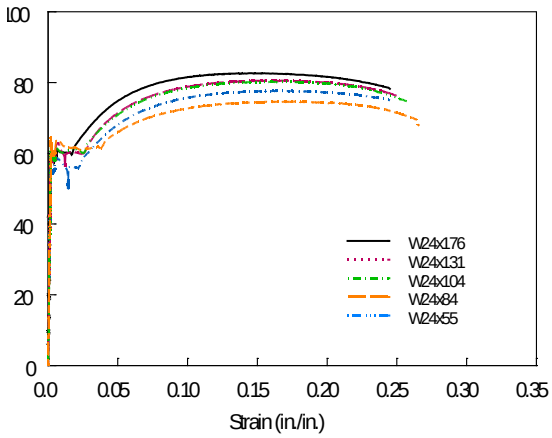

(b) Phase 1: Webs

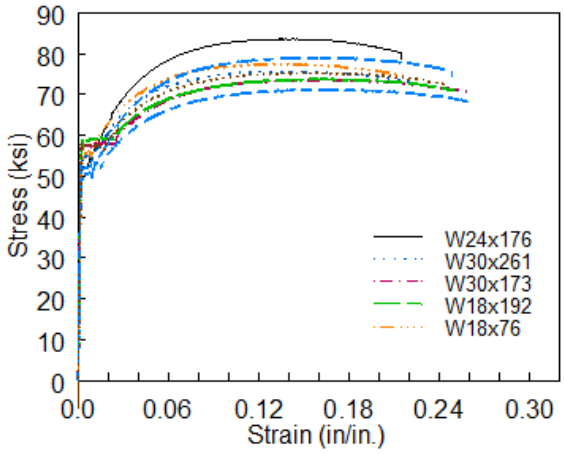

(c) Phase 2A: Flanges

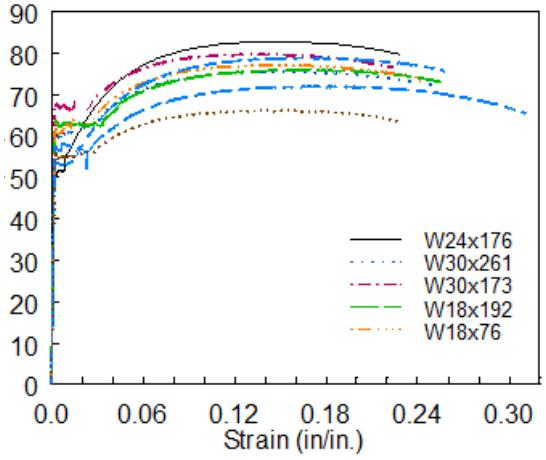

(d) Phase 2A: Web

Figure 3.9 Engineering Strain versus Stress Curves

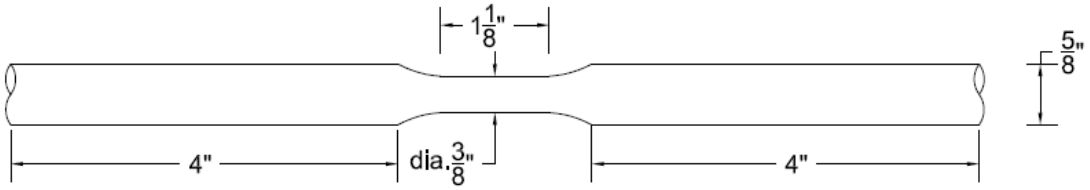

Figure 3.10 Dimensions of Cyclic Coupons

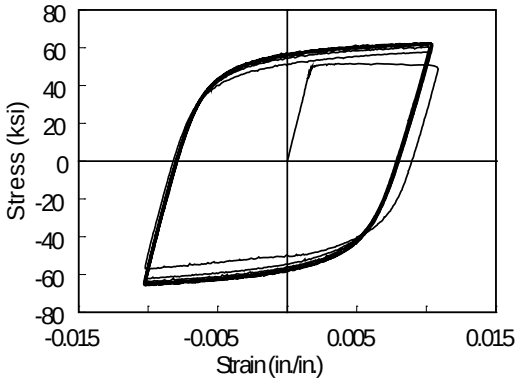

(a) Coupon 1 (Strain Range= 0.02 in./in.)

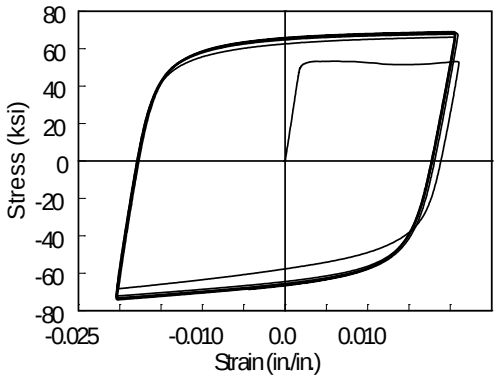

(b) Coupon 2 (Strain Range= 0.04 in./in.)

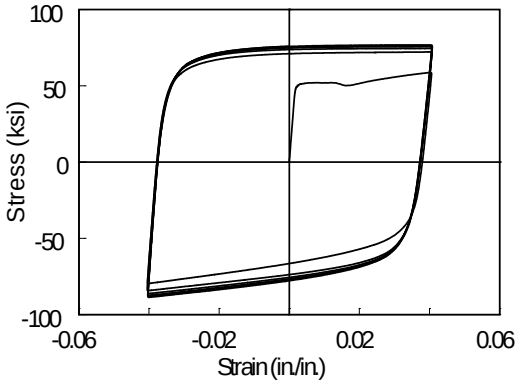

(c) Coupon 3 (Strain Range= 0.08 in./in.)

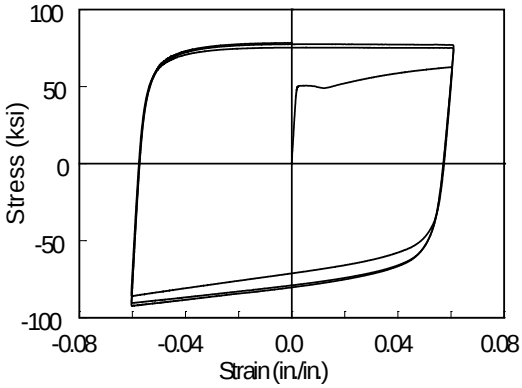

(d) Coupon 4 (Strain Range= 0.12 in./in.)

Figure 3.11 Cyclic Coupon Test Results

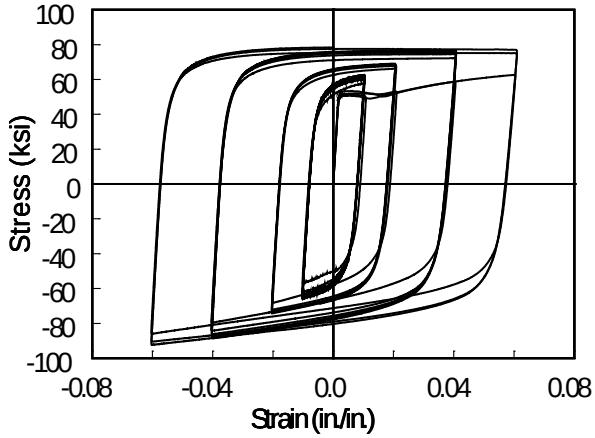

Figure 3.12 Composite Plot of Cyclic Test Data

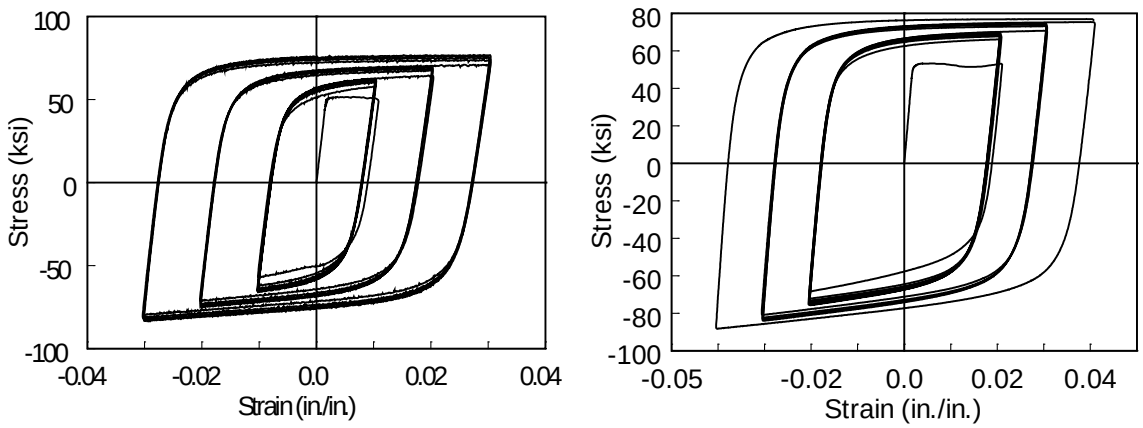

(a) Coupon 1 (b) Coupon 2

Figure 3.13 Cyclic Coupon Test Results with Extra Strain Range Levels

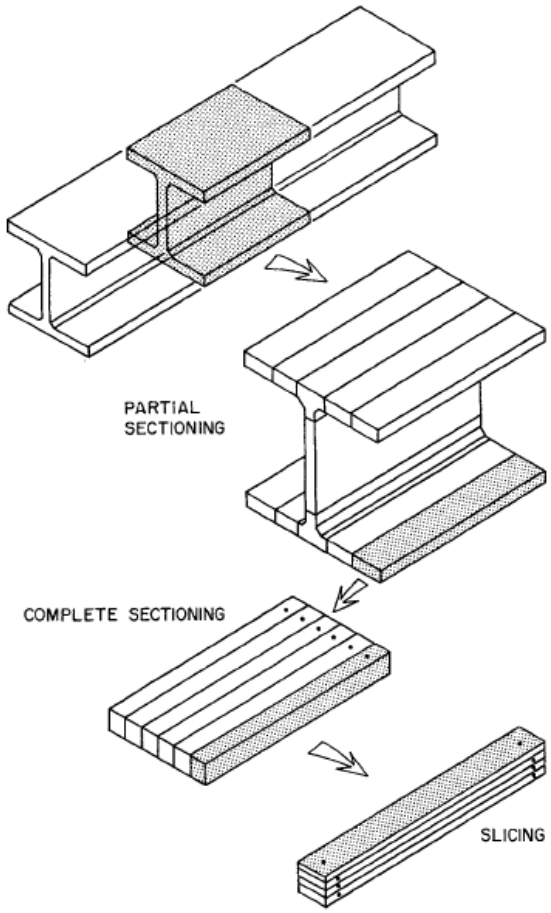

Figure 3.14 Steps in Sectioning Method (Tebedge 1973)

(a) Saw Cutting (Partial Sectioning)

(b) Complete Sectioning

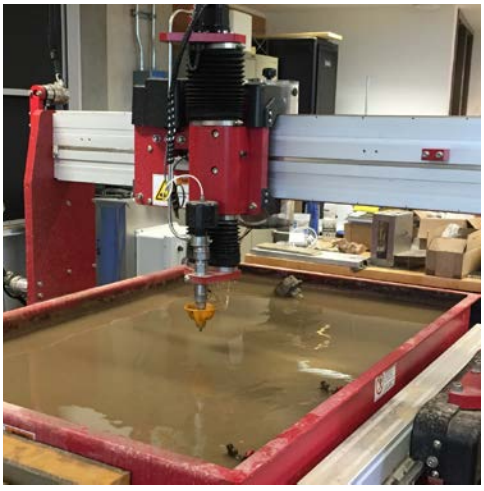

(c) Slicing

Figure 3.15 Steps in Sectioning Method

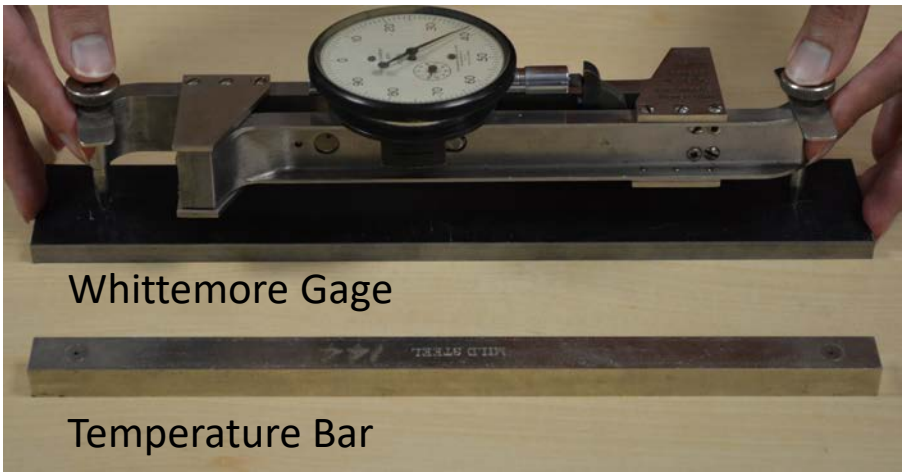

Figure 3.16 Measuring Tecnique

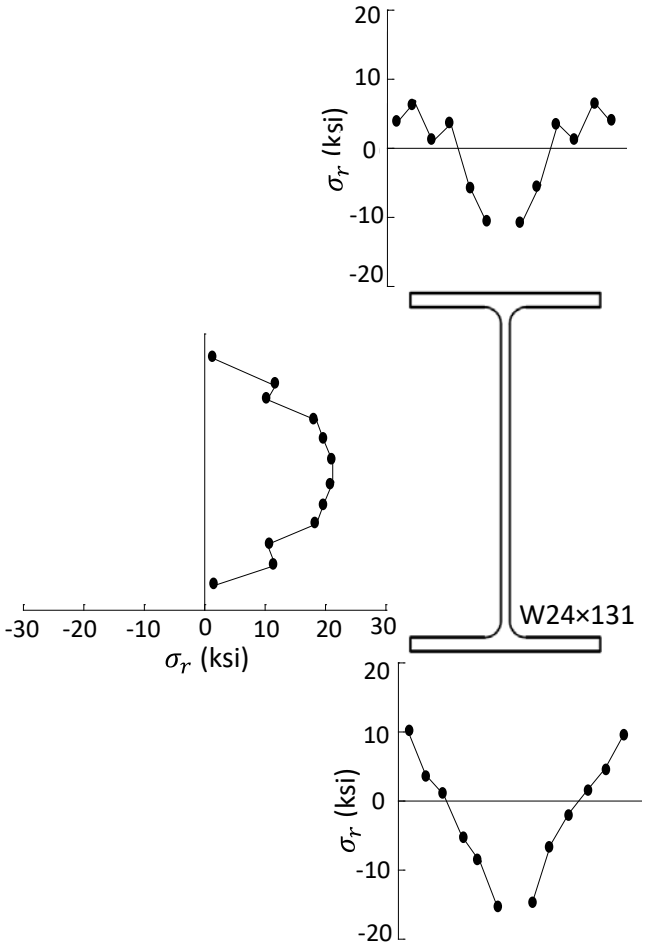

Figure 3.17 Residual Stress Distribution in W24x131

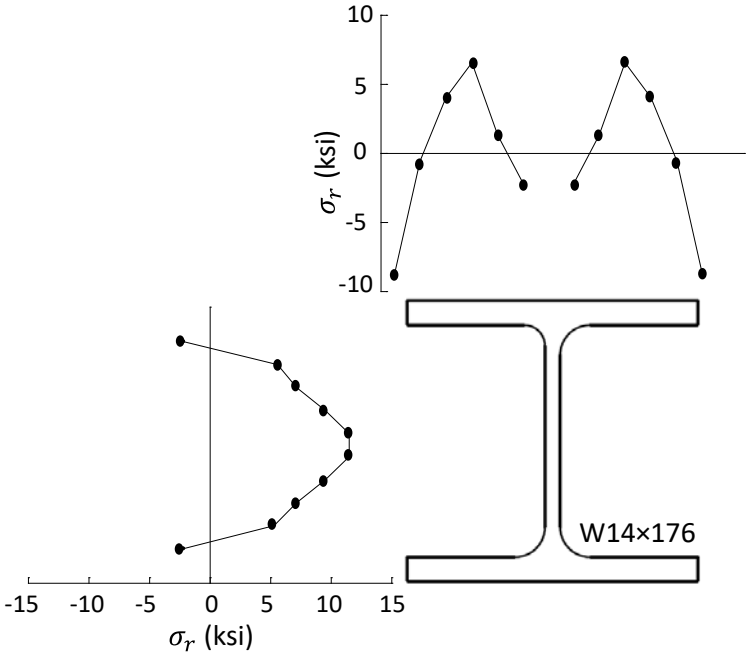

Figure 3.18 Residual Stress Distribution in W14x176

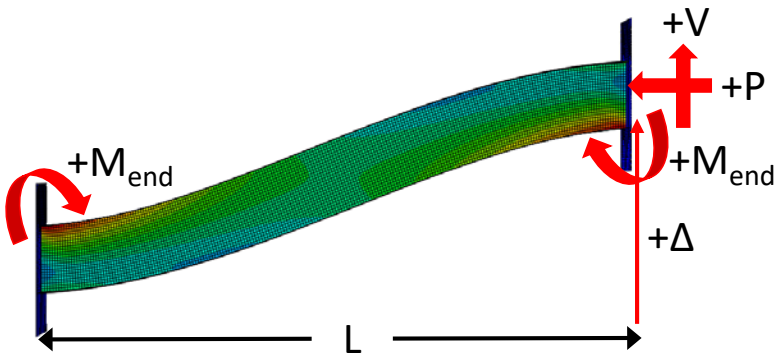

Figure 3.19 Sign Convention

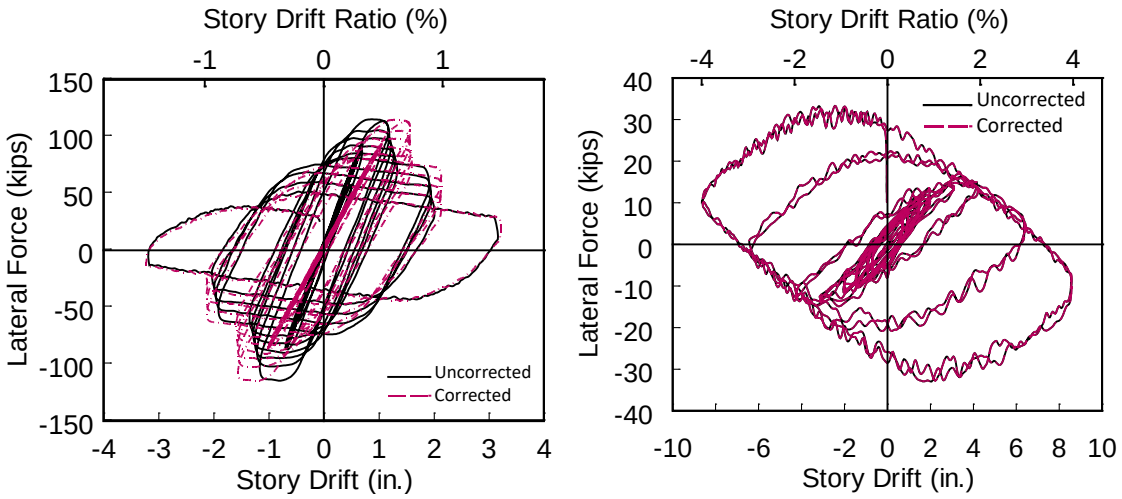

(a) Specimen 2H (b) Specimen 6H

Figure 3.20 Corrected versus Uncorrected Hysteresis Responses

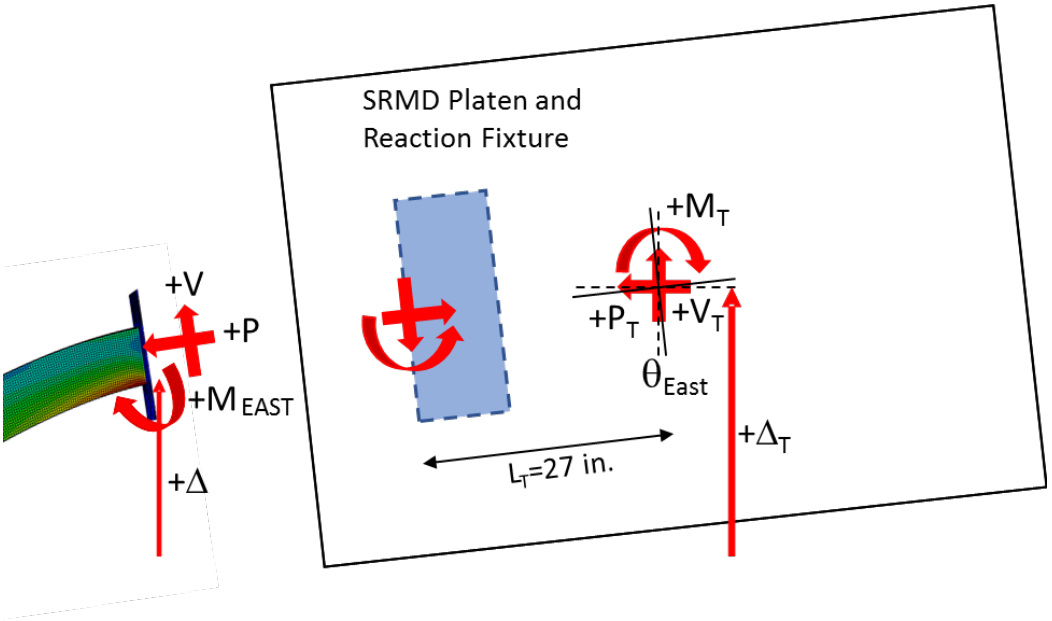

Figure 3.21 Shake Table Free Body Diagram

4 EXPERIMENTAL RESULTS

4.1 Introduction

In this chapter, the observed performance and recorded response of all thirty-seven column specimens are summarized and compared. Further information on the test results can be found in Appendix A, Ozkula and Uang (2015) and Ozkula et al. (2017). Table 4.1 and Table 4.2 summarize loading scheme, governing buckling mode, and maximum drift information of each test.

Columns with three different nominal depths were tested to investigate the depth effect. Longitudinal loading schemes used in this testing program consisted of constant axial load and varying axial load to study cyclic behaviors of interior and exterior columns in SMFs, respectively. The Fixed-fixed end condition was used on most specimens, while some others were subjected to a fixed-flexible boundary condition, giving insights into the boundary condition effect. The effect of weak-axis and bidirectional bending on the cyclic response of the columns was also addressed.

4.2 Progressive Damage History of Sections

Eleven different sections with three nominal depths (W30, W24 and W18) were examined in this study. The damage progression of all specimens is summarized in Table 4.3 and Table 4.4. Although there are some exceptions (such as Group 5 specimens), the general failure modes of these deep sections consisted of an interactive (or simultaneous) web and flange local buckling and global buckling in the form of lateral-torsional buckling (LTB). Generally, twisting of columns started after local buckling occurred, and in some cases it led to global buckling. Initiation of local buckling occurred earlier when the level of axial load increased.

The first major limit state was flexural yielding. The Group 1 (W24×176 section) specimen with a low axial load (C_a = 0.2) experienced a much longer yield length ($L_{yield} \approx$ 80 in.) and was dominated by LTB at 4% story drift ratio (SDR). This was followed by minor flange local buckling. The same section columns (1M and 1H) with higher axial load levels (C_a = 0.4, 0.6) experienced severe flange and web local buckling at 2% and 0.75% SDR, respectively. Local buckling triggered flexural strength degradation. LTB initiated at 1.5% SDR and 0.75% SDR for moderate and high axial load levels respectively.

Specimen 2L, 2M, and 2H (W24×131 section) in Group 2 experienced severe interactive web and flange local buckling at 3%, 1.5%, and 0.75%, respectively. It was clear that the initiation of local buckling was affected significantly by the level of axial load. When the axial load was increased, column behavior became dominant. LTB was not observed in this group. Group 3 showed similar behavior to Group 2 and Group 1, respectively. Since the section of Group 3 specimens was more slender then that of Group 2 specimens, initiation of local buckling started earlier. Group 4 (W24×84) specimens experienced severe web and flange buckling fallowed by global buckling such as LTB. Group 5 (W24×55) specimens failed due to elastic LTB with little sign of local buckling as the member slenderness (L/r_y = 161.2) was 2.3 times that of Group 2 specimens. Plastic hinge did not form at column ends.

After evaluating the damage of columns with five W24 sections tested during Phase 1 research, some columns for Phase 2A testing were selected to reproduce the unexpected failure mode—the combination of local and global bucking—which was observed in Groups 1 and 4. Group 12 (W30×261), Group 15 (W18×192) and Group 16 (W18×130) experienced both interactive web and flange local buckling and LTB. On the other hand,

Group 13 (W30×173), Group 14 (W30×90), and Group 15 (W18×192) experienced only interactive flange and web local buckling.

In summary, two major failure modes were observed in deep column tests. The first mode was web and flange local buckling without out-of-plane deformation. The second failure mode was a combination of (flange and web) local buckling and LTB. In some cases, LTB was first observed, which would then trigger a form of flange local buckling. Alternatively, local buckling would occur first, then followed by LTB. Regardless of the sequence of local buckling and LTB, this failure mode is defined as "coupled" buckling in this study.

Prior to the NIST deep column test program, AISC sponsored a research project to evaluate cyclic behavior of shallow columns (Newell and Uang 2006). Nine shallow and stocky W14 columns with the following slenderness parameters were tested:

$$3.1 \leq \lambda_f 7.14;\ 6.9 \leq \lambda_w \leq 17.7; 42.2 \leq \lambda_L \leq 47.9 \qquad (4.1)$$

Note that these stocky sections had slenderness ratios for WLB and LTB that were significantly lower than those of the NIST specimens tested in this research. These W14 columns did not experience global buckling and web buckling was either not observed or very minor. Even under high constant axial load levels reaching 35% to 75% of P_y in compression, these columns were able to reach story drifts of 0.07 and 0.09 radians with minor strength degradation. Flange local buckling was the typical failure mode for these column. Note that the buckling modes observed in the deep column specimens of this research was very different from that observed in the AISC test program. A procedure to identify the governing buckling mode is presented in Chapter 6.

4.3 Backbone Curve and Plastic Rotation Capacity

For comparison purposes, cyclic backbone curve of each cyclically loaded specimen was constructed from the first cycle response at each story drift level as shown in Figure 4.1(a) ; this definition is consistent that defined in ASCE 41 (ASCE 2013). Note in the figure that the column end moment has been normalized by M_{pc} defined Eq. (3.4). Once the backbone curve is constructed, the plastic rotation can be determined as that defined in Figure 4.1(b). Table 4.5 and Table 4.6 summarize plastic rotation capacities and strain hardening ratios for Phase 1 and Phase 2A specimens, respectively. Plastic rotational capacity R_p is defined as the ratio of θ_p over θ_y.

4.4 Slenderness Parameters

Experimental tests of thirty-seven deep columns with a nominal depth of 30 in., 24 in., and 18 in. covered the following range of slenderness for Phase 1 specimens

$$4.81 \leq \lambda_f \leq 6.94;\ 28.7 \leq \lambda_w \leq 54.6;\ 71.1 \leq \lambda_L \leq 161.2 \quad (4.2a)$$

and,

$$3.27 \leq \lambda_f \leq 8.52;\ 16.7 \leq \lambda_w \leq 57.5;\ 61.19 \leq \lambda_L \leq 103.35 \quad (4.2b)$$

for Phase 2A sections.

Figure 4.2 and Figure 4.3 show the effect of slenderness ratios on the column flexural strength degradation, post-peak stiffness deterioration, and axial shortening. As shown in Figure 4.2(a), more compact sections exhibit higher ductility and less axial shortening than more slender sections when comparing them at the same story drift ratio. Group 3 and Group 4 specimens exhibit similar ductility and axial shortening. Further analysis indicates that web and flange slenderness ratios both influences column behaviors.

Sensitivity analysis was performed and the effect of slenderness ratio is further discussed in Chapter 5.

4.5 Section Depth Effect

In Phase 1, five different W24 sections were tested and the cyclic behaviors were examined. In Phase 2A, W30 and W18 sections were added to the testing matrix to verify if findings from W24 sections can be extrapolated to deeper (W30) and shallower (W18) sections.

Figure 4.4(a) illustrates three clusters of specimen groups with similar flange and web slenderness ratios. For example, Cluster A consists of Group 11 (W24×176), Group 12 (W30×261), and Group 16 (W18×130) specimens; all have similar flange and web slenderness ratios but different nominal depths. All Cluster A specimens exhibited Coupled Buckling (CB) failure mode under cyclic loading. Similarly, Cluster B consists of Group 2 (W24×131) and Group 13 (W30×173), and Cluster C consists of Group 3 (W24×104) and Group 17 (W18×76). The specimens in the two latter clusters also behaved similarly and exhibited the same in-plane plastic hinging mode.

Figure 4.4(b) also demonstrates that specimens in the same cluster tend to exhibit similar backbone curves with similar initial stiffness, maximum flexural strength, and post-buckling response. For Cluster B, even though the normalized flexural strengths are quite different between Specimens 13M and 2M, the post-buckling stiffnesses illustrating strength degradation behavior are nearly identical. In summary, sections with similar flange and web slenderness characteristics behave and response similarly to cyclic loading regardless of the section nominal depths.

4.6 Axial Shortening

With the presence of an applied constant compression, most of the column specimens showed significant shortening after severe local buckling or global buckling occurred. The measured shortenings are summarized in Figure 4.5. Specimen are ordered based on their section slenderness ratios from low to high and grouped based on their axial load levels. For instance, Specimen 15L is the most compact section while Specimen 14 is the most slender section among the specimens subjected to low level of axial force (C_a = 0.2). Figure 4.5(a) shows that those meeting the AISC (2010b) compactness limits for highly ductile members experienced exponential growth in axial shortening after 2% SDR. For columns that that exceed highly ductile flange and/or web slenderness requirement, the exponential growth in axial shortening started much earlier. Grouping the specimens based on the axial force level, Figure 4.6 shows the comparison of axial shortening for a given SDR.

Specimens 3L and 17L do not satisfy flange slenderness requirement for SMFs while Specimen 4L exceeds web slenderness limits. Axial shortening in these specimens was similar to each other even though the specimen (4L) with high web slenderness ratio experienced slightly larger axial shortening (2% of L) at the same SDR. This shows that flange and web slenderness limits are equally important factors influencing axial shortening in the columns. The same observation was valid for the same columns subjected to a moderate level of axial load (C_a = 0.4). Under moderate level of axial load, exponential growth in axial shortening began at 0.5% SDR, while it occurred later at 1% SDR when the same columns were subjected to low level of axial load (C_a = 0.2).

4.7 Axial Force Effect

4.7.1 Axial Load Level Effect

Two plots are presented for each group in Figure 4.6. The first plot compares shortenings measured at the end of each test, while the second plot compares shortenings observed at the same drift level to show the effect of axial force. It is obvious that when the axial load increased, axial shortening increased drastically. This was mainly due to severe flange and web local buckling as well as, when occurred, LTB.

The effect of compressive axial load level on the column response was also evaluated by comparing the backbone curves shown in Figure 4.7. It is clear that when the applied compressive load increases, the rate of cyclic and in-cycle flexural strength deterioration aggravates drastically, leading to significant reduction in the plastic rotation capacity.

4.7.2 Varying Axial Force Effect

Figure 4.8(a) shows the backbone curve comparison between Specimen 1H subjected to a constant axial force and Specimen 11H-VA subjected to a varying axial load. The maximum strength increased in the varying axial load case. In addition, since the demand was smaller for the column subjected to varying axial load, local buckling initiation was delayed. Figure 4.8(c) illustrates that axial shortening of Specimen 1H is three times of that measured in Specimen 11H-VA. These comparisons indicate that the cyclic behaviors of the two columns are very different in terms of maximum strength, post-buckling flexural strength, stiffness deterioration, and axial shortening. Therefore, behaviors of exterior columns deserve further investigation. The backbone curves of interior and exterior columns need to be distinguished for seismic design applications.

4.8 Loading Protocol Effect

4.8.1 Monotonic vs. Cyclic Loading

The influence of loading history on the cyclic responses is illustrated in Figure 4.9, where data from cyclically loaded test is superimposed on data from a monotonic test. The comparison in this figure demonstrates the distinction between monotonic and cyclic loading. Whereas the monotonic response curve is considered as a characteristic property of the specimen, the cyclic skeleton curve will vary depending on the loading history applied to the specimen. Three monotonic tests were performed in this study. In Phase 1, Specimen 2L-P was monotonically loaded up to 4% SDR and then the reversed AISC symmetric cyclic loading was applied.

Figure 4.10 illustrates cyclic versus monotonic response of Specimen 2L and 2L-P, respectively. The failure mode of both specimens was the interactive flange and web local buckling. Global buckling was not observed in both tests. At 4% SDR, monotonically loaded column showed minor local buckling at one flange, and the axial shortening was 0.5 in. On the other hand, the same section (W24×131) under cyclic loading had 3.2 in. axial shortening at 4% SDR due to severe local buckling at both flanges in the plastic hinge regions. For Specimen 2L-P, the test continued after 4% monotonic drift and the column was subjected to the reversed AISC loading protocol. Test results showed that after the reversed loading protocol, Specimen 2L-P exhibited an axial shortening 43% larger than Specimen 2L. This was because the cyclic lateral drifts were applied to the already damaged cross-section of Specimen 2L-P. Consequently, web and flange local deformation

was more severe than that observed in Specimen 2L as shown in Figure 4.10(a). Expectedly, axial shortening was also more severe in Specimen 2L-P.

In Phase 2A, Specimen 12LM-P was loaded up to 11% SDR monotonically. This specimen's failure mode was different from its nominally identical section (12LM) subjected to cyclic loading (see Figure 4.11). Because Specimen 12LM underwent many inelastic drift cycles, it experienced more yielding than its counterpart, which was loaded monotonically. Longer yielded portions of Specimen 12LM had lower flexural and torsional stiffness, making it prone to global buckling instability. Indeed, global out-of-plane buckling coupled with FLB and WLB was observed in Specimen 12LM, while Specimen 12LM-P failed merely due to local buckling. Lastly, axial shortening of the cyclically loaded specimen is eight times greater than the monotonically loaded specimen at the same drift level. Comparisons of these responses clearly demonstrates the effect of loading protocol on the governing buckling mode.

4.8.2 Far-field vs. Near-field Loading

Assuming that the AISC loading scheme A up to the first cycle of 4% SDR as demonstrated in Figure 3.5(a) represents the seismic demand of a far-field ground motion, and the loading sequence shown in Figure 3.5(d) represents the demand of a near-fault ground motion (Krawinkler et al. 1996), a comparison can be made between the performance of Specimens 2M and 8M. Figure 4.12 shows that the near-fault loading protocol was less demanding in terms of energy dissipation demand and column axial shortening, although the residual drift could be larger. Figure 4.9 depicts the cyclic backbone curve comparisons between the symmetric loading protocol and Near-fault loading protocol. Up to 1% SDR, both specimens show similar backbone curve. However,

after 1% SDR, flexural strength of the specimen subjected to far-filed loading protocol deteriorated much faster than that of specimen subjected to near-field loading protocol. This is because of the inelastic cumulative damage due to many high-amplitude cycles of the standard AISC loading protocol. It is clear that the backbone curves and axial shortening are affected by the lateral loading sequence. In this research, lower (AISC loading) and upper (monotonic loading) bounds of backbone curves will be (see Chapter 8).

4.9 Strong Axis, Weak Axis vs. Biaxial Bending

In Phase 1, Specimen 7M was subjected to biaxial bending with 30% of the strong-axis lateral drift imposed on the weak-axis bending. Its performance was compared to its nominally identical specimen 2M subjected to unidirectional loading. As shown in Figure 4.13, the strength degradation, axial shortening, and failure modes of these two specimens were insensitive to the bi-axial loading effect. Energy dissipation of these two specimens was the same in the strong axis direction. Since specimen 7M was also subjected to lateral loading in weak-axis direction, the cumulative energy dissipation considering both directions was much larger than its counterpart. Since the objective of this research was to develop a simplified backbone curve model for nonlinear modeling of steel columns, no adjustments is necessary for plastic deformation capacity of the steel columns subjected to bidirectional bending.

Phase 1 test results also offer the opportunity to characterize hysteretic behavior of steel columns subjected to weak-axis bending with a constant axial load. Specimen 6L was highly ductile, exhibiting no local buckling even at 7% drift. Indeed, plastic rotation capacity of the weak-axis specimen is much higher than its nominally identical specimens

bended about strong-axis. Figure 4.14(b) shows the relationship between the measured lateral load and story drift. Based on Eq. (3.3), the computed end moment consists of two components: the primary and secondary moments. Figure 4.14(b) shows that the secondary moment was significant for the weak-axis bending specimen but negligible for the strong-axis bending case. Axial shortening was limited in weak-axis bending test as no local buckling occurred. AISC Specification (AISC 2010c) does not distinguish strong- and weak-axis bending behavior in terms of compactness requirement. Test results indicate that their results are very different; thus, the compactness requirement for weak-axis bending can be relaxed and be treated separately. More research is needed to further investigate this issue.

4.10 Boundary Condition Effect

As shown in Figure 4.15(a) through Figure 4.17(a), the moment-rotation relations of three sets of nominally identical specimens with fixed-fixed and fixed-flexible boundary conditions are similar in terms of the maximum strength. Figure 4.15(b) through Figure 4.17(b) show that the governing buckling mode did not change regardless of changing in boundary conditions. Column axial shortening of the fixed-fixed case is double of that measured in fixed-flexible test as shown in Figure 4.15(c) through Figure 4.17(c). This is because of the simultaneous formation of local buckling at both ends of the specimens subjected to the fixed-fixed boundary condition. Fixed-fixed boundary condition does not accurately represent the end condition of first-story columns in SMFs. However, results from fixed-fixed test can be adjusted to account for the flexible end effect, an issue to be discussed further in Chapter 8.

4.11 Acknowledgements

The text below is reproduced verbatim as it appears in the acknowledgments section on page xvii per the UCSD Office of Graduate Studies Formatting Requirements.

Chapter 4 of this dissertation is based on material published by University of California, San Diego, titled “ATC-106: Seismic behavior and design of deep, slender wide-flange structural steel seam-column members” with author Uang, C.-M. (2017). In this chapter, materials currently being prepared for submission for publication by University of California, San Diego, titled “ATC-106 Phase 2A: Seismic behavior and design of deep, slender wide-flange structural steel beam-column members” with co-authors Chansuk, P., and Uang, C.-M. (2017). These materials were also published by Engineering Journal, titled “Observations from cyclic tests on deep, wide-flange beam-columns” with co-authors Harris, J., and Uang, C.-M. (2017). The dissertation author is the first author of these reports and paper.

Additionally, these materials published by Structural Stability Research Council, titled “Observations from cyclic tests on deep , slender wide-flange structural steel beam-column members”, with co-authors Uang, C., and Harris, J. (2015). The dissertation author is the second author of these paper.

Table 4.1 Phase 1 Testing Summary

Group No.	Specimen Designation	Section	Loading Scheme	Max Drift	Failure Modes
1	1L	W24×176	A	7%	CB
	1M			4%	
	1H			2%	
2	2Z	W24×131	A	7%	ALB
	2L			4%	
	2L-P		B	4%	
	2M		A	3%	
	2H			1.5%	
3	3L	W24×104	A	4%	ALB
	3M			1.5%	
	3H			1%	
4	4L	W24×84	A	3%	CB
	4M			2%	
5	5L	W24×55	A	2%	CB
	5LM			1%	
	5M			0.75%	
6	6L	W24×131	A	7%	ALB
	6L-P		B	10%	
	6H		A	4%	
7	7M		C	3%	
8	8M		D	-2%/+6%	

Table 4.2 Phase 2A Testing Summary

Group No.	Specimen Designation	Section	Loading Scheme	Max Drift	Failure Modes
11	11M	W24×176	A	3%	CB
	11H-VA		B	3%	
	11H-BC		C	3%	
12	12LM	W30×261	A	3%	CB
	12LM-P		Pushover	11%	ALB
13	13M	W30×173	A	1.5%	ALB
	13M-BC		C	2%	
14	14L	W30×90	A	2%	ALB
15	15L	W18×192	A	5%	CB
16	16M	W18×130	A	3%	CB
	16M-BC		C	4%	
17	17L	W18×76	A	5%	ALB

Table 4.3 Phase 1: Column Damage Progression

Spec.	Section	C_a	Yielding	Local Buckling	Twisting	LTB
1L	W24×176	0.2	1.5% (2^{nd})	-4% (1^{st})	-4% (1^{st})	-4% (1^{st})
2L	W24×131		1.5%	3% (1^{st})	-	-
3L	W24×104		1%	2%(2^{nd})	-3% (1^{st})	-
4L	W24×84		1%	-1.5% (2^{nd})	-2% (2^{nd})	-2% (2^{nd})
1M	W24×176	0.4	1% (2^{nd})	-2% (1^{st})	-1.5% (2^{nd})	-1.5% (2^{nd})
2M	W24×131		1% (4^{th})	-1.5%(1^{st})	-	-
3M	W24×104		+1% (1^{st})	-0.75% (6^{th})	-0.75% (1^{st})	-
4M	W24×84		0.75%	1%(2^{nd})	-2% (3^{rd})	-2% (3^{rd})
1H	W24×176	0.6	0.75% (2^{nd})	-0.75 (6^{th})	-1.5% (1^{st})	0.75% (6^{th})
2H	W24×131		0.75%(6^{th})	-0.75%(3^{rd})	-	-
3H	W24×104		0.75% (2^{nd})	-0.75% (2^{nd})	0.75% (2^{nd})	-

Table 4.4 Phase 2A: Column Damage Progression

Spec.	Section	C_a	Yielding	Local Buckling	Twisting	LTB
11M	W24×176	0.4	1% (2nd)	-2% (1st)	+1.5% (1st)	-1.5% (1st)
11H-VA		0.6	-	2% (2nd)	1.5% (1st)	-1.5% (1st)
11H-BC			-	2% (1st)	2% (1st)	2% (1st)
12LM	W30×261	0.3	1.5%	2% (2nd)	2% (1st)	2% (1st)
13M	W30×173	0.4	1% (2nd)	1% (4th)	-	-
13M-BC			-	-1.5% (1st)	-	-
14L	W30×90	0.2	0.75%	-1.5% (1st)	-1% (1st)	-
15L	W18×192		1.5%	-	4% (1st)	4% (1st)
16M	W18×130	0.4	0.75% (1st)	-	1.5% (1st)	2% (1st)
16M-BC			-	-	2% (1st)	2% (2nd)
17L	W18×76	0.2	1%	-2% (1st)	-1.5% (1st)	-

Table 4.5 Phase 1: Slenderness Effect

Specimen	M_{max} (kip-ft)	M_{max}/M_{pc}	θ_{yc} (×0.01 rad)	θ_p (×0.01 rad)	R_p
1L	3148	1.4	1.5	3.7	2.5
1M	2423	1.3	1.0	2.3	2.3
1H	2010	1.5	0.6	1.2	2.0
2Z	2327	1.5	1.5	6.5	4.3
2L	1655	1.1	1.7	2.0	1.2
2M	1430	1.2	0.9	1.0	1.1
2H	1084	1.2	0.5	0.4	0.8
3L	1262	1.0	1.2	1.4	1.2
3M	880	0.9	0.7	0.4	1.0
3H	779	1.1	0.5	0.4	0.8
4L	1039	1.1	0.9	1.5	1.7
4M	897	1.2	0.7	0.7	1.0
5L	599	1.0	0.9	0.6	0.7
5LM	594	1.1	0.9	0.2	0.2
5M	494	1.1	0.6	NA	NA
6L	453.58	1.3	2.0	5.6	2.8
6L-P	405.94	1.1	2.4	4.8	2.0
6H	337.42	1.6	1.2	2.8	2.3

Table 4.6 Phase 2A: Slenderness Effect

Specimen No.	M_{max} (kip-ft)	M_{pc} (kip-ft)	M_{max}/M_{pc}	θ_y (×0.01 rad)	θ_p (×0.01 rad)	R_p
11M	2367.4	1713.8	1.38	0.491	2.323	4.7
11H-VA	2657.8	1265.1	2.10	0.287	3.063	10.7
11H-BC	1761	1266.1	1.39	0.639	1.575	2.5
12LM	4496.5	3924.7	1.15	0.934	1.787	1.9
12LM-P	4844.6	3947.8	1.23	1.205	7.482	6.2
13M	2452.1	2514.3	0.98	0.636	0.242	0.4
13M-BC	2618.5	2521.2	1.04	1.041	0.702	0.7
14L	1395.9	1411.1	0.99	0.77	0.32	0.4
15L	2502.7	2051.4	1.22	1.11	3.067	2.8
16M	1405.7	934.1	1.50	0.565	2.36	4.2
16M-BC	1315.9	1006.7	1.31	1.064	2.603	2.4
17L	802.5	768.2	1.04	0.958	1.012	1.1

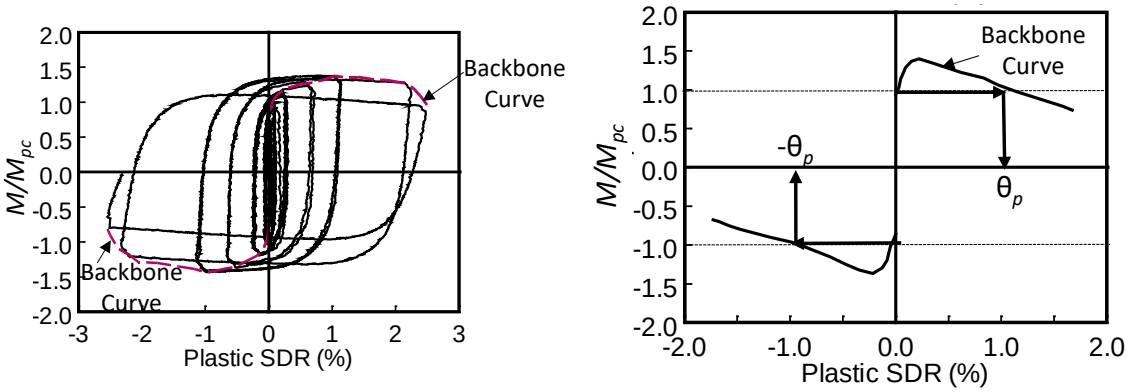

(a) Backbone Curve (b) Plastic Rotation Capacity

Figure 4.1 Definition of Backbone Curve and Plastic Rotation Capacity

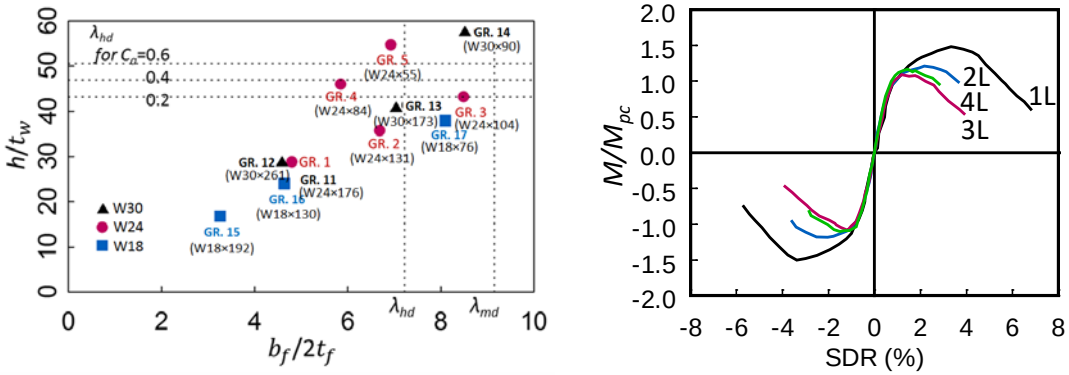

(a) Comparison of Backbone Curves

(b) Failure Modes

Figure 4.2 Effect of Slenderness Ratio

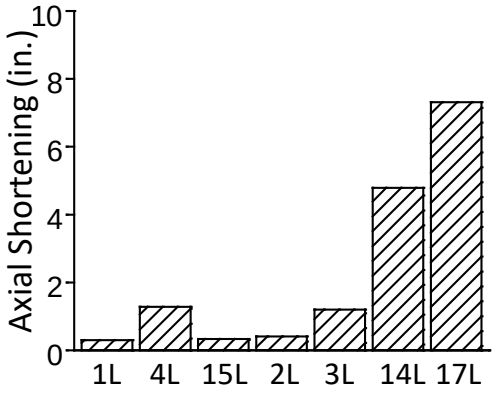

(a) Low Axial Load (at 2% SDR)

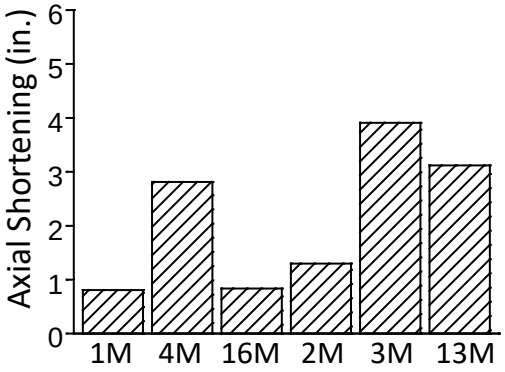

(b) Medium Axial Load (at 1.5% SDR)

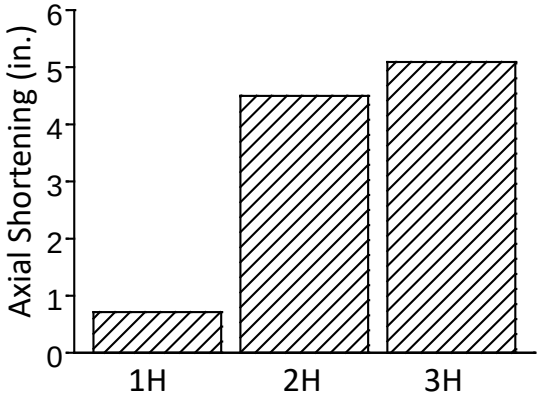

(c) High Axial Load (at 1% SDR)

Figure 4.3 Effect of Slenderness Ratio on Axial Shortening

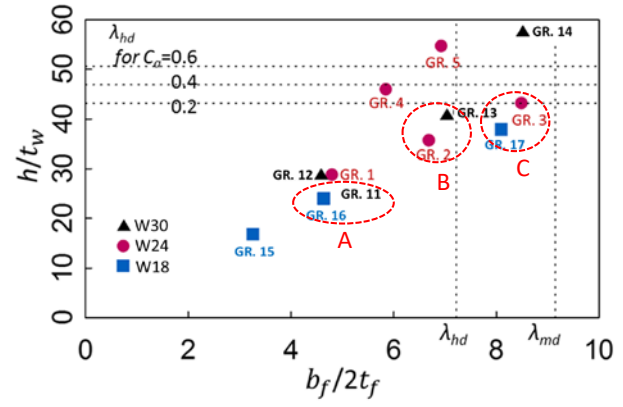

(a) Web to Flange Slenderness

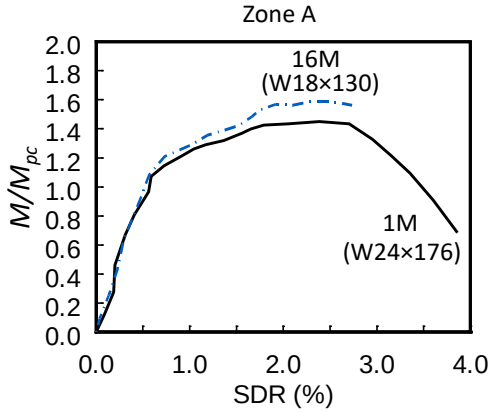

(a) CB Failure Mode

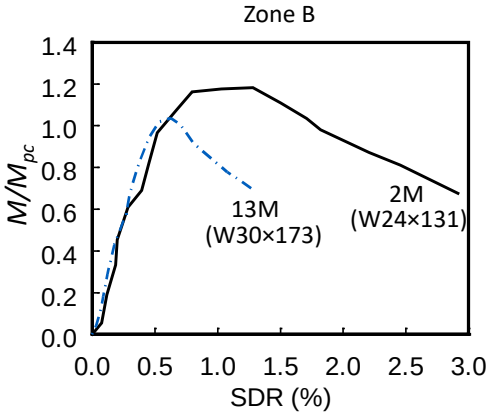

(b) ALB Failure Mode

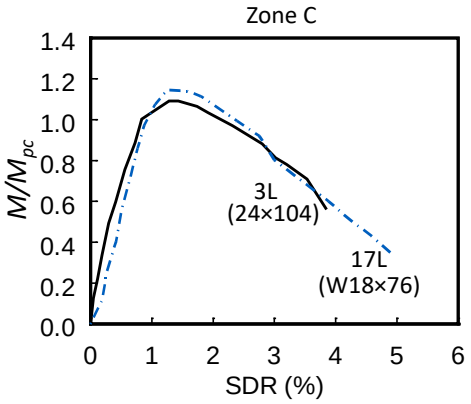

(c) ALB Failure Mode

Figure 4.4 Section Depth Effect

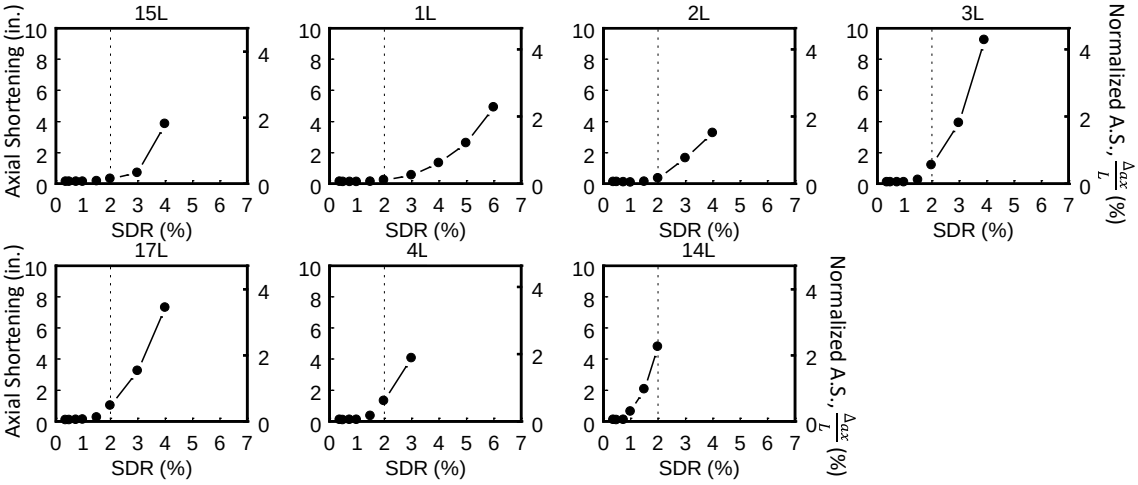

(a) $C_a = 0.2$

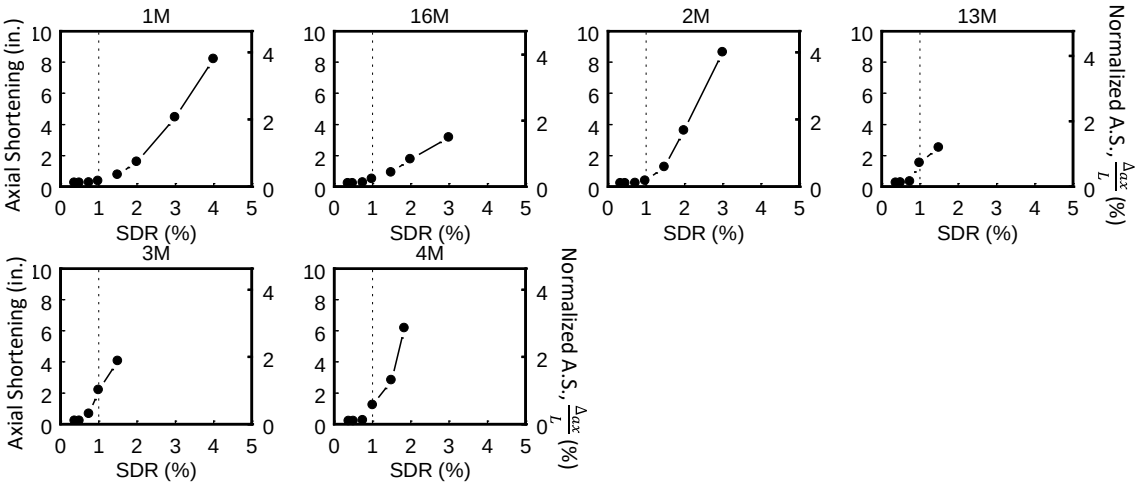

(b) $C_a = 0.4$

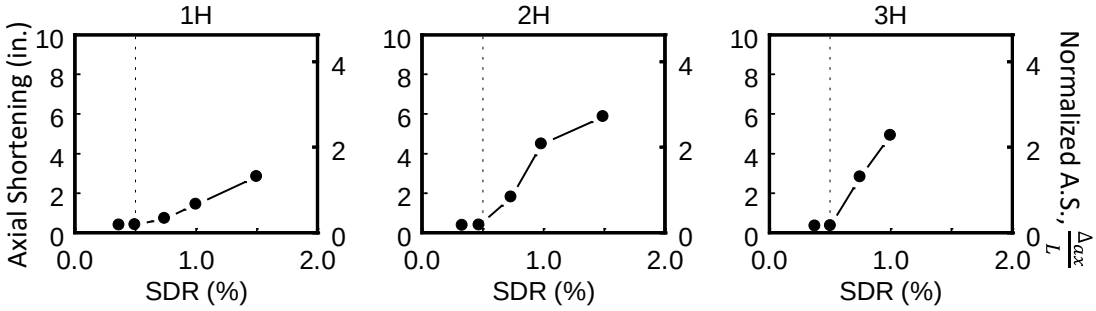

(c) $C_a = 0.6$

Figure 4.5 Axial Shortening

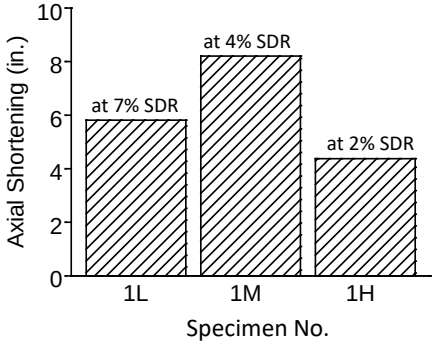

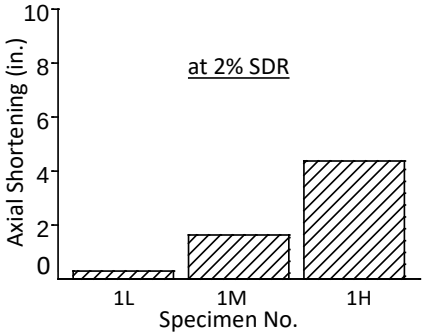

(a) Group 1 (W24×176 Section)

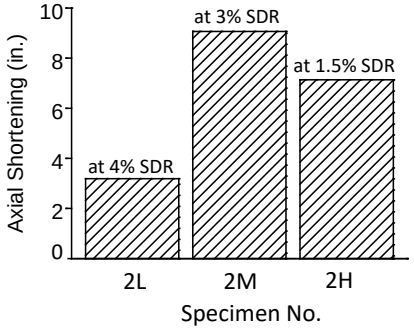

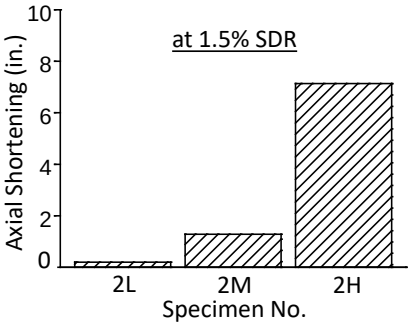

(b) Group 2 (W24×131 Section)

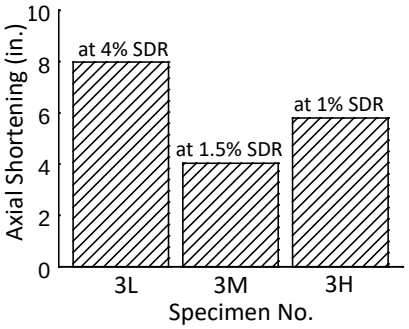

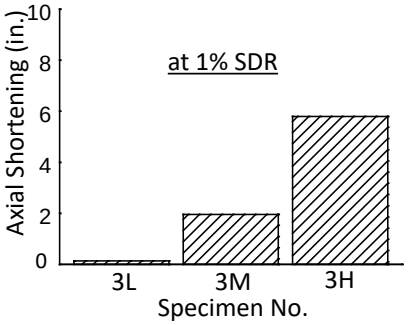

(c) Group 3 (W24×104 Section)

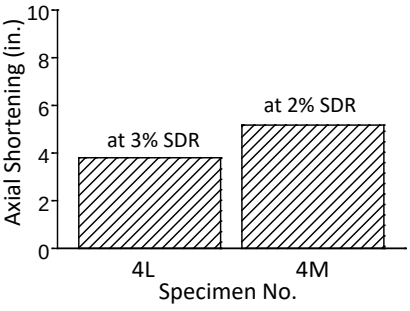

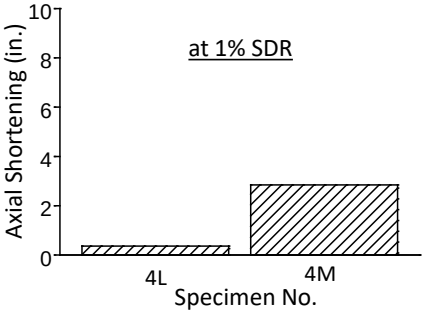

(d) Group 4 (W24×84 Section)

Figure 4.6 Column Axial Shortening (Axial Load Level Effect)

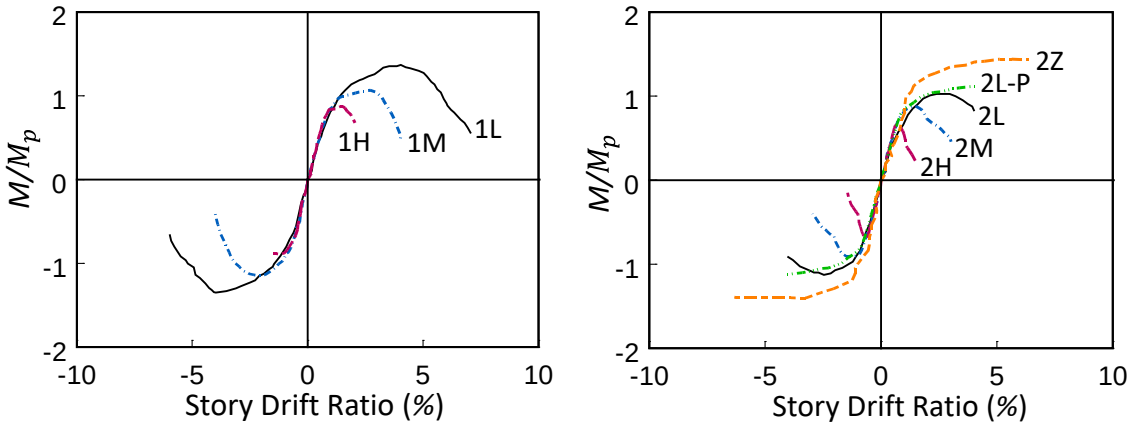

(a) Group 1: W24×176 Section (b) Group 2: W24×131 Section

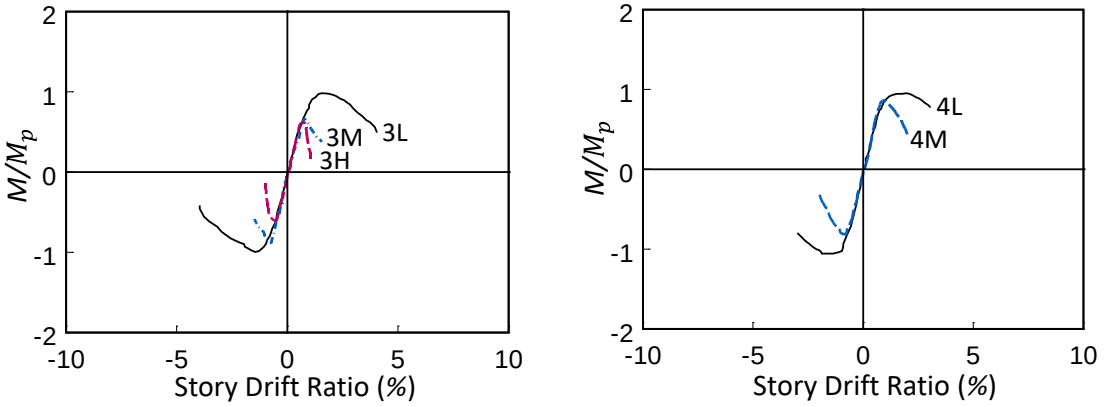

(c) Group 3: W24×104 Section (d) Group 4: W24×84 Section

Figure 4.7 Comparison of Backbone Curves (Axial Load Level Effect)

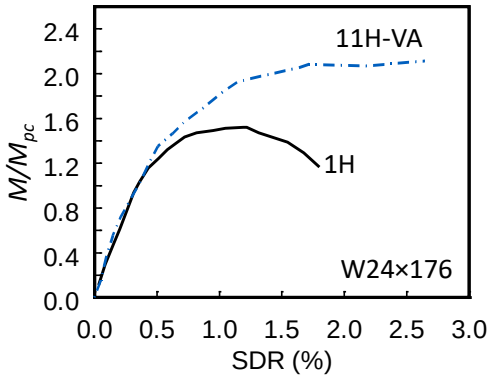

(a) Normalized Moment vs. SDR (%)

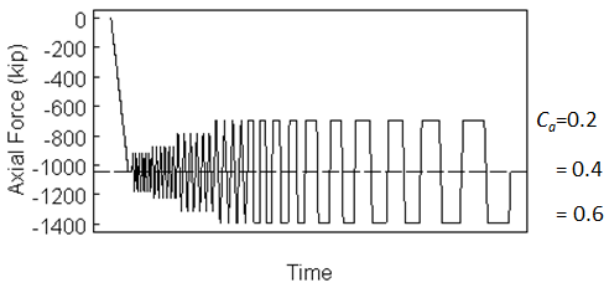

(b) Axial Load Variation

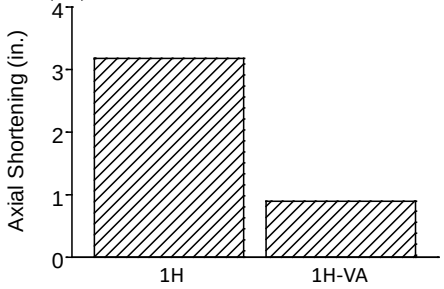

(c) Axial Shortening Comparison

(d) Specimen 11H-VA

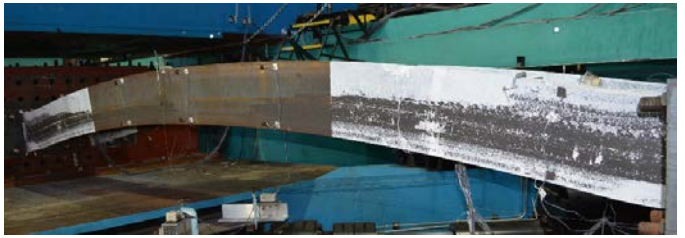

(e) Specimen 1H

Figure 4.8 Varying Axial Force vs. Constant Axial Force

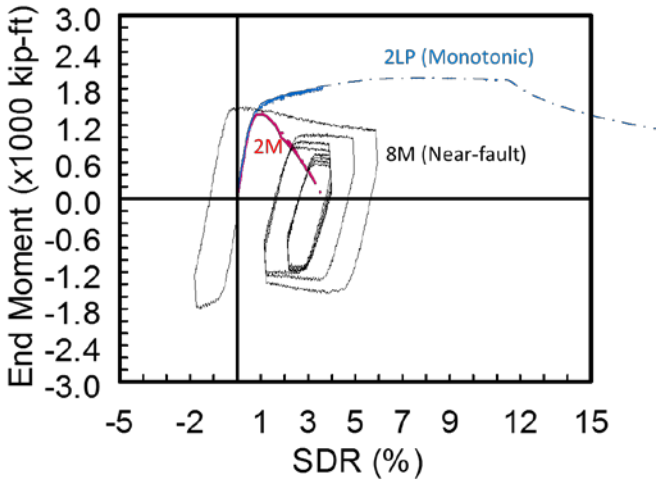

Figure 4.9 Loading Sequence Effect

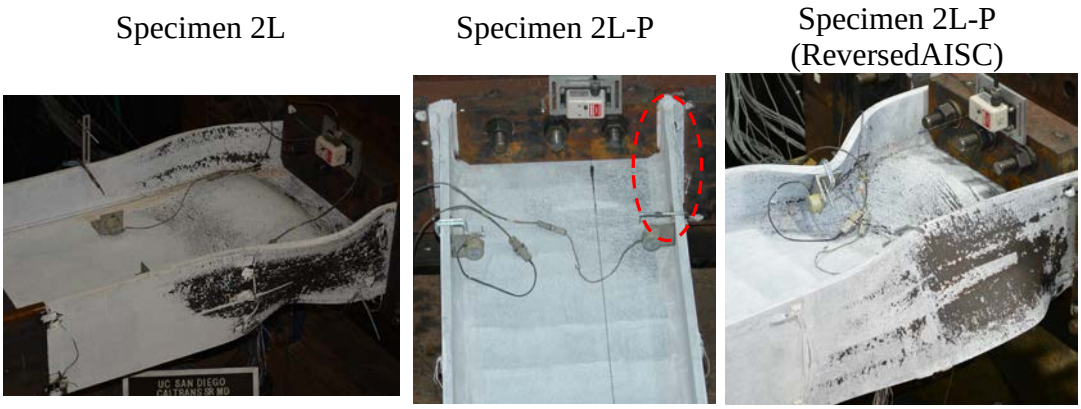

(a) Local Buckling Pattern

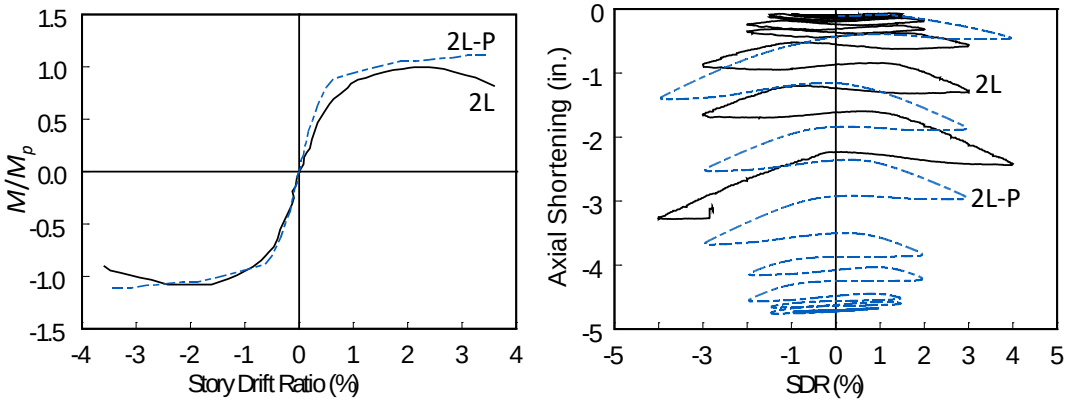

(b) Cyclic Backbone Curve (c) Axial Shortening

Figure 4.10 Monotonic vs. Cyclic Loading Effect (Phase 1)

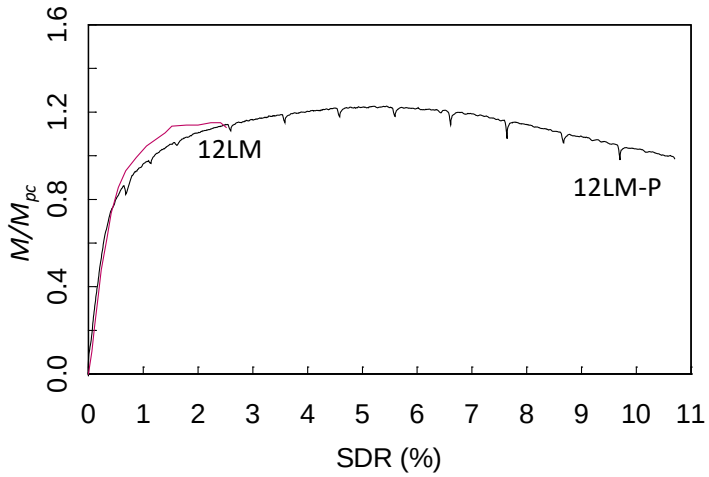

(a) Normalized Moment vs. SDR (%)

(b) Specimen 12LM

(c) Specimen 12LM-P

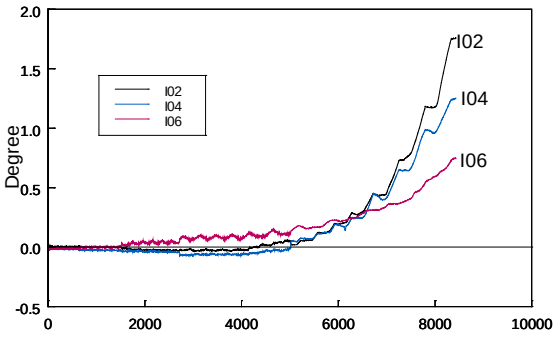

(d) Rotation in East-West Direction

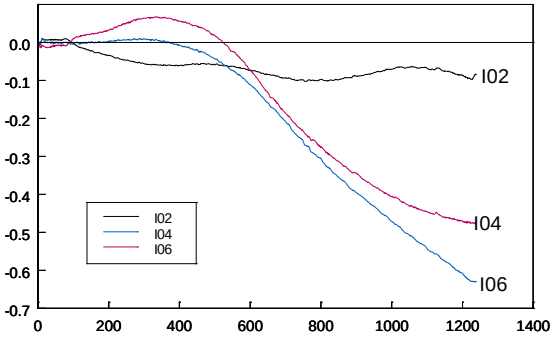

(e) Rotation in East-West Direction

Figure 4.11 Monotonic vs. Cyclic Loading (Phase 2A)

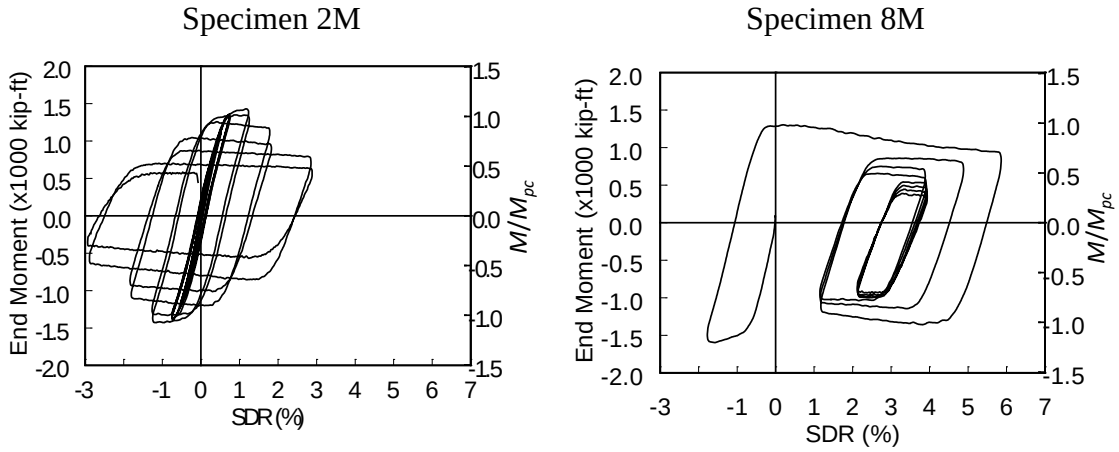

(a) Hysteresis Response

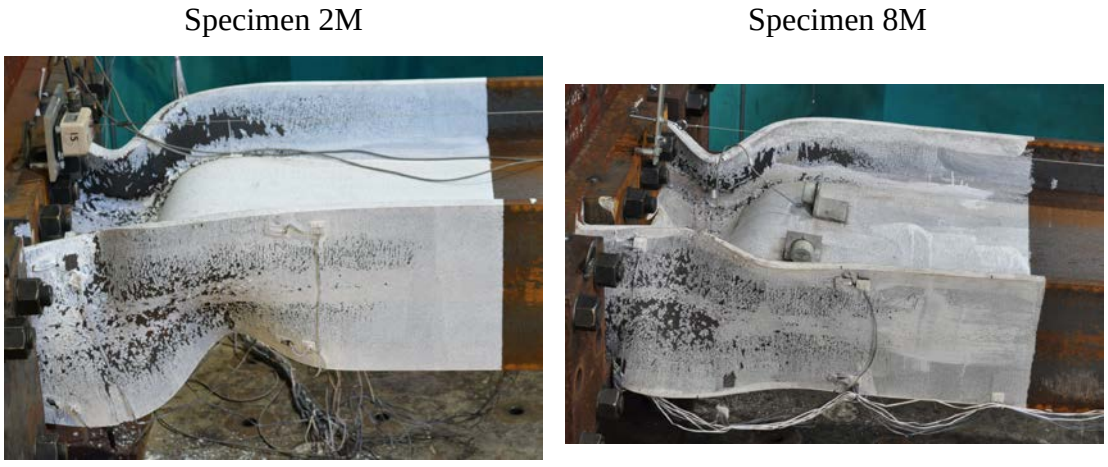

(b) Local Buckling Pattern

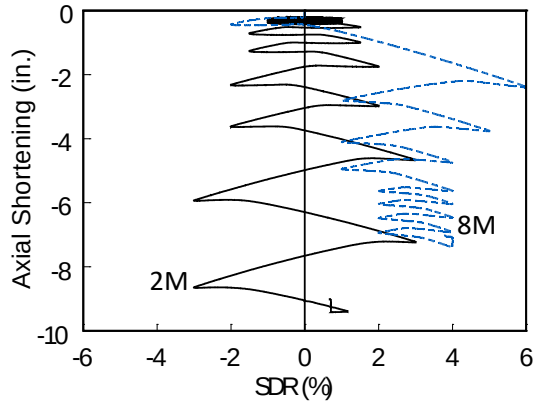

(c) Axial Shortening

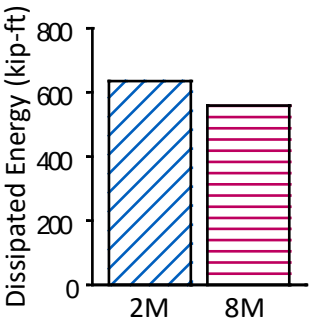

(d) Energy Dissipation

Figure 4.12 Comparison of Response of Far-field and Near-fault Ground Motion Effect

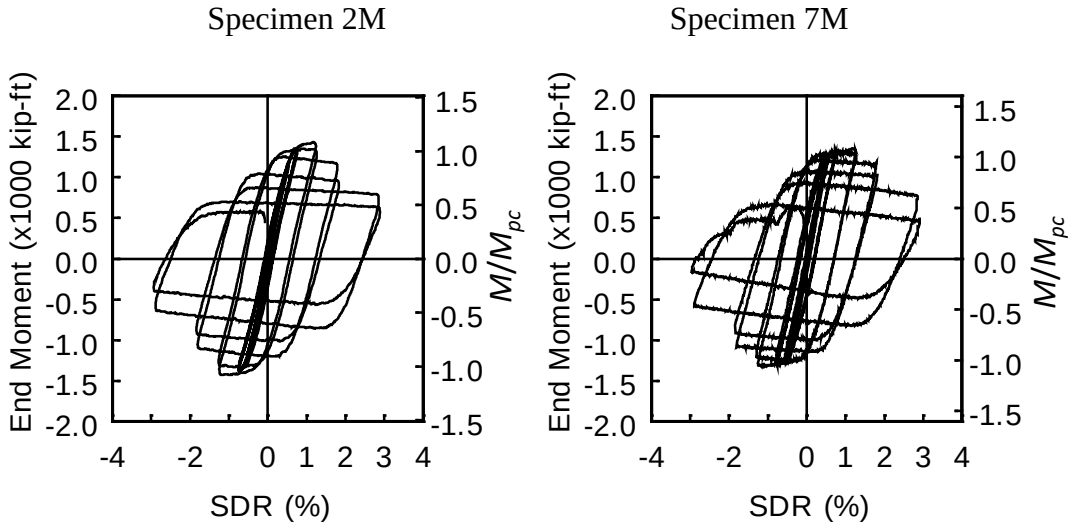

(a) Strong-Axis Hysteresis Response

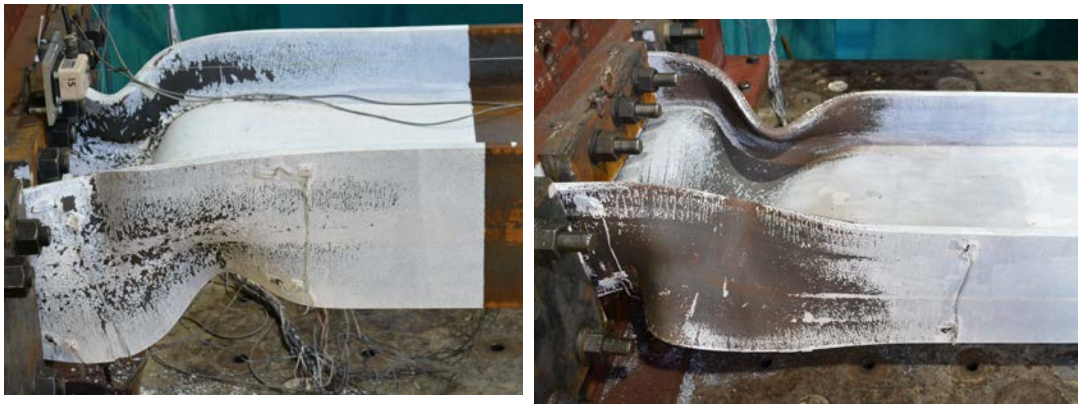

(b) Local Buckling Pattern

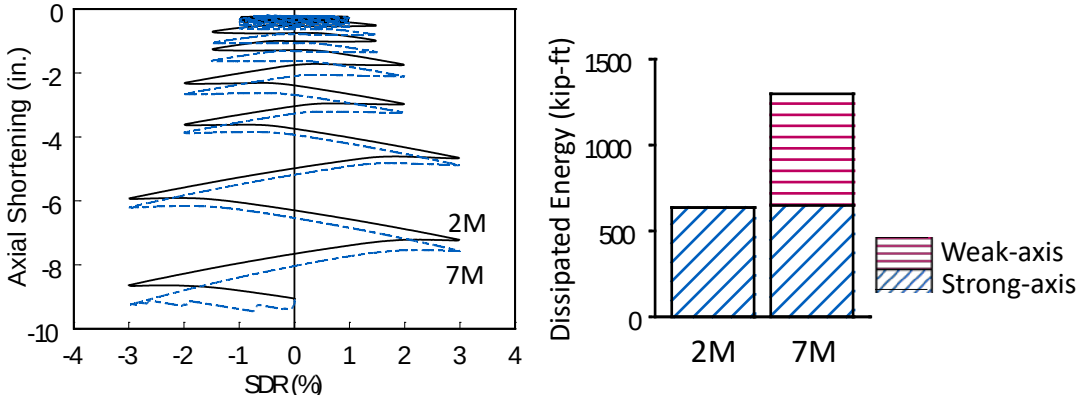

(c) Axial Shortening (d) Energy Dissipation

Figure 4.13 Effect of Biaxial Bending

Specimen 2L Specimen 6L

(a) Failure Mode Comparison

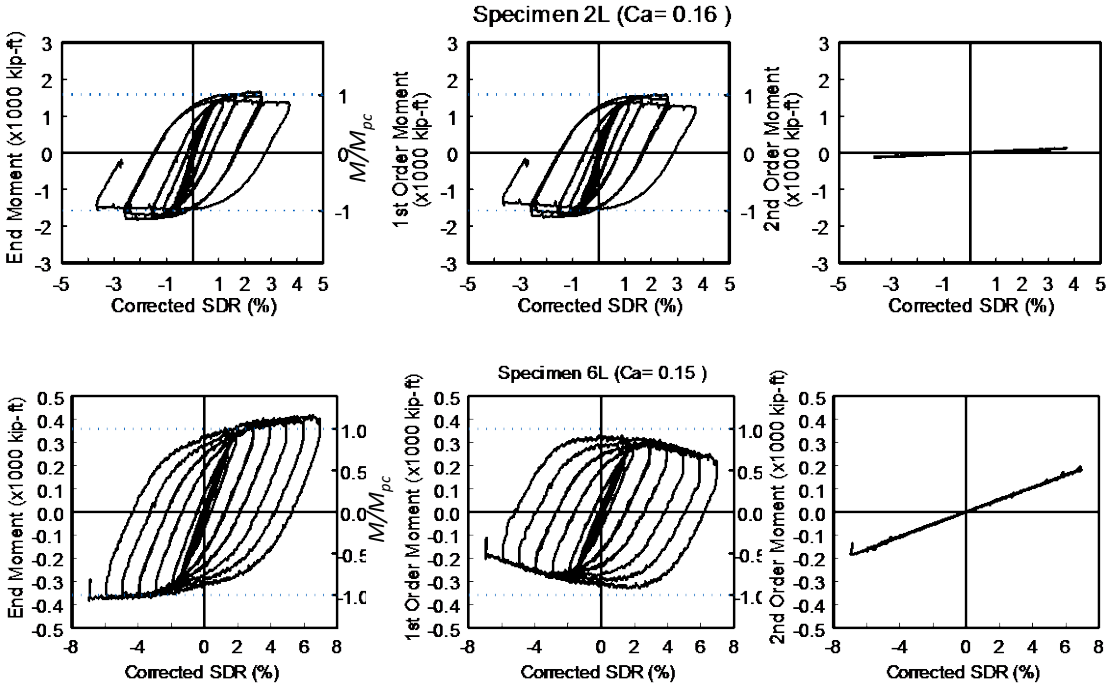

(b) Global Response Comparison

Figure 4.14 Strong Axis Bending vs. Weak Axis Bending

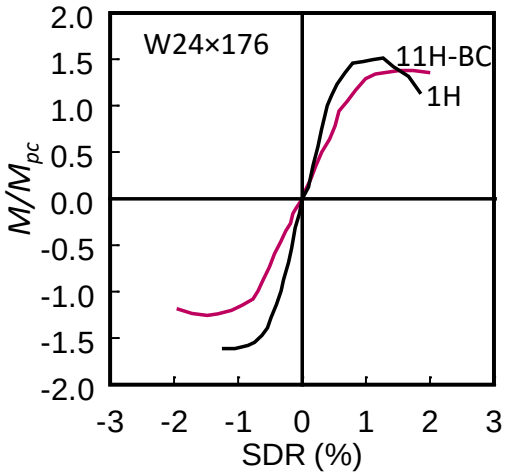

(a) Backbone Comparison

Specimen 1H

Specimen 11H-BC

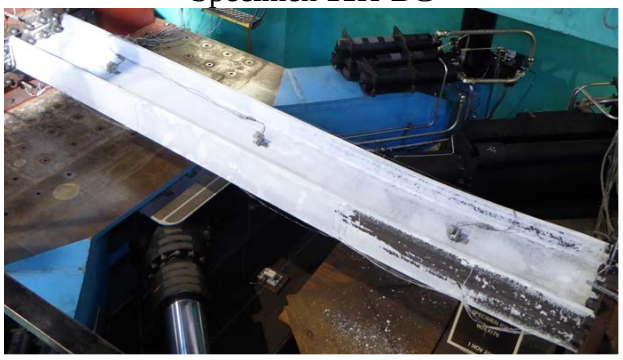

(b) Failure Modes

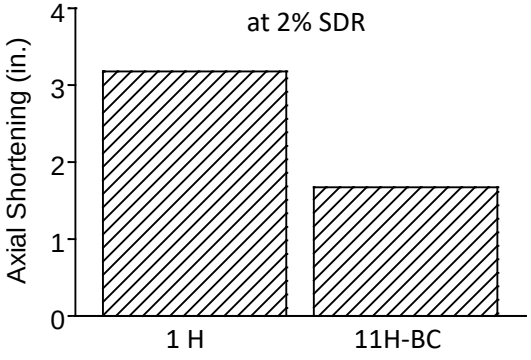

(c) Axial Shortening

Figure 4.15 Boundary Condition Effect (W24×176 Columns)

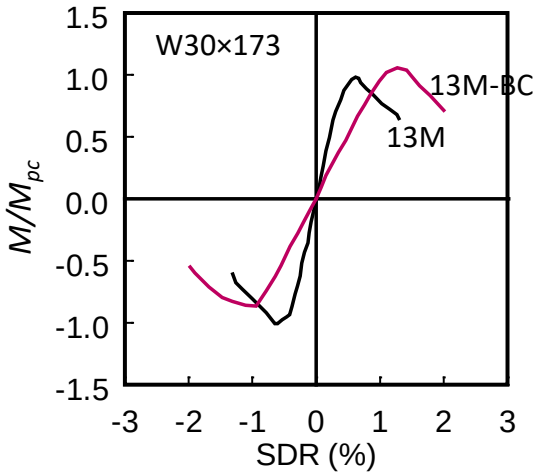

(a) Backbone Comparison

Specimen 13M

Specimen 13M-BC

(b) Failure Modes

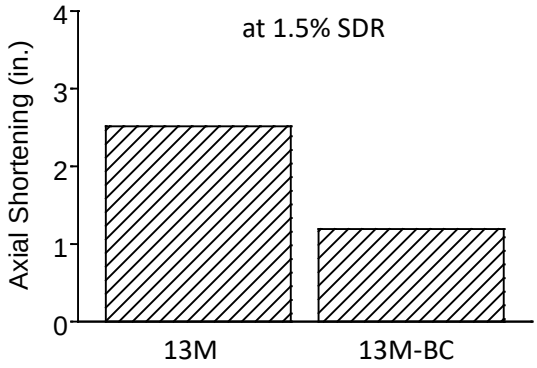

(c) Axial Shortening

Figure 4.16 Boundary Condition Effect (W30×173 Columns)

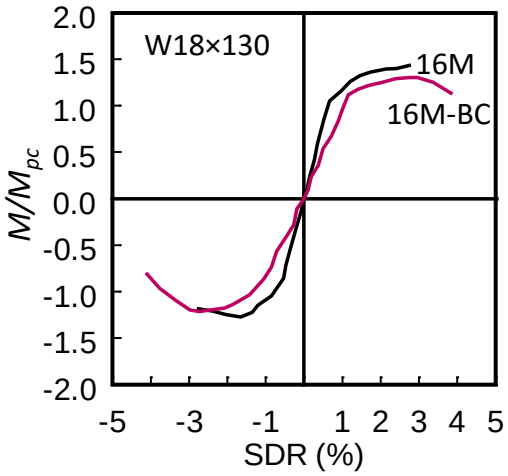

(a) Backbone Comparison

Specimen 16M Specimen 16M-BC

(b) Failure Modes

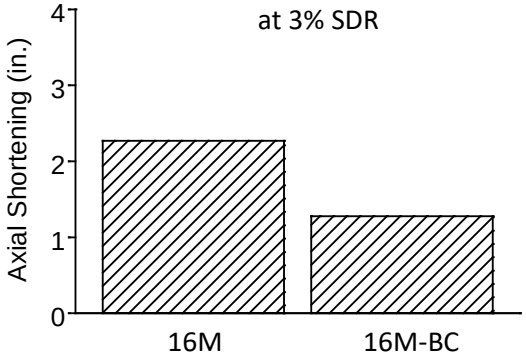

(c) Axial Shortening

Figure 4.17 Boundary Condition Effect (W18×130 Columns)

5 FINITE ELEMENT ANALYSIS OF COLUMN MODELS

5.1 Introduction

To generate a holistic database, one-hundred and ten wide-flange columns were modeled and subjected to axial force and lateral drift (either monotonic or cyclic) using finite element simulation. Model validation was conducted utilizing experimental data. The effect of initial imperfections and residual stresses on the column response were investigated. Furthermore, a sensitivity analysis on material parameters was performed.

5.2 Modelling Techniques

Test setup was modeled and analyzed using commercially available finite element software ABAQUS-CAE (2010). The model simulated global behavior, yielding pattern, and strength degradation in the specimen resulting from local buckling and interaction with LTB. The analytical model of steel beam-column was meshed using the general-purpose shell element type (S4R). This quadratic doubly curved shell elements can capture the large deformation expected severe local buckling within the cross-section. Reduced integration and hourglass control were also implemented in the model.

Translation and rotation in all three directions was constrained at both ends of the 18-ft. long column model for the fixed-fixed boundary condition simulation (see Figure 5.1). For the fixed-flexible boundary condition simulation, the same amount of strong-axis rotation as that applied in testing was prescribed to the model's column top. To be consistent with the test set-up, no additional lateral bracing was provided. An axial load was first applied to the longitudinal (i.e., U_3) direction up to a target force level with a force control method and then applied lateral drift using a displacement control method in the transverse (i.e., U_2) direction was then imposed (see Figure 3.5 and Figure 3.6). The same

loading protocols implemented in testing (see Chapter 3) were used in the finite element simulation.

5.3 Cyclic Material Properties

A typical stress-strain curve of a tensile steel coupon test is characterized by an elastic region, a short region of yielding with constant strength, material hardening region, and a strength softening branch leading to a rupture in the coupon. This monotonic strain hardening can be modeled with an isotropic hardening rule, which the material yield surface expands as plastic strain increases as shown in Figure 5.2. For cyclic loading, however, yield stress of a reverse loading branch is different from the stress achieved at the load reversal point due to the Bauschinger effect. This effect cannot be modelled with the isotropic hardening rule that only allows the material to yield at the same magnitude of the maximum or minimum stress experienced in the previous cycle [see Path ABCFG in Figure 5.2(b)]. On the other hand, kinematic hardening rule captures the Bauschinger effect and also allows the yield surface to translate in stress space during plastic straining while maintaining the same size as shown in Figure 5.2(c). Path ABCDE in Figure 5.2(b) demonstrates kinematic hardening behavior for cyclic loading.

The ABAQUS-CAE material library offers a model that simulates both the isotropic and kinematic hardening behavior. The model is based on the Von Misses yield surface, an associated flow rule, and a hardening law that includes both nonlinear isotropic and nonlinear kinematic hardening components.

Cyclic coupon tests were conducted in this research (see Figure 3.12). A stabilized curve was obtained from the test data and used to calibrate the nonlinear kinematic and

isotropic hardening parameters (see. Backstress defined as the center of a yield surface in each strain range is calculated as follows

$$\alpha_i = \sigma_i - \sigma^s \tag{5.1}$$

where σ^s is the stabilized size of the yield surface and can be obtained from the fallowing equation

$$\sigma^s = \frac{\sigma_1 + \sigma_n}{2} \tag{5.2}$$

Least square fit approach was used to calibrate the initial kinematic hardening slope, *C*, and the rate of departure from this initial slope, γ, based on the following expression

$$\alpha = \frac{C}{\gamma}\left(1 - e^{-\gamma\varepsilon^{pl}}\right) + \alpha_1 e^{-\gamma\varepsilon^{pl}} \tag{5.3}$$

Isotropic hardening parameters, θ_∞, which is the maximum change in size of the yield surface, and *b*, which is the rate of change of yield surface size as plastic strain develops, are calibrated as

$$\sigma^0 = \sigma|_0 + \theta_\infty\left(1 - e^{-b\varepsilon^{pl}}\right) \tag{5.4}$$

To calibrate a cyclic plastic model for a given material, it is necessary to provide the cyclic test data of that material over the entire range of strain to be predicted by the model (see .Figure 5.3). However, large-strain cyclic testing is difficult due to buckling of the test coupons. To improve accuracy for large strain range, the material parameters can be modified. Since hardening modulus of the cyclic curve is similar to the monotonic hardening modulus, the shape of the cyclic curve can be approximated based on the

monotonic curve for strain range larger than that provided by the experimental data as shown in Figure 5.4.

To verify the material model at the coupon level, a finite element model with the geometry of the cyclic coupons was analyzed under cyclic loading. Figure 5.5(b) shows the correlation between the predicted response and the cyclic coupon test data for one set of kinematic hardening parameters. Defining more than one set of parameters improves the accuracy of Bauschinger effect as shown in Figure 5.5(c). However, it overestimates the maximum strength, and the strain hardening slope does not accurately represent the cyclic test results. Therefore, only one set of kinematic hardening parameters (C and γ) were used in the subsequent numeric simulation.

5.4 Effect of Residual Stresses

Residual stresses primarily result from an uneven cooling after a hot rolling process of a steel member and is inherent in the test column specimens. The magnitude and distribution of residual stress in two specimens were examined and shown in Figure 3.17. Residual stress in longitudinal direction can influence the compressive strength of an axially loaded or flexural member. Early research on column behavior established that the presence of residual stress also decreased the initial yield load of the section (Bjorhovde 1972). Newell (2008) observed that the ductility of columns was not significantly affected by residual stresses. Since residual stress is inherent in all test specimens, experimental data provides insights into the effect of residual stresses on the performance of columns subjected to both axial and lateral loading.

Figure 5.6 shows monotonic responses of a W24×104 column modelled with and without residual stresses. Inclusion of residual stress in the model softens the transition from elastic to plastic behavior (i.e., the initial elastic stiffness softens earlier and gradually decreases). No other significant effect on the global behavior was observed. Residual stresses were included in the model when correlation between model predictions and test data was analyzed. But residual stress was ignored in the parametric studies.

5.5 Geometric Imperfections

Another factor that influences the column capacity is the initial geometric imperfection. To trigger local and global instabilities, geometric imperfections can be introduced to finite element model by superimposing buckling modes obtained from eigenvalue analysis. Global out-of-straightness imperfection recommended by AISC (2010c) is equal to L/1,000 [see Figure 5.7(a)]. Local web and flange imperfections expected from manufacturing process is limited by ASTM (2003). Figure 5.7(b) demonstrates the web and flange geometric imperfections implemented in the simulations. Figure 5.7(c) shows that initial imperfections has a minor effect on the global response of the column. Initial imperfections were included in test correlation studies, but not in parametric studies.

5.6 Correlation of Test Specimens

Model validation was conducted using experimental data. Figure 5.8(a) through Figure 5.15(a) show global response comparisons between the Phase 1 test data and the finite element predictions. Since the test setup cannot constitute the ideal fixed-fixed

boundary conditions, test results were adjusted to remove the effect of end plate flexibility (see Section 3.8).

Material properties presented in Section 3.6 and Section 5.3 were used in this validation process. Even though residual stresses and initial geometric imperfections do not significantly affect the overall predicted behavior of simulated columns as discussed in Sections 5.4 and 5.5, they were included in the models for correlation study. Figure 5.8(b) through Figure 5.15(b) show the deformed shapes of the specimens tested in Phase 1 study and the predicted deflected shapes based on finite element models. The buckling modes observed from tests were well predicted by finite element simulation. In particular, the simulation accurately predicted the out-of-plane LTB buckling of the W24×176 column (Figure 5.8).

Similarly, columns tested in Phase 2A program are correlated with finite element analysis as illustrated in Figure 5.16 as an example. In general, the global response curves (load-displacement and moment-rotation relations) and the deformed shapes predicted by finite element simulation closely resembled the actual behavior of the test specimens. Since the finite element models reasonably predicted test results, they were utilized to predict behavior of other columns subjected to various axial load levels with lateral drifts in the following parametric study.

5.7 Parametric Study

In order to investigate the effect of section compactness on column cyclic behaviors, finite element analysis was conducted on one-hundred and ten wide-flange sections ranging from nominal depths of 44 in. to 10 in. as shown in Table 5.2 through

Table 5.4. These selected sections form a holistic database covering broad ranges of section and member slenderness ratios ($2.62 \leq \lambda_f \leq 9.92;\ 5.66 \leq \lambda_w \leq 57.5;\ 41.1 \leq \lambda_L \leq 130$). Figure 5.17 shows the flange and web width-to-thickness ratios being considered with respect to the seismic compactness limits (AISC 2010b). The flange and web compactness limits for highly ductile members are 7 and 43.2, respectively, given elastic modulus E = 29,000 ksi, yield stress F_y = 50 ksi, and axial load ratio C_a = 0.6. The majority of the sections satisfy both the AISC 341 flange and web compactness requirements to be classified as highly ductile members. Sections with flange slenderness between λ_{hd} and λ_{md} are qualified for intermediate moment frames.

To investigate the cyclic behavior of the columns, AISC seismic loading protocol for testing steel moment connections was used (AISC 2010b). Focusing on the cyclic behavior of interior columns, three constant levels of axial force (C_a = 0.2, 0.4, and 0.6) were applied to the models with a fixed-fixed boundary condition. Then, displacement controlled lateral cyclic loading is applied. For each section, three different yield stresses (F_y= 50, 55, and 65 ksi) were simulated in the finite element analysis to investigate the effect of material properties.

In addition, some columns were subjected to other loading protocols to examine loading history effect, boundary condition effect, and varying axial load effect. Detailed results of parametric study are provided in Appendix B.

5.7.1 Section Depth Effect

In Phase 1 study, Group 1 specimens (W24×176) exhibited a combined local and global buckling as their failure mode. Results from parametric study confirmed that deeper

and shallower sections with slenderness ratios similar to Group 1 section exhibited the same failure mode as shown in Figure 5.18. Therefore, both test data and numerical simulation showed that the combined local and global buckling failure mode is not unusual. Categorization of column buckling modes is presented in Chapter 6.

5.7.2 Axial Load Level Effect

Figure 5.19 shows the global response of three W24×176 columns (Group 1 specimens) subjected to three different axial load levels. Increase in axial load level drastically aggravated the post-buckling strength degradation and axial shortening of the column when comparing at the same drift. Comparison of the backbone curves of these simulated columns also shows that flexural strength and plastic rotation capacity of the column is reduced significantly when subjected to higher axial compression. These observations hold true for all finite element simulation conducted on one-hundred and ten different columns (see Appendix B).

5.7.3 Varying Axial Load Effect

As discussed in Chapter 4, mainly three different levels of constant axial load representative of gravity loads on first-story interior columns in SMFs with two-to-twenty stories are used in testing. To examine the behavior of first-story exterior columns, effect of varying axial force was also studied. Figure 5.20 shows that local buckling starts much earlier and strength degradation aggravates more drastically for interior columns subjected to constant axial load level. However, failure modes are the same for both constant and varying axial load cases. Both experimental and numerical results indicate that cyclic

responses of interior and exterior columns are different and need to be treated separately in modelling and design.

5.7.4 Boundary Condition Effect

Experimental results showed that due to relaxation at the top of the column, the overall behavior of fix-flexible boundary condition has different than fix-fix boundary condition case. Numerical simulations verified the results of experimental tests and it was found that regardless of the boundary conditions, the failure mode of the sections does not change (see Figure 5.21). Due to relaxation at the top of the column, this end remains elastic while the fix end prone to yielding and local buckling. Since the local buckling causes the axial shortening, fix-fix boundary condition shortens as twice as the fix-flexible boundary condition case.

5.7.5 Monotonic vs. Cyclic Loading Effect

Prior to full-scale testing, comparison of monotonic and cyclic loading effect revealed that cyclic loading subjects specimens to a considerable amount of yielding and strain hardening, which trigger global instabilities. Pre-test simulation also suggested that out-of-plane global instability might not occur under monotonic loading because the column did not have the chance to experience significant yielding and strain hardening as its cyclic counterpart did. This phenomenon was indeed observed in testing of Group 12 specimens in Phase 2A (see Figure 4.11). Figure 5.22 shows the hysteretic responses and the failure modes of two W30×261 columns subjected to monotonic and cyclic loading. Note that monotonic (push-over) loading does not trigger global buckling and cannot reflect in-cycle or cyclic strength deterioration. Therefore, post-buckling strength

degradation is much less compared to the response of cyclically loaded specimen. Axial shortening of monotonically loaded sections is also very low compared to that observed in the cyclic loading case.

5.7.6 Far-field vs. Near-field Loading Effect

Test results show that loading history plays a significant role in the response of a column. The same observation is confirmed in numerical analysis as shown in Figure 5.23. The responses are from two models subjected to the standard AISC loading protocol and the near-fault loading protocol (Krawinkler et al. 1996), respectively. The latter model exhibit more ductile behavior compared to its counterpart, which undergoes the standard cyclic loading simulating far-field seismic demand. The initial large-magnitude lateral drift in the positive direction of the near-field loading protocol shown in Figure 3.5(d) causes strength retention, which leads to increase in member's peak strength. For far-filed loading case, the post-buckling strength degradation is more severe mainly due to numerous loaded cycles with large amplitudes. Even though the hysteresis responses are very different for these two loading cases, the failure mode of the section is not effected by the loading history. Effects of loading history is discussed in more details in Chapter 7.

5.8 Shallow versus Deep Columns

Newell and Uang (2008) tested W14 columns in an AISC-sponsored research project and showed that these columns had very large inelastic deformation capacities even under the presence of very high axial compression. The highly ductile sections of the tested columns shown in Figure 5.24(a) had d/b_f ratios approximately equal to 1. Test results showed that these columns featured a very stable cyclic response and only showed limited

axial shortening as depicted in Figure 5.24 (b) and (c), respectively. The buckling modes of these sections were the same, which were governed by flange local buckling without any out-of-plane deformation. Web local buckling was not observed in these columns, except for the one with a W14×132 section which experienced very minor web buckling at a high axial force level. In practice, a "shallow" column is loosely defined as that with a nominal depth of the section no larger than 14 in.; otherwise, it is called a "deep" column. Based on the results from both the AISC-sponsored and NIST-sponsored test programs, it appears that significant local buckling and axial shortening, which was accompanied by a significant strength degradation, would only occur in deep columns. It will be shown in this section that the "deep column phenomenon" will also occur in some shallow columns.

Figure 5.25 shows the depth-to-width ratios of AISC W-shapes as a function of the weight per linear foot. The depth-to-width ratio has a range between 1 to 3.3. Flange and web slenderness ratios of W-shapes are also shown in Figure 5.26, with red lines indicating their respective depth-to-width ratio groups. Most shallow sections (W14, W12, and W10) have depths that are approximately equal to their flange widths ($d/b_f \approx 1$). However, some have depths that are as large as three times of their flange widths (Figure 5.27).

Figure 5.28 shows the predicted buckling mode and global response of three shallow columns with d/b_f less than 1.5. Like the response of AISC test columns, these three numerically simulated columns showed excellent energy dissipation capability. When the width of these sections was reduced such that $1.5 \leq d/b_f \leq 2.5$, Figure 5.29 shows that significant buckling dominated the response and strength degradation was obvious. The deep column phenomenon when the depth-to-width ratio was even higher ($1.5 \leq d/b_f \leq 2.5$); see Figure 5.30.

Figure 5.31 compares the cyclic response of a deep column (W21×132) and a shallow column (W10×30) in terms of buckling mode, hysteresis response, post-buckling strength degradation, and axial shortening; the sections of these two columns had similar slenderness ratios and depth-to-width ratio. Numerical simulation showed that the behavior of these two columns was similar. Figure 5.32 further demonstrates that W14 columns, depending on the depth-to-width ratio, can buckle in one of the three different buckling modes (see Chapter 6 for classification of the buckling mode), and axial shortening can be significant when the "deep column phenomenon" occurs. Other than classifying a section as either deep or shallow, it may be more appropriate to call those with the "deep column phenomenon" as "shortening-sensitive" section. Chapter 6 will present a procedure that uses a parameter ζ in Eq. (6.15) to identify the governing buckling mode. With this parameter, Figure 5.33 shows the domain of shortening-sensitive" section.

5.9 Acknowledgements

The text below is reproduced verbatim as it appears in the acknowledgments section on page xvii per the UCSD Office of Graduate Studies Formatting Requirements.

Chapter 5 of this dissertation is based on material published by Structures Congress, titled "Classifying cyclic buckling modes of steel wide-flange columns under cyclic loading" with co-authors Harris, J., and Uang, C. (2015). Materials were also submitted for publication by EuroSteel Conference, titled "Cyclic backbone curves for steel wide-flange columns: A numerical study" with co-authors Harris J.L., and Uang C.-M. (2017). The dissertation author is the first author of these papers.

Table 5.1 Kinematic and Cyclic Hardening Parameters for ABAQUS Models

Strain Range	θ_∞	b	C	γ
±1%	28.75	0.9159	1278.5	110.5
±2%			250	11.2
±3%			124.95	9.64
±4%			80.83	3.16
Two Parameters for ±1%			16780 895.9	520.3 144.7

Table 5.2 Parametric Study: Column Sections with SFB Mode

Section	A	λ_f	λ_w	λ_L	L
W14×233	68.5	4.62	10.7	43.9	180
W14×370	109	3.10	6.89	42.15	180
W14×455	134	2.62	5.66	41.10	180
W14×193	56.8	5.45	12.8	44.4	180
W14×132	38.8	7.15	17.7	47.9	180
W14×176	51.8	5.97	13.7	44.8	180
W12×252	74.1	2.89	6.96	53.9	180
W12×170	50	4.03	10.1	55.9	180
W12×152	44.7	4.46	11.2	56.4	180
W12×87	25.6	7.48	18.9	46.9	144
W12×65	19.1	9.92	24.9	47.7	144
W12×58	17.0	7.82	27.0	47.8	120
W10×88	26.0	5.18	13.0	45.6	120
W10×68	19.9	6.58	16.7	46.3	120
W10×112	32.9	4.17	10.4	44.8	120
W10×49	14.4	8.93	23.1	47.2	120
W10×33	9.71	9.15	27.1	61.9	120

Table 5.3 Parametric Study: Column Sections with ALB Mode

Section	A	λ_f	λ_w	λ_L	L
W33×130	38.3	6.73	51.7	75.3	180
W33×141	41.5	6.01	49.6	74.1	180
W30×108	31.7	6.89	49.6	78.1	168
W30×124	36.5	5.65	46.2	75.3	168
W30×173	50.9	7.04	40.8	61.4	210
W30×90	26.3	8.52	57.5	101.4	212
W30×211	62.3	5.74	34.5	75.6	264
W27×102	30.0	6.03	47.1	78.1	168
W27×161	47.6	6.49	36.1	66.9	216
W24×76	22.4	6.61	49.0	75.0	144
W24×131	38.6	6.70	35.6	72.7	216
W24×104	30.7	8.50	43.1	74.2	216
W24×55	16.2	6.94	54.6	89.6	120
W21×93	27.3	4.53	32.3	65.2	120
W21×132	38.8	6.01	28.9	73.7	216
W21×147	43.2	5.44	26.1	73.2	216
W21×111	32.6	7.05	34.1	74.5	216
W21×62	18.3	6.70	46.9	81.4	144
W21×73	21.5	5.60	41.2	79.6	144
W18×65	19.1	5.06	35.7	71.0	120
W18×71	20.9	4.71	32.4	70.6	120
W18×106	31.1	5.96	27.2	72.2	192
W18×76	22.3	8.11	37.8	81.2	212
W18×86	25.3	7.20	33.4	73.0	192
W14×74	21.8	6.41	25.4	48.4	120
W14×82	24.0	5.92	22.4	48.4	120
W14×68	20.0	6.97	27.5	48.8	120
W14×53	15.6	6.11	30.9	75.0	144
W14×48	14.1	6.75	33.6	75.4	144
W14×38	11.2	6.57	39.6	77.4	120
W12×50	14.6	6.31	26.8	61.2	120
W12×35	10.3	6.31	36.2	72.7	112

Table 5.4 Parametric Study: Column Sections with CB Mode

Section	A	λ_f	λ_w	λ_L	L
W40×297	87.3	4.80	36.8	74.6	264
W40×362	106	3.99	30.5	73.3	264
W40×324	95.3	4.40	34.2	73.7	264
W36×330	96.9	4.49	31.4	75.2	288
W36×487	143	3.19	21.4	72.7	288
W36×256	75.3	3.53	33.8	72.5	192
W36×170	50.0	5.47	47.7	71.1	180
W36×210	61.9	4.48	39.1	69.8	180
W33×291	85.6	4.60	31.0	71.7	264
W33×354	104	3.85	25.7	70.6	264
W33×169	49.5	4.71	44.7	72.0	180
W30×261	77.0	4.59	28.7	74.8	264
W30×326	95.9	3.75	23.4	73.3	264
W30×261	77.0	4.59	28.7	59.5	210
W30×148	43.6	4.44	41.6	75.4	172
W27×129	37.8	4.55	39.7	76.0	168
W27×217	63.9	4.71	28.7	72.3	240
W27×307	90.2	3.46	20.6	70.4	240
W24×250	73.5	3.49	20.7	68.8	216
W24×335	98.3	2.73	15.6	66.9	216
W24×94	27.7	5.18	41.9	72.7	144
W24×103	30.3	4.59	39.2	78.4	156
W24×176	51.7	4.81	28.7	71.1	216
W24×84	24.7	5.86	45.9	110.8	216
W21×166	48.8	4.57	25.0	72.2	216
W21×201	59.3	3.86	20.6	71.5	216
W18×130	38.3	4.65	23.9	71.1	192
W18×211	62.3	3.02	15.1	76.6	216
W18×130	38.3	4.65	23.9	78.5	212
W18×192	56.20	3.27	16.7	76.0	212
W12×22	6.48	4.74	41.8	70.8	60

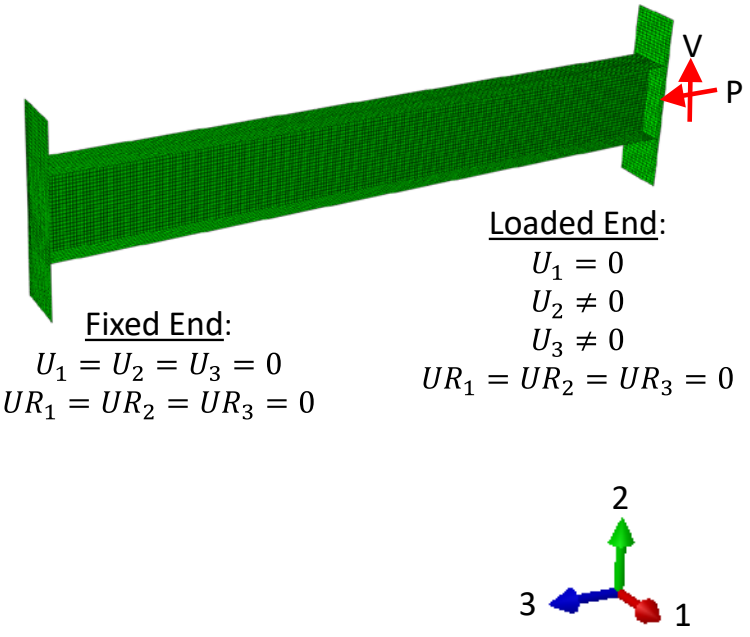

Figure 5.1 Boundary Conditions for Finite Element Model

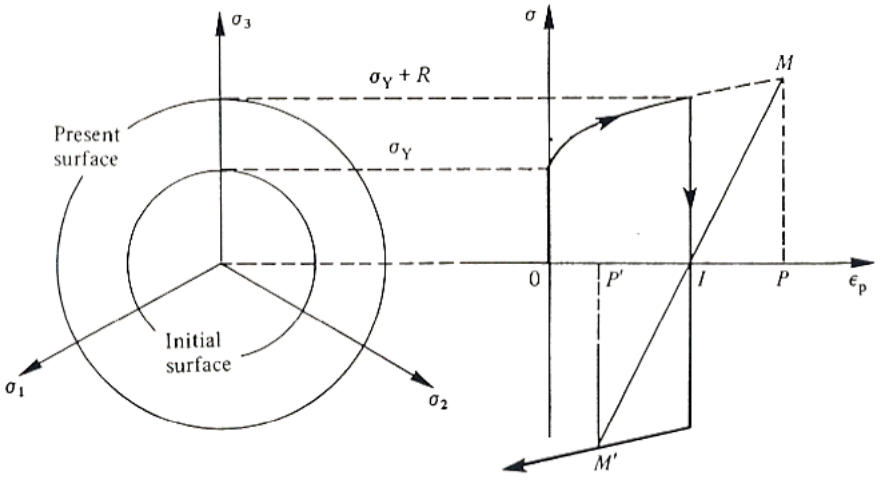

(a) Yield Surface Development and Isotropic Hardening Rule

Figure 5.2 Material Model in ABAQUS

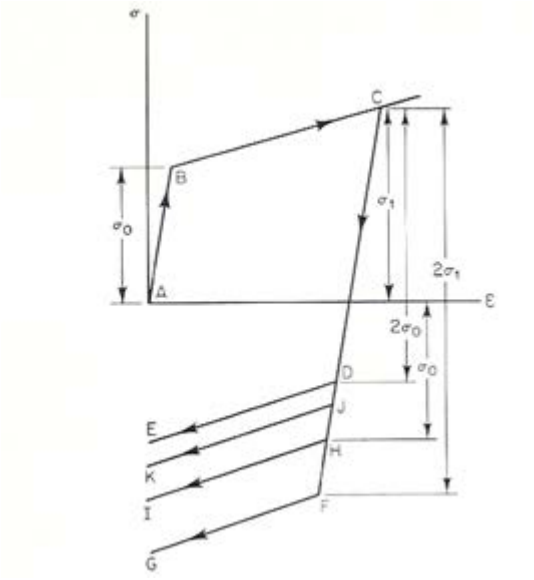

(b) Isotropic and Kinematic Hardening Paths

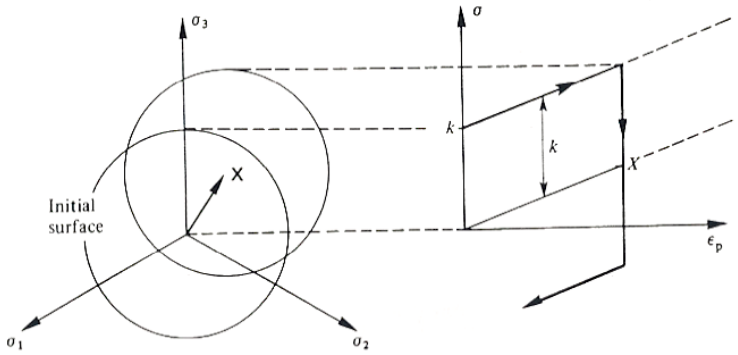

(c) Kinematic Hardening

Figure 5.2 Material Model in ABAQUS (Cont.)

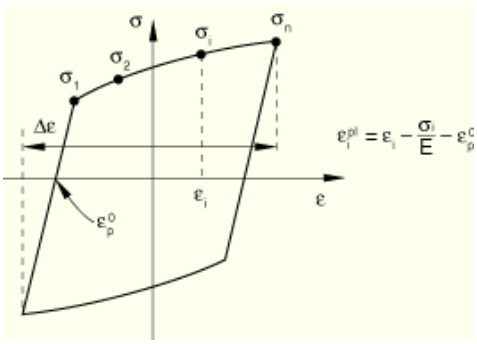

(a) Stress-Strain Data for Stabilized Cycle

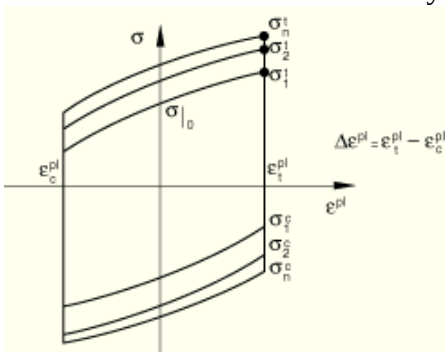

(b) Stress-Strain Data for Isotropic Hardening

Figure 5.3 Stress-Strain Data in ABAQUS

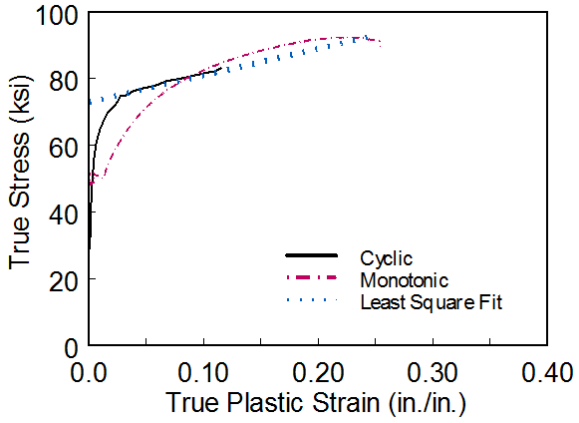

Figure 5.4 Least Square Fit to Stabilized Cyclic Curve

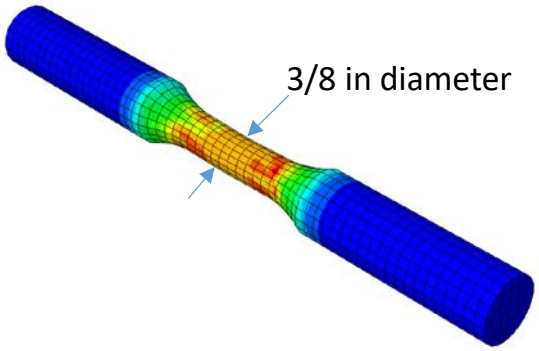

(a) Finite Element Model of Cyclic Test Coupon

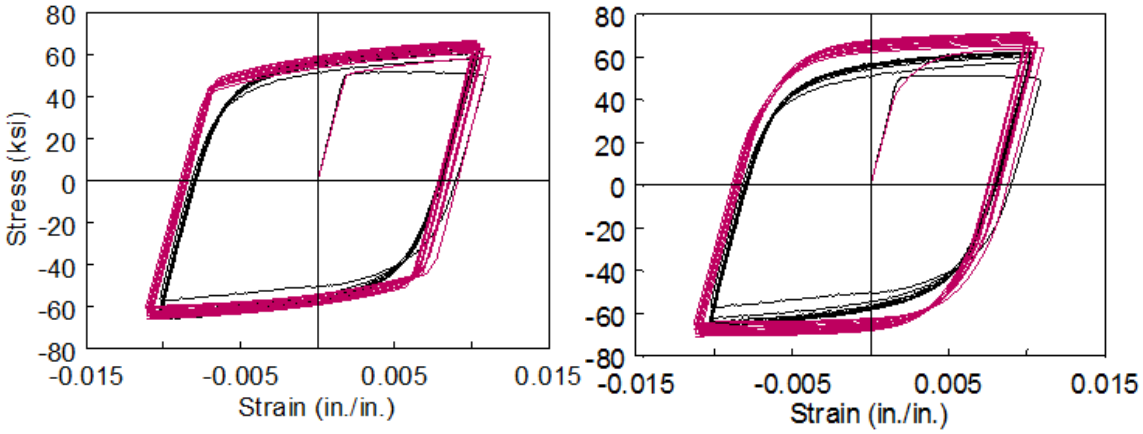

(b) with One Set of C and γ Parameters (c) with Two Set of C and γ Parameters

Figure 5.5 Correlation with Cyclic Coupon Test Results

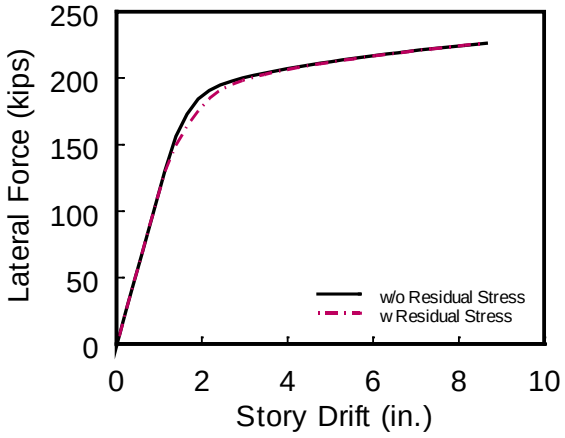

(a) Lateral Force vs. Story Drift

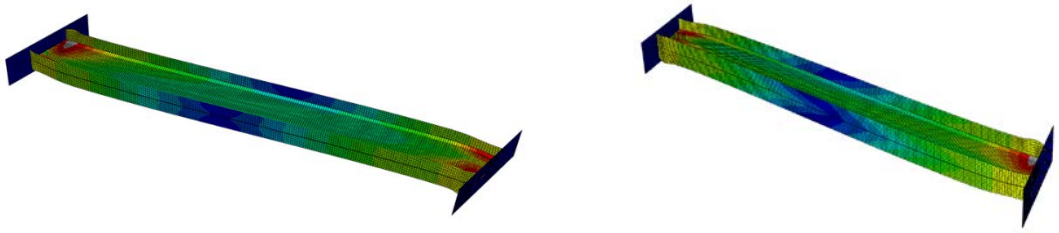

(b) without Residual Stresses (c) with Residual Stresses

Figure 5.6 Effect of Residual Stresses on Global Behavior (Model 2LP)

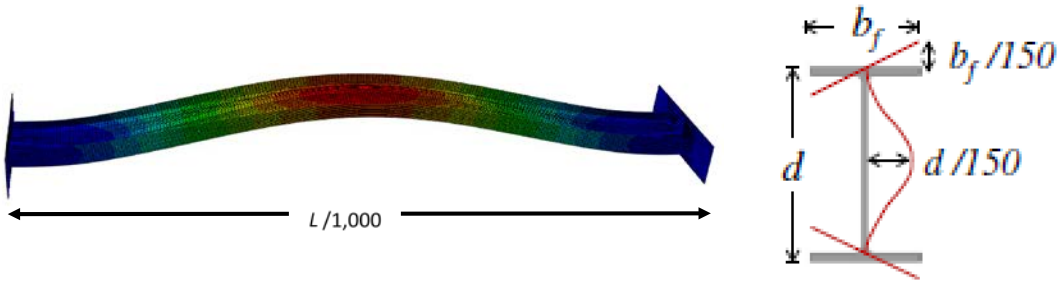

(a) Global Imperfection (b) Local Imperfection

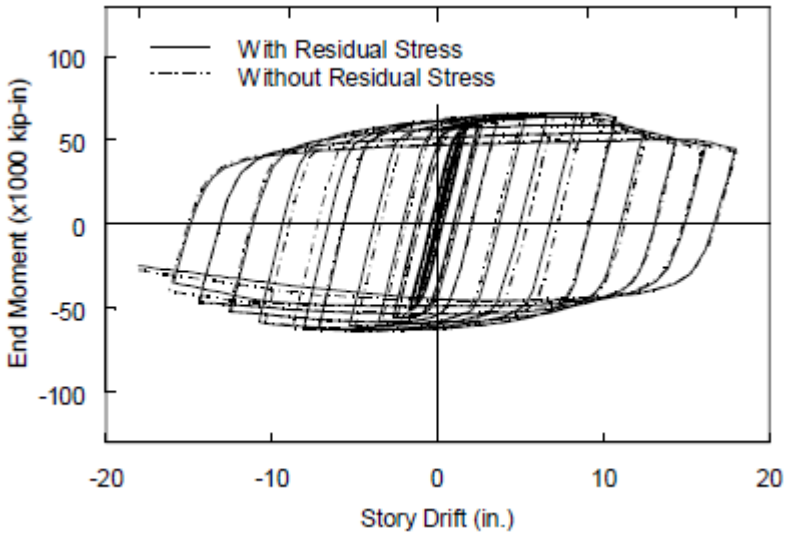

(c) Global Response Behavior (W24×279, C_a=0.2)

Figure 5.7 Effect of Initial Geometric Imperfections

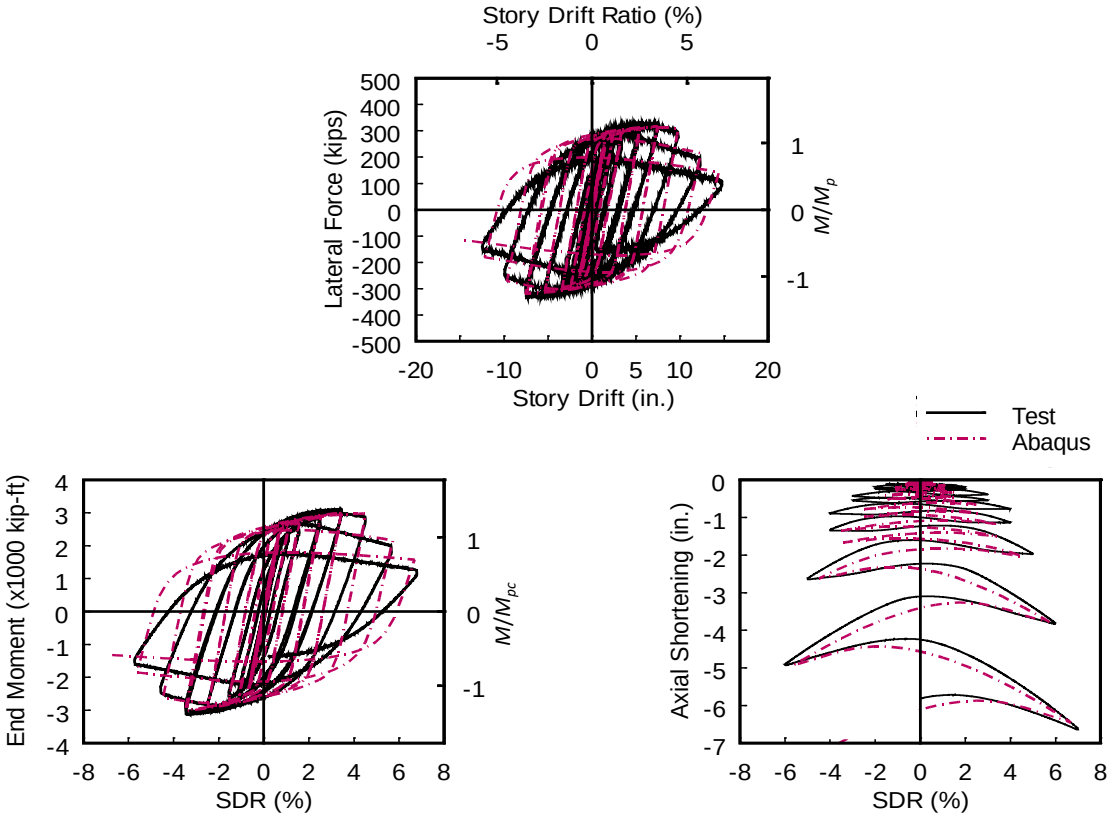

(a) Global Response

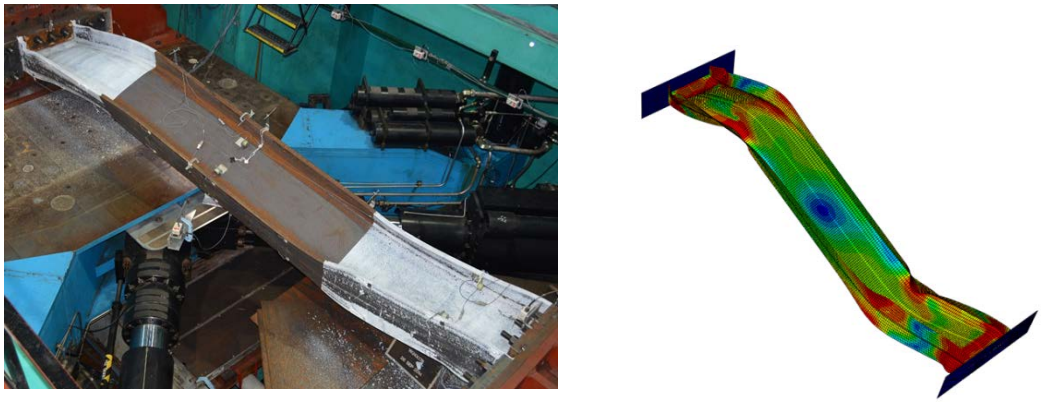

(b) Failure Mode

Figure 5.8 Correlation of Specimen 1L Response

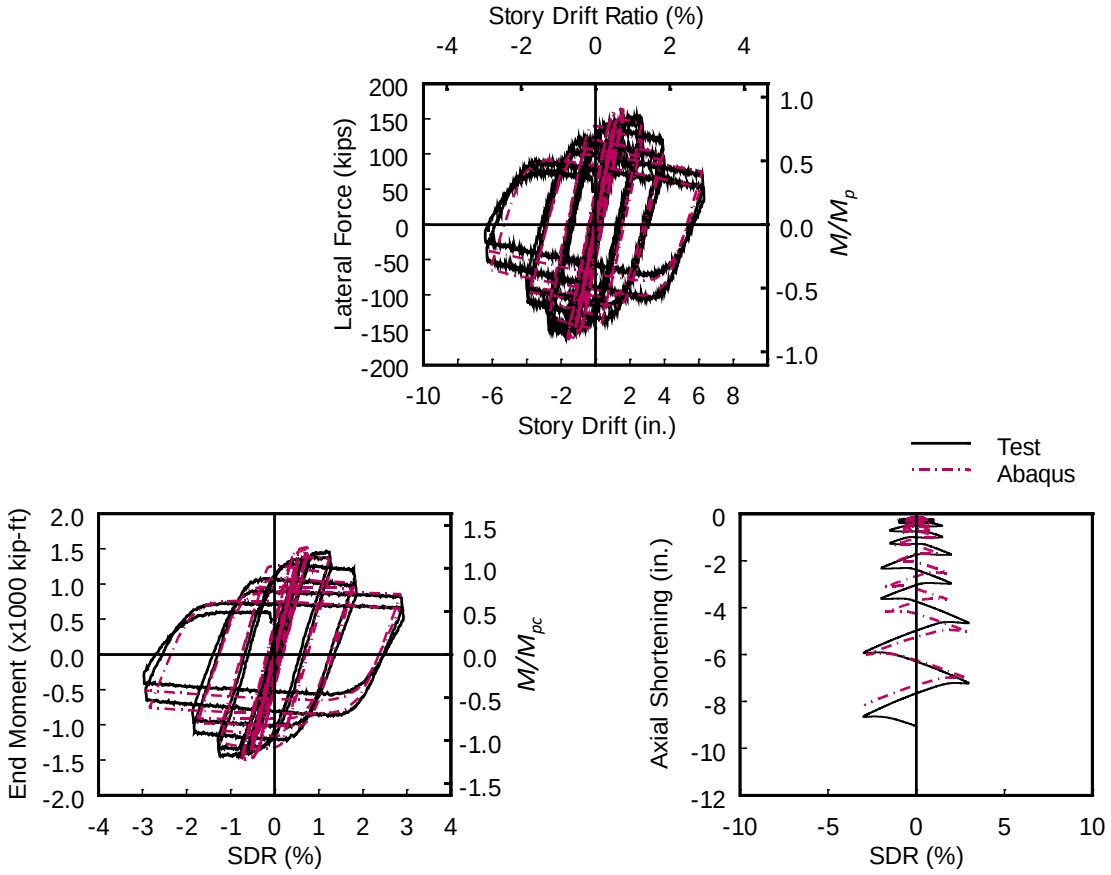

(a) Global Response

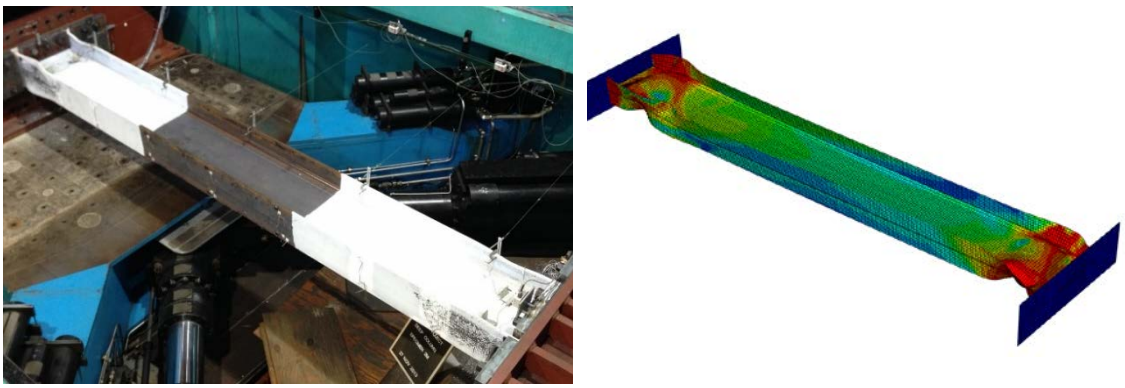

(b) Failure Mode

Figure 5.9 Correlation of Specimen 2M Response

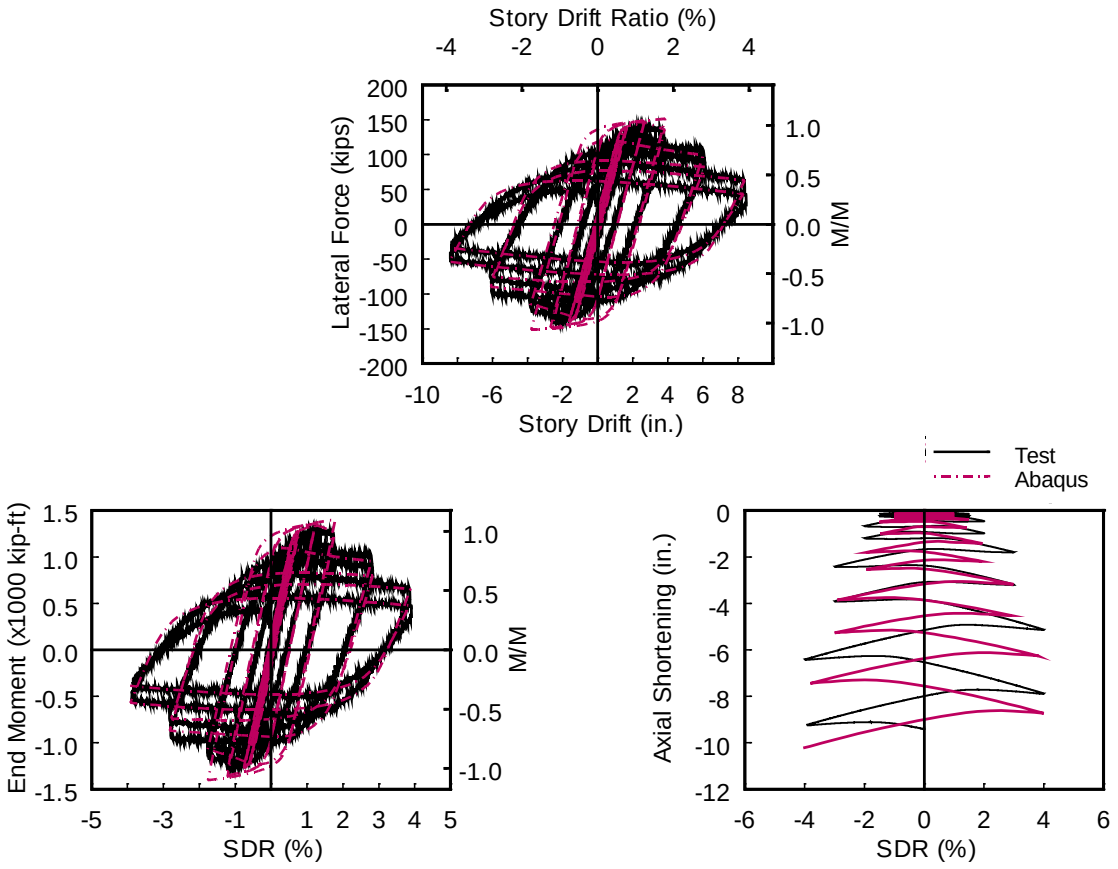

(a) Global Response

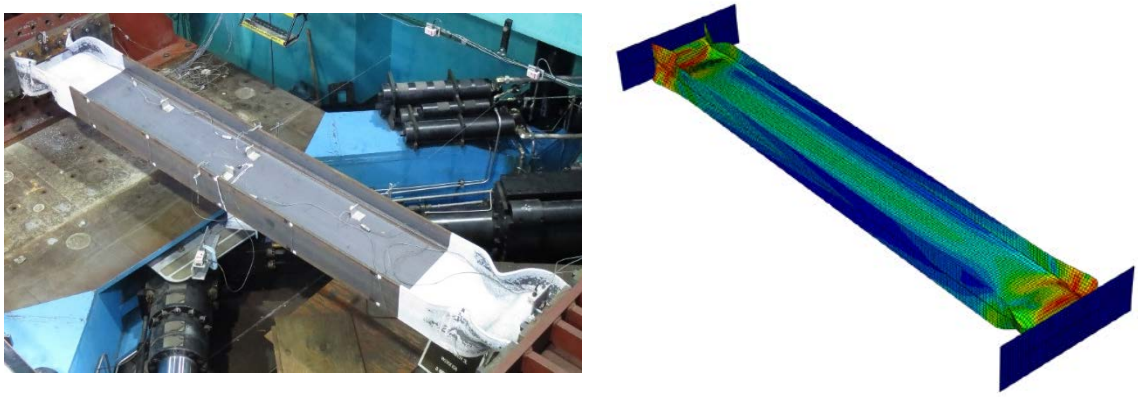

(b) Failure Mode

Figure 5.10 Correlation of Specimen 3L Response

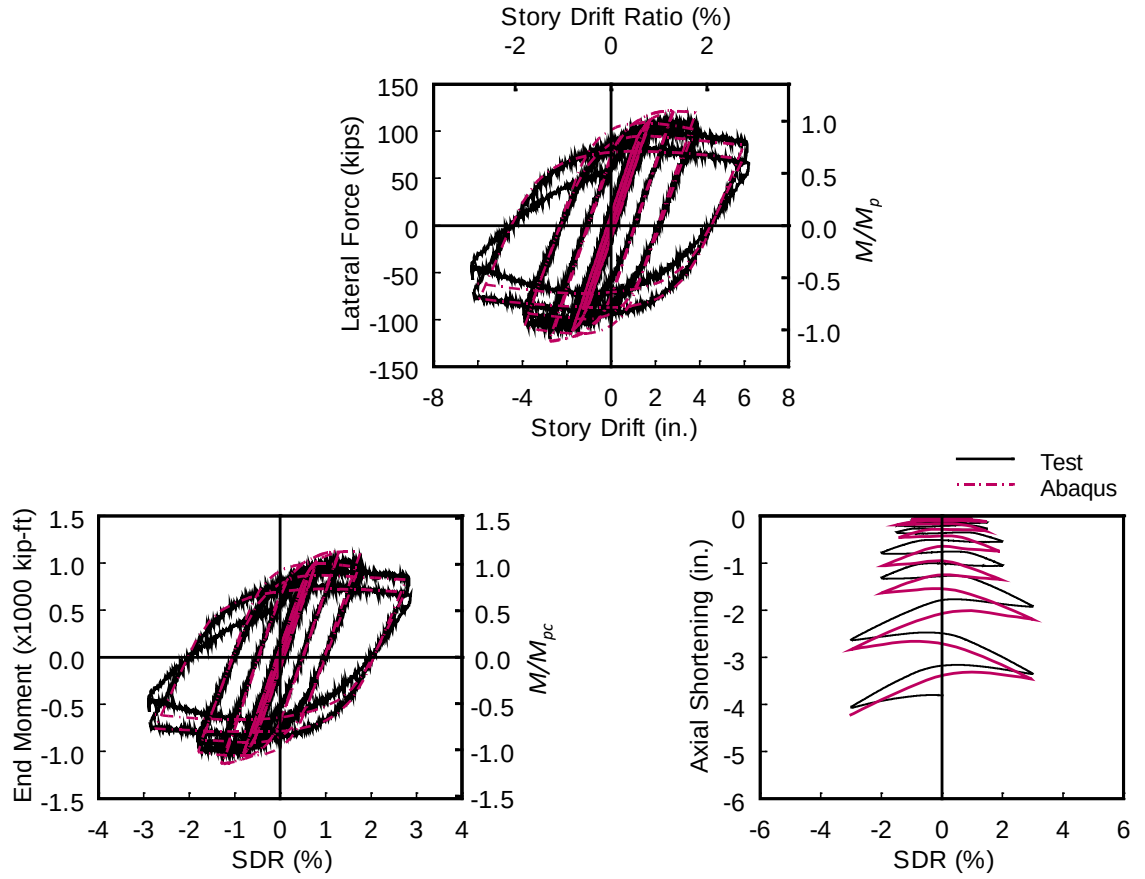

(a) Global Response

(b) Failure Mode

Figure 5.11 Correlation of Specimen 4L Response

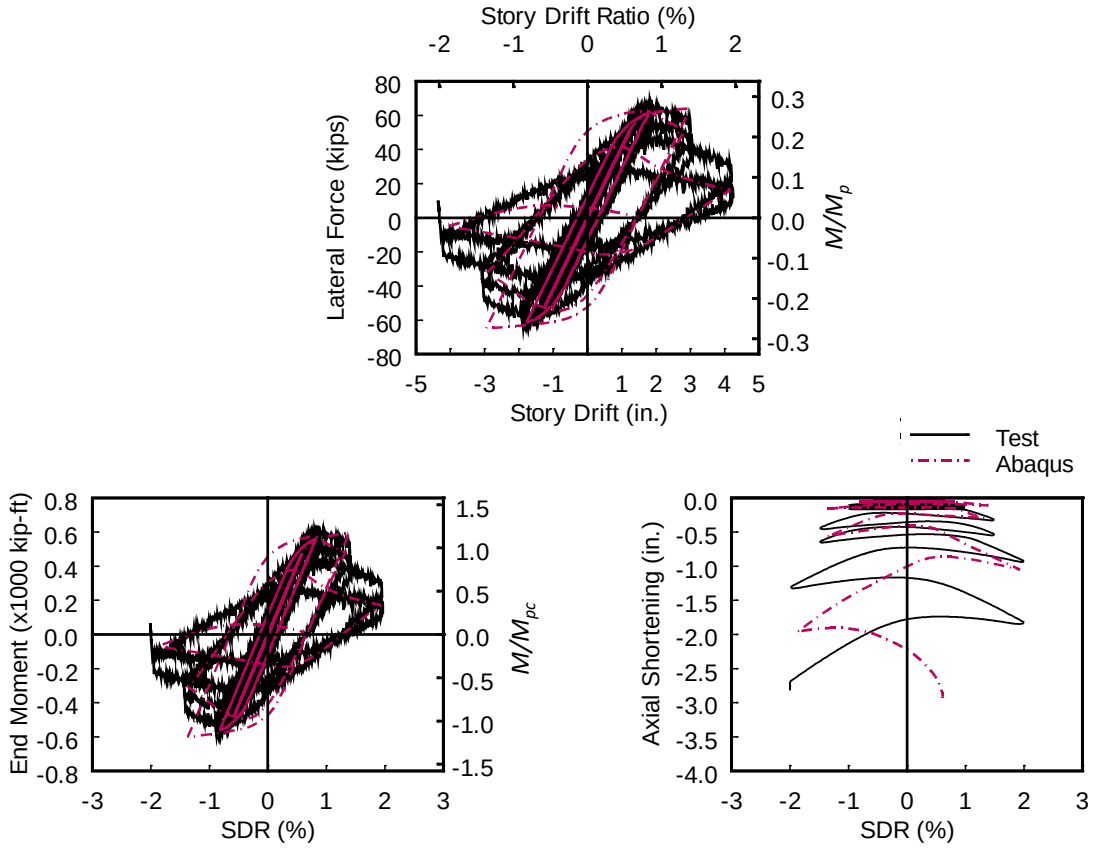

(a) Global Response

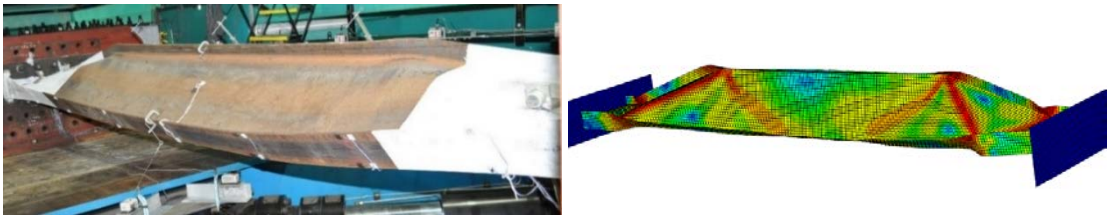

(b) Failure Mode

Figure 5.12 Correlation of Specimen 5L Response

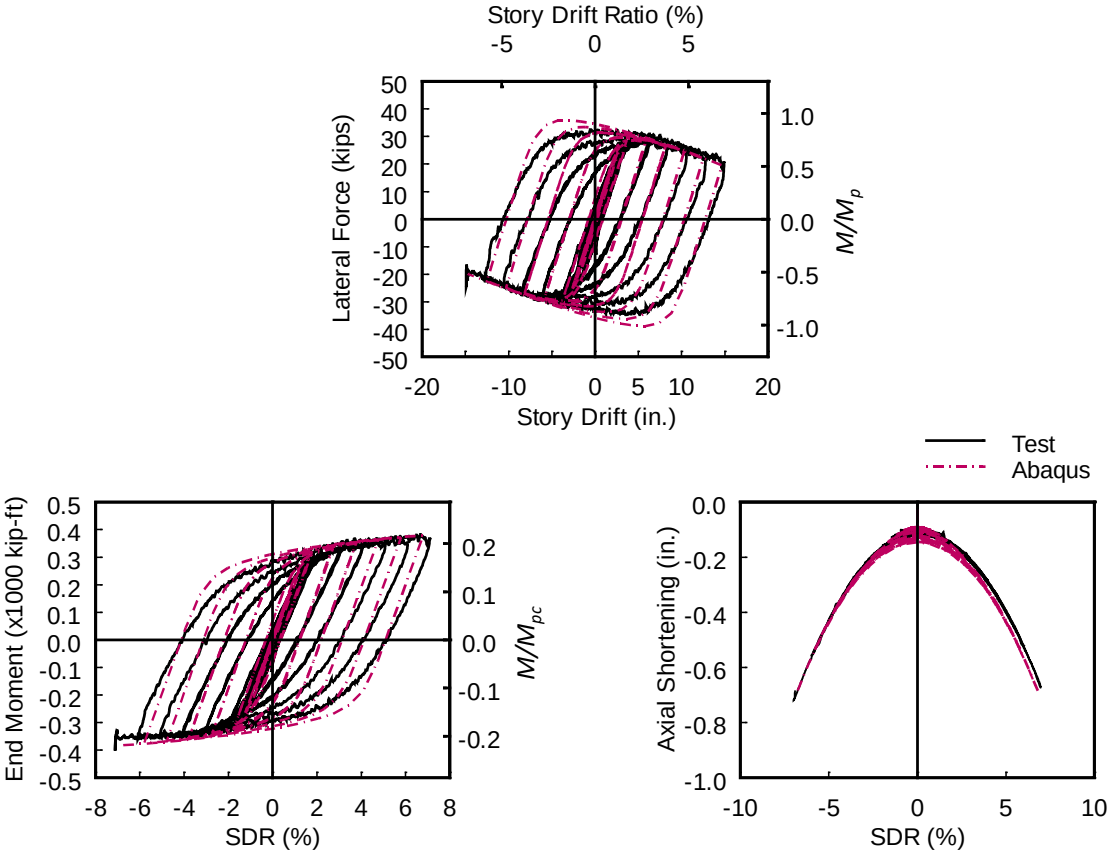

(a) Global Response

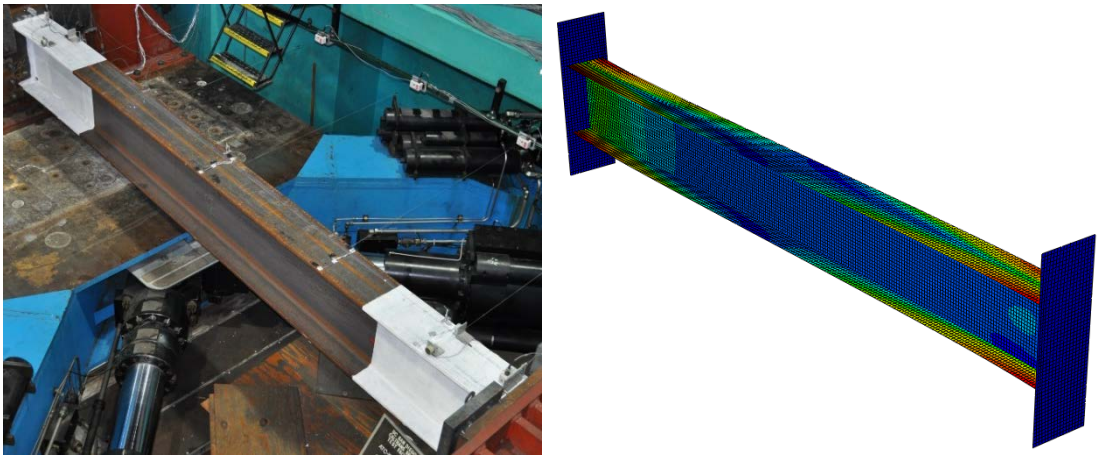

(b) Failure Mode

Figure 5.13 Correlation of Specimen 6L Response

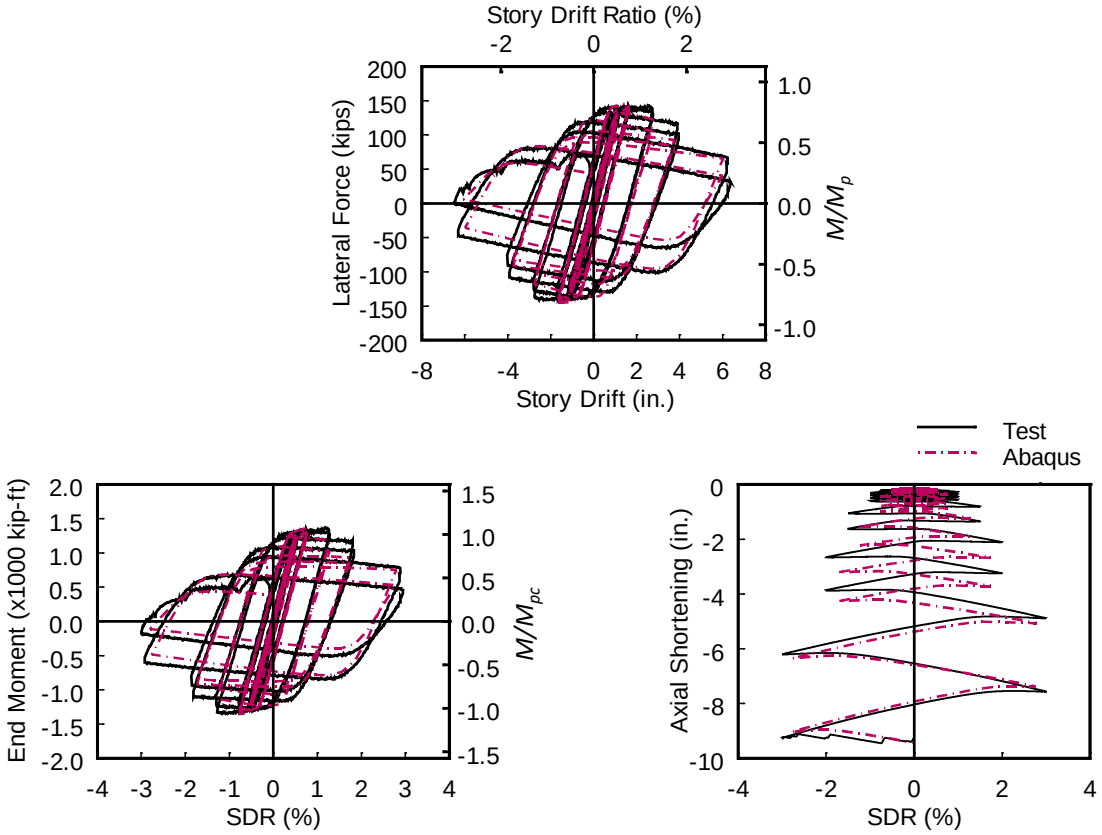

(a) Global Response

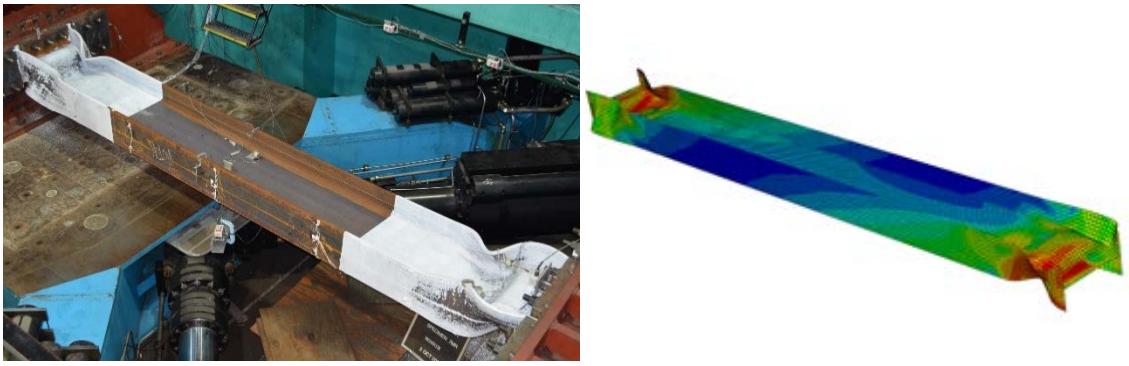

(b) Failure Mode

Figure 5.14 Correlation of Specimen 7M Response

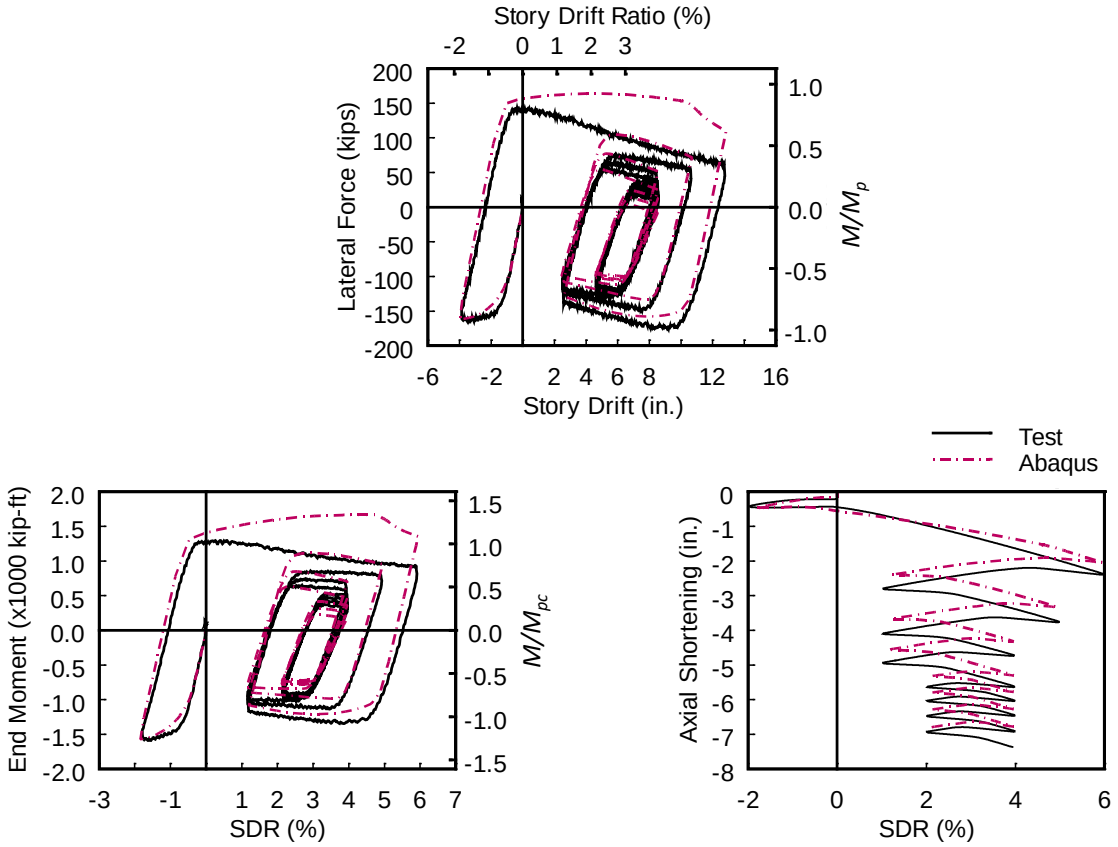

(a) Global Response

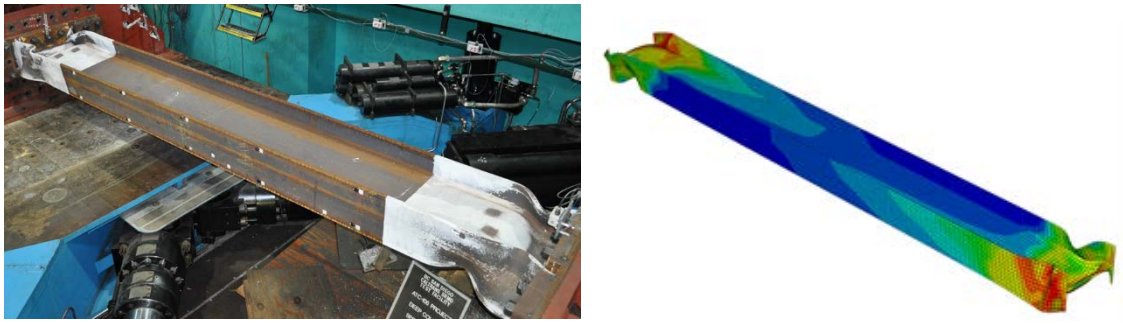

(b) Failure Mode

Figure 5.15 Correlation of Specimen 8M Response

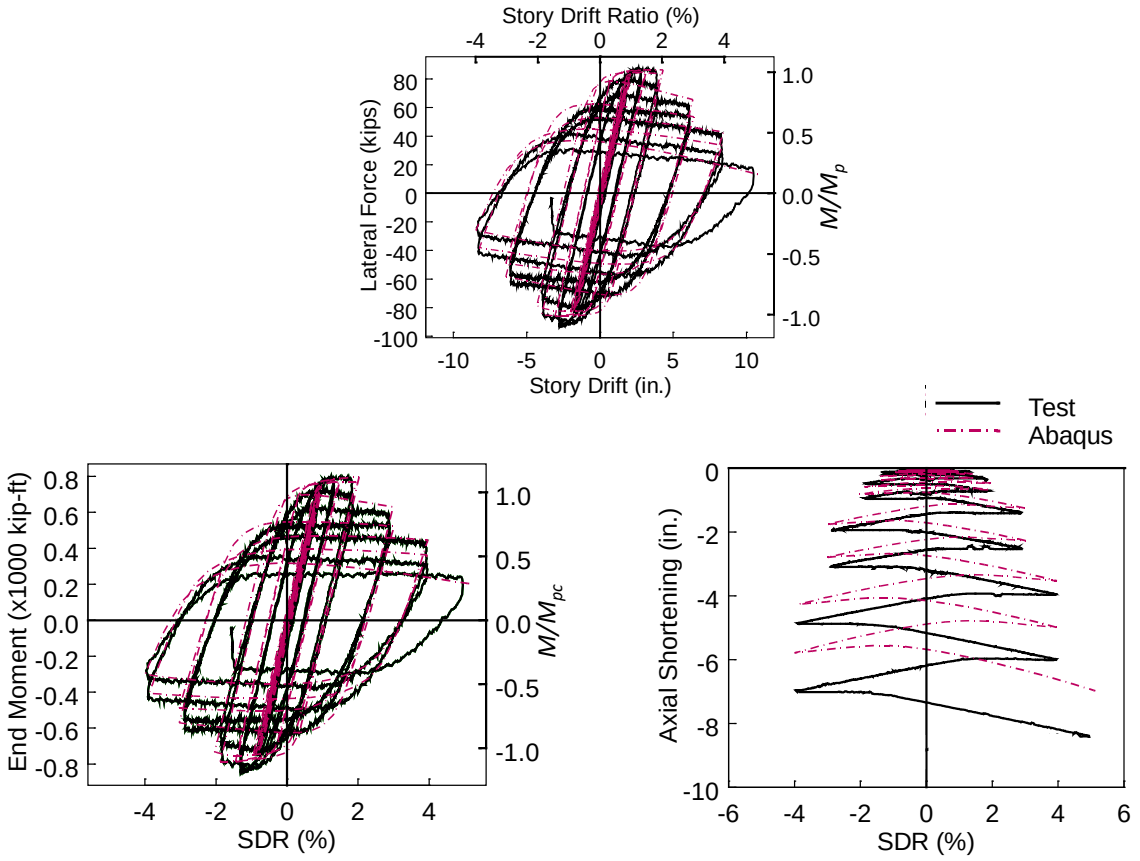

(a) Global Response

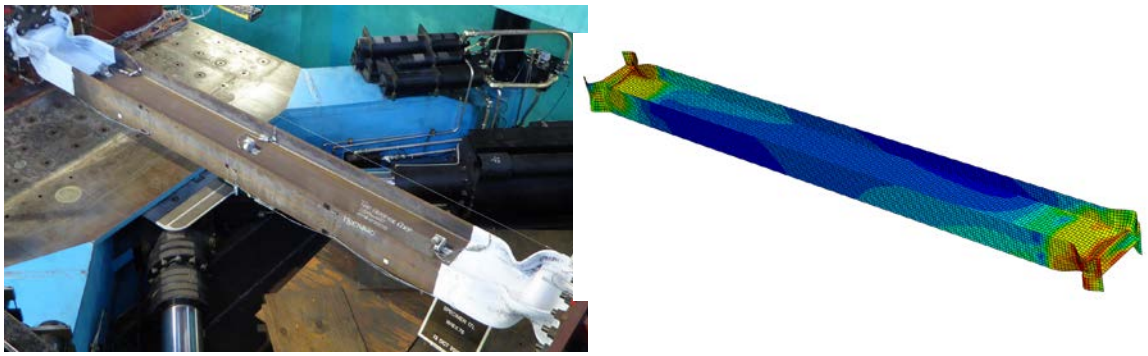

(b) Failure Mode

Figure 5.16 Correlation of Specimen 17L Response

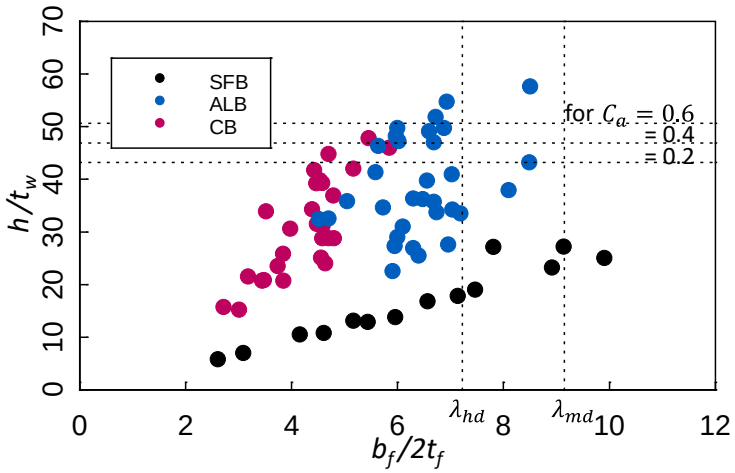

Figure 5.17 Flange vs. Web Slenderness Ratios of Parametric Study Sections

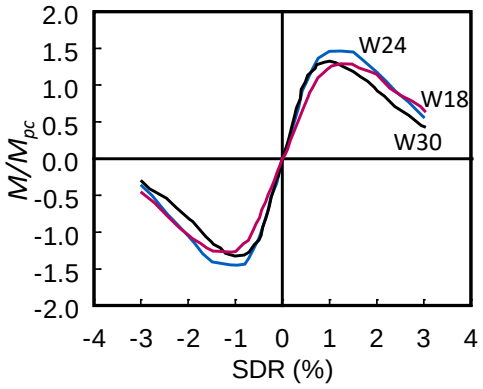

(a) Global Response

W18×130 W24×176 W30×261

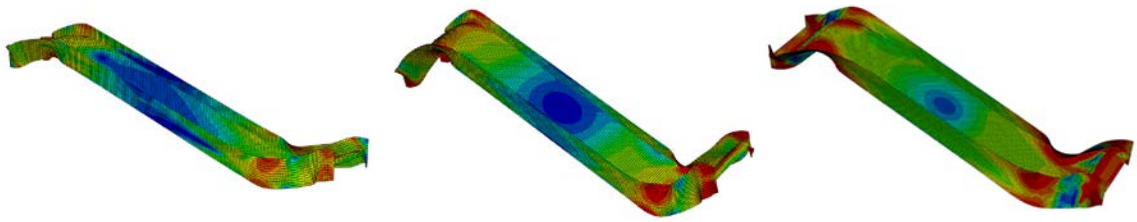

(b) Failure Mode

Figure 5.18 Section Depth Effect

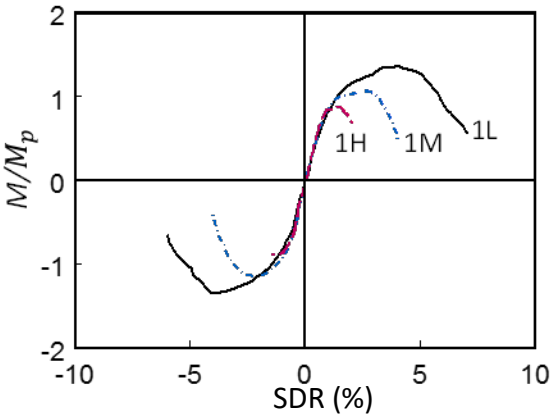

(a) Global Response

W24×176 (C_a=0.2) W24×176 (C_a=0.4) W24×176 (C_a=0.6)

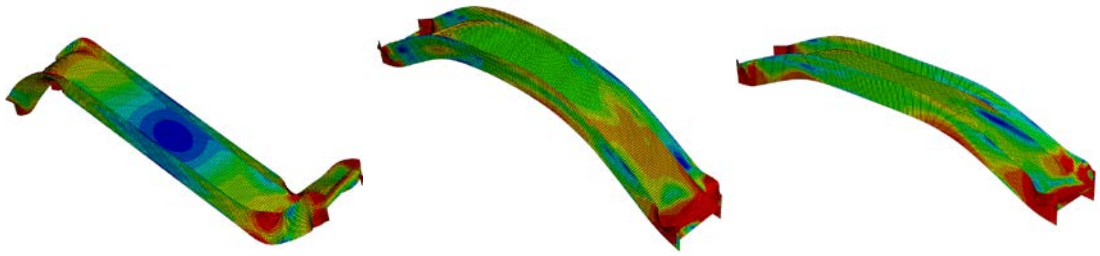

(b) Failure Mode

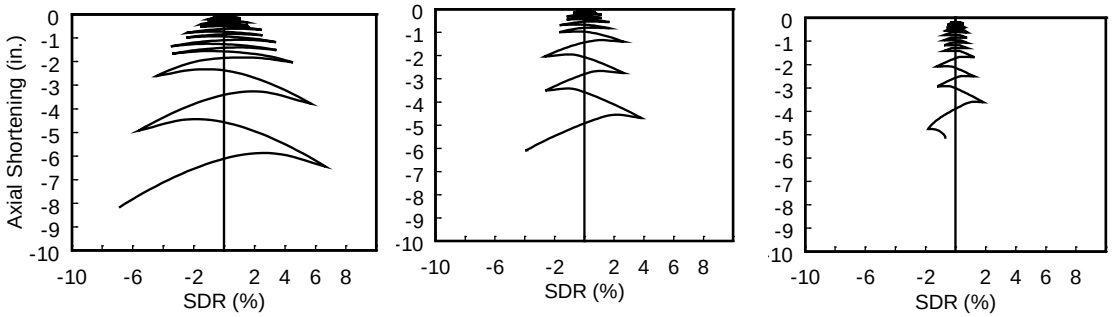

(c) Axial Shortening

Figure 5.19 Axial Load Level Effect

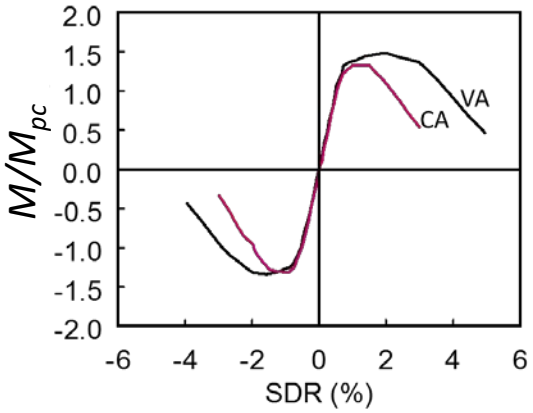

(a) Global Response

Constant Axial Force Varying Axial Force

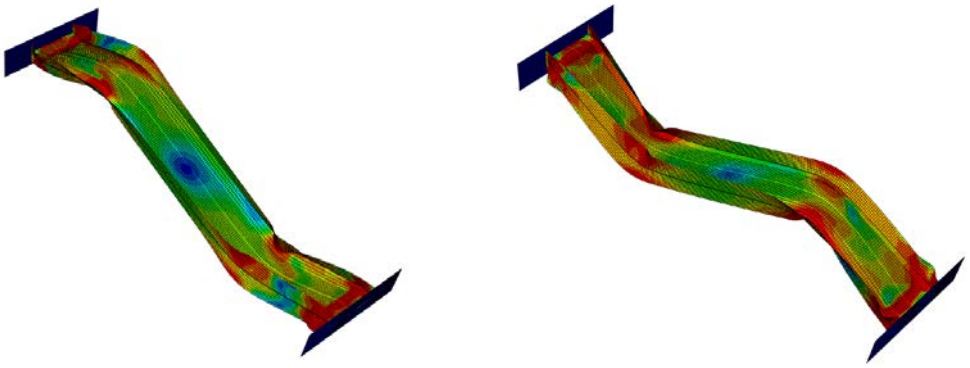

(b) Failure Mode

Figure 5.20 Varying Axial Force Effect (W24×176 Column with C_a = 0.2)

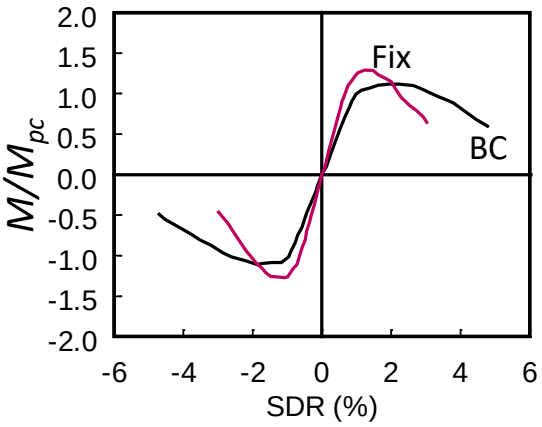

(a) Global Response

Fixed-Fixed Boundary Condition Fixed-flexiable Boundary Condition

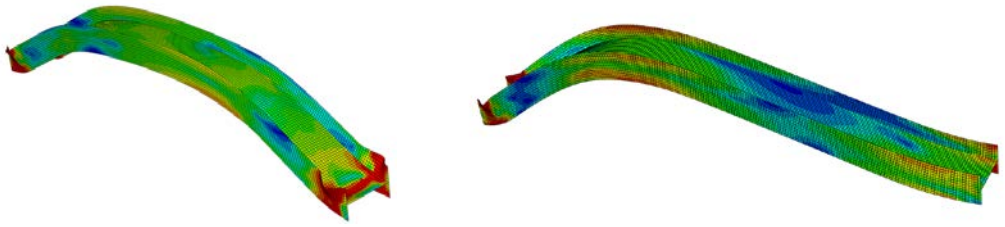

(b) Failure Mode

Figure 5.21 Boundary Condition Effect (W18×130 Column with C_a = 0.2)

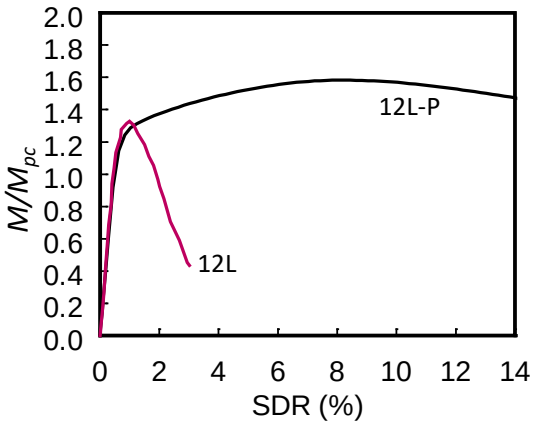

(a) Global Response

Monotonic Cyclic

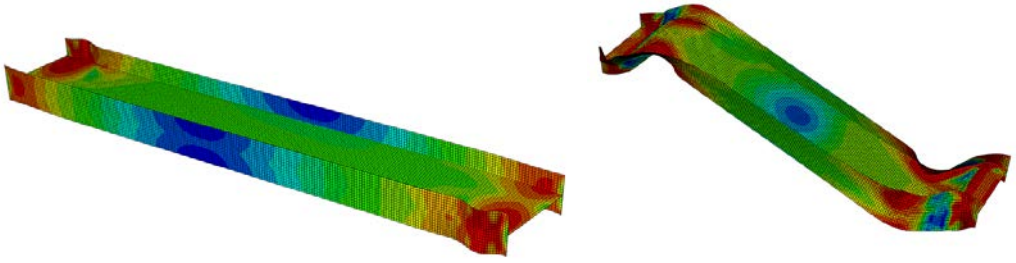

(b) Failure Mode

Figure 5.22 Monotonic vs. Cyclic Loading (W30×261 Column with C_a = 0.2)

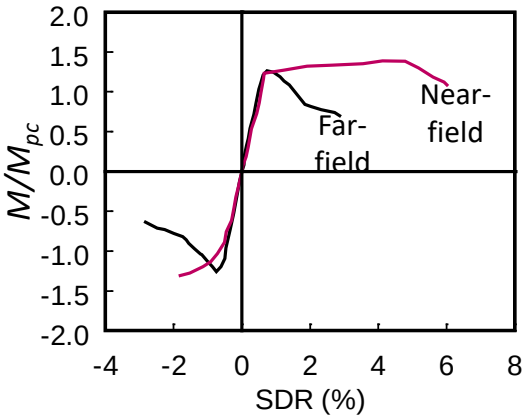

(a) Global Response

Far-field Loading

Near-field Loading

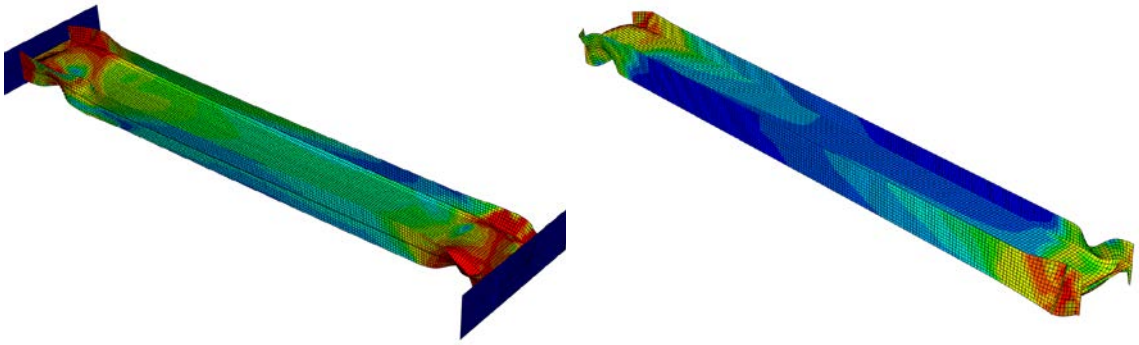

(b) Failure Modes

Figure 5.23 Far-field vs. Near-field Loading (W24×131)

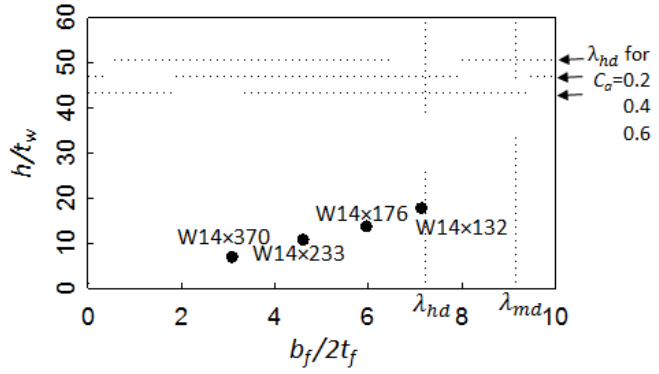

(a) Flange Slenderness

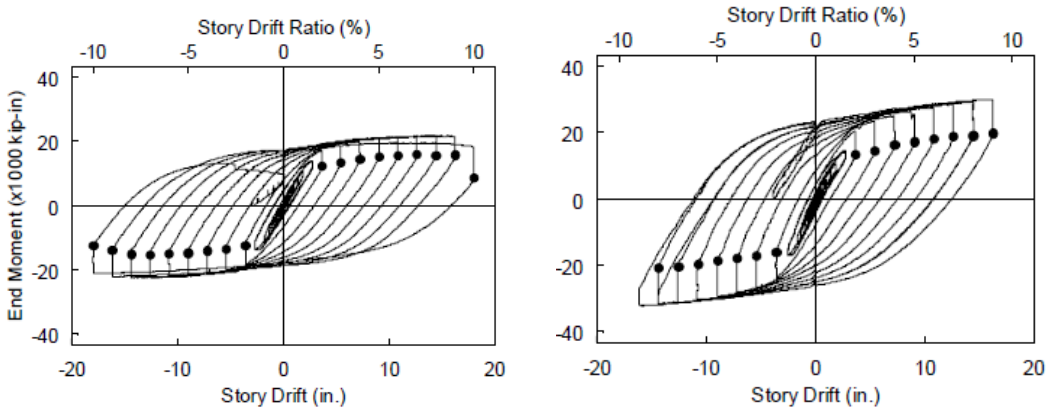

(b) Comparison of End Moment vs. Drift Response

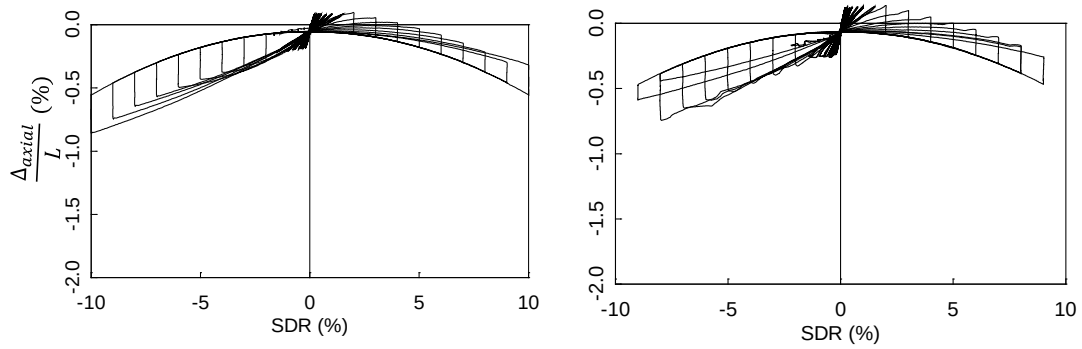

(c) Comparison of Axial Shortening vs. Story Drift Ratio

Figure 5.24 AISC Column Test Sections (C_a=0.61) (Newell, 2008)

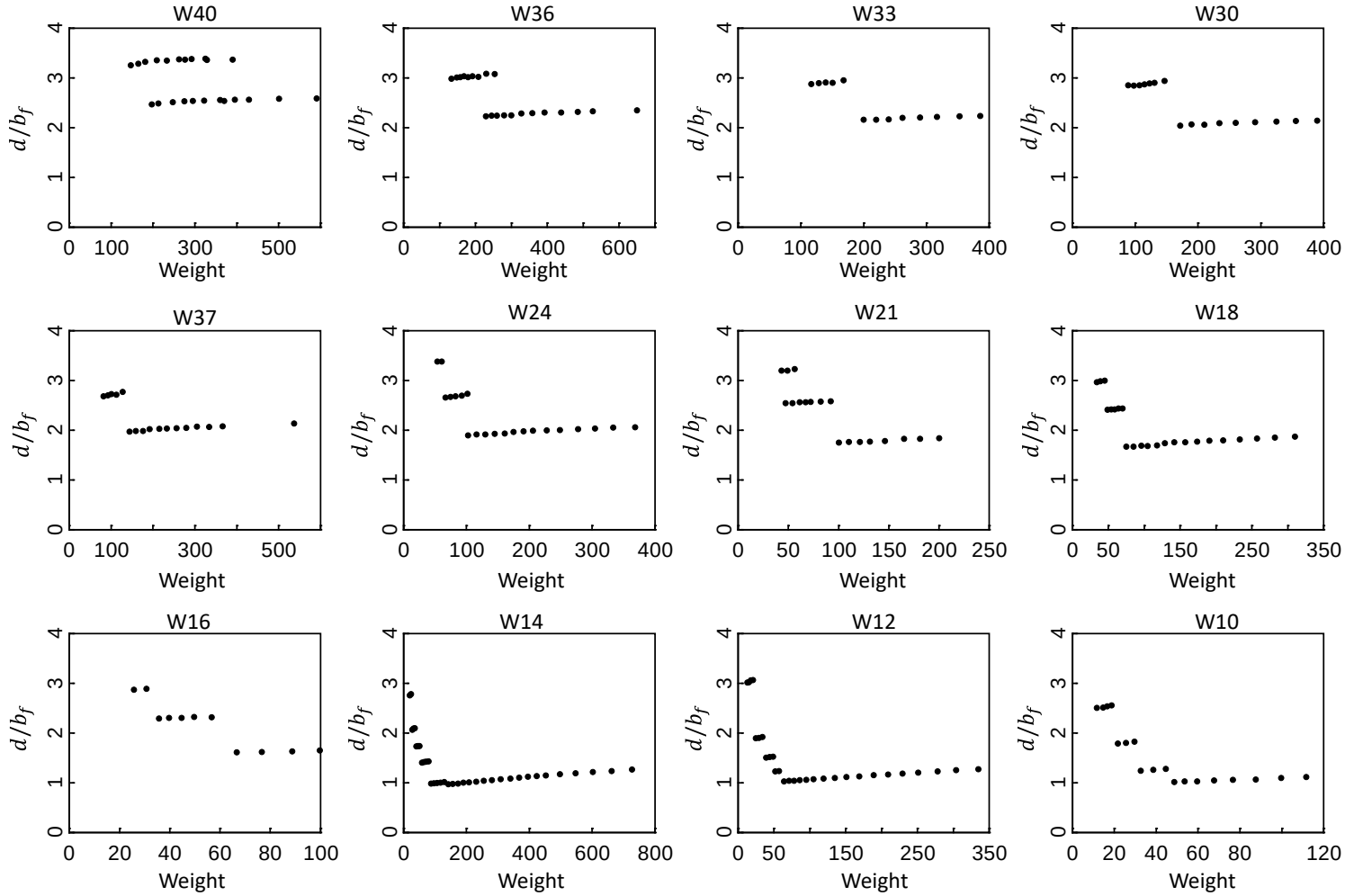

Figure 5.25 Depth-to-Width Ratios of AISC W-shape Sections

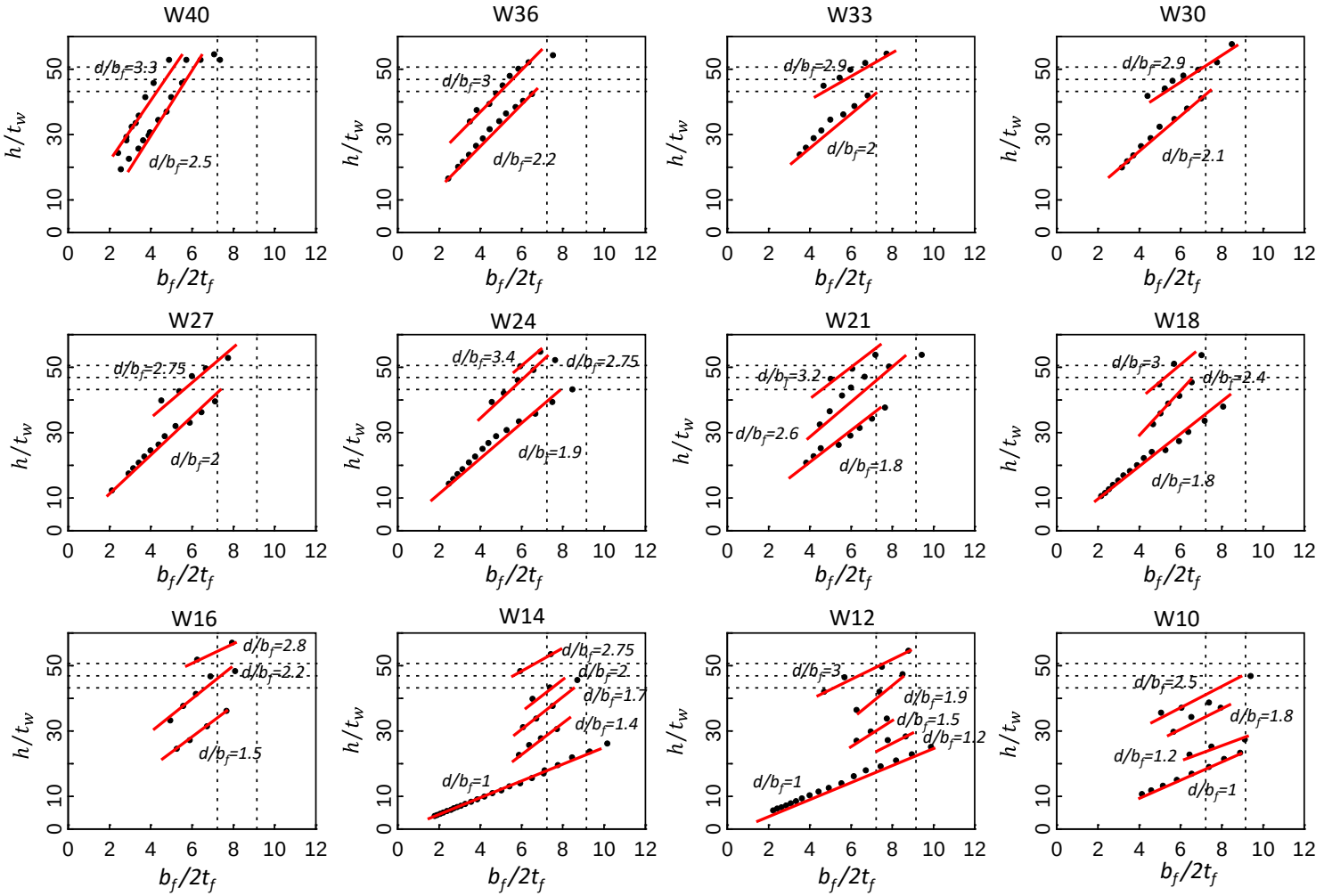

Figure 5.26 Flange to Web Slenderness Ratios with Depth-to-Width Ratios

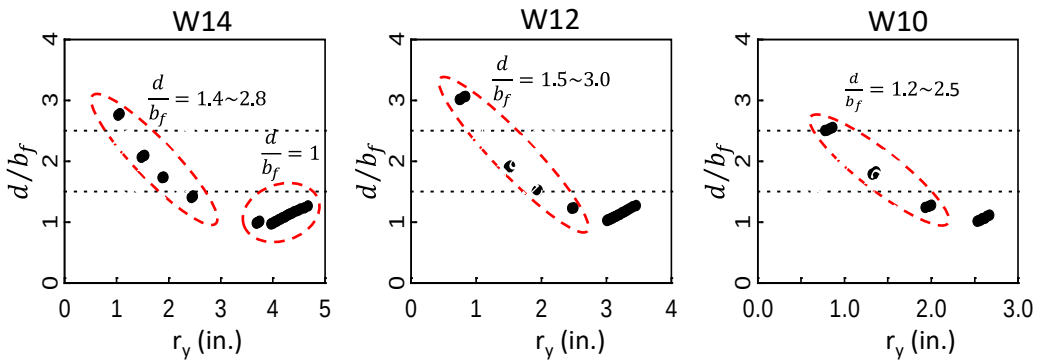

Figure 5.27 Depth-to-Width Ratio vs. Radius of Gyration, r_y

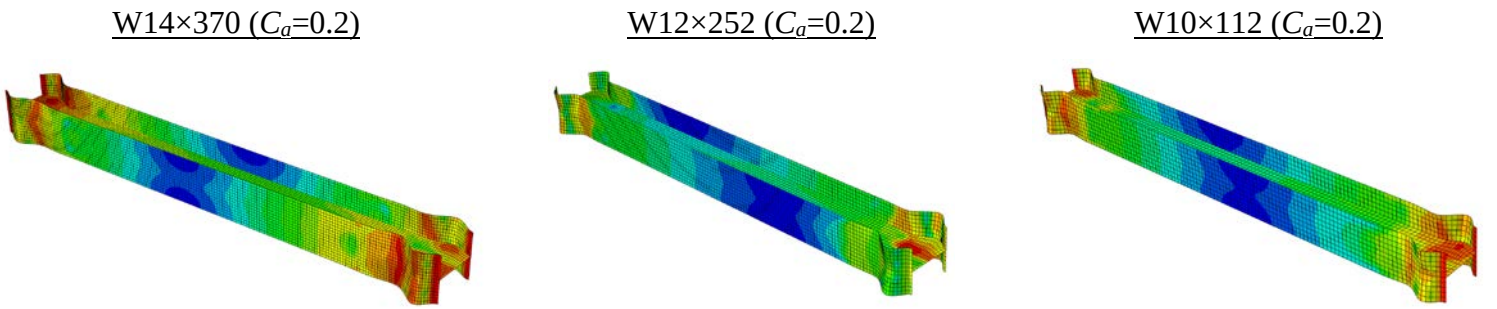

(a) Buckling Modes

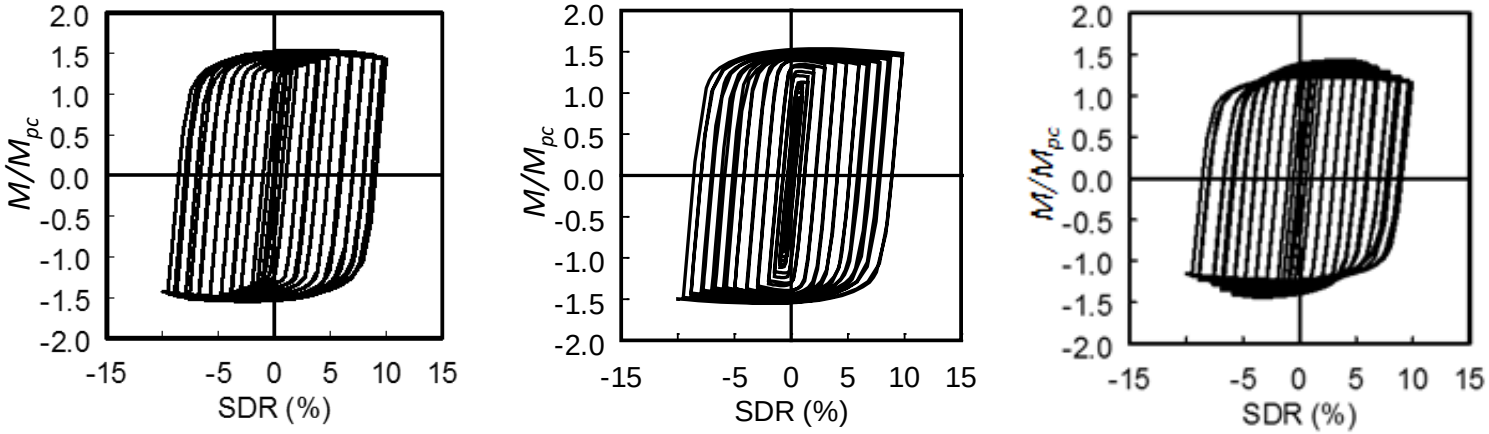

(b) Global Responses

Figure 5.28 Response of Shallow-section Columns with $d/b_f \leq 1.5$

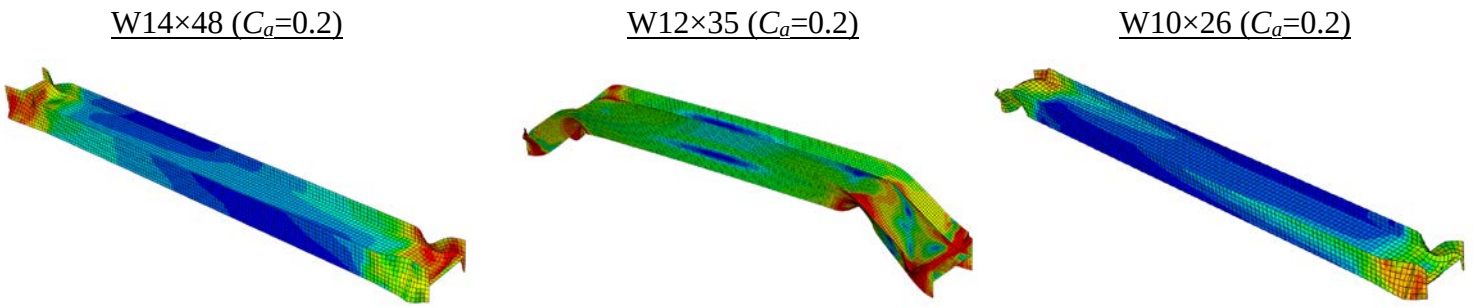

(a) Buckling Modes

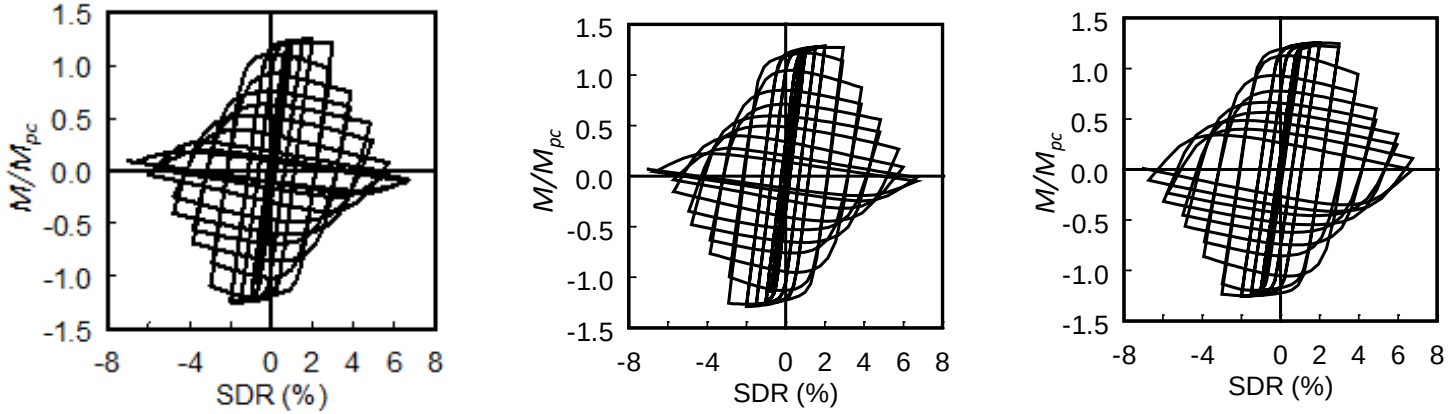

(b) Global Responses

Figure 5.29 Response of Shallow-section Columns with $1.5 \leq d/b_f \leq 2.5$

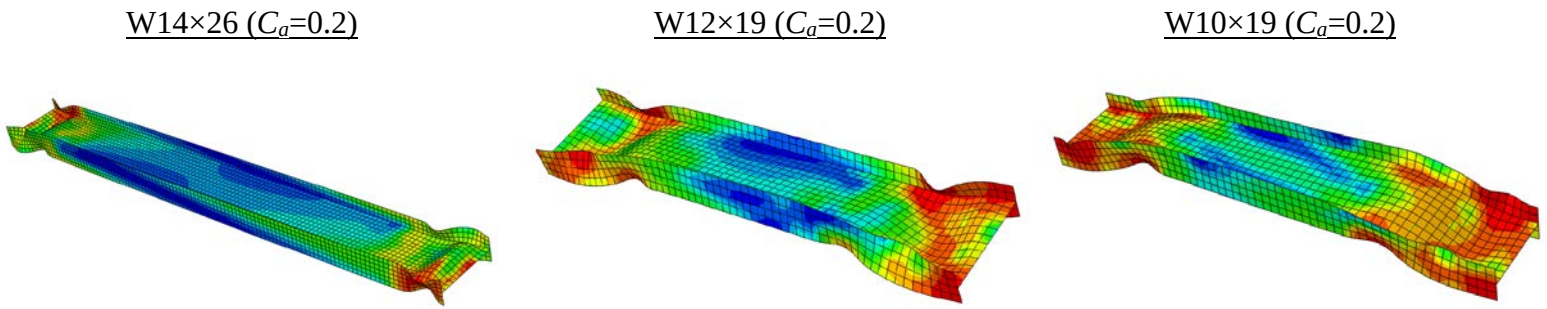

(a) Buckling Modes

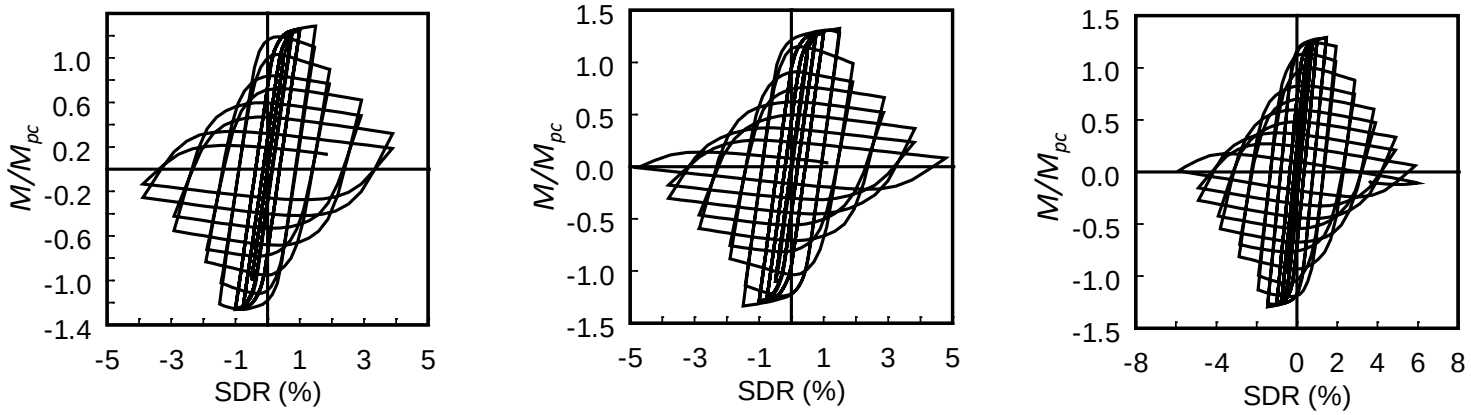

(b) Global Responses

Figure 5.30 Response of Shallow-section Columns with $d/b_f \geq 2.5$

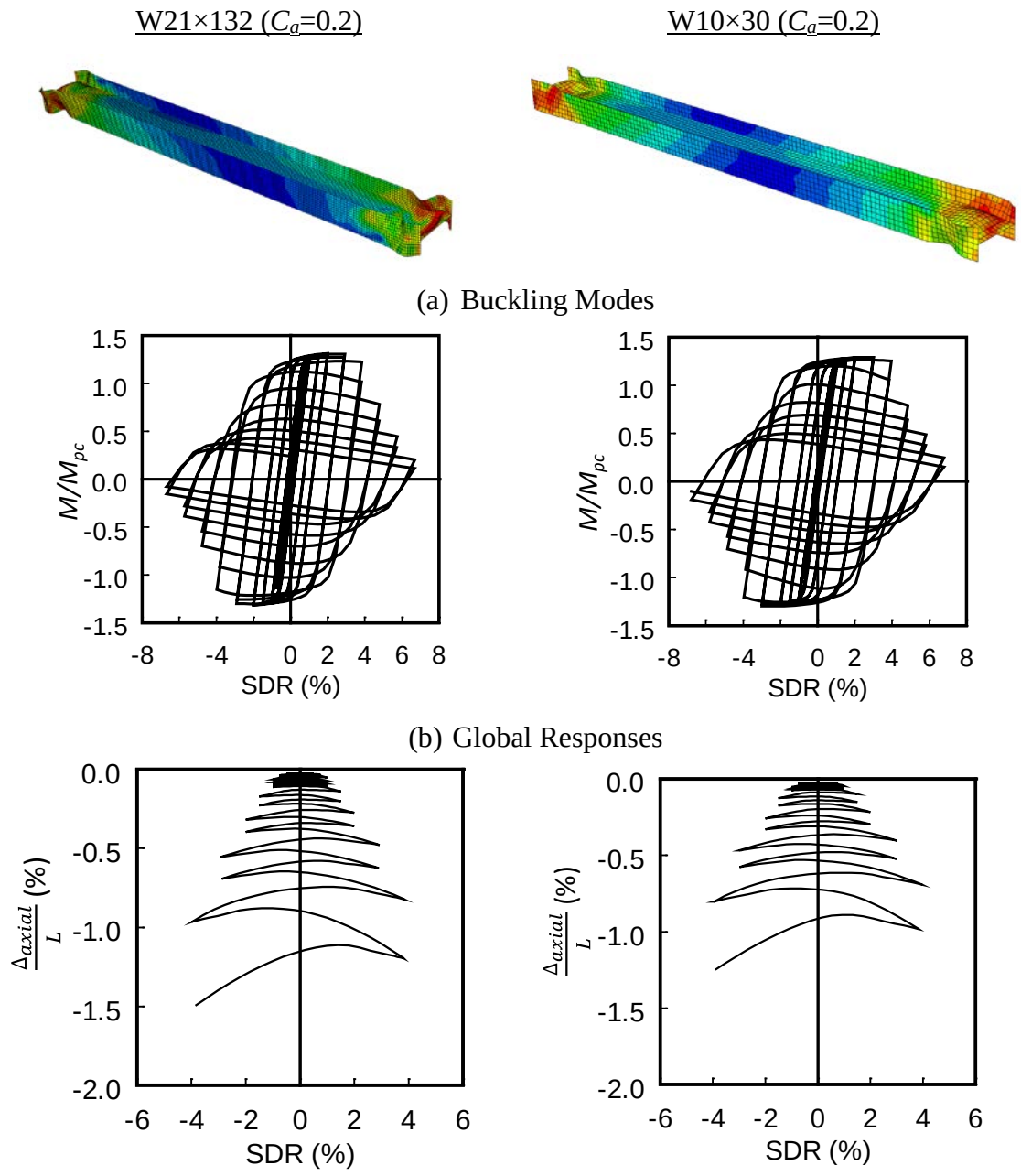

Figure 5.31 Response Comparison of One Deep and One Shallow Columns with Similar Section Slenderness Ratios and Depth-to-Width Ratio

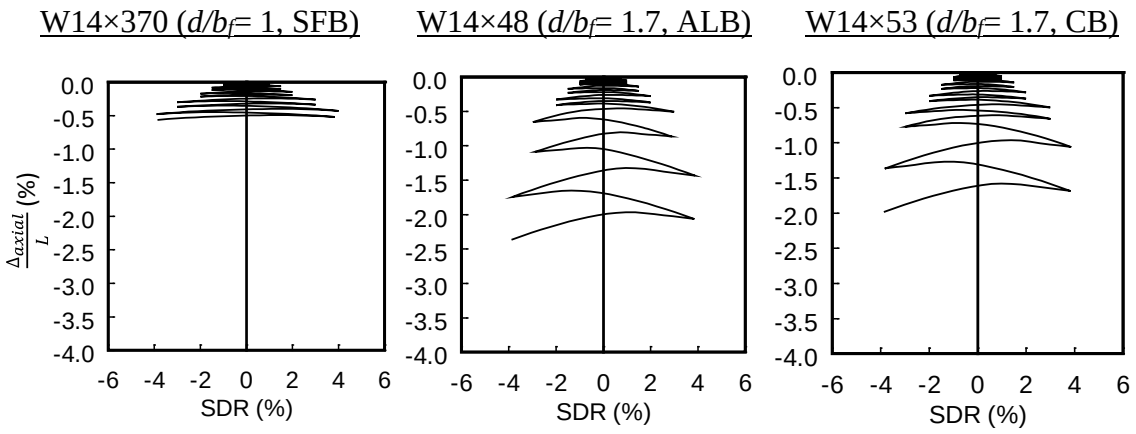

Figure 5.32 W14 Sections with Different Buckling Modes (at 4% SDR, C_a=0.2)

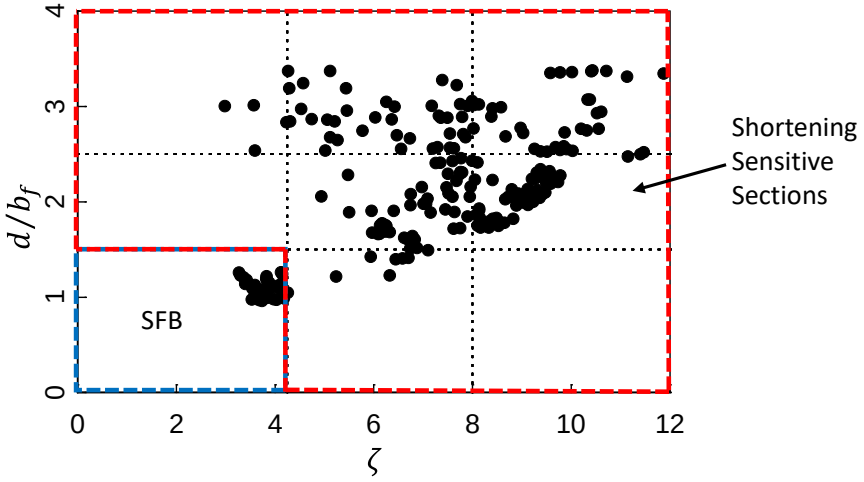

Figure 5.33 Shortening Sensitive Sections

6 CATEGORIZATION OF COLUMN BUCKLING MODE UNDER CYCLIC LOADING

6.1 Introduction

Cyclic test data of large-size, full-scale steel columns under high axial load and transverse drift is limited. Newell and Uang (2006) tested nine W14 sections with varying axial compression for braced-frame application in an AISC-sponsored program. FLB governed the response of these tests, and the hysteretic response was very stable even under high axial compression (C_a =0.83). The ranges of the slenderness parameters for these nine specimens were as follows:

$$3.1 \leq \lambda_f \leq 7.14;\ 6.9 \leq \lambda_w \leq 17.7;\ 42.2 \leq \lambda_L \leq 47.9 \tag{6.1}$$

Thirty-seven deep columns (W30, W24, and W18 sections) that are more representative of those commonly used for the construction of moment frames in high seismic regions were tested in Phase 1 and 2A of this research. The section and member slenderness parameters of these columns were much larger than those tested by Newell and Uang:

$$3.27 \leq \lambda_f \leq 8.52;\ 23.9 \leq \lambda_w \leq 57.5;\ 61.19 \leq \lambda_L \leq 161.2 \tag{6.2}$$

One column (W24×55) that had the highest λ_L (=161.2) experienced LTB in the elastic range during testing. All the other specimens developed plastic hinges at both ends of the column; however, the failure modes varied significantly between the columns. The formation of plastic hinges affected the global response and axial shortening of the column.

The governing buckling mode was in the form of either local buckling, global LTB, or a combination of the two. Additionally, all columns tested in this research experienced significant column shortening, as seen in Figure 4.5, while the W14 columns did not, which further demonstrates the effect of the buckling mode on the column response.

Combining the test data from both the AISC and this research programs. Figure 6.1 shows that the cyclic backbone curves are very different, with the AISC W14x176 column showing a much more stable response than that of the other two W24 columns. Figure 6.1(b) shows that the axial shortening is also affected by the failure mode. Instead of combining all the test results into a single database to develop design recommendations and to establish response parameters for modelling purposes, it is necessary to first establish a criterion to distinguish different buckling modes and categorize the data accordingly. Design recommendations and response parameters then can be established for each buckling mode to accurately predict column behavior.

6.2 Observed Buckling Modes

According to AISC 341 (2010b), all the nine W14 columns and the majority of the deep columns tested in this research met the AISC highly ductile section requirements (λ_{hd}). Some only satisfied the requirements for a moderately ductile section (λ_{md}). Most specimens were subjected to reverse curvature bending (fixed-fixed boundary condition) with the inflection point in the vicinity of the mid-height of the column. A992 steel (F_y = 50 ksi) was specified for all test specimens. The observed buckling behaviors of all test

specimens are grouped into three categories—symmetric flange buckling (SFB), anti-symmetric local buckling (ALB), and coupled buckling (CB).

6.2.1 Symmetric Flange Buckling (SFB) Mode

For a highly ductile section with relatively low λ_f and λ_w values, each flange at the plastic hinge location would buckle locally in a symmetric (or 'mirrored') manner with respect to the web (see Figure 6.2) . This "symmetric flange buckling" (SFB) mode requires a relatively stocky web in order to provide sufficient rotational restraint to the flanges. A W14×176 column with C_a = 0.39 shows such local buckling mode as shown in Figure 6.2. In the tests, web buckling either did not occur or was delayed until very large drift ratios. Since web local buckling either did not occur or was minor, "web" was ignored in the naming of SFB. Strength degradation due to this buckling mode was relatively minor.

A special case occurs when the value of λ_f is very low (say, under 3.0). For such very stocky sections, which generally occur in the form of built-up I-sections, FLB ceases to occur when plastic hinges develop. No W14 or W24 columns tested fall into this special case, but numerical simulations show this phenomenon.

6.2.2 Anti-symmetric Local Buckling (ALB) Mode

As the values λ_f and λ_w increase, the tested W-shapes experienced both FLB and WLB and this two local buckling modes interact each other. However, both AISC 360 and 341 neglect such interaction, treating each independently in design. The only exception is that the limiting λ_r value in AISC 360 to distinguish between a non-compact and a slender

sections in compression from flexure considers the degree of rotational restraint provided by the web:

$$\lambda_r = 0.95\sqrt{\frac{k_c E}{0.7F_y}} \tag{6.3a}$$

where

$$k_c = \frac{4}{h/t_w} \tag{6.3b}$$

where this combined local buckling mode develops, FLB and WLB occur simultaneously as the web does not have sufficient rotational stiffness to provide a fix-ended boundary condition for the flanges. Instead, the web would buckle while trying to remain perpendicular to the flange at the web-flange junction. The flanges would buckle in an anti-symmetric mode, meaning that two halves of the same flange on each side of the web would buckle in the opposite directions (see Figure 6.3). Since WLB also participates, the post-buckling strength would degrade significantly when this "anti-symmetric local buckling" (ALB) mode occurs.

A column that developed plastic hinges with ALB at both ends was expected to remain in-plane. But testing showed that some out-of-plane movement of the column between hinges occurred when local buckling was significant. The column either showed single or reverse curvature bending out-of-plane. When the local buckling pattern at both ends of the column was symmetric with respect to the column midspan, as shown in Figure 6.3(a), both plastic hinges would result in movement out-of-plane in the same direction (single curvature bending). On the other hand, a reverse-curvature out-of-plane movement

would occur when the ALB patterns at both ends of the column were opposite, as shown in Figure 6.3(b). In general, the column segment between two plastic hinges was relatively straight, not like the profile due to a flexural buckling or LTB. Therefore, this kind of out-of-plane movement should not be misinterpreted as flexural buckling or LTB. Whether one column would move in either single or reverse curvature bending after ALB was random, depending on the initial geometrical imperfections, especially cross-section imperfections at the plastic hinge locations.

When ALB occurred at both ends, limited testing showed that the residual compressive strength of the damaged column can be estimated as a weak-axis-governed compressive strength calculated with a pin-pin boundary condition and an effective length taken as the distance between the two plastic hinges. For instance, Specimen 2L was cyclically tested up to 4% drift only. It was then axially compressed in its residual position to evaluate the residual axial capacity of the damaged column. The specimen eventually experienced out-of-plane flexural buckling with a critical buckling load of 1,500 kips. Assuming an effective length factor of 1.0 and using a member length equal to the distance between the two severely buckled regions (= 187 in.), the computed strength per AISC 360 (AISC 2010c) was 1,465 kips, which correlated well with the measured value.

6.2.3 Coupled Buckling (CB) Mode

W30, W24 and W18 column specimens experienced coupled buckling (CB) involving both ALB and LTB while developing plastic hinges at both ends. This unique buckling mode had some features. First, the flanges of these columns were classified as

highly ductile and were stockier with low values of λ_f. Second, the yielded length (or "plastic hinge" length) was very long. Because local buckling of these stockier sections was delayed, the sections near the column ends continued to strain harden and reached a high flexural strength, which resulted in a much longer yielded region at each end (compared the yielded lengths in Figure 6.3 and Figure 6.4). The compressive flange with a much longer yielded length tended to buckle about its strong axis, which triggered LTB of the column. Third, the inelastic deformation capacity (or ductility) was high.

Two scenarios were possible. The first scenario started with ALB at both ends, followed by LTB at higher drift levels. The resulting LTB global buckling pattern can be further subdivided into two cases: either single or reverse curvature, depending on the direction of ALB of "compressive" flanges. The "compressive" flange efers to that causd by lateral drift only. Figure 6.4(a) shows an example when LTB resulted in a reverse-curvature global deformation in the out of plane of the applied moment. In this case, each flange at one (east) end buckled alternatively under cyclic loading in the out-of-plane direction due to LTB; the buckling direction of these two flanges at one end was the same (i.e., upward in the test confuguration). The same occurred at the other (west) end of the column, except that the direction of movement of both flanges was opposite (downward) to that at the east end. Figure 6.4(b) shows an example when LTB resulted in a single-curvature buckling mode in the out of plane. The test specimen was nominally identical to that in Figure 6.4(a), except that the constant compression force was tripled. In this case, all four compressive flanges buckled out-of-plane in the same (upwards) direction.

Figure 6.4 shows examples of coupled buckling when ALB occurred first, followed by LTB. When the section was even stockier, ALB would not occur before LTB developed. This second scenario of coupled buckling is demonstrated in Figure 6.5(a). At high drift levels, FLB would also develop; see the second photo in Figure 6.5(a). It should be noted that this LTB is not the same as the "conventional" FLB where the flange buckles due to uniform compression across the width of the flange. Instead, this FLB is the result of the flange bent about its strong-axis due to LTB.

In summary, the coupled buckling in Figure 6.5(a) is termed CB-GL herein because global LTB proceeds local buckling. Figure 6.4(b) is repeated in Figure 6.5(b) and the buckling mode is termed CB-LG because local buckling proceeds global LTB. The LTB mode mentioned above refers to inelastic LTB where the flanges had experienced significant yielding. The test data on which the above observations were made had an λ_L ranging from 35 to 100. One W24×55-specimen tested, had λ_L equal to 161. This specimen failed in elastic LTB, with no yielding or local buckling (see Figure 6.6**)**. Although AISC 341 does not provide a limiting value for λ_L, columns that would buckle in the elastic range should be avoid for SMF design.

Figure 6.7 compares the characteristics of ALB and CB. Figure 6.7(a) shows that two half flanges on each side of the web buckled under compressive force when ALB is the governing failure mode. In CB case, however, only one half flange on one side of the web buckled due to large compressive force induced by in-plane and out-of-plane flexure as shown in Figure 6.7(b). The other half flange experienced stress unloading due to the

out-of-plane movement LTB. Material stiffness of the half flange that experienced unloading was equal to elastic modulus (E), while the other half flange that buckled experienced a decrease in stiffness to tangent modulus (E_t). As a result, specimens failed in CB mode have higher lateral strength, greater ductility, and lower axial shortening compared to those exhibiting ALB mode.

6.3 Classification of Buckling Method

According to the classical plate theory (Timoshenko, 1968), the elastic buckling stress (F_{cr}) of a plate under uniform axial force can be expressed as

$$F_{cr} = k\frac{\pi^2 E}{12(1-\upsilon^2)(b/t)^2} \tag{6.4}$$

where γ (=0.3) is the Poisson ratio, and k is the plate buckling coefficient, which is a function of the type of stress, edge boundary condition, and length-to-width ratio. For the flanges of a W-shape sections, k represents the rotational restraint provided by the web at the flange-web junction. For simplicity, AISC 360 and 341 treat FLB and WLB as independent limit states, the only exception being that the interaction between the two is considered in λ_r for compression member design in AISC 360.

Seif and Schafer (2016) used finite strip method to derive simplified empirical expressions for plate buckling coefficients that incorporate the effect of web-flange interaction in W-shapes. Sections were simplified to their centerline geometry and analyzed under different loading conditions: axial compression and bending about the major and minor geometric axes. The cross-section elastic buckling stress, f_{crl}, is

determined from the finite strip analysis. Note for sections in compression, f_{crl} is simply P_{crl}/A_g, where P_{crl} is the local buckling load and A_g is the gross area of the cross-section. For the sections in bending, f_{crl}, is M_{crl}/S, where M_{crl} is the local buckling moment, S is the elastic section modulus, and f_{crl} is the maximum compressive fiber stress taken from a centerline model of the cross section.

Seif and Schafer (2016) then derived the equivalent plate buckling coefficients from local buckling stresses. The results were compared with the existing design provisions and used for development of new design guidelines. Re-writing Eq. (6.4) for FLB:

$$f_{crb} = k_f \frac{\pi^2 E}{12(1-\upsilon^2)}\left(\frac{t_f}{b}\right)^2 \tag{6.5}$$

where k_f is the plate buckling coefficient for flange element, and b $(=b_f/2t_f)$ is the unsupported flange width. Setting $f_{crb} = f_{crl}$ and solving for k_f:

$$k_f = f_{crl} \frac{12(1-\upsilon^2)}{\pi^2 E}\left(\frac{b}{t_f}\right)^2 \tag{6.6}$$

Similarly, for web element:

$$k_w = f_{crl} \frac{12(1-\upsilon^2)}{\pi^2 E}\left(\frac{h}{t_w}\right)^2 \tag{6.7}$$

To consider flange-web interaction, Eq. (6.6) can be substituted into Eq. (6.7). Thus, plate buckling coefficients of flange and web elements have the following relationship:

$$k_w = k_f \left(\frac{h}{t_w}\right)^2 \left(\frac{t_f}{b}\right)^2 \tag{6.8}$$

Based on Figure 6.8 and Figure 6.9. Seif and Schafer (2016) proposed the following expression for k_w:

$$\frac{1}{k_w} = \frac{1.5}{\left[\left(\frac{h}{t_w}\right)\left(\frac{2t_f}{b_f}\right)\right]^{2.5}} + 0.18 \tag{6.9}$$

In evaluating the adequacy of the k factor proposed by Johnson (1986), Han and Lee (2016) proposed a new plate buckling coefficient, *k*, to include the interaction between FLB and WLB. Classical plate theory was used to derive differential equations for a plate subjected to uniform compressive force:

$$\frac{\partial^2 M_x}{\partial x^2} + \frac{2\partial^2 M_{xy}}{\partial x \partial y} + \frac{\partial^2 M_y}{\partial y^2} = N_x \frac{\partial^2 w}{\partial x^2} \tag{6.10}$$

Since it was mathematically difficult to solve Eq. (6.10) for close-form solutions when boundary conditions are complicated, the weighted-residual method was used to obtain approximate solutions. To account for the interaction between the web and the flange, Han and Lee (2016) used rotational springs at the flange-web junction as shown in Figure 6.10; the proposed rotational stiffness per unit length for a half flange of a W-shape section is

$$\bar{\zeta} = \frac{1}{2} C_s \frac{D_w}{h} \tag{6.11a}$$

where

$$D_w \left(= \frac{E t_w^3}{12(1-\nu^2)}\right) \tag{6.11b}$$

is the flexural rigidity of the web, and C_s is a non-dimensional web stiffness factor

$$C_s = \frac{2\pi c \sinh^2 \pi c}{(\sinh \pi c \cosh \pi c - \pi c)} \tag{6.12}$$

In Eq. (6.12), c is the aspect ratio of the web, defined as h/a, where a is the half buckling wave length of the flange. To derive a conservative elastic buckling stress for FLB, Han and Lee proposed that a equals to 3 times $b_f/2$. In this study, aspect ratio of the buckled web, c, was found by utilizing Phase 1 test data. The buckled wave length was measured and the numerical models were compared with the experimental tests measurements. Based on the numerical simulation results, the fallowing equation was proposed to calculate the aspect ratio of the web, c:

$$c = \frac{2h/b_f}{3.93\left(\frac{t_w}{t_f}\right) + 3.54} \tag{6.13}$$

Han and Lee found that the effect of web restraint is better evaluated in terms of the relative flexural stiffness ratio between the flange and the web:

$$\zeta = \frac{D_f/b}{\bar{\zeta}} \tag{6.14a}$$

where

$$D_f \left(= \frac{E t_f^3}{12(1-\nu^2)}\right) \tag{6.14b}$$

is the flexural rigidity of the flange: Substituting Eq. (6.11a) into (6.14a), the following expression is derived for ζ:

$$\zeta = \left(\frac{2}{C_s}\frac{\lambda_w}{\lambda_f}\right)\left(\frac{t_f}{t_w}\right)^2 = \xi\left(\frac{t_f}{t_w}\right)^2 \tag{6.15}$$

where ξ is defined as

$$\xi = \left(\frac{2}{C_s}\frac{\lambda_w}{\lambda_f}\right) \tag{6.16}$$

Note that Eq. (6.15) is a section parameter and is independent of the member buckling parameter, λ_L.

Based on the identified buckling modes presented in the previous section, it is obvious that the rotational restraint provided by the web to stabilize the compressive flange is an important parameter for predicting the governing buckling mode. Figure 6.11 presents the test data of W14 columns from Newell and Uang (2008) and deep columns from this research program, where the last two terms in Eq. (6.15) are used as the abscissa and ordinate in the plot, respectively. Two curves representing ζ equal to 4.25 and 8 are also shown in the figure. It shows that these two constant-ζ curves provide good boundaries to separate the three identified buckling modes.

6.4 Verification of Proposed Buckling Mode Classification

Cyclic response and governing buckling mode of one-hundred and ten W-shape sections reported in Chapter 5 were examined in this study. In addition, sensitivity analysis was conducted to understand the effect of key parameters such as flange and web

slenderness ratios. Figure 5.17 shows the slenderness ratios of selected sections, and their failure modes are color-coded with black, blue, and red for SFB, ALB, and CB, respectively. Parametric study shows that shallow sections exhibit SFB buckling mode, which requires a relatively stocky web in order to provide sufficient rotational restraint to the flanges. As shown in Figure 6.12, no deep sections listed in AISC (2010a) exhibit SFB, only shallow sections do. Deeper sections failed due to either local buckling only (ALB) or a combination of local and global buckling (CB) as shown in Figure 6.13 and Figure 6.14. Figure 6.15 presents the selected sections as a function of ξ and $\left(t_f/t_w\right)^2$. Two curves representing ζ equal to 4.25 and 8 are also shown in the figure. These two constant ζ curves provide good boundaries to separate the three identified buckling modes for both the test and the parametric study results. Figure 6.16 shows the proposed criteria on all W-shape AISC sections. Note that the proposed variables ζ and $\left(t_f/t_w\right)^2$ of AISC sections has a narrow range from 1 to 4. Therefore, they are only valid under this limit. Any sections with the parameters outside of this range require further investigation.

Additionally, sensitivity analysis was conducted by considering the limit discussed above. As shown in Figure 6.17, slightly changing the web and flange thicknesses alters the slenderness ratios of W12, W24 and W36 sections Table 6.1 lists the slenderness ratios of the modified sections. As shown in Figure 6.18, numerical analysis was conducted using the geometry of the modified sections to verify the adequacy of the proposed web restrain parameter, ζ. Figure 6.19 demonstrates that the proposed model still provides good boundaries to separate the three buckling modes for the modified sections.

Fogarty and El-Tawil (2017) studied the collapse response of deep steel columns and observed a counterintuitive trend on web-to-thickness ratio. The authors halved and doubled the web thicknesses of W24×117, W27×146 and W36×487 sections. They observed that a decrease in the web thickness could lead to better behavior than the original section while an increase could lead to worse behavior. To test the limit of this counterintuitive trend, the web thickness of W36×487 section was quartered and quadrupled (see Figure 6.20). Results shows that the quadrupled-web section performed similarly to the doubled-web section, but the quartered-web section performed much worse than the original and the halved-web section. This phenomenon can be explained with the proposed buckling mode classification parameter (web restrain parameter, ζ).

Figure 6.21 illustrates the proposed buckling mode classification parameter versus depth-to-thickness ratio of the modified W36×487 sections. The web restraint parameter ζ in abscissa becomes smaller when web thickness becomes stockier. Both experimental tests and numerical study show that stockier web provides more stable hysteresis loops. However, when local buckling is followed by significant global buckling, one half flange on each side of the web experience stress unloading due to localized tensioning induced by the global out-of-plane movement. This enables one half flange to maintain its initial elastic modulus E as another half experiences decrease in material stiffness (reduces to tangent modulus, E_t). Therefore, a section with higher web restraint that fails in ALB mode may not have a better cyclic behavior compared to another section with lower web restraint that fails in CB mode because of the stress unloading effect.

Figure 6.21 depicts that the halved-web section and the original section have similar behavior since they both fail in CB mode while the doubled and quadrupled-web section

performed worse because they experience ALB failure mode. For the quartered-web section, the web thickness is drastically reduced and the failure mode switches to shear buckling at the web. As a result, the quartered-web section performs much worse than any other sections. Note that the doubled and quadrupled-web sections have web restraint coefficients less than 4.25, and would be classified into SFB failure mode if following the proposed criterion based on AISC W-shape sections. However, sections in SFB category only comprise of shallow columns. These artificial sections are deep sections, and therefore, cannot exhibit SFB failure mode. Instead, they experienced ALB failure. One must not be misled by the inappropriate range of the web restraint parameters of built-up sections or artificial sections. As mentioned earlier, the proposed parameter and its limit is most relevant to AISC W-shape sections.

6.5 Acknowledgements

The text below is reproduced verbatim as it appears in the acknowledgments section on page xvii per the UCSD Office of Graduate Studies Formatting Requirements.

Chapter 6 of this dissertation is based on material published by Structures Congress, titled “Classifying cyclic buckling modes of steel wide-flange columns under cyclic loading” with co-authors Harris, J., and Uang, C. (2015). Materials were also submitted for publication by EuroSteel Conference, titled “Cyclic backbone curves for steel wide-flange columns: A numerical study” with co-authors Harris J.L., and Uang C.-M. (2017). The dissertation author is the first author of these papers.

Table 6.1 Proporties of Modified Sections

Section	λ_f	λ_w	λ_L	C_a	Buckling Mode
W12A	4.0	8.8	47.3	0.2	SFB
W12B	3.8	10.4	46.1		ALB
W24A	4.0	22.5	56.5		ALB
W24B	5.0	35.1	55.9		CB
W36A	3.8	34.4	61.2		CB
W36B	3.8	28.7	63.7		ALB

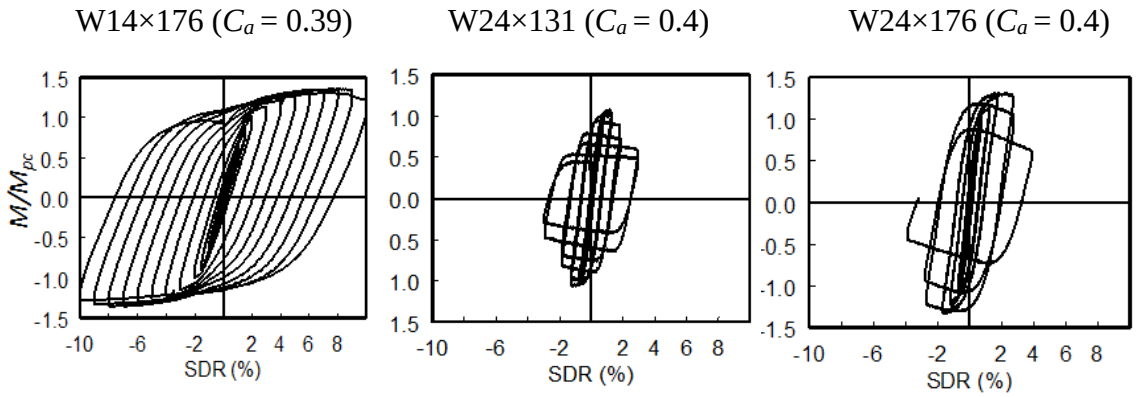

(a) Normalized Moment vs. Story Drift Ratio

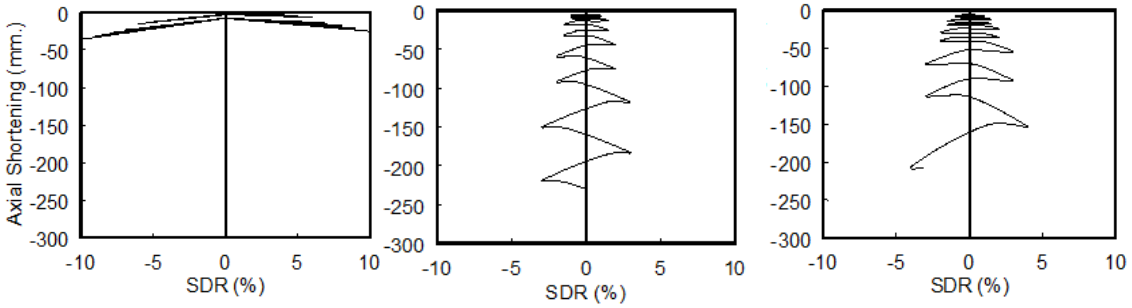

(b) Axial Shortening vs. Story Drift Ratio

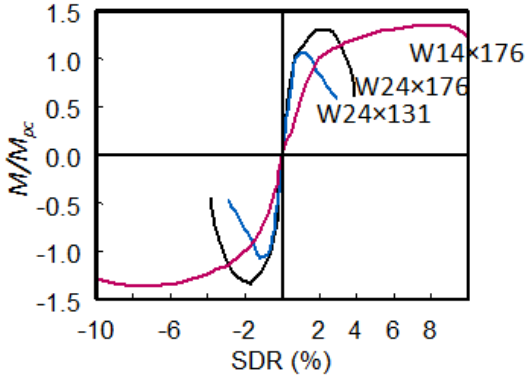

(c) Backbone Curve Comparison

Figure 6.1 Cyclic Behavior and Axial Shortening of Different Buckling Modes

East End Overall West End

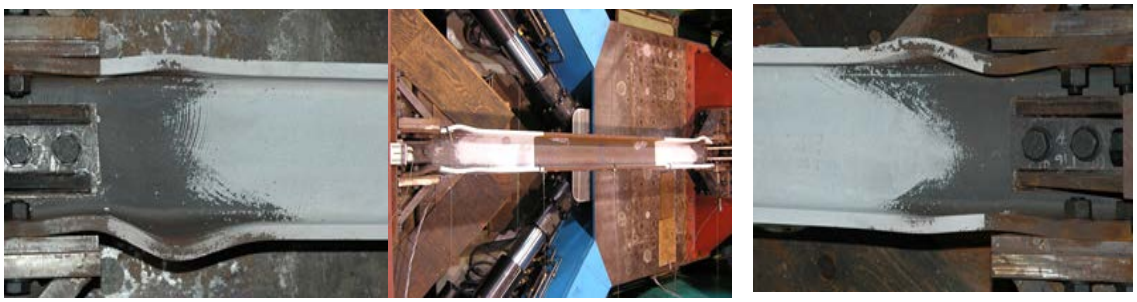

Figure 6.2 Symmetric Flange Buckling (SFB) Mode (W14×176, C_a = 0.39)

East End Overall West End

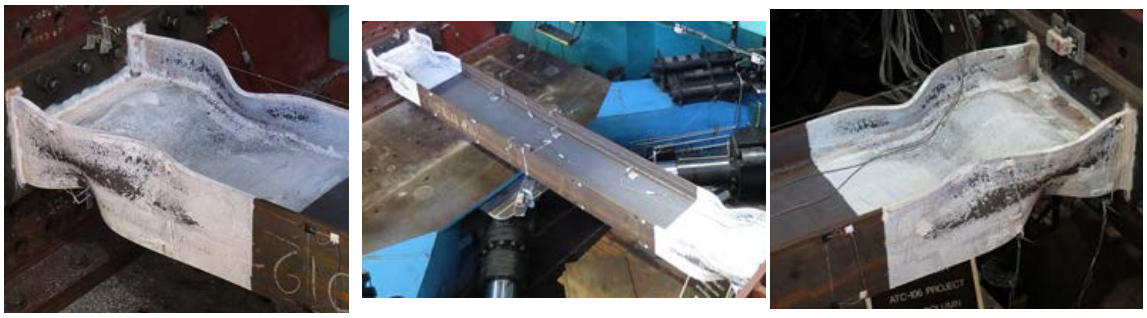

(a) Type S: Single-Curvature Out-of-Plane Movement (C_a = 0.6)

(b) Type D: Double-Curvature Out-of-Plane Movement (C_a = 0.2)

Figure 6.3 Antisymmetric Local Buckling (ALB) Mode (W24×104)

East End Overall West End

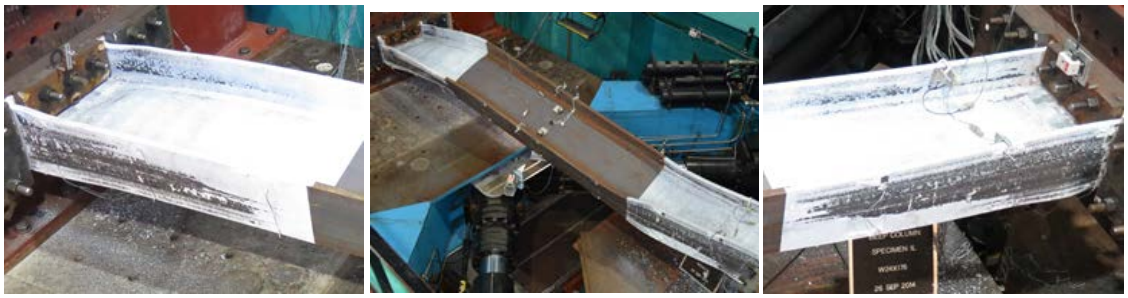

(a) Type D: Double-Curvature Out-of-Plane LTB (C_a = 0.2)

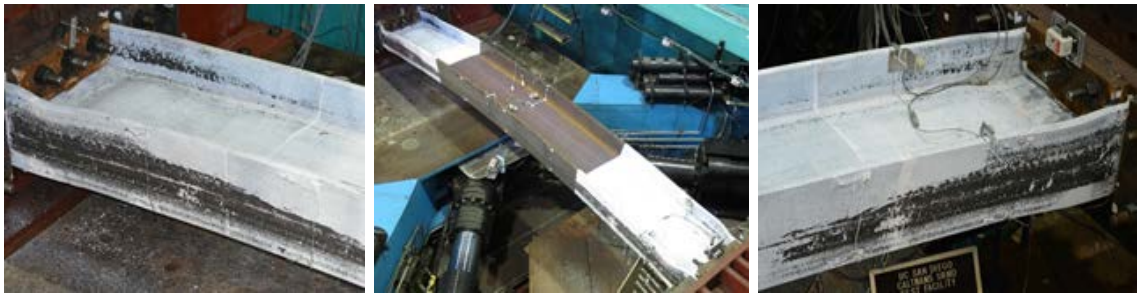

(b) Type S: Single-Curvature Out-of-Plane LTB (C_a = 0.6)

Figure 6.4 Coupled Buckling Mode (CB) (W24×176)

Overall West End

(a) CB-GL (W18×192, C_a = 0.4)

(b) CB-LG (W24×176, C_a = 0.6)

Figure 6.5 Two Types of Coupled Buckling Mode

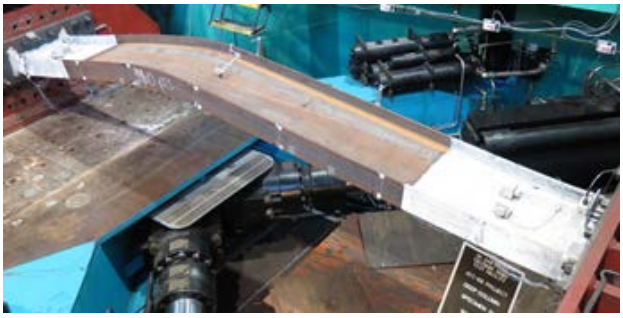

(a) Elastic LTB (W24×55) (b) Plastic LTB (W18×192)

Figure 6.6 Elastic vs. Plastic LTB

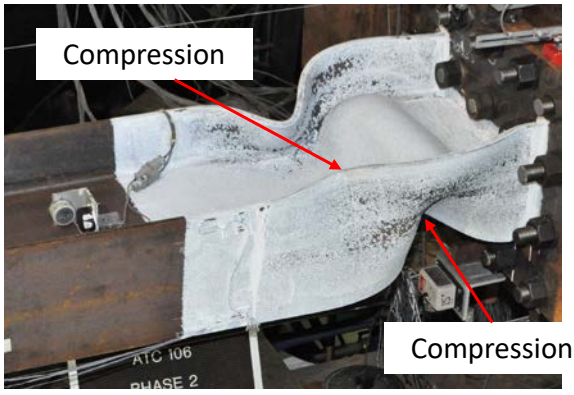

(a) ALB

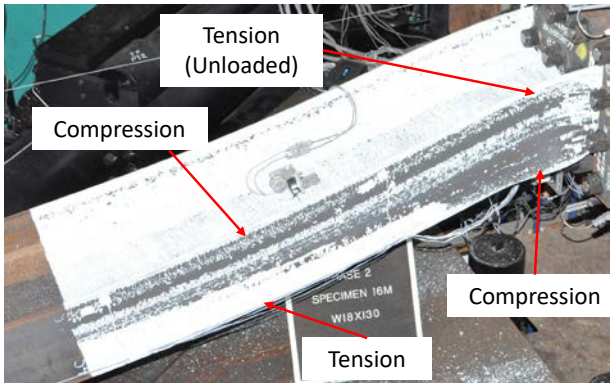

(b) CB

Figure 6.7 Characteristics of ALB and CB Modes

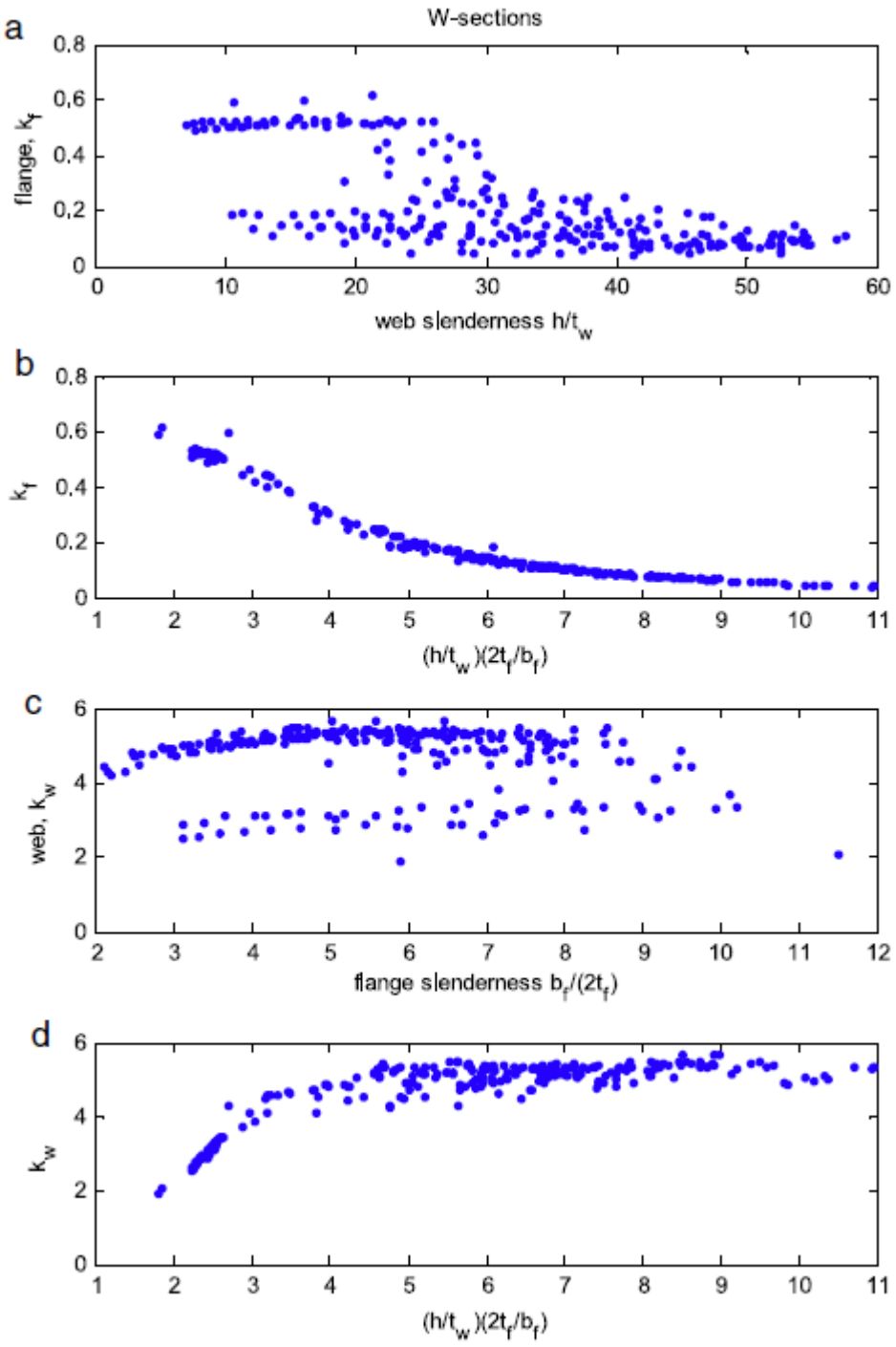

Figure 6.8 Flange and Web Local Buckling Coefficients for W-sections under Axial Loading (Seif and Schafer 2016)

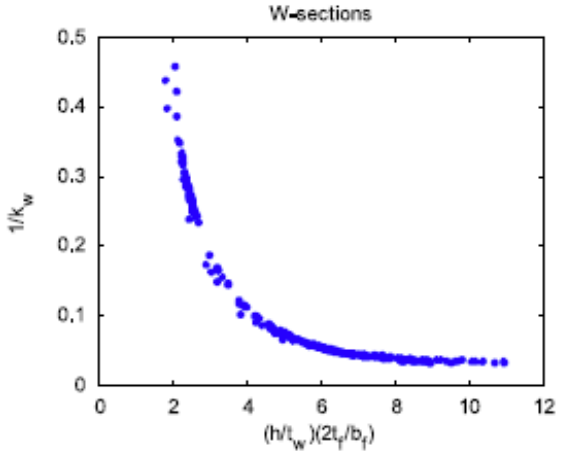

Figure 6.9 *(h/t_w)(2t_f/b_f)* vs. *1/k_w* Relationship (Seif and Schafer, 2016)

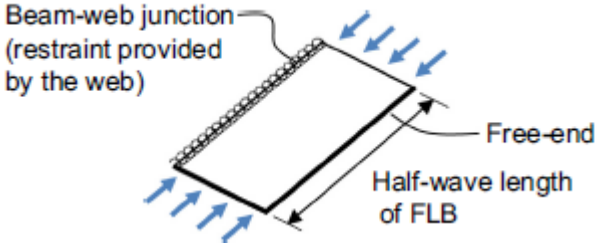

Figure 6.10 Rotational Restraint Provided by Web at Flange-web Junction (Han and Lee 2016)

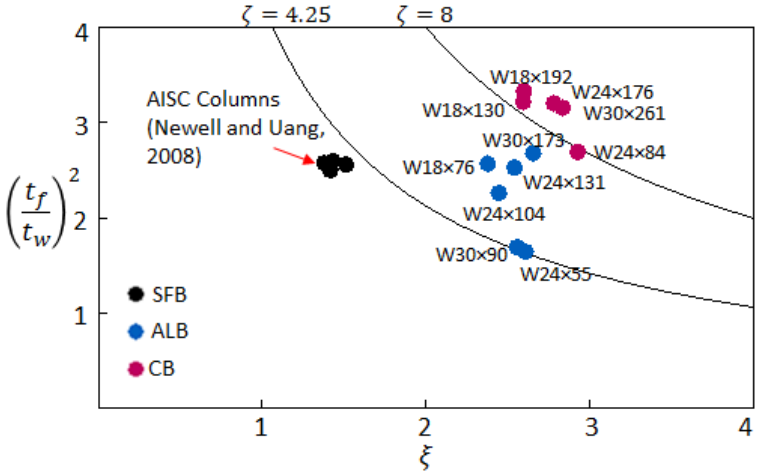

Figure 6.11 Validation of Proposed Buckling Classification Criterion with Tested Columns

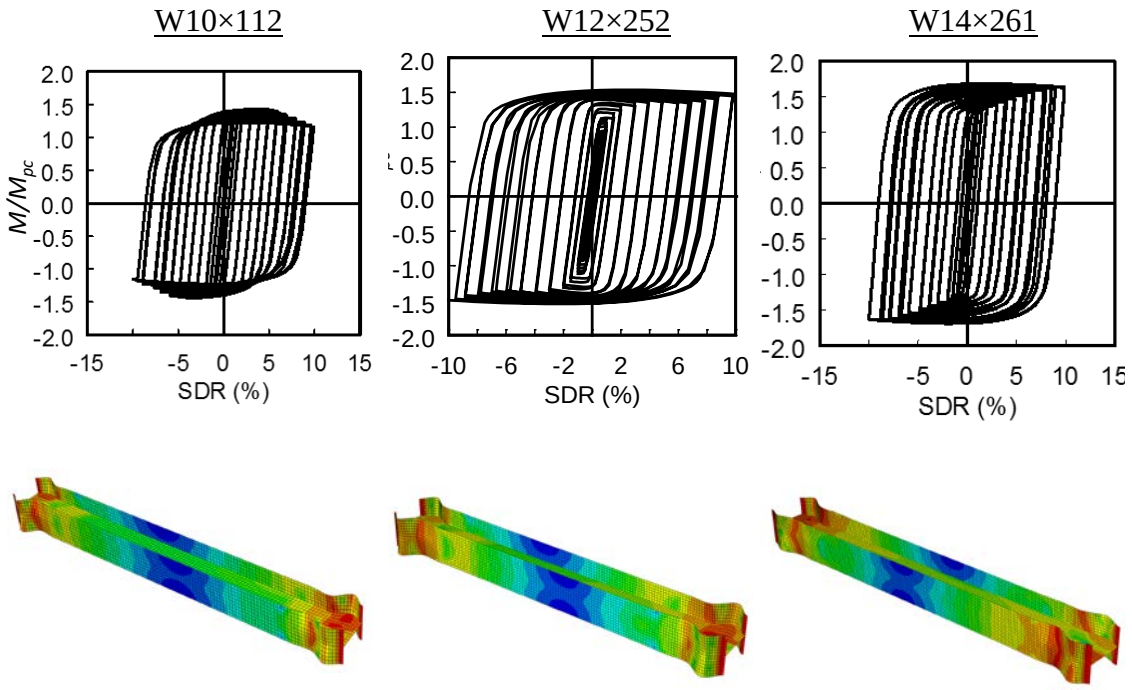

Figure 6.12 SFB Failure Mode

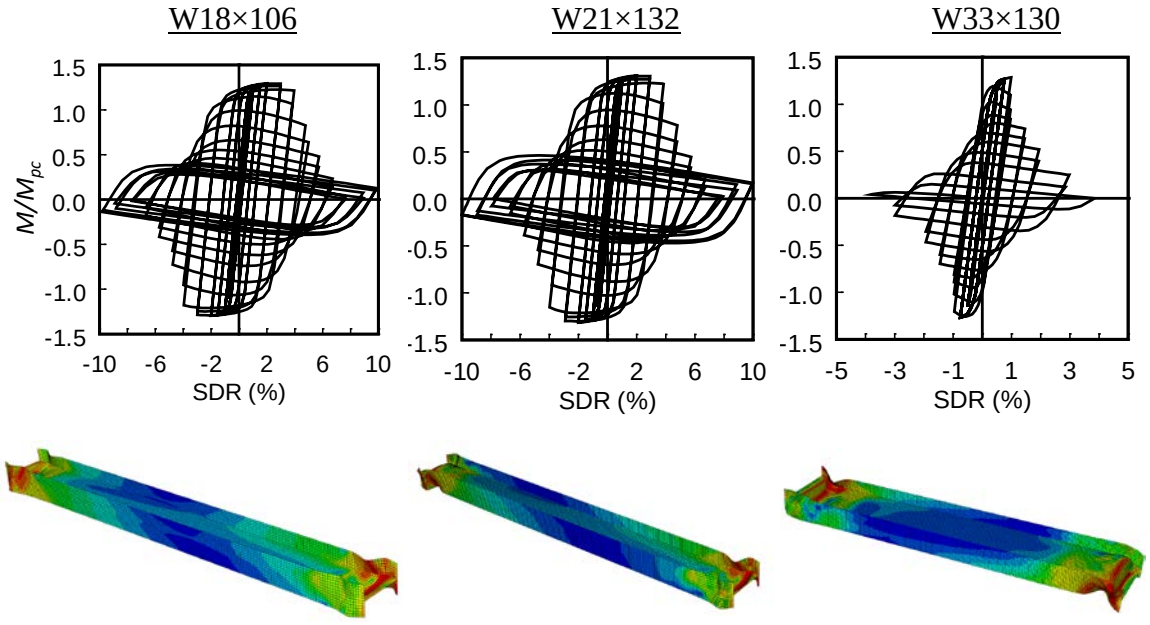

Figure 6.13 ALB Failure Mode

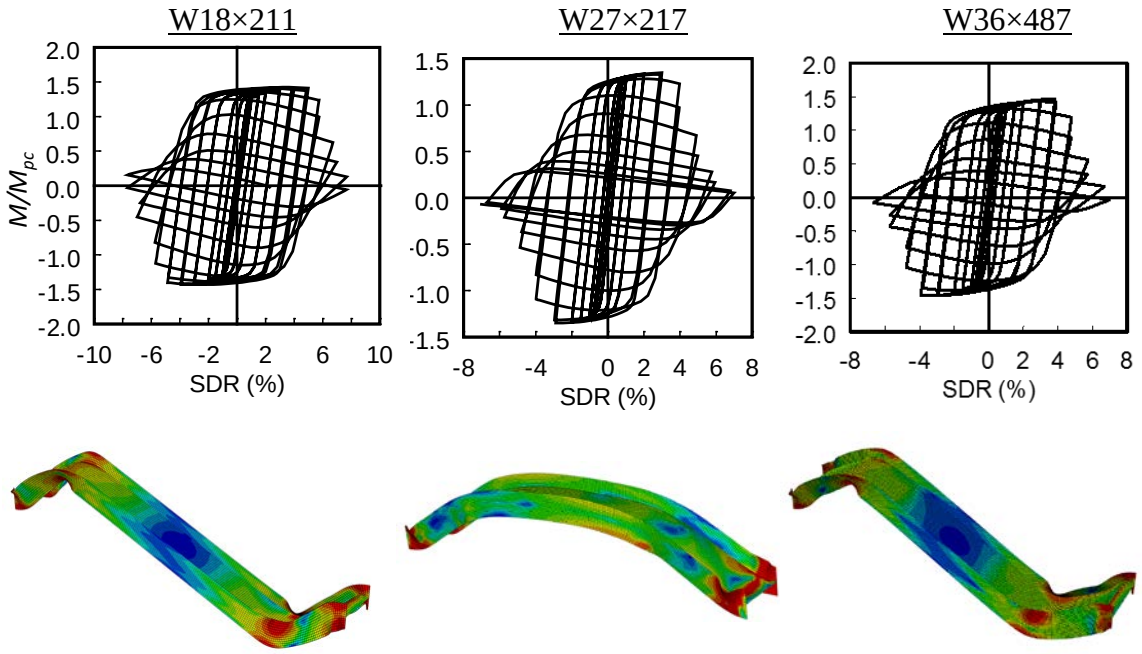

Figure 6.14 CB Failure Mode

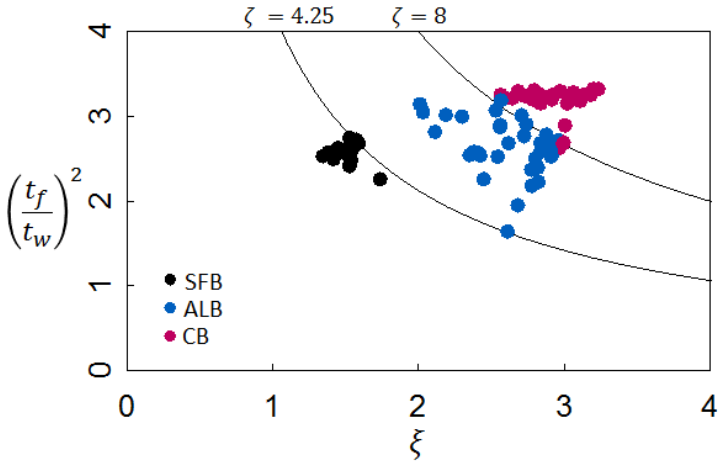

Figure 6.15 Validation of Proposed Buckling Classification Criterion with Numerical Simulated Columns

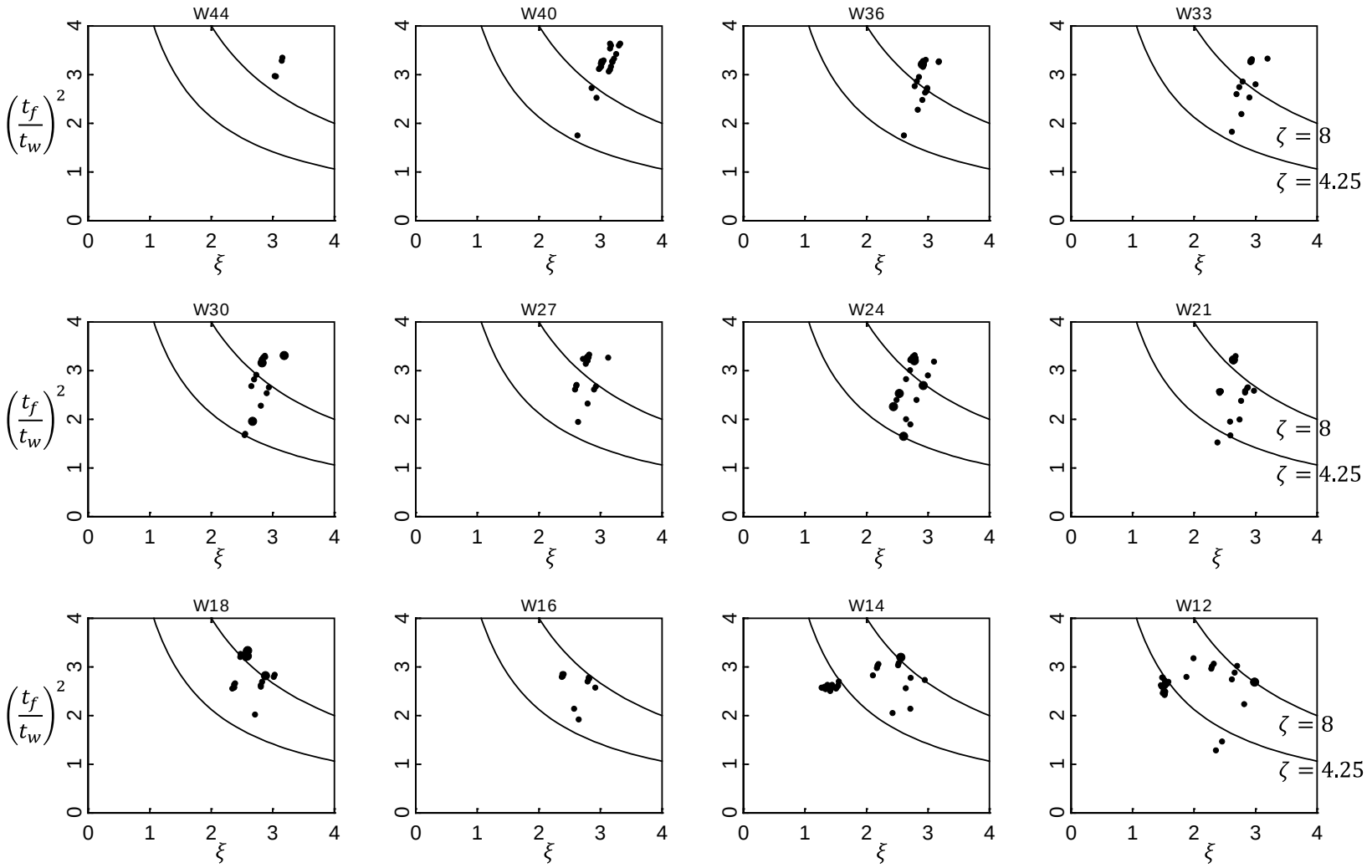

Figure 6.16 Proposed Buckling Mode Classifications for AISC W-shaped Sections

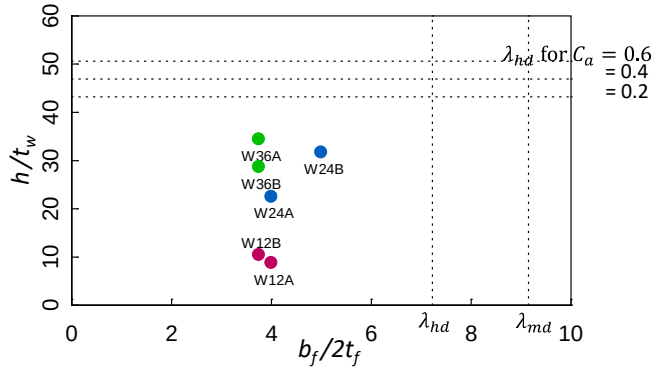

Figure 6.17 Slenderness Ratios of Artificial Sections

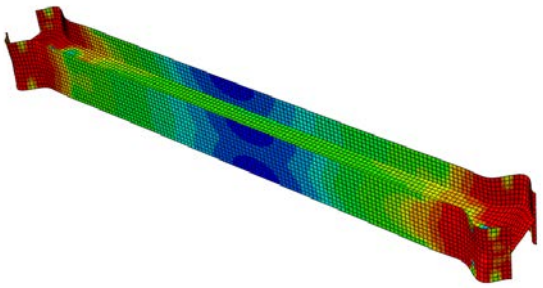

(a) Model W12A

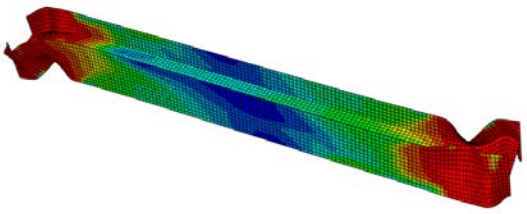

(b) Model W12B

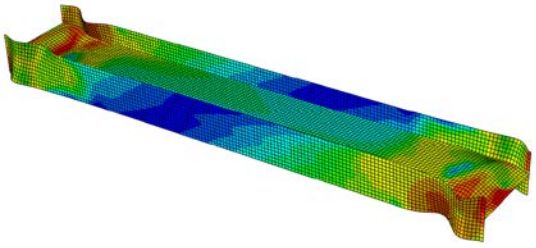

(c) Model W24A

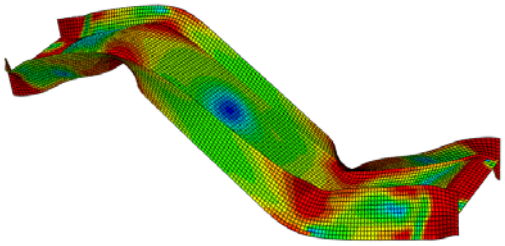

(d) Model W24B

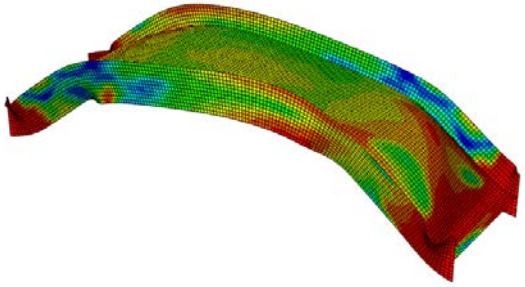

(e) Model W36A

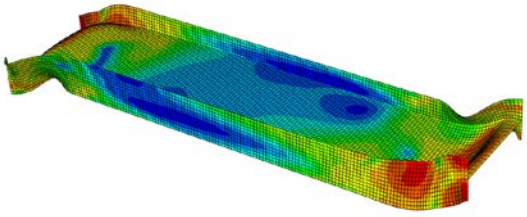

(f) Model W36B

Figure 6.18 Buckling Modes of Artificial Sections

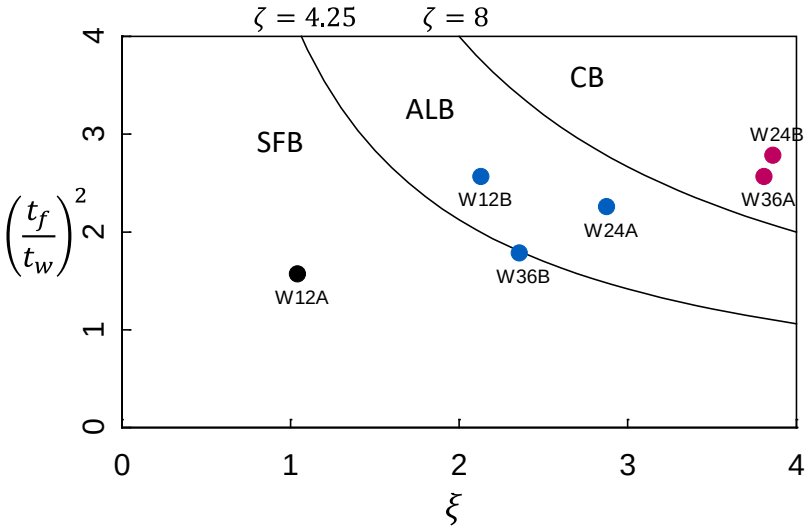

Figure 6.19 Validation of Proposed Buckling Classification Criterion on Columns with Modified Sections

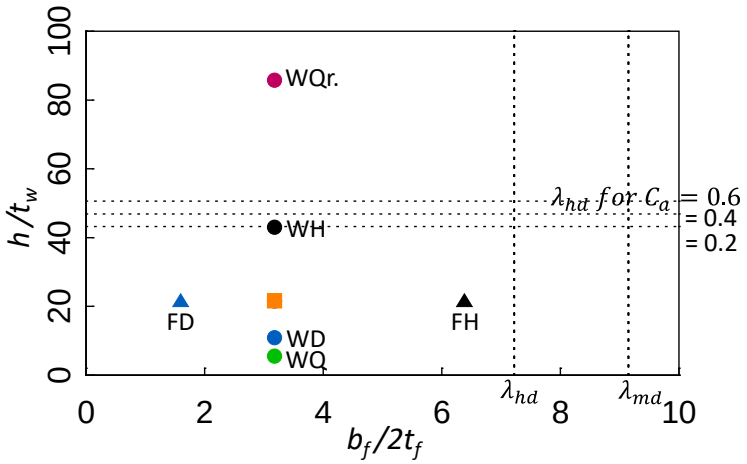

Figure 6.20 Slenderness Ratios of W36×487 (Fogarty and El-Tawil, 2017)

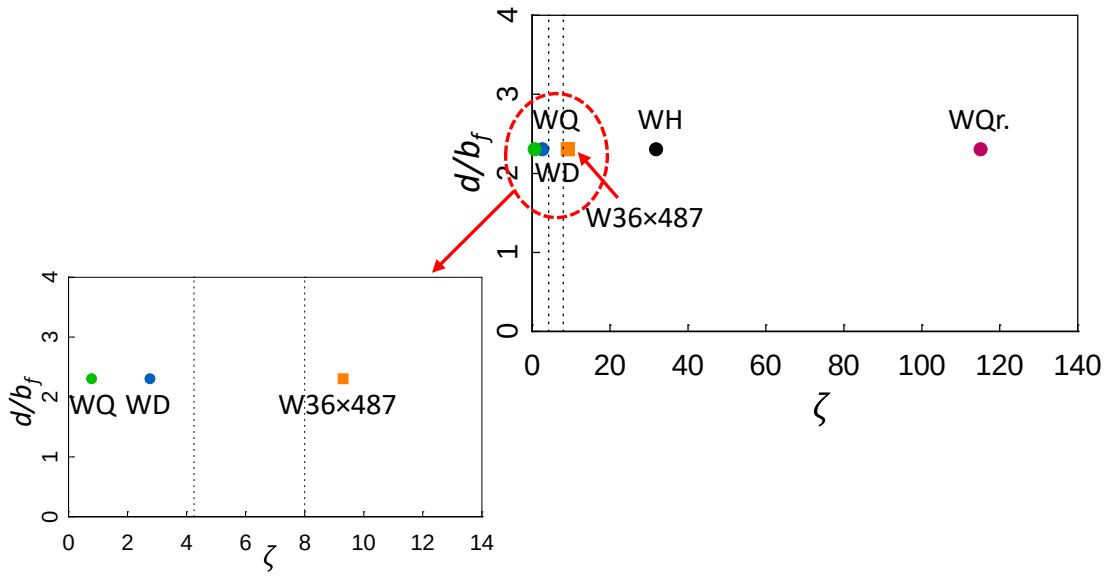

Figure 6.21 Proposed Web Restrain Parameter to Classify Buckling Modes

7 PLASTIC HINGE MODELLING OF DEEP COLUMNS

7.1 Introduction

Steel moment frames can be analyzed by concentrated hinge models, distributed hinge models or continuum finite element models to predict the seismic response. Concentrated hinge models are commonly used in practice due to their simplicity and efficiency. The plastic hinge moment capacity of a section is significantly affected by factors such as axial force levels, material properties and slenderness ratios of the section. This chapter provides detailed guidance to determine properties of concentrated hinges for modeling steel beam-columns. As discussed in previous chapters, the loading protocol affects the cyclic behavior of the sections. Therefore, backbone model criteria for both monotonically and cyclically loaded columns that define the upper and lower bounds of backbone curves will be presented.

7.2 Nonlinear Structural Analysis and Design of Buildings

Although buildings are usually designed for seismic resistance using elastic analysis, most will experience significant inelastic deformations under large earthquakes. Under this extreme conditions, current performance-based design methods require nonlinear analysis methods to predict the realistic behavior of the structure. Building code analysis such as ASCE 7 (ASCE 2010), ASCE 41 (ASCE 2013), and FEMA P-695 (FEMA 2009) are some examples of performance-based design approaches that apply nonlinear analysis. Utilizing these guidelines and standards, nonlinear analysis can be applied to design and assess the performance of buildings which are subjected to earthquake loading. When creating the nonlinear structural model, the modeling decisions are highly influenced by knowing which structural demand parameters need to be estimated by the structural

analysis. To be able to find how much these demand parameters are affected, it is crucial to decide what components of the building will be included in the model for the nonlinear structural analysis.

Once a decision has been made for which components to include in the structural models, then each component needs to be identified as either deformation-controlled or force-controlled members. Displacement-controlled members are those that have reliable inelastic deformation capacity without substantial strength decay, whereas force-controlled actions are associated with brittle modes where inelastic capacity cannot be assured (ASCE 2013). Deformation-based actions are represented by inelastic elements, and force-control actions are represented by elastic elements in the structural model.

To create structural simulation model, the type of structural discretization should be selected. Concentrated hinge models, distributed fiber models, and continuum finite elements models are the three main types of model discretization. The concentrated and fiber models are discrete models that use macro-level components to represent specific structural elements and behaviors, such as beam element, a plastic hinge zone in a beam or wall, etc. On the other hand, continuum models are micro-level models that describe the behavior at the material level, where a structural element is discretize into finite elements; finite element simulation presented in Chapter 5 falls in this category. The hinge and fiber models are represented by a combination of elastic and inelastic elements. This chapter focuses on the recommendations for concentrated plastic hinge models for deep beam-columns.

7.3 Concentrated Plastic Hinge Models

Plasticity theory is often used to model column elements with force-moment (*P-M*) interaction. Concentrated plastic hinge models represent all the critical deformation modes of an inelastic component, such as the response of the column and/or beam plastic hinge, in a computationally efficient spring-type element (see Figure 7.1). Nonlinear concentrated plastic hinge characteristics are defined by a moment-rotation response as shown in Figure 7.2. Zone 1 indicates the elastic portion of the backbone curve. Zone 2 and 3 defines the pre- and post-buckling regions, respectively. The backbone curve defines the bounds within the hysteretic response of the component is confined. According to ASCE 41 (ASCE 2013), a backbone curve shall be drawn through each point of peak displacement during the first cycle of each increment of loading (see Figure 4.1).

Key parameters of an idealized backbone curve are usually derived by utilizing the regression analysis to evaluate the important parameters based on the behavior seen in test results and parametric study. Based on the observations made from both tests and numerical simulation, zone 4 is deleted and the proposed backbone curve for columns is shown in Figure 7.3. As discussed in Chapter 4 and Chapter 5, columns subjected to AISC cyclic loading protocol deteriorate much faster in the post-buckling region than the near-fault loading protocol due to relatively large number of inelastic cycles of symmetric loading protocol (far-field loading).

Figure 4.9 shows the identical column with three different loading history. Red, black, and blue backbone curves represent the symmetric AISC cyclic loading, near-fault loading protocol, and monotonic loading, respectively. AISC cyclic loading protocol is conservative, while the monotonic loading is overly unconservative for the calibration of

component deterioration models. Ideally, a component model should be created and calibrated to capture both of these behaviors and to respond differently under monotonic versus cyclic loading. In this study, the symmetric (AISC) loading protocol was utilized as the lower bound while the monotonic loading was used as upper bound of the backbone curves.

The flexural hinging response of columns may vary dramatically depending on the cross-section element, level of axial load, and the element slenderness ratios. As shown in previous chapters, very stocky columns, such as heavy W14 columns, tend to have very stable hysteretic response. On the other hand, deep and slender columns can experience rapid strength and stiffness degradation in the post-buckling region. Shallow and stocky columns, mainly exhibit the SFB mode, limiting the axial shortening due to flange buckling with no or little web buckling. But deep columns are prone to considerable axial shortening due to buckling.

It is crucial to determine an appropriate functional form by selecting reasonable predictive variables from analytical and empirical equations so the cyclic behavior of columns could be predicted. Therefore, nonlinear multivariate regression analysis was performed to define the key parameters that are shown in Figure 7.3. Previous analytical research and observations from experimental testing showed that the rotation capacity of steel columns are influenced by the interaction of flange local buckling, web local buckling, and LTB. Parametric studies also support this observation.

For cyclic modeling, the regression analysis method was utilized by Uang and Fan (2000) to account for the interaction between web and flanges in beams with a Reduced Beam Section (RBS). Newell and Uang (2008) also used the same approach to investigate

the cyclic behavior of W14 columns; the study indicated a strong influence of web local buckling and weak influence of LTB for shallow and stocky columns. Lignos et al. (2008) adopted the same regression analysis method for modelling deterioration parameters of plastic hinges in the beams.

In this study, flange and web local slenderness parameters ($\lambda_f = b_f/2t_f$ and ($\lambda_w = h/t_w$, respectively) are accounted. In addition, global slenderness, L/r_y, depth-to-width ratio, d/b_f and unbraced length-to-depth ratio, L/d, are also included (see Figure 7.4). Sensitivity analysis in the regression analysis was performed to find the statistical importance of each parameter. Using the stepwise multivariate regression analysis approach, only the variables that are statistically important were included in the predictive equation. To predict the response variable (RV), the following general nonlinear model is used:

$$RV = \alpha {\lambda_f}^a {\lambda_w}^b {\lambda_L}^c \left(1 - \frac{P_u}{P_y}\right)^d \left(\frac{d}{b_f}\right)^e \left(\frac{L}{d}\right)^f (F_y)^h \tag{7.1}$$

where

α= constant to be determined from regression

b_f= flange width

t_f= flange thickness

h= clear distance between flanges

t_w= web thickness

L= unbraced length

r_y= radius of gyration about y-axis

P_u= applied axial force

P_y= axil yield strength

d= depth

Eq. (7.1) can be linearized by taking the logarithm of both sides of the equation:

$$\log(RV) = \log(\alpha) + a\log\lambda_f + b\log\lambda_w + c\log\lambda_L + d\log\left(1 - \frac{P_u}{P_y}\right) + e\log\left(\frac{d}{b_f}\right) + f\log\left(\frac{L}{d}\right) + h\log(F_y) \quad (7.2)$$

Coefficient a to h and α are to be determined from regression analysis. Since both test data and parametric study results show interaction between the flange and web local buckling as well as global buckling, the predictive model reflects the coupling of local and global buckling failure modes.

7.4 Plastic Hinge Modeling of Columns

7.4.1 Database

The recommended equations are based on the test data and parametric study results of columns that range in size from W10 to W44 sections. Fixed-fixed boundary conditions are applied and the columns are subjected to the symmetric (AISC) loading protocol. The applicability of these equations are limited to the range of parameters included in the parametric study described in Chapter 5 (see Figure 7.5). Column axial loads are limited to the range of 0.15-0.75P/P_{yn}. Member slenderness (L/r_y) was in the range of 31 to 71 for shallow sections and 48 to 130 for deep columns. For the shallow column sections (W10 to W14), the depth-to-flange ratio (d/b_f) ranged from 1.0 to 3.1, while this ratio is from 1.7 to 3.3 for deep columns (see Figure 7.6). Figure 7.5 shows that the ratio between λ_f and λ_w is bounded by 2.25 and 9.5.

7.4.2 Monotonic Backbone Curve

It was shown in Chapters 4 and 5 that a monotonically loaded column cannot strain harden enough to produce a CB mode. Therefore, unlike cyclic loading cases, two buckling modes (SFB and ALB) are applicable for the monotonically loading case. Very stocky sections with a d/b_f ratio less than 1.5 is subjected to the SFB mode and sections with higher d/b_f ratio will experience ALB mode only. Coupled buckling was not observed for monotonically loaded sections.

7.4.2.1 Zone 1 Elastic Flexural Stiffness, K_e

The rotational stiffness used by ASCE 41 to calculate the yield rotation is based on the Euler-Bernoulli beam theory for double-curvature bending. Therefore,

$$K_e = \frac{6EI_x}{L}\left(1 - \frac{P_u}{P_e}\right) \tag{7.3a}$$

where

$$P_e = \frac{\pi^2 EI_x}{L^2} \tag{7.3b}$$

Conceptually the elastic beam in Figure 7.1(b) has its proper flexural stiffness, and the rotation springs are modelled as rigid-plastic. When a software is used, however, the infinite stiffness of the rigid-plastic springs can be replaced by one with, say, 10 times of the elastic stiffness of the member. To maintain the same overall stiffness of the member, the elastic stiffness of the elastic beam between rotational springs can be increased as follows.

$$EI^* = \frac{EI_{x,c}}{1 - 6/60} = 1.1EI_{x,c} \tag{7.4}$$

Flexural Yield Strength, M_y: The *P-M* interaction equation in AISC 360 can be used

(a) when $P_u/P_y \geq 0.2$

$$M_y = \frac{9}{8} M_p \left(1 - \frac{P_u}{P_y}\right) \tag{7.5}$$

(b) when when $P_u/P_y < 0.2$

$$M_y = M_p \left(1 - \frac{P_u}{2P_y}\right) \tag{7.6}$$

Yield rotation, θ_y: The yield rotation is computed as follows:

$$\theta_y = M_y/K_e \tag{7.7}$$

7.4.2.2 Zone 2:

Pre-buckling rotation, θ_{M2} and maximum moment, M_{max} is defined in this zone.

Maximum Moment, M_{max}: A strain hardening parameter, α^m which depends on the local and global slenderness ratios as well as the applied load ratio is used to compute M_{max}:

$$M_{max} = \alpha_m M_y \tag{7.8}$$

The coefficient of determination, R^2, in a regression analysis meausres the quality of regression. An R^2 value of 1 indicates a perfect correlation between actual and predicted response. The following equation are obtained from regression:

- for column with SFB mode ($R^2 = 0.96$):

$$\alpha_m = 2.74{\lambda_f}^{-0.33} \left(1 - \frac{P}{P_y}\right)^{-0.60} \tag{7.9}$$

- for columns with ALB or CB modes ($R^2 = 0.90$):

$$\alpha_m = 4.57{\lambda_f}^{-0.20}{\lambda_w}^{-0.22} \left(1 - \frac{P}{P_y}\right)^{-0.60} \tag{7.10}$$

- for all buckling modes ($R^2 = 0.88$):

$$\alpha_m = 3.09{\lambda_f}^{-0.27}{\lambda_w}^{-0.07}\left(1 - \frac{P}{P_y}\right)^{-0.60} \tag{7.11}$$

As shown above, when the columns are categorized based on their buckling modes, the R^2 values improve, indicating that it is prudent to use either Eq. (7.9) or (7.10) for the particular buckling mode under consideration. Also, since the flange and web slenderness ratios are highly correlated for the sections grouped under the SFB mode, only one parameter is kept and the other one is eliminated. Since is the dominant mode, λ_f is kept in Eq. (7.10).

For columns with ALB and CB modes, however, both flange and web slenderness ratios become equally important as shown in Eq. (7.10). This result is in agreement with the observation from test and numerical studies. Also note that the exponent of the axial force term is the same for all three equations regardless of their buckling modes.

Pre-buckling Plastic Rotation, θ_{p2}^m: The Pre-buckling plastic rotation can be calculated from Eq. (7.12) and Eq. (7.13). For information, Eq. (7.14) which does not distinguish buckling modes is also presented.

- for columns with SFB mode ($R^2 = 0.91$):

$$\theta_{p2}^m = 10^{-1.93}{\lambda_f}^{-1.44}\left(1 - \frac{P}{P_y}\right)^{0.85}\left(F_y\right)^{1.37} \tag{7.12}$$

- for columns with ALB or CB mode ($R^2 = 0.85$):

$$\theta_{p2}^m = 10^{2.78}{\lambda_f}^{-0.31}{\lambda_w}^{-1.91}\left(1 - \frac{P}{P_y}\right)^{1.40}\left(F_y\right)^{-0.30} \tag{7.13}$$

- for all buckling modes ($R^2 = 0.73$):

$$\theta_{p2}^{m} = 10^{1.34}\lambda_f{}^{-0.67}\lambda_w{}^{-0.95}\left(1-\frac{P}{P_y}\right)^{1.05}\left(F_y\right)^{-0.18} \quad (7.14)$$

7.4.2.3 Zone 3:

Post-buckling Plastic Rotation, $\boldsymbol{\theta_{p3}^{m}}$

The Post-buckling rotation can be determined as follows.

- for columns with SFB mode ($R^2 = 0.92$)

$$\theta_{p3}^{m} = 10^{-0.48}\lambda_f{}^{-0.47}\left(1-\frac{P}{P_y}\right)^{1.57}\left(F_y\right)^{0.29} \quad (7.15)$$

- for columns with ALB or CB mode ($R^2 = 0.80$)

$$\theta_{p3}^{m} = 10^{2.42}\lambda_f{}^{-0.21}\lambda_w{}^{-0.1}\left(1-\frac{P}{P_y}\right)^{2.10}\left(F_y\right)^{-1.45} \quad (7.16)$$

- for all buckling modes ($R^2 = 0.68$);

$$\theta_{p3}^{m} = 10^{1.68}\lambda_f{}^{-0.09}\lambda_w{}^{-0.29}\left(1-\frac{P}{P_y}\right)^{1.94}\left(F_y\right)^{-0.91} \quad (7.17)$$

7.4.3 Cyclic Backbone Curves

7.4.3.1 Zone 1

The elastic stiffness, K_e, and flexural yield moment, M_y, are the same as those for monotonic loading (see Section 7.4.2.1).

7.4.3.2 Zone 2

Maximum Moment, $\boldsymbol{M_{max}}$: Similar to the monotonic backbone curve, the maximum moment can be determined as follows,

$$M_{max} = \alpha_c M_y \quad (7.18)$$

where α_c is the cyclic strain hardening

- for columns with SFB mode ($R^2 = 0.88$):

$$\alpha_c = 10^{0.44}{\lambda_f}^{-0.49}\left(1-\frac{P}{P_y}\right)^{-0.36} \tag{7.19}$$

- for columns with ALB mode ($R^2 = 0.91$):

$$\alpha_c = 10^{0.34}{\lambda_f}^{-0.2}\,{\lambda_w}^{-0.1}\left(1-\frac{P}{P_y}\right)^{-0.36} \tag{7.20}$$

- for columns with CB mode ($R^2 = 0.86$):

$$\alpha_c = 10^{0.55}\left(\frac{\lambda_w}{\lambda_f}\right)^{-0.13}{\lambda_L}^{-0.2}\left(1-\frac{P}{P_y}\right)^{-0.36} \tag{7.21}$$

- for all buckling modes ($R^2 = 0.70$):

$$\alpha_c = 10^{0.2}{\lambda_w}^{-0.12}{\lambda_L}^{-0.05}\left(1-\frac{P}{P_y}\right)^{-0.36} \tag{7.22}$$

Similar to the monotonic loading case, the exponent of axial load term is the same for all buckling modes. Only $\lambda_f$appears in the equation for the SFB and both λ_w and λ_f appear in the equation for ALB and CB mode; note that the exponent for λ_f is positive for the latter mode.

Pre-buckling Plastic Rotation, $\boldsymbol{\theta_{p2}^{C}}$:

- for columns with SFB mode ($R^2 = 0.91$):

$$\theta_{p2}^{C} = 10^{-3.0}{\lambda_f}^{-1.8}\left(1-\frac{P}{P_y}\right)^{1.5}\left(F_y\right)^{2.0} \tag{7.23}$$

- for columns with ALB mode ($R^2 = 0.85$)

$$\theta_{p2}^{C} = 10^{0.1}{\lambda_f}^{-0.5}\,{\lambda_w}^{-1.9}\left(1-\frac{P}{P_y}\right)^{2.5}\left(F_y\right)^{0.9} \tag{7.24}$$

- for columns with CB mode ($R^2 = 0.93$):

$$\theta_{p2}^{C} = 10^{1.7}\left(\frac{\lambda_w}{\lambda_f}\right)^{-2.1} {\lambda_L}^{-0.3}\left(1-\frac{P}{P_y}\right)^{2.8}\left(F_y\right)^{-0.3} \quad (7.25)$$

- for all buckling modes ($R^2 = 0.77$);

$$\theta_{p2}^{C} = 10^{0.24}{\lambda_w}^{-1.6}\,{\lambda_L}^{-0.42}\left(1-\frac{P}{P_y}\right)^{3.04}\left(F_y\right)^{0.81} \quad (7.26)$$

Post-buckling Plastic Rotation, $\boldsymbol{\theta_{p3}^{C}}$:

- for columns with SFB mode ($R^2 = 0.90$):

$$\theta_{p3}^{C} = 10^{-3.98}{\lambda_f}^{-0.79}\left(1-\frac{P}{P_y}\right)^{1.94}\left(F_y\right)^{2.08} \quad (7.27)$$

- for columns with ALB mode ($R^2 = 0.90$);

$$\theta_{p3}^{C} = 10^{1.1}{\lambda_f}^{-0.47}\,{\lambda_w}^{-2.2}\left(1-\frac{P}{P_y}\right)^{2.74}\left(F_y\right)^{0.89} \quad (7.28)$$

- for columns with CB mode ($R^2 = 0.86$);

$$\theta_{p3}^{C} = 10^{1.18}\left(\frac{\lambda_w}{\lambda_f}\right)^{-0.67} {\lambda_L}^{-0.65}\left(1-\frac{P}{P_y}\right)^{3.35}\left(F_y\right)^{-0.38} \quad (7.29)$$

- for all buckling modes ($R^2 = 75\%$):

$$\theta_{p3}^{C} = 10^{2}{\lambda_w}^{-0.40}\,{\lambda_L}^{-1.04}\left(1-\frac{P}{P_y}\right)^{3.19}\left(F_y\right)^{-0.36} \quad (7.30)$$

7.5 Verification of Proposed Backbone Curves

Regression equations shows that the coefficient of determination, R^2 of the regression equations increases when the sections are categorized by their failure modes. The scatter in the predicted versus actual term become more when the sections are combined together. For monotonic loading, Figure 7.7 to Figure 7.9 compare the predicted

and actual values of the strain hardening factor, pre-buckling plastic rotation and post-buckling plastic rotation, respectively for the monotonic backbone curves. A similar comparison for the cyclic loading case is presented in Figure 7.10 to Figure 7.13. Figure 7.14 depicts the actual versus predicted backbone curve terms and Table 7.1 shows the values of these parameters based on the experimental test data. Sample plots are shown in Figure 7.15 to compare the results of test data and the proposed backbone curves. As shown in the figure that the proposed backbone curve depicts a good bound for the hysteresis loops of the experimental test data.

The proposed cyclic backbone curves are also compared to those from test data. Table 7.1 summarizes the test specimens used for the comparison; specimens from both AISC testing and this research program are included. The tabulated values are also presented graphically in Figure 7.14. In addition, cyclic backbone curves established from the proposed equation in Section 7.4.3 are also superimposed to the experimentally determined hysteretic responses of four deep columns tested in this research in Figure 7.15. Considering the complex future of column buckling, these two figures show that the predictions are reasonable.

Table 7.1 Comparison of Cyclic Backbone Curve Parameters with Test Data

Buckling Mode	Group (Section)	C_a	α_c		θ_{2p}^c		θ_{3p}^c	
			Test	Pred.	Test	Pred.	Test	Pred.
SFB	AISC (W14×132)	0.2	1.11	1.21	0.060	0.049	-	0.044
		0.4	1.48	1.35	0.050	0.031	-	0.024
		0.6	1.52	1.59	0.04	0.016	-	0.010
	AISC (W14×176)	0.2	1.37	1.32	0.06	0.068	-	0.051
		0.4	1.46	1.47	0.06	0.043	-	0.028
		0.6	1.60	1.73	0.06	0.022	-	0.012
	AISC (W14×233)	0.2	1.30	1.49	0.07	0.108	-	0.061
		0.4	1.40	1.67	0.06	0.068	-	0.034
ALB	Group 2 (W24×131)	0.2	1.17	1.12	0.020	0.011	0.032	0.041
		0.4	1.19	1.23	0.007	0.006	0.025	0.021
		0.6	1.22	1.38	0.002	0.002	0.010	0.008
	Group 3 (W24×104)	0.2	1.12	1.05	0.009	0.006	0.027	0.024
		0.4	1.08	1.15	0.003	0.003	0.010	0.012
		0.6	1.14	1.29	0.002	0.002	0.004	0.005
	Group 13 (W30×173)	0.4	1.10	1.16	0.002	0.003	0.011	0.012
	Group 14 (W30×90)	0.2	1.08	1.02	0.003	0.004	0.016	0.013
	Group 17 (W18×76)	0.2	1.15	1.08	0.009	0.009	0.039	0.033
CB	Group 1 (W24×176)	0.2	1.48	1.30	0.030	0.040	0.039	0.032
		0.4	1.45	1.41	0.022	0.020	0.016	0.014
		0.6	1.52	1.59	0.008	0.008	0.010	0.005
	Group 4 (W24×84)	0.2	1.16	1.14	0.020	0.020	0.016	0.020
		0.4	1.20	1.24	0.006	0.010	0.012	0.009
	Group 12 (W30×261)	0.4	1.23	1.38	0.022	0.027	0.016	0.024
	Group 15 (W18×192)	0.2	1.35	1.30	0.021	0.054	0.032	0.034
	Group 16 (W18×130)	0.4	1.60	1.41	0.025	0.026	0.013	0.014

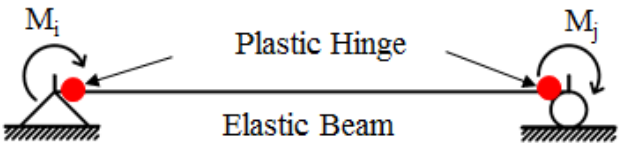

(a) Concentrated Plasic Hinge

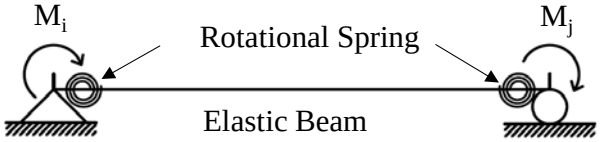

(b) Idealized Concentrated Plasic Hinge

Figure 7.1 Concentrated Plastic Hinge Model

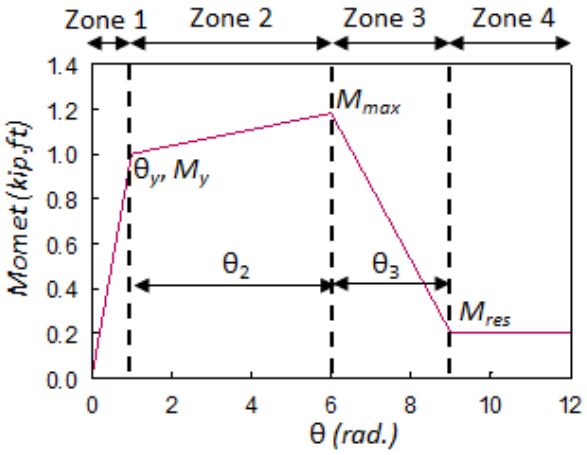

Figure 7.2 Idealized Backbone Curve for Columns (adapted from ASCE 41)

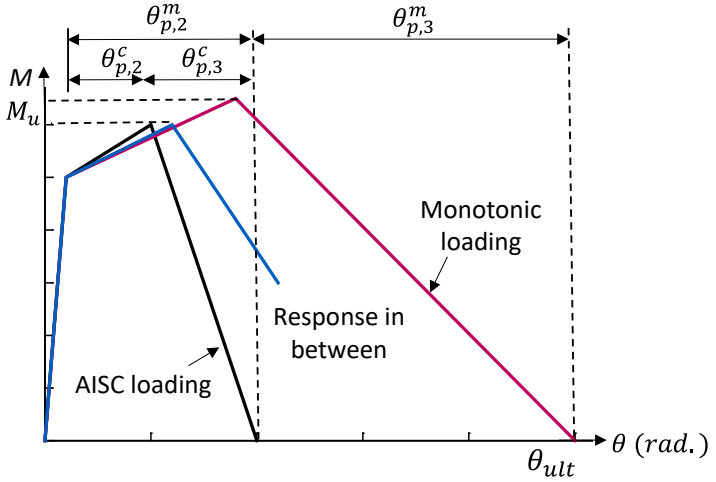

Figure 7.3 Proposed Idealized Monotonic and Cyclic Backbone Curves

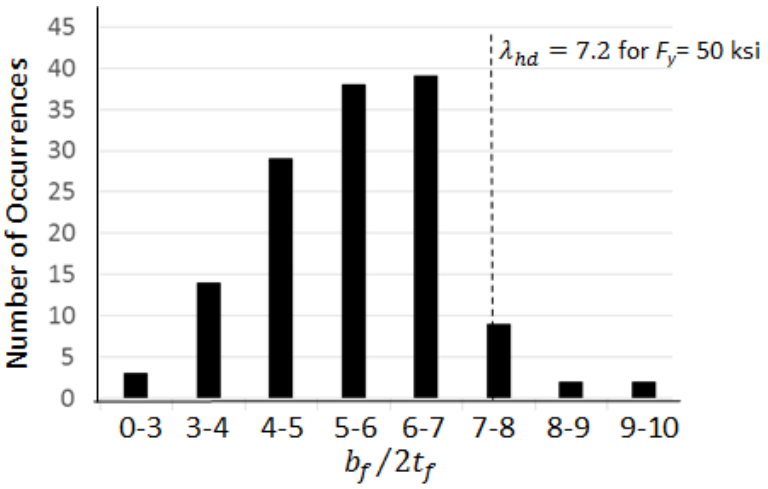

(a) Flange Slenderness

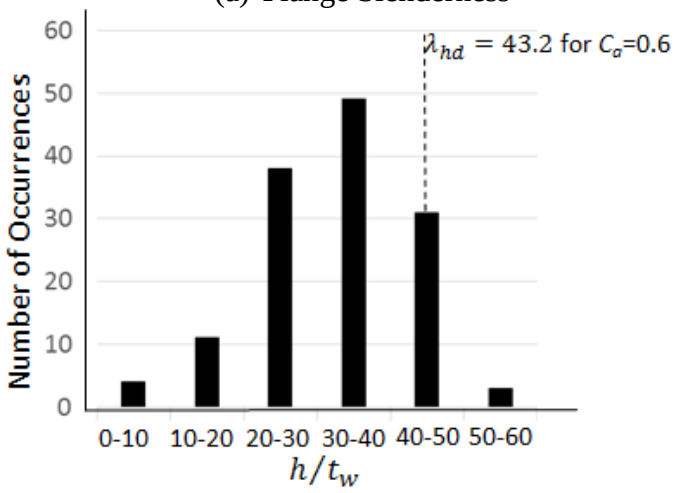

(b) Web Slenderness

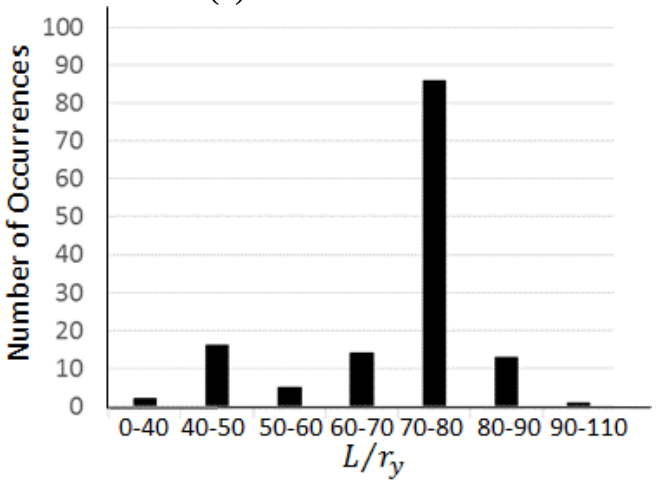

(c) Member Slenderness

Figure 7.4 Slenderness Histograms

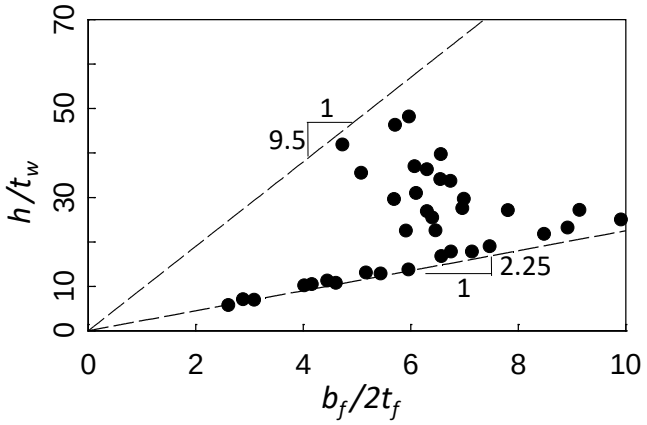

(a) Shallow Sections (W14,W12, and W10)

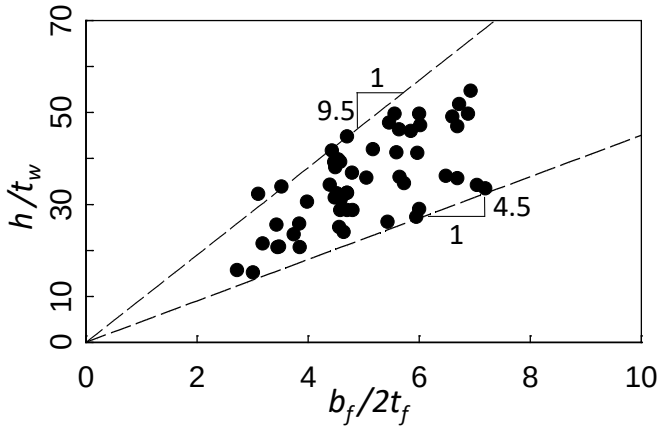

(b) Deep Sections (W16 to W44)

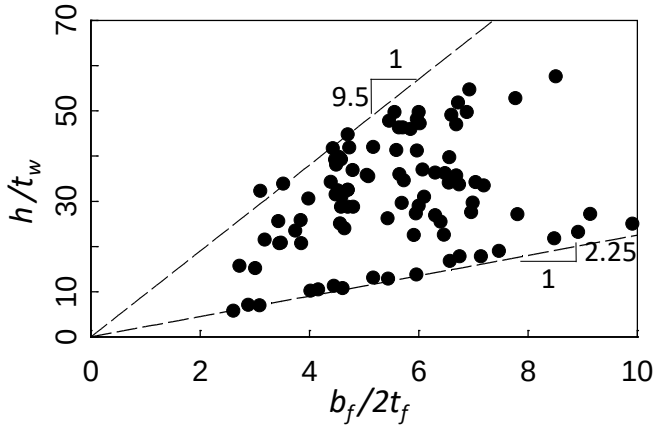

(c) All Sections

Figure 7.5 Distribution of Column Models in the Web-to-Flange Slenderness Domain

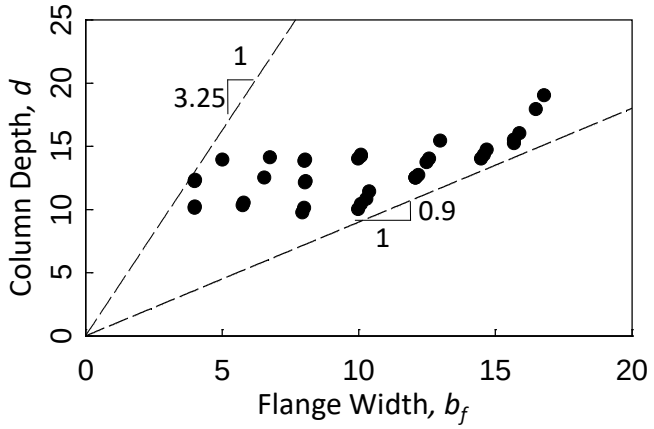

(a) Shallow Sections (W14, W12, and W10)

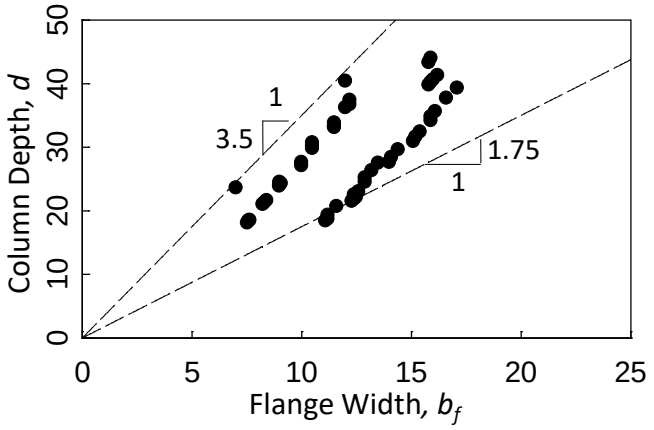

(b) Deep Sections (W16 to W44)

Figure 7.6 Distribution of Column Models in the Flange Width to Column Depth Domain

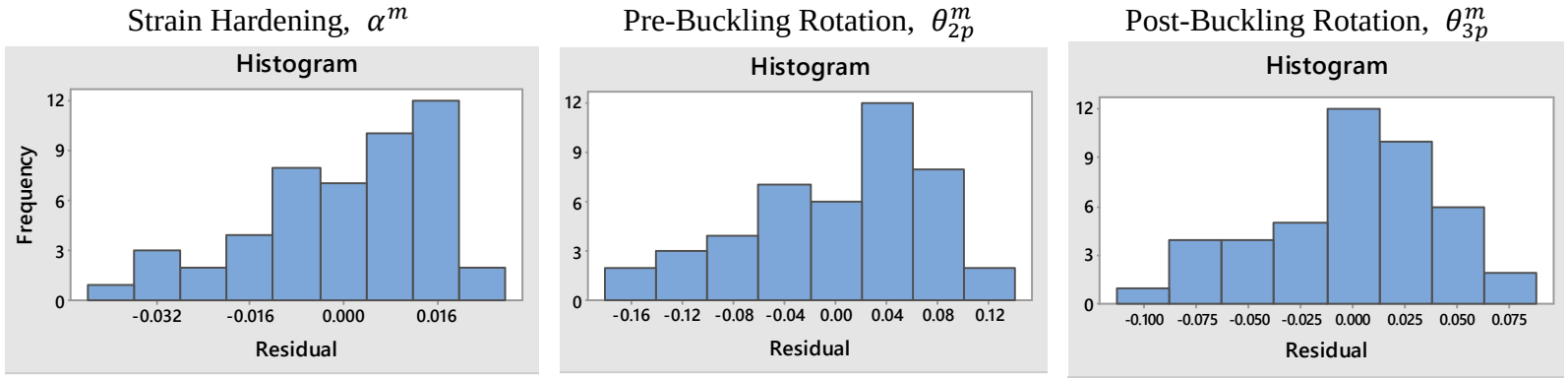

(a) Histogram

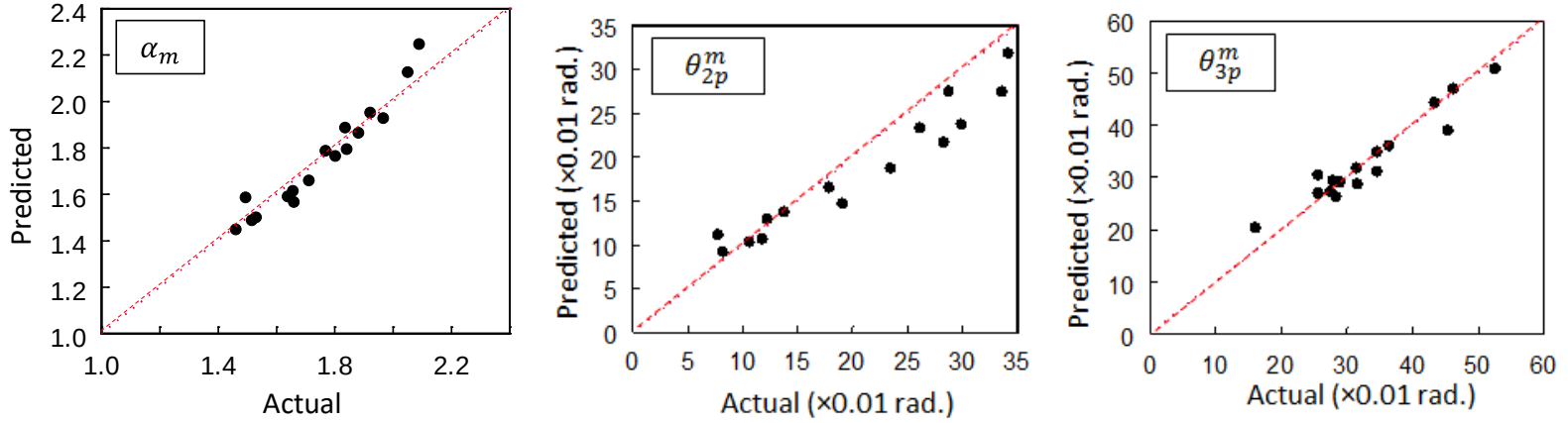

(b) Predicted vs. Actual Values

Figure 7.7 Comparison of Monotonic Backbone Curve Parameters (SFB Mode)

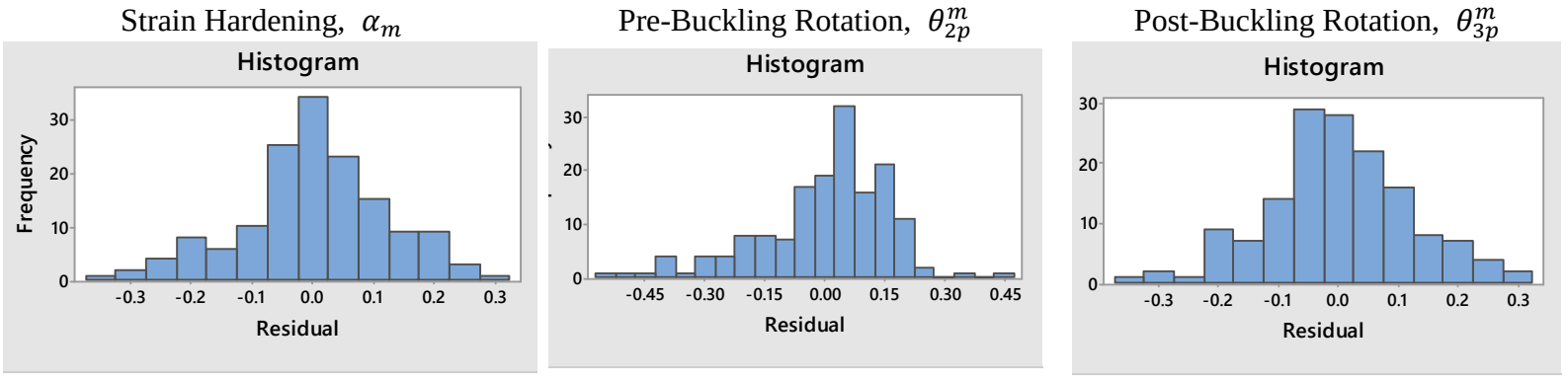

(a) Histogram

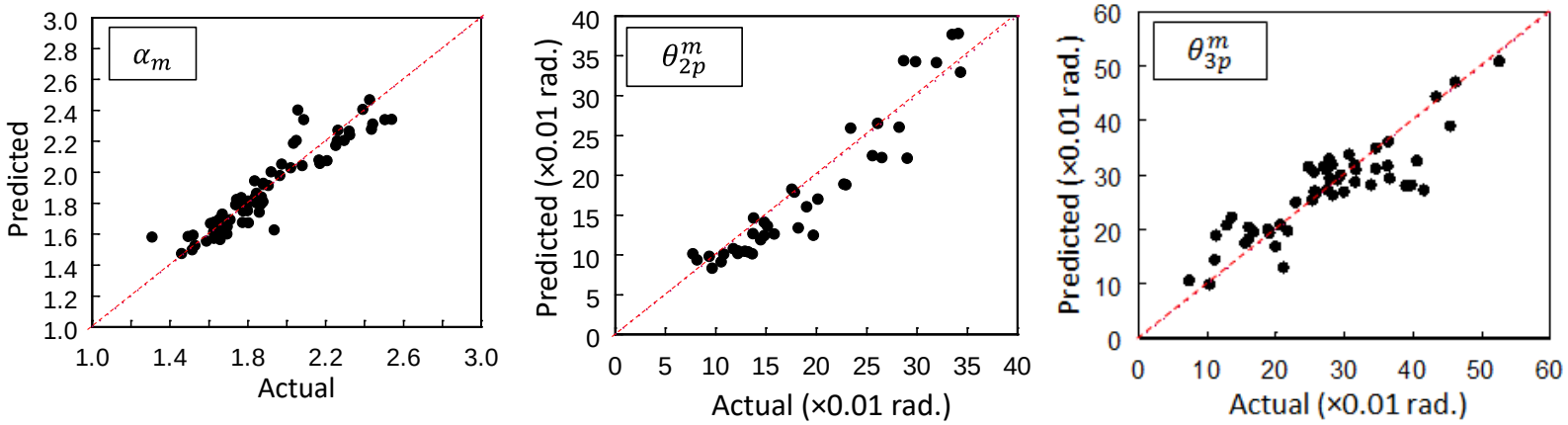

(b) Predicted vs. Actual Values

Figure 7.8 Comparison of Monotonic Backbone Curve Parameters (ALB and CB Modes)

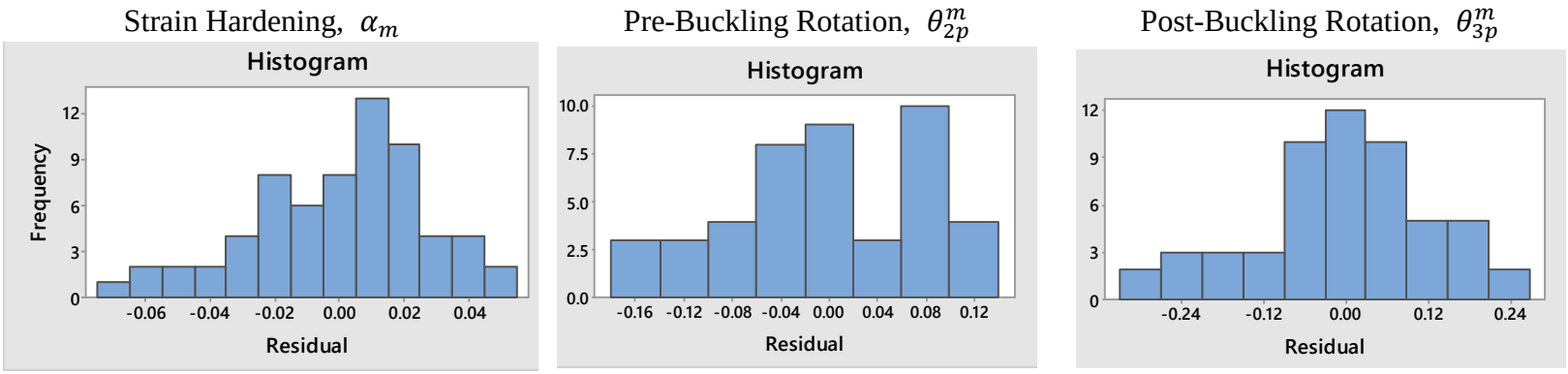

(a) Histogram

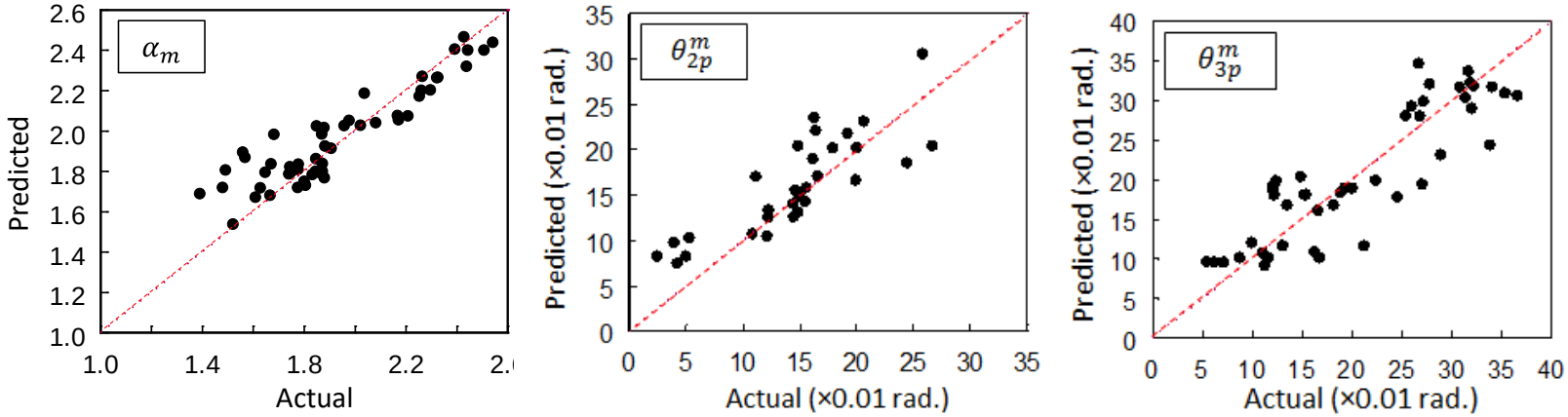

(b) Predicted vs. Actual Values

Figure 7.9 Comparison of Monotonic Backbone Curve Parameters (All Buckling Modes)

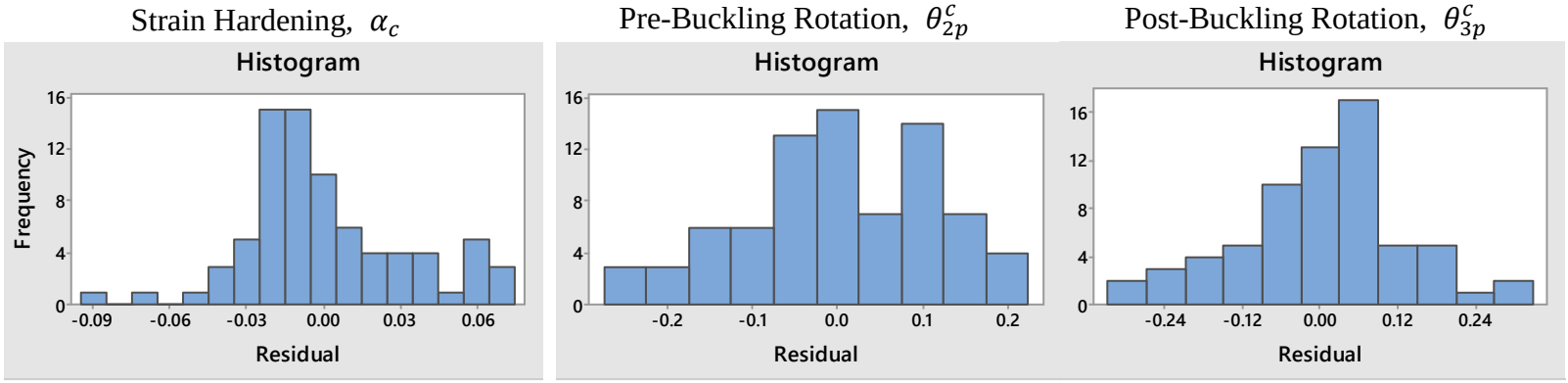

(a) Histogram

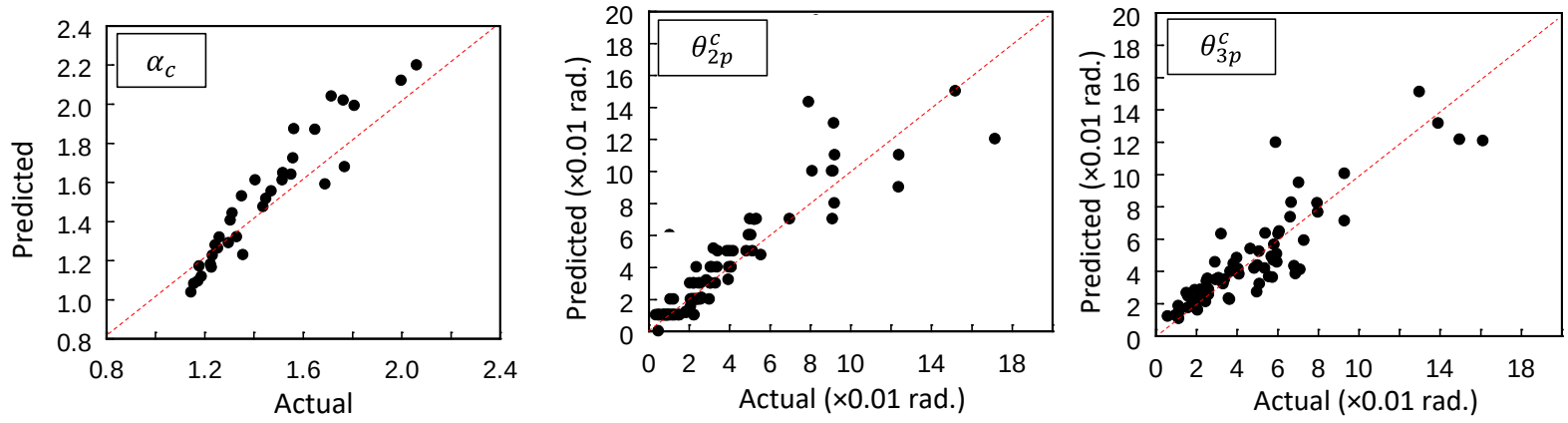

(b) Predicted vs. Actual Values

Figure 7.10 Comparison of Cyclic Backbone Curve Parameters (SFB Mode)

Strain Hardening, α_c | Pre-Buckling Rotation, θ_{2p}^c | Post-Buckling Rotation, θ_{3p}^c

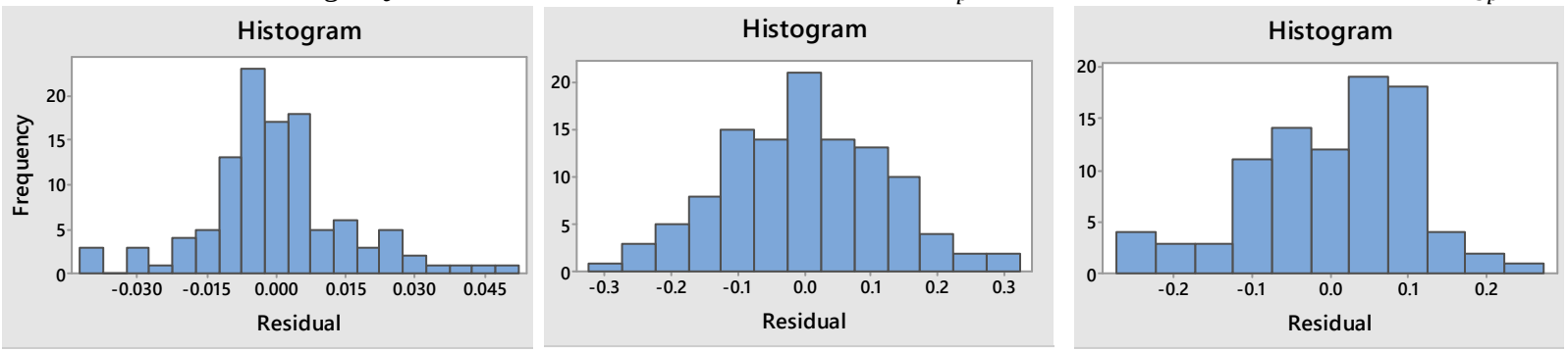

(a) Histogram

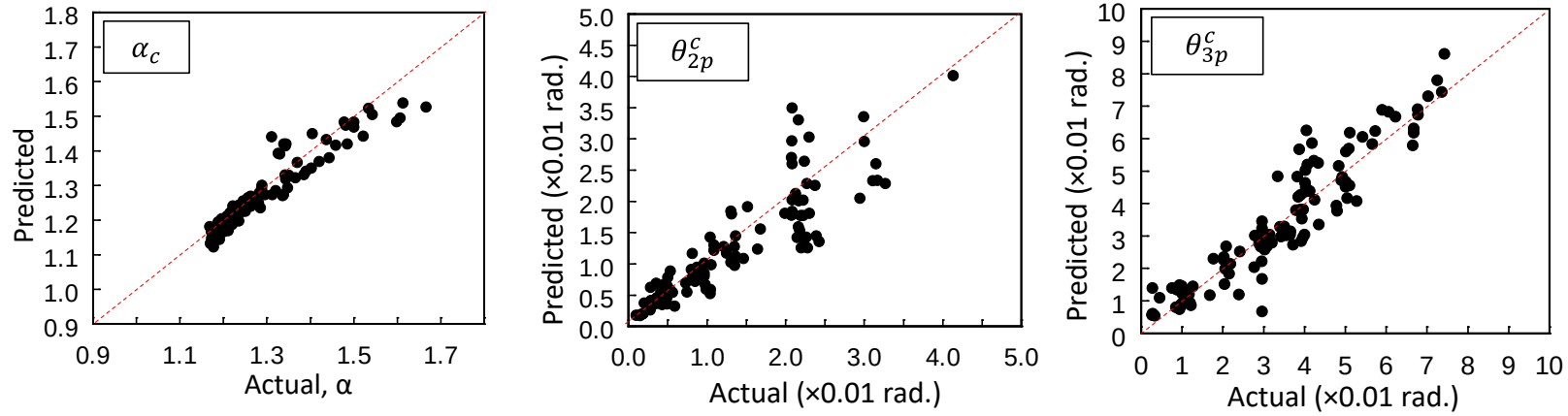

(b) Predicted vs. Actual Values

Figure 7.11 Comparison of Cyclic Backbone Curve Parameters (ALB Mode)

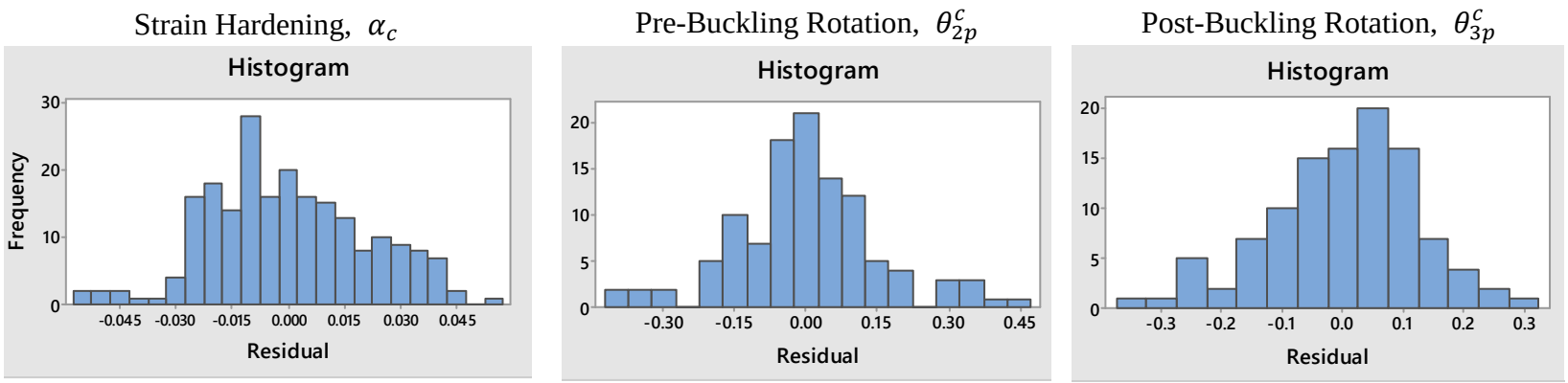

(a) Histogram

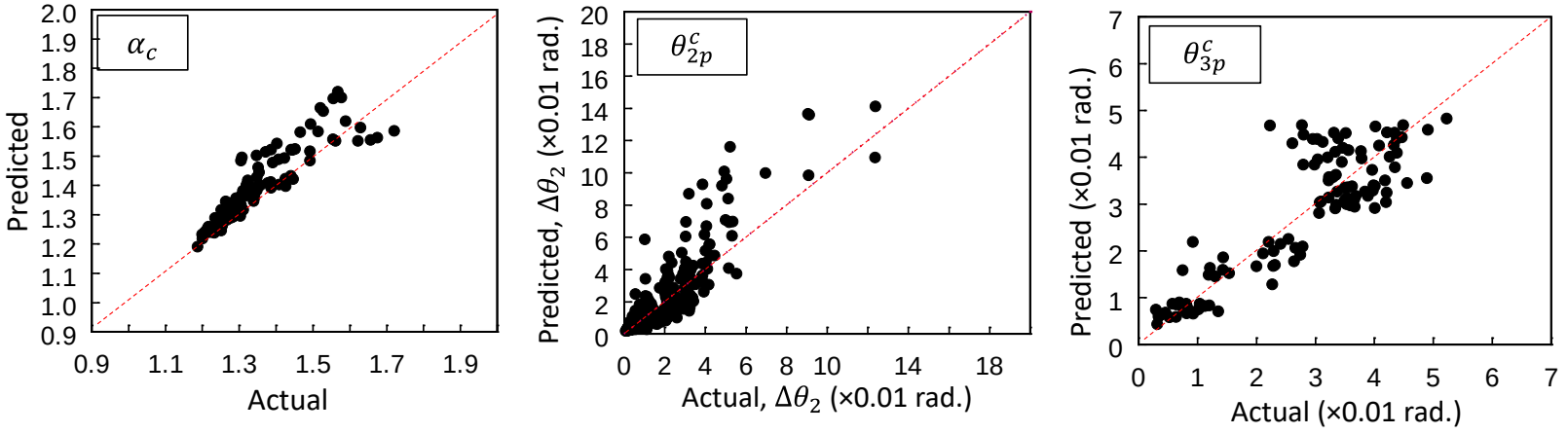

(b) Predicted vs. Actual Values

Figure 7.12 Comparison of Cyclic Backbone Curve Parameters (CB Mode)

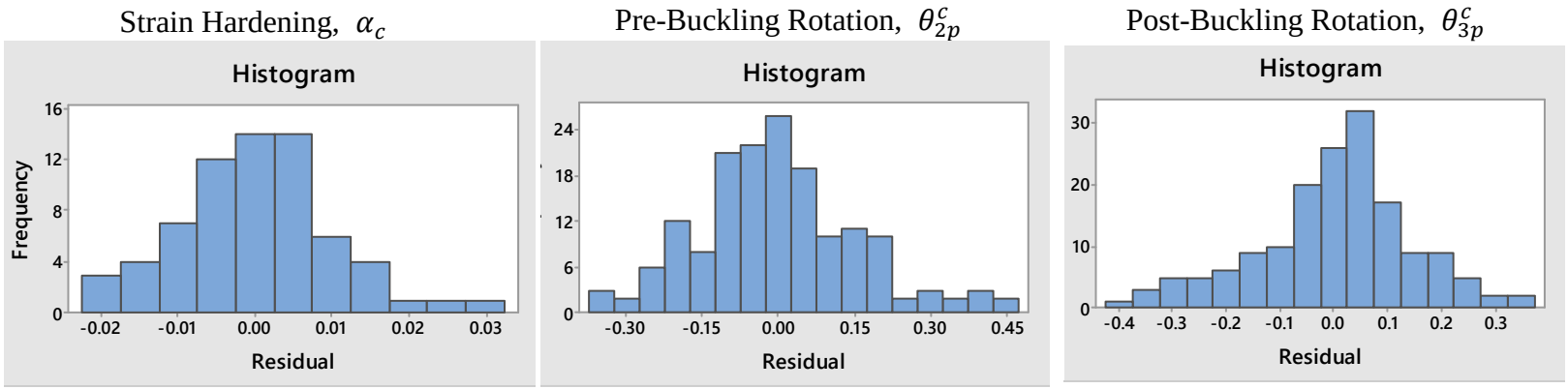

(a) Histogram

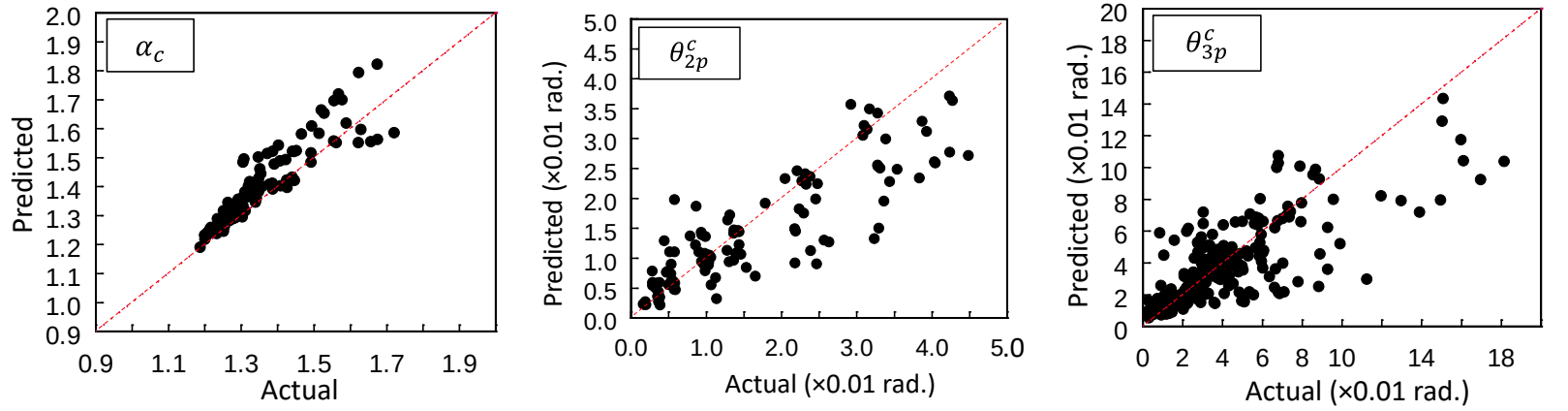

(b) Predicted vs. Actual Values

Figure 7.13 Comparison of Cyclic Backbone Curve Parameters (All Buckling Modes)

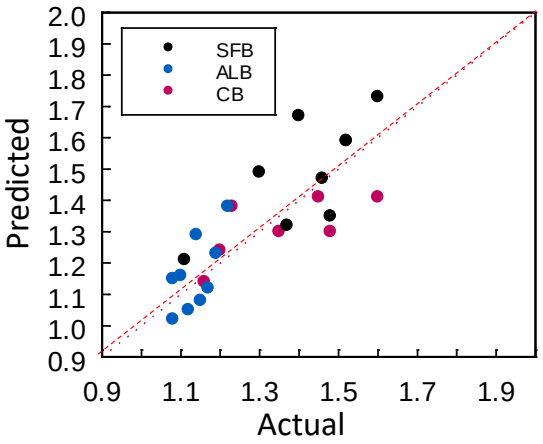

(a) Strain Hardening, α^c

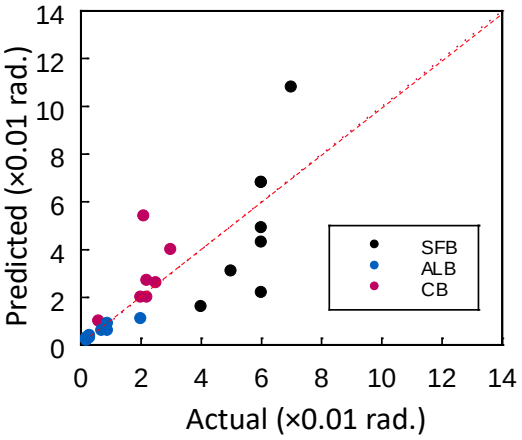

(b) Pre-buckling Plastic Rotation, θ_{2p}^c

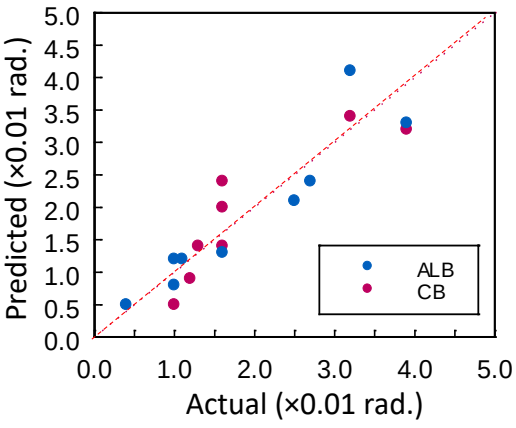

(c) Post-Buckling Rotation, θ_{3p}^c

Figure 7.14 Comparison of Predicted and Experimental Cyclic Backbone Curve Parameters

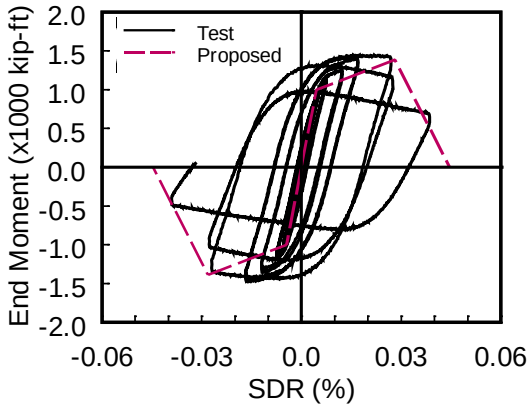

(a) Specimen 1M (W24×176)

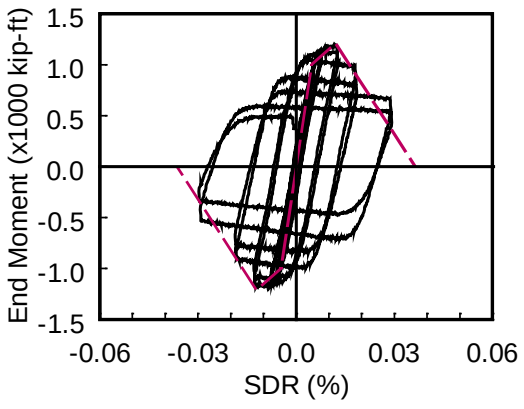

(b) Specimen 2M (W24×131)

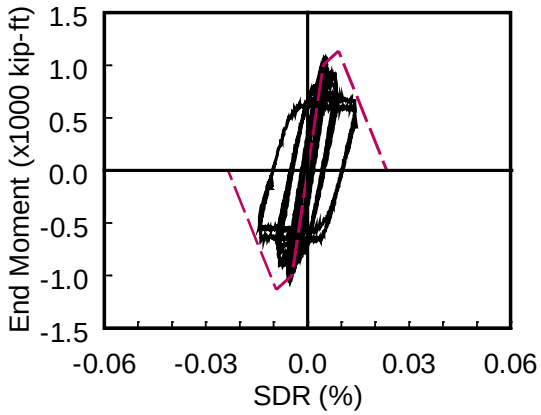

(c) Specimen 3M (W24×104)

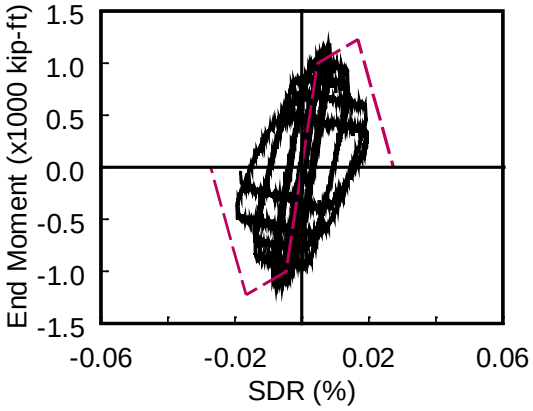

(d) Specimen 4M (W24×84)

Figure 7.15 Comparison of Proposed Cyclic Backbone Curves with Experimentally Determined Deep-Column Hysteretic Responses (C_a = 0.4)

8 LIMITING WEB SLENDERNESS FOR COLUMN SHORTENING CONTROL

8.1 Introduction

Cyclic testing of deep columns in this research program showed that these columns would experience significant buckling and axial shortening even though the cross sections of these columns met the AISC 341 (2010b) highly ductile requirement for use in SMF. Significant shortening occurred because web local buckling interacted with flange local buckling. Such significant shortening did not occur in testing shallow and stocky W14 columns (Newell and Uang 2008) because web local buckling did not occur. These observations were also confirmed by numerical simulation reported in Chapter 5. It was also shown in Chapter 5 that the deep column phenomenon could also occur in lighter shallow columns when the depth-to-width ratio was high. In this chapter, a novel approach was proposed for the development of a limiting slenderness ratio for the web such that significant axial shortening can be avoided.

8.2 Critical Story Drift Ratio

8.2.1 Definition

It was observed from testing reported in Chapter 4 and numerical simulation in Chapter 5 that axial shortening at one end of the column increased significantly when it reached 0.5%. Figure 8.1(a) shows a typical axial shortening response, where the normalized axial shortening at one end of the column is presented. Thus, the SDR corresponding to 0.5% normalized axial shortening is defined as the critical SDR. Figure 8.1(b) shows that this critical SDR usually corresponded to the peak strength of the column.

It is understandable because a rapid strength degradation was usually also accompanied by a rapid increase of axial shortening.

It was reported in Chapter 5 that a total of 550 numerically simulated columns were analyzed under cyclic loading. The majority of these models experienced the deep-column phenomenon. By applying the above 0.5% axial shortening criterion, the critical SDR ratios were determined. A multivariate regression analysis was then performed, which resulted in the following expression with a standard deviation 0.20:

$$SDR_{cr} = 15.14\lambda_w^{-0.96}\left(1 - \frac{P_u}{P_y}\right)^{2.35} F_y^{-0.68} \tag{8.1}$$

Test and numerical results suggest that axial shortening increases with the presence of web buckling and the regression Eqn. (8.1) confirms this observation. For the purpose of deriving a highly ductile limit (λ_{hd}) for λ_w that has a form similar to the one in AISC 341, the exponents for λ_w and F_y Eq. (8.1) were fixed to –1 and –0.5, respectively. The revised expression after another regression give the following expression with a standard deviation of 0.23:

$$SDR_{cr} = 10.96\lambda_w^{-1}\left(1 - \frac{P_u}{P_y}\right)^{2} F_y^{-0.5} \tag{8.2}$$

For moment connection prequalification testing, Chapter K of AISC 341 requires a story drift capacity of 0.04 rad for SMF design (0.02 rad for IMF) design. Therefore, the limiting λ_w can be solved from the above equation by setting the left side to 0.04. This is valid if columns in the first story have fixed-fixed boundary condition. But this not the case for a typical moment frame. It was shown in Chapter 4 that the story drift capacity is larger when the top end of the column can rotate. Furthermore, the story drift capacity would

increase when the axial compression is not constant; using a near-fault type loading protocol would also increase the story drift capacity. Therefore, the SDR on the left-hand side of Eq. (8.2) needs to be adjusted as follows:

$$(SDR_{cr})_e = \frac{0.04}{\gamma} \tag{8.3a}$$

where the modifying factor, γ, is composed of four components:

$$\gamma = \gamma_s \gamma_b \gamma_l \gamma_a \tag{8.3b}$$

where

γ_s = system factor = $\begin{cases} 1 \text{ for SMF} \\ 2 \text{ for IMF} \end{cases}$

γ_b = boundary condition factor

γ_l = lateral loading sequence factor

γ_a = Axial force factor.

Boundary Condition Factor, γ_b

Consider the column shown in Figure 8.2. For an elastic column, the moment at the base can be computed as follows:

$$M_B = \frac{2EI}{L}(2\theta_A + \theta_B - 3\psi) \tag{8.4a}$$

where the clockwise rotation has a positive sign. For a fixed-fixed boundary condition, $\theta_A = \theta_B = 0$, $\psi = \frac{\Delta}{L} = SDR$, and the base moment is

$$M_B = \frac{-6EI}{L} SDR \tag{8.4b}$$

When the top end of the column is allowed to rotate, express the top end rotation at point A as a fraction of *SDR*:

$$\theta_A = \rho(SDR) \tag{8.5}$$

The base moment is

$$M_B = \frac{2EI}{L}[\rho(SDA) - 3SDR]$$

$$= \frac{-6EI}{L}\left[\left(1 - \frac{\rho}{3}\right)SDA\right] \tag{8.6}$$

The above case is equivalent to a fixed-fixed boundary condition but with an effective SDR of

$$(SDR)_e = \left(1 - \frac{\rho}{3}\right)SDR \tag{8.7}$$

Some test specimens reported in Chapter 4 with a flexible end had a value of ρ equal to 1.0. The effective SDR is 2/3 that of the fixed-fixed case. This relation is valid in the elastic region

Three pairs of specimens were tested with fixed-fixed and fixed-flexible boundary conditions. Figure 8.3 shows the critical SDR as defined previously; the values of SDR_{cr} are also listed in Table 8.1. When the top end was allowed to rotate, the critical SDR when the axial shortening reached 0.5% of the column height was increased. The ratios were 1.18 (1H and 11H-BC pair), 1.27 (13M and 13M-BC pair), and 1.24 (16M and 16M-BC pair), with an average of 1.23. Round this value to the following for γ_b:

$$\gamma_b = 1.25 \tag{8.8}$$

8.2.2 Lateral Loading Sequence Factor, γ_l

Specimens 2M and 8M reported in Chapter 4 were used to evaluate the lateral loading sequence effect. Specimen 2M was loaded with the AISC loading sequence and the critical SDR was 1.62%. With the near-field loading sequence, Specimens 8M had a much larger critical SDR (5.00%). When subjected to an actual earthquake, the response curve of the columns in a moment frame is likely to be bounded like that shown in Figure 8.4. If the average critical SDR (= 3.31%) is used, it is about twice the critical SDR (1.62%) for the AISC loading sequence case. Since it is uncertain what represents the realistic backbone curve, a conservative value of 1.33 instead of 2.0 was assumed for γ_l.

$$\gamma_l = 1.33 \tag{8.9}$$

8.2.3 Axial Loading History Effect, γ_a

As shown in Figure 8.5, responses from two specimens (1H and 11H-VA) can be used to evaluate the effect of varying axial load on the critical SDR. Specimen 1H was subjected to a constant axial compression, while Specimen 11H-VA was subjected to a varying axial load. Since local buckling was delayed, critical SDR for the latter case was larger. The effect of the varying axial load on the critical SDR can also be observed from the backbone curves of three numerically simulated columns in Figure 8.6. More research is needed to evaluate the varying axial load effect for interior columns. For interior columns, the value of γ_a is taken as 1.0.

$$\gamma_a = 1.0 \tag{8.10}$$

8.3 Proposed Web Slenderness Ratios

Based on the information provided above, the value of γ for SMF equals 1.6625 (3.325 for IMF). Based on Eq. (8.3), the value of $(SDR_{cr})_e$ equals 0.024 rad. for SMF (0.012 rad. for IMF). Equating this value to Eq. (8.2):

$$0.024 = 10.96\lambda_w^{-1}\left(1 - \frac{P_u}{P_y}\right)^2 F_y^{-0.5} \tag{8.11}$$

Substituting P_u/P_y for C_a, the resulting λ_w, which is defined as λ_{hd} per AISC 341, is

$$\lambda_{hd} = 2.68(1 - C_a)^2\sqrt{\frac{E}{F_y}} \tag{8.12}$$

For IMF, the λ_{md} is

$$\lambda_{md} = 5.36(1 - C_a)^2\sqrt{\frac{E}{F_y}} \tag{8.13}$$

Figure 8.7 shows the impact of the proposed web slenderness limits; the impact is more to SMF than IMF columns. Also, the impact is much more significant at higher axial force level. Figure 8.8 shows the impact of the proposed web slenderness limits on the available W-shapes in the AISC Steel Construction Manual; for comparison purposes, the limits based on AISC 341 (2010b) are also shown. Note that many deep sections with narrower flanges are disqualified for use in SMF design.

To check the accuracy of the proposed web slenderness limits, Figure 8.9 shows the axial shortening of four tested columns. The web slenderness ratios of Specimens 4L and 14L exceeded the proposed λ_{hd} value, and, therefore, it is expected to see an axial shortening larger than 0.5% of the column length at each end at an effective SDR of 0.024 rad. This is indeed the case as shown in Figure 8.9(b) and (c). On the other hand, since

Specimens 1L and 2L satisfy the proposed web slenderness limit, Figure 8.9(d) and (e) show that the axial shortening is limited when the SDR reaches 0.024 rad.

8.4 Limitations of Proposed Web Slenderness Limits

The above limiting ratios should be applied with limitations. To assure adequate ductility in compression members with plastic hinges, for plastic design the design strength in compression should not exceed $0.75P_y$ per AISC 360 (2010c). This plastic analysis requirement does not include the cyclic loading effect. For cyclically loaded columns, this limit is too relaxed. It is suggested that the C_a value be limited to 0.5, a value similar to that specified in ASCE 41 (ASCE 2013) to distinguish between the deformation-controlled and force-controlled columns.

Figure 8.10 and Figure 8.11 show the effect of member slenderness ratio, L/r_y, on the buckling mode of W24×55 and W24×104 column. Note that the fixed-fixed boundary condition provides a more critical, and hence conservative, situation for establishing the upper bound L/r_y value beyond which global member buckling is more likely to occur. Both experimental and numerical studies showed that the member slenderness did not significantly affect the column cyclic response as long as the ratio was not higher than 120. Since AISC 341 does not provides a limit on L/r_y, the following is recommended:

$$\frac{L}{r_y} \leq 120 \tag{8.14}$$

Table 8.1 Critical SDR for Deep Column Test Specimens

Specimen No.	SDR_{cr} (×0.01 rad)
1H	1.34
11H-BC	1.58
11H-VA	1.92
13M	1.26
13M-BC	1.60
16M	2.12
16M-BC	2.63
2M	1.62
8M	5.00

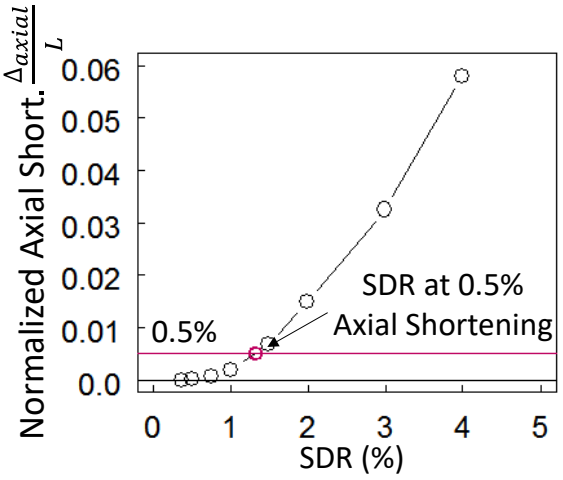

(a) Axial Shortening vs. SDR

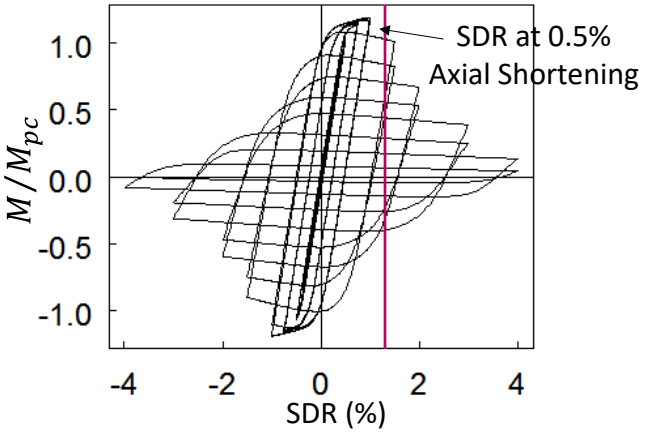

(b) Moment-Rotation Curve

Figure 8.1 Critical Story Drift Ratio

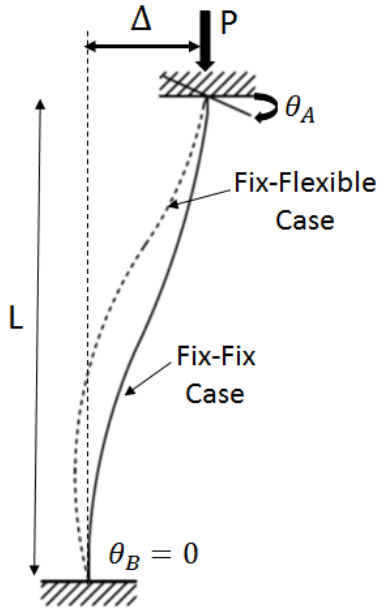

Figure 8.2 Rotation at Column Top

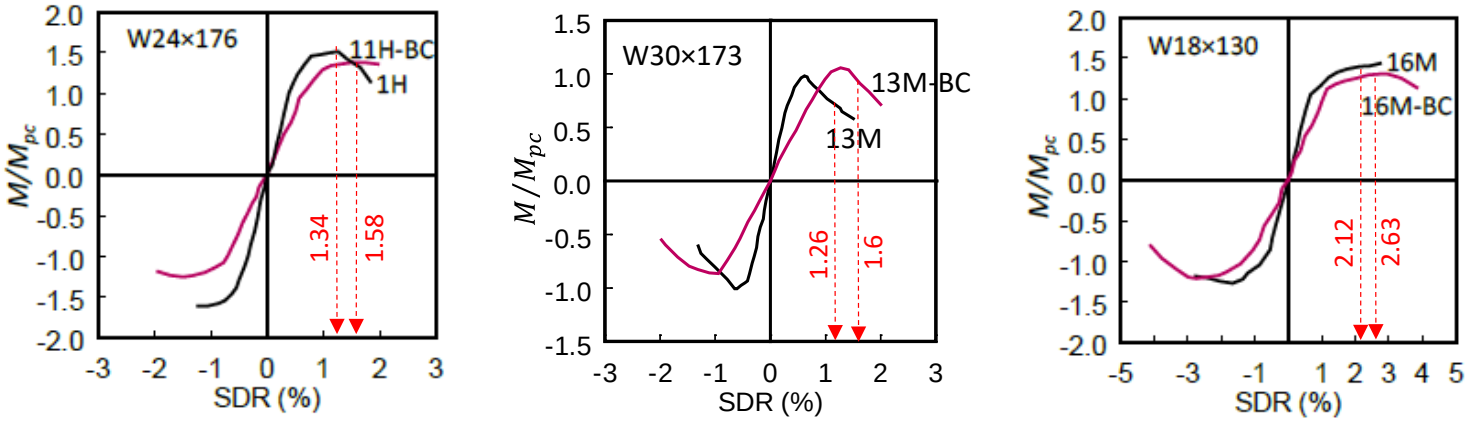

(a) Backbone Curves

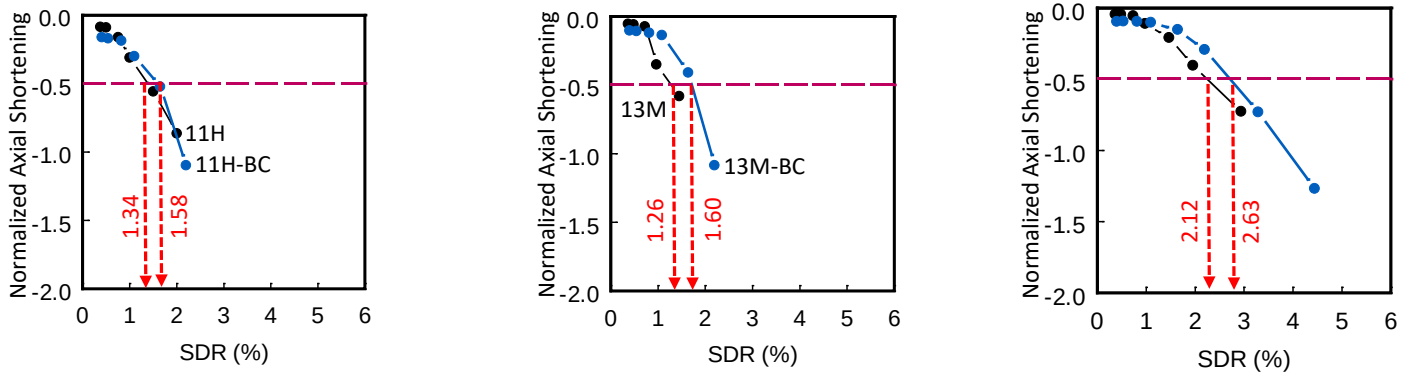

(b) Axial Shortening vs. SDR

Figure 8.3 Boundary Condition Effect

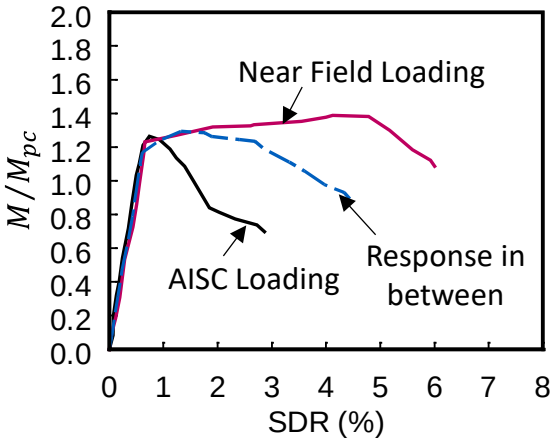

Figure 8.4 Lateral Loading Sequence Effect

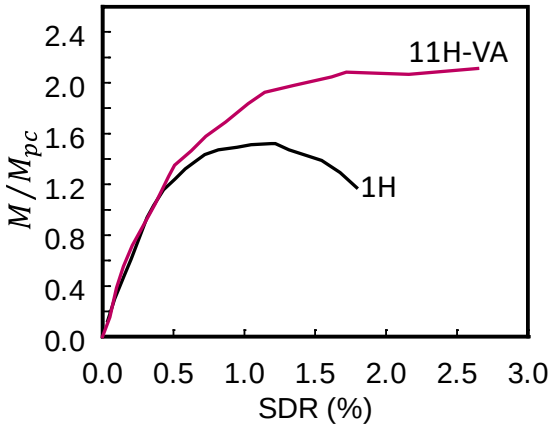

Figure 8.5 Axial Loading History Effect on Test Specimens (W24×176)

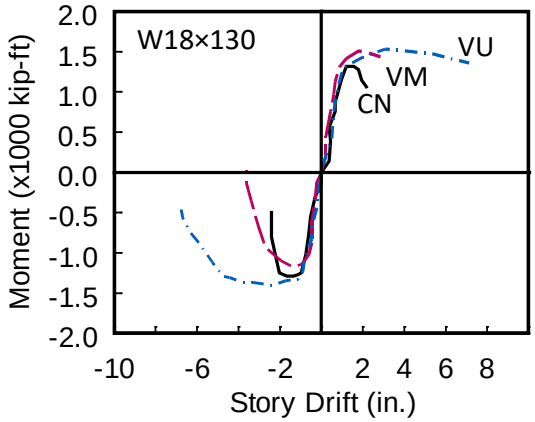

(a) Backbone Curves

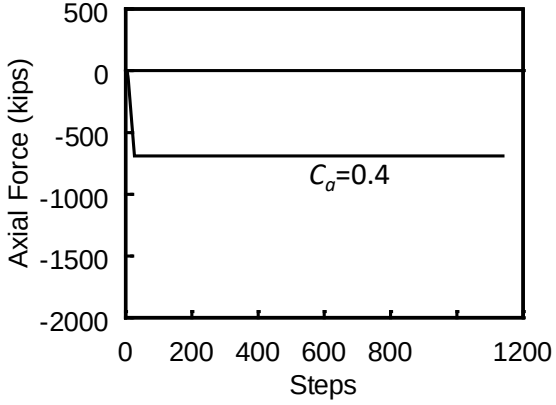

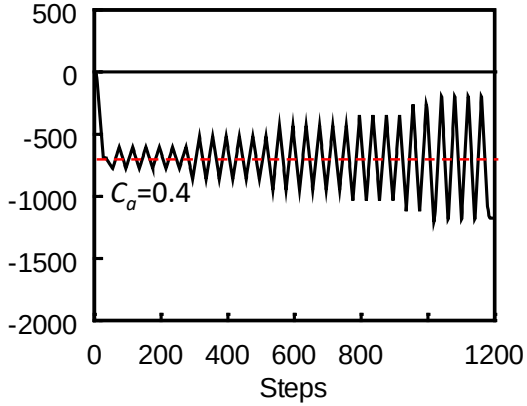

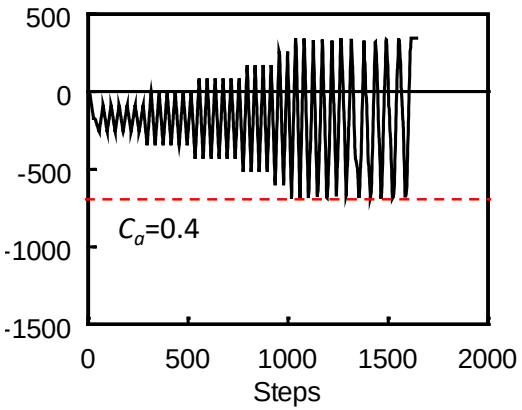

(b) Constant Axial Force (c) Varying Axial Load (+0.1/+0.7%) (d) Varying Axial Load (-0.2/+0.7%)

Figure 8.6 Axial Loading History Effect on Numerically Simulated Columns (W18×130)

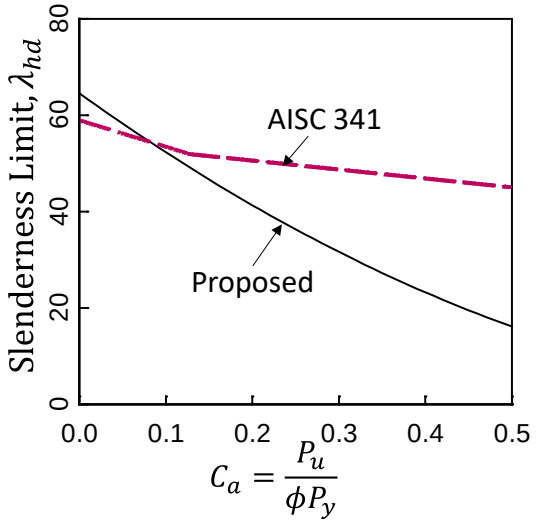

(a) SMF

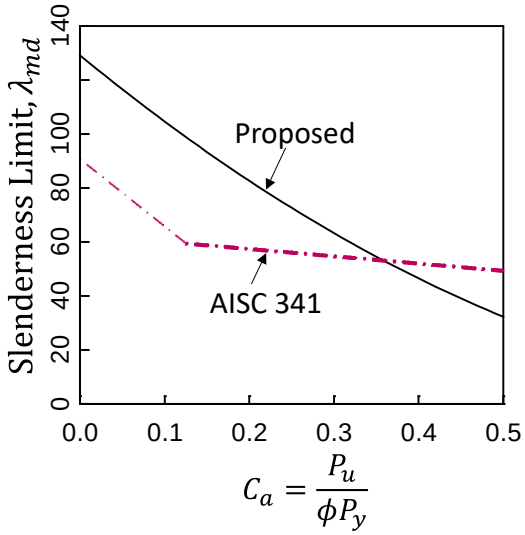

(b) IMF

Figure 8.7 Proposed and AISC 341 Web Slenderness Limits

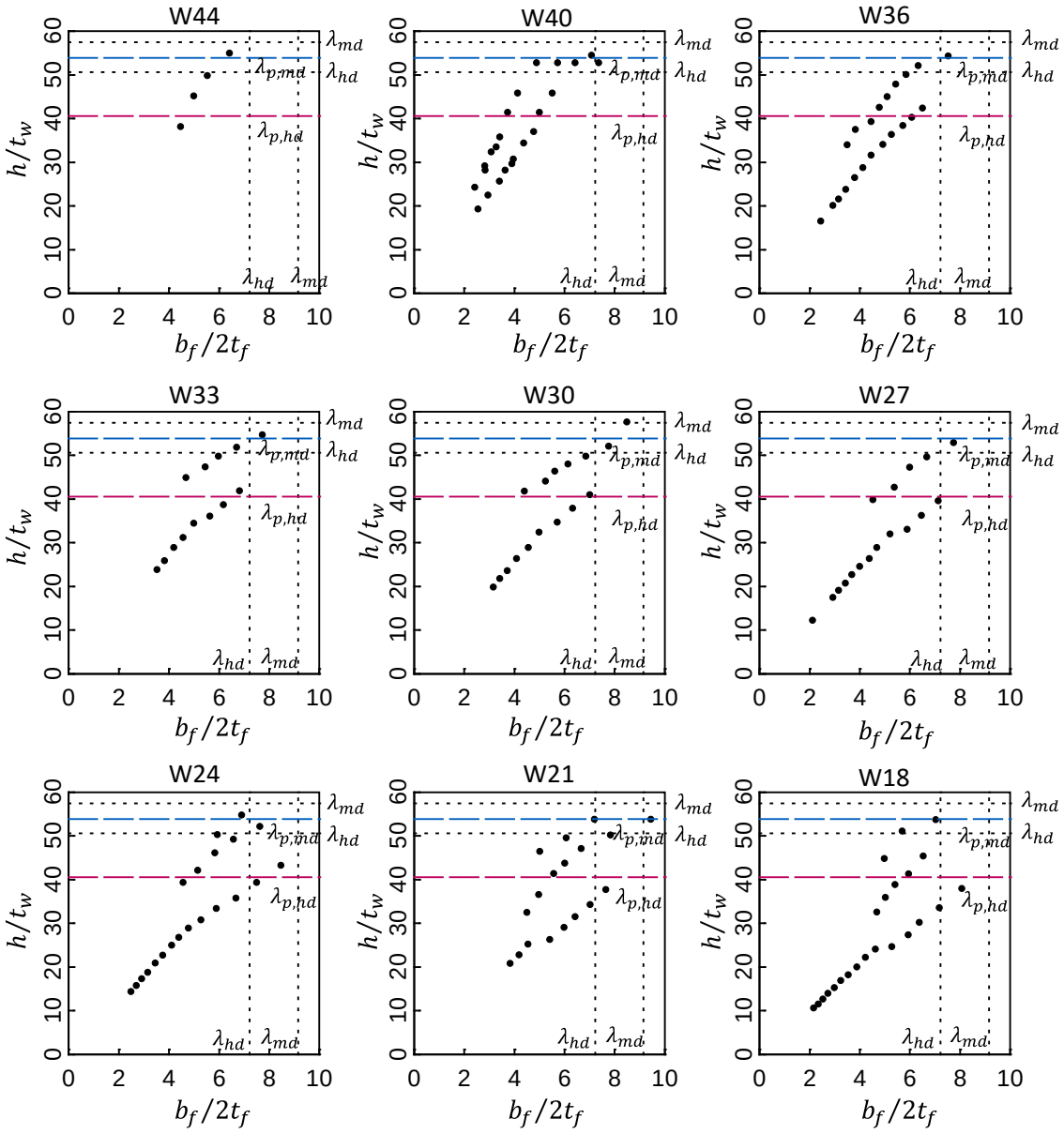

Figure 8.8 Impact of Proposed Web Slenderness Limits on Section Selection (C_a= 0.2)

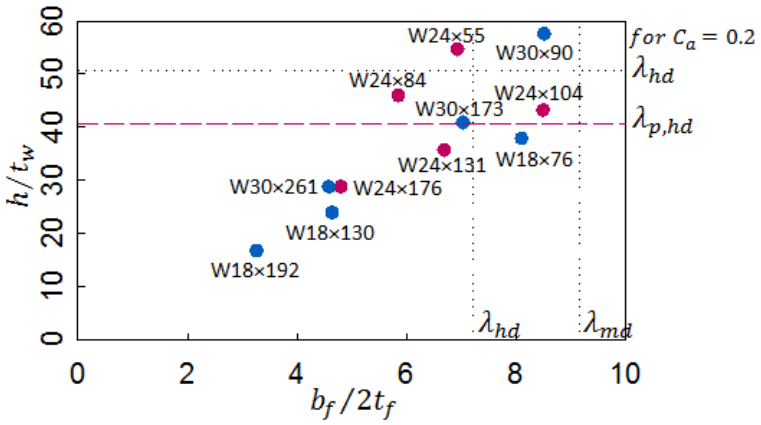

(a) AISC width-to-thickness ratio with proposed web slenderness limits

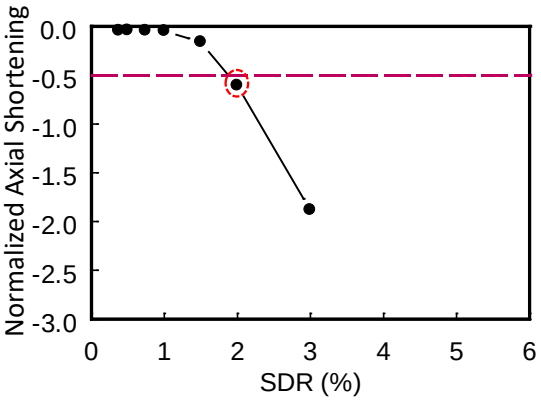

(b) Specimen 4L (W24×84)

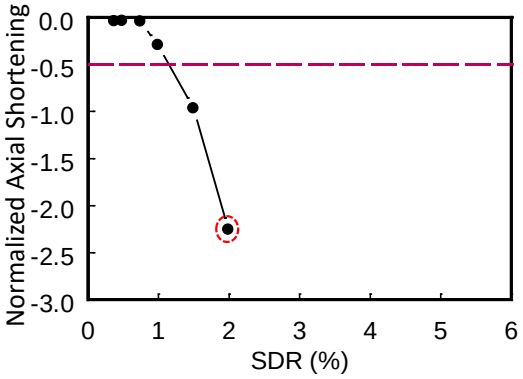

(c) Specimen 14L (W30×90)

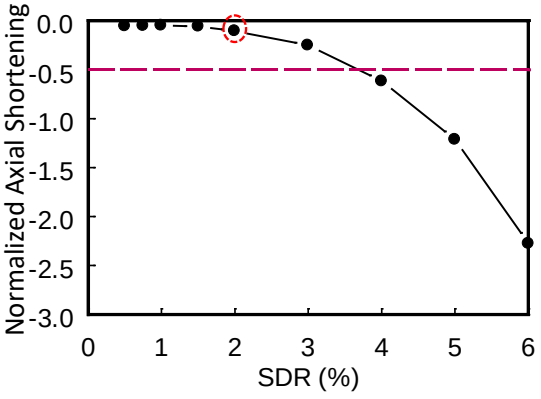

(d) Specimen 1L (W24×176)

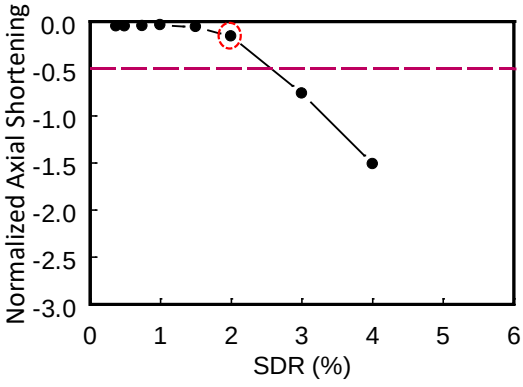

(e) Specimen 2L (W24×131)

Figure 8.9 Validation of Proposed Web Slenderness

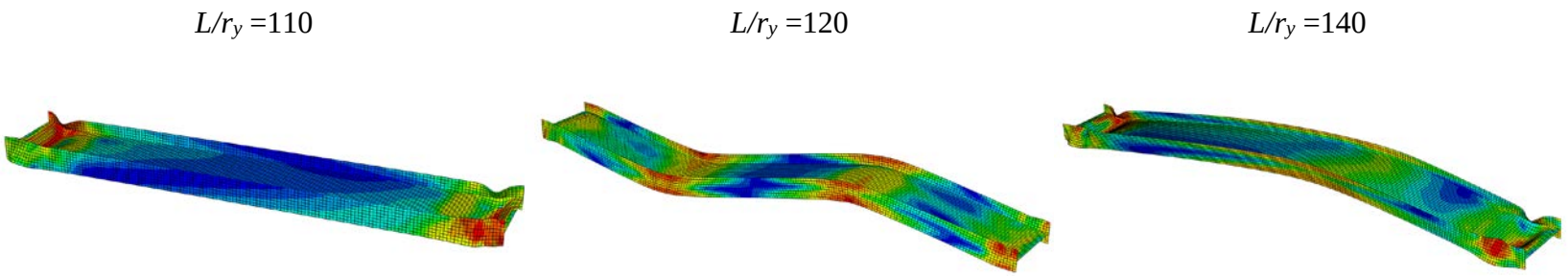

(a) Fixed-fixed Boundary Condition

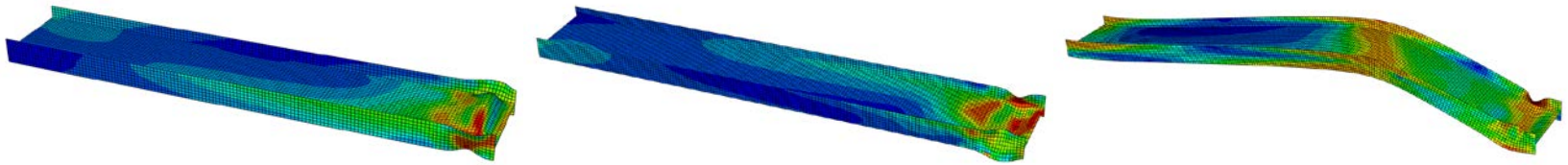

(b) Fixed-flexible Boundary Condition

Figure 8.10 Member Slenderness Limits (W24×55)

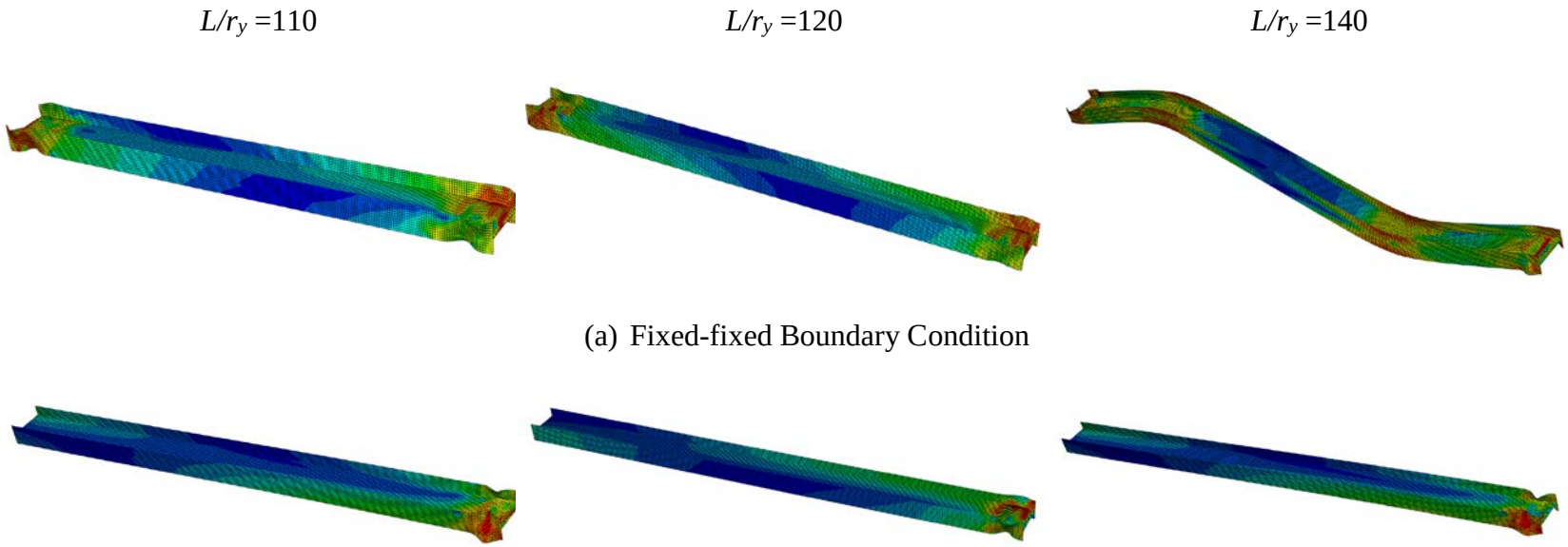

(a) Fixed-fixed Boundary Condition

(b) Fix-flexible Boundary Condition

Figure 8.11 Member Slenderness Limits (W24×104)

9 SUMMARY AND CONCLUSIONS

9.1 Summary

The response and design of steel wide-flange beam-columns are governed by local buckling and global buckling. The vulnerability for local buckling is measured by the width-thickness ratio of λ_f (= $b_f/2t_f$, where b_f = flange width, and t_f = flange thickness) for flange local buckling (FLB) and λ_w (= h/t_w, where h = web height, and t_w= web thickness) for web local buckling (WLB); the global buckling [either flexural buckling or lateral-torsional buckling (LTB)] is measured by λ_L (= L/r_y, where L is the column length, and r_y is the radius of gyration about the weak-axis). Research on the cyclic behavior of shallow columns (e.g., W14 columns with a nominal depth of 14 in.) under axial compression and cyclic drift for braced frame applications has been conducted in an AISC-sponsored research project (Newell and Uang 2008). FLB governed the response of these columns, and the hysteretic response was very stable even under high axial compression. But limited numerical simulation of deeper columns (e.g., W27 columns) showed a much less ductile response with a significant strength degradation due to local buckling.

Deep columns are preferred by designers for Special Moment Frame (SMF) applications in high seismic regions because, to meet the story drift requirement specified in ASCE 7 (ASCE 2013), the large moment of inertia about the strong-axis will result in lighter and more economical sections for the columns. Since deep sections have larger λ_f and λ_w values for both flanges and web as well as a larger λ_L value, they are prone to both local buckling and out-of-plane (LTB) when subjected to both axial compression and cyclic bending. Since first-story columns in an SMF are expected to form plastic hinges during a significant seismic event, yet research on deep columns was very limited, NIST

developed a comprehensive research plan to study the seismic behavior and design of deep, slender wide-flange structural steel beam-columns (NIST 2013). The plan included studies at the member, subassemblage, and system levels. This research project addresses the cyclic behavior, modeling, and design of deep columns at the member level.

Thirty-seven full-scale deep columns were tested in two phases of this NIST-sponsored research. Cyclic testing showed that these columns would experience significant buckling and axial shortening even though the cross sections of these columns met the highly ductile (λ_{hd}) requirement specified in the AISC Seismic Provisions, or AISC 341 (AISC 2010b), for use in SMF. Significant shortening occurred because WLB interacted with FLB; such interaction was not considered in AISC 341. Significant shortening of the columns was also not observed in testing shallow and stocky W14 columns (Newell and Uang 2008) because WLB did not occur. One "unexpected" failure mode involving both local buckling and LTB was also observed in some column tests. To enhance the database for both cyclic modeling and design recommendation, a parametric study of 110 beam-columns that covered a wide range of slenderness ratios, axial force levels, and yield stresses with high-fidelity ABAQUS nonlinear finite element simulation was also conducted.

Results from both tests and numerical simulation were then used for the following three tasks. Since a variety of failure modes were observed, the first task was to develop a practical procedure that designers can use to identify the governing buckling mode; a total of three major buckling modes were proposed. For using in ASCE 41-type (ASCE 2013) performance-based simulation of SMF seismic response, the second task was to develop backbone curves (both cyclic and monotonic loading) for each of the buckling mode.

Significant shortening was consistently observed from both tests and numerical simulation in deep columns, although these column sections met the AISC 341 highly ductile requirement. To avoid this undesirable failure mode, a novel approach that used column shortening as the limit state was developed and used to derive a limiting column web slenderness ratio for potential adoption by AISC 341.

9.2 Conclusions

Based on the test results of thirty-seven deep column specimens with axial compression and cyclic drift, the following conclusions can be made.

(1) The slenderness ratios (λ_f and λ_w) for local buckling had a significant effect on the buckling mode (local versus global buckling) as long as the member slenderness (λ_L) is less than 120. The level of axial load significantly affected the plastic rotation capacity. The presence of an axial compression produced significant local buckling and axial shortening.

(2) Using a very compact section with low width-to-thickness ratios can change the failure mode from local buckling to LTB. Such change was due to a more significant strain hardening, which lengthened the yielded length and triggered LTB. Similarly, a column that experienced LTB under cyclic loading may not have the same matter under monotonic loading due to a lack of cyclic hardening.

(3) Wide-flange sections with similar flange and web slenderness ratios performed correspondingly regardless of difference in nominal depths.

(4) Columns with the top end allowed to rotate performed better than those with fixed-fixed boundary condition.

(5) Near-fault loading was found to be less damaging in terms of energy dissipation demand and column axial shortening, although the residual drift could be larger.

(6) The majority of tests conducted in this research project was for interior first-story columns, where the column axial load remained more or less constant. Cyclic testing with varying axial load for exterior columns showed that the performance was improved.

(7) Specimens with weak-axis bending were very ductile, showing little local buckling up to a very high drift level. Biaxial bending tended to cause more severe local buckling and a more rapid degradation in strength.

The following conclusion can be made on numerical simulation using nonlinear finite element analysis.

(8) With kinematic and isotropic hardening properly calibrated with cyclic coupon test results, nonlinear finite element simulation that considered large deformations could reliably predict the cyclic response and buckling mode.

The following conclusions can be made on the classification of cyclic buckling mode and a proposed procedure to identify governing buckling mode.

(9) Combining the findings from both AISC- and NIST-sponsored test programs, three governing buckling modes were identified: symmetric flange buckling (SFB), anti-symmetric local buckling (ALB), and coupled buckling (CB).

(10) SFB would develop in shallow and stocky columns where the web has a low λ_w ratio to stabilize flanges. Deep columns would buckle in either ALB or CB mode. Shallow columns with a narrow flange width would also behave like a deep column. The ζ parameter [see Eq. (6.15)] can be used to identify the governing buckling mode.

The following conclusions can be made on the development of backbone curves.

(11) Researchers have been using database with available column test data to develop cyclic backbone curves (Elkady and Lignos, 2017, Bech et al., 2017) This research clearly shows that the column cyclic response would be affected by the governing buckling mode, which in turn is a function of the section slenderness ratios. Therefore, expressions that define the key parameters for the monotonic and cyclic backbone curves for each of the three buckling modes were developed separately in this research (see Chapter 7).

(12) Key parameters for the SFB mode are a function λ_w in addition to the yield stress and axial force level. Both λ_w and λ_f play a role for the parameters in the ALB mode. In addition, λ_L also plays a role for the parameters of CB.

The following conclusions can be made on the development of limiting λ_w ratios to control axial shortening of the columns.

(13) Since columns that met the AISC 341 compactness requirement cannot prevent significant buckling and axial shortening, an approach that used the shortening as the limit states was adopted to derive alternative λ_{hd} limits for both SMF and IMF (Intermediate Moment Frames) for potential adoption by the AISC Seismic Provisions.

(14) A comparison of the ASCE 341 and proposed λ_{hd} limits shows that the current AISC requirement is non-conservative for SMF columns when the axial force level was high (C_a > 0.1). On the other hand, the proposed limit indicates that the AISC requirement is conservative for IMF columns in the low axial force range (C_a < 0.35).

REFERENCES

ABAQUS-FEA/CAE. (2011). Dassault Systemes Simulia Corp., RI.

AISC. (2010a). *Code of standard practice for steel buildings and bridges,* AISC 303-05, American Institute of Steel Construction Chicago, IL.

AISC. (2010b). *Seismic provisions for structural steel buildings,* ANSI/AISC 341-05, American Institute of Steel Construction Chicago, IL.

AISC. (2010c). *Specification for structural steel buildings,* ANSI/AISC 360-05, American Institute of Steel Construction, Chicago, IL.

ASCE. (1971). *Plastic design in steel, A guide and commentary*, Second Edition, American Society of Civil Engineers, New York, NY.

ASCE. (2010). *Minimum design loads for buildings and other structures,* ASCE 7, American Society of Civil Engineers, Reston, VA.

ASCE. (2013). *Seismic rehabilitation of existing buildings,* ASCE 41, American Society of Civil Engineers, Reston, VA.

ASTM. (2003). *Standard definitions of terms relating to constant- amplitude low-cycle fatigue testing*, ASTM Standard E466.

Auger, K., Balazadeh-Minouei Y., Elkady, A., Imanpur, A., Leclerc., M., Lignos, D., Toutant., G., and Tremblay, R. (2016). "Multi-directional structural component hybrid testing system for the assessment of the seismic response of steel I-shaped columns," *Proc., 11th Pacific Structural Steel Conference*, Shanghai, China.

Bertero, V., Popov, E., and Krawinkler, H. (1972). "Beam-column subassemblages under repeated loading," *Journal of the Structural Division*, ASCE, Vol. 98, No. ST5, 1137-1159.

Bech, D., Tremayne, B., and Houston, J. (2015). "Proposed changes to steel column evaluation criteria for existing buildings." *Proc., 2nd ATC-SEI Conference on Improving the Seismic Performance of Existing Building and Other Structures*, San Francisco, CA, USA.

Black, C., Makris, N., and Aiken, I. (2002). "Component testing, stability analysis and characterization of buckling restrained braces," *Report No. PEER-2002/08*, Pacific Earthquake Engineering Research Center, University of California, Berkeley, CA.

Bjorhovde, R., Galambos, T., and Ravindra, K. (1978). "LRFD criteria for steel beam-columns." *Journal of the Structural Division*, ASCE, Vol. 104, No. ST9, 1371-1387.

Clark, P., Frank, K., Krawinkler, H., and Shaw, R. (1997). "Protocol for fabrication, inspection, testing, and documentation of beam-column connection tests and other experimental specimens." *SAC Joint Venture.*

Chaboche, J.L. (1986). "Time-independent constitutive theories for cyclic plasticity." *International Journal of Plasticity*, Vol. 2, 149-188.

Cheng, X., Chen, Y., and Nethercot, D.A. (2013). "Experimental study on H-shaped steel beam-columns with large width-thickness ratios under cyclic bending about weak-axis." Engineering Structures, 49, 264-274.

Chi, B., Uang, C.-M. (2002). "Cyclic response and design recommendations of reduced beam section moment connections with deep columns." *Journal of Structural Engineering*, 128(4), 464-473.

Elkady, A., and Lignos, D.. (2012). "Dynamic stability of deep slender columns as part of special MRFs designed in seismic regions: finite element modeling." *Proc., 1st Inernational Conference on Performance-Based and Life-Cycle Structural Engineering (PLSE)*, Hong Kong, China.

Elkady, A., and Lignos, D.G. (2013). "Collapse assessment special steel moment resisting frames designed with deep members." *Proc. Vienna Congress on Recent Advantages in Earthquake Engineering and Structural Dynamics (VEESD)*, Vienna, Austria.

Elkady, A., and Lignos, D. G. (2014). "Modelling of the composite action in fully restrained beam-to-column connections: Implications in the seismic design and collapse capacity of steel special moment frames. " *Earthquake Engineering & Structural Dynamics,* 43(13), 1935-1954.

FEMA. (2000a). *Prestandard and commentary for the seismic rehabilitation of buildings*, FEMA 356, Federal Emergency Management Agency, Washington D.C.

FEMA. (2000b). *Recommended seismic design criteria for new steel moment-frame buildings*, FEMA 350, Federal Emergency Management Agency, Washington D.C.

FEMA. (2000c). *State of the art report on system performance of steel moment frames subject to earthquake ground shaking*, FEMA 355C, Federal Emergency

Management Agency, Washington D.C.

FEMA. (2009) *Qualification of building seismic performance factors*, FEMA P-695, Federal Emergency Management Agency, Washington D.C.

Fogarty, J., and El-Tawil, S. (2016). "Collapse resistance of steel columns under combined axial and lateral loading", *Journal of Structural Engineering*, Vol. 142, No. 1, ASCE.

Freund. R., Wilson, W., and Sa, P. (2006). *Regression analysis*, Second Edition, Elsevier Inc., Oxford, UK.

Galambos, T.V. (1964). "Combine bending and compression." Structural Steel Design, Ronald Press, New York.

Galambos, T.V. (1968). "Deformation and energy absorption capacity of steel structures in the inelastic range." *Bulletin No.8*, American Iron and Steel Institute, New York, NY.

Galambos, T. (1998). *Guide to stability design criteria for metal structures*, Fifth Edition, John Willey & Sons, Inc., New York, NY.

Haaijer, G., and Thurlimann, B. (1960). "On inelastic buckling in steel." Trans. ASCE, 124, 60-2. *American Iron and Steel Institute*, No. 8.

Han, K.-H., and Lee, C.-H. (2016). "Elastic flange local buckling of I-shaped beams considering effect of web restraint," *Thin-walled Structures*, Vol. 105, 101-111, Elsevier.

Ibarra, L.F., Medina, R.A., and Krawinkler H. (2005). "Hysteretic models that incorporate strength and stiffness deterioration," *Earthquake Engineering and Structural Dynamics*, 34:1489-1511.

Jez-Gala, C. (1962). "Residual stresses in rolled I sections." *Proc. Of the Institution of Civil Engineers*, 23(3), 361-378.

Johnson, D.L. (1986). "An investigation into the interaction of flanges and webs in wide flange shapes." *Proc., Stability Aspects of Industrial Buildings*, April 16-17, 397-405.

Kaufmann, E.J., Metrovich, B., and Pense, A.W. (2001). "Characterization of cyclic inelastic strain behavior on properties of A572 Gr. 50 and A913 Gr. 50 rolled sections." *Report No. 01-13* National Center for Engineering Research, Advanced Technology for Large Structural Systems.

Kemp, A.R. (1985). "Interaction of plastic local and lateral buckling." *Journal of Structural Engineering*, ASCE, 111(10), 2181-2196.

Kemp, A.R. (1996). "Inelastic local and lateral buckling in design codes." Journal of Structural Engineering, 122(4), 374-382.

Kimura, Y., and MacRae, G. (2004). "Effect of cantilever column flexural characteristic on braced frame displacements." *13th Word Conference in Earthquake Engineering*, August-1, 2004, Vancouver, Canada.

Krawinkler, H., Zohrei, M., Lashkari-Ivani, B., Cofie, N., and Hadidi-Tamjed, H. (1983). "Recommendations for experimental studies on the seismic behavior of steel components and materials." *Report No. 61*, Department of Civil Engineering, Stanford University, Stanford, CA.

Krawinkler, H. (1996). "Cyclic loading histories for seismic experimentation on structural components." *Earthquake Spectra*, 12(1).

Krawinkler, H., Gupta, A., Medina, R. and Luco, N. (2000). "Loading histories for seismic performance testing of SMRF components and assemblies." *Report No. SAC/BD-00/10. SAC Joint Venue*, Sacramento, CA.

Krawinkler, H. (2009). "Loading histories for cyclic tests in support of performance assessment of structural components." *Pacific Earthquake Engineering Research Center Annual Conference*. San Francisco, California: PEER.

Krawinkler, H., Zareian, F., Lignos, D.G., and Ibarra L.F. (2010). "Significance of modeling deterioration in structural components for predicting the collapse potential of structures under earthquake excitation." *Advanced in Performance-Based Earthquake Engineering*, 1007/978-90-481-8746-1.

Lamarche, C.P., and Tremblay, R. (2011). "Seismically induced cyclic buckling of steel columns including residual-stress and strain-rate effects." *Journal of Construction Steel Research*, 67(9), 1401-1410.

Lay, M.G., and Galambos, T.V. (1965). "Inelastic steel beams under uniform moment." *Journal Structural Division*, ASCE, 91(6), 67-94.

Lay, M.G., and Galambos, T.V. (1967). “Inelastic beams under moment gradient.” *Journal Structural Division*, ASCE, 93(1), 381-399.

Lignos, D.G., and Gantes, C.J. (2005). “Design considerations for the effects of near-fault ground motions on steel structures”, *Proc. 5th National Conference on Steel Structures*, Xanthi, Greece.

Lignos, D.G., Krawinkler, H. (2007). “A database in support of modeling of component deterioration for collapse prediction of steel frame structures.” *Structural Engineering Research Frontiers*, ASCE.

Lignos, D.G., Krawinkler, H., Whittaker, S.S., (2008). “Collapse tests of two scale models of a steel frame structure.” *Proc. 6th Network for Earthquake Engineering Simulation Annual Meeting,* Portland, Oregon, June 18-20, 2008.

Lignos, D.G., Krawinkler, H., Zareian, F. (2009). “Modeling of component deterioration for collapse prediction of steel frames.” *Proceedings of 6th International Conference on Behavior of Steel Structures in Seismic Areas, STESSA 2009*, Philadelphia, Pennsylvania, USA.

Lignos, D.G., Krawinkler, H., (2010). “Deterioration modeling of steel components in support of collapse prediction of steel moment frames under earthquake loading.” *Journal of Structural Engineering*, 137(11), 1291-1302.

Luxion, W.W. (1948). “Plastic behavior of WF beams.” *Report No. Fritz Laboratory Reports*, 203.1, 1268.

Nakashima, M., Takanashi, K., and Hiroto K., (1990). “Test of steel beam-columns subject to sidesway.” *Journal of Structural Engineering*, 116(9), 2516-2531.

Nakashima, M., Morino, S., and Koba, S. (1991). “Statistical evaluation of strength of steel beam columns.” *Journal of Structural Engineering*, ASCE, 117(11), 3375-3395.

NEHRP. (2017). “Guidelines for nonlinear structural analysis for design of buildings: part II-a steel moment frames,” *NIST-GCR-11-917-13*, Gaithersburg, MD.

Newell, J.D. and Uang, C.-M. (2006). “Cyclic behavior of steel columns with combined high axial load and drift demand.” *Report No. SSRP-06/22*. Department of Structural Engineering, University of California, San Diego.

Newell, J.D. and Uang, C.-M. (2008). "Cyclic behavior of steel wide-flange columns subjected to large drift," *Journal of Structural Engineering*, Vol. 134, No. 8, 1334-1342, ASCE.

NIST (2011). *Research plan for the study of seismic behavior and design of deep, slender, wide-flange structural steel-beam-column members*. NIST-GCR-11-917-13. Produced by the NEHRP Consultants Joint Venture, a partnership of the Applied Technology Council and the Consortium of Universities for Research in Earthquake Engineering, for the National Institute of Standards and Technology, Gaithersburg, MD.

MacRae, G. (1990). "The seismic response of steel frames." *Report No. 90-6*, Department of Civil Engineering, University of Canterbury, New Zealand.

MacRae, G., Urmson, C.R., Walpole, W.R., Moss, P., Hyde, K., and Cliftoon C. (2009). "Axial shortening of steel columns in buildings subjected to earthquakes." *Bulletin of the New Zealand Society for Earthquake Engineering*, Vol. 42, No. 4, December.

Medina, R. (2003). "Seismic demands for mondeteriorating frame structures and their dependence on ground motions." *Ph.D. Dissertation*, Dept. of Civil and Environmental Engineering, Stanford Univ., Palo Alto, CA.

Okazaki, T., Liu, D., Nakashima, M., and Engelhardt, M. (2006). "Stability requirements for beams in seismic steel moment frames." *Journal of Structural Engineering*, ASCE, 132(9), 1334-1342.

Ozkula, G., and Uang, C.-M. (2015). "Seismic behavior and design of deep, slender wide-flange structural steel beam-column members," *Rep. No. SSRP-15/06*, Department of Structural Engineering, University of California, San Diego, La Jolla, CA.

Ozkula, G., Harris, J., and Uang, C.-M. (2017a). "Observations from cyclic tests on deep, wide-flange beam-columns", *Engineering Journal*, 1st Quarter, AISC, 45-59.

Ozkula, G., Harris, J., and Uang, C.-M. (2017b). "Classifying cyclic buckling modes of steel wide-flange columns under cyclic loading," *Structures Congress*, 155-167, ASCE/SEI, Denver, Colorado.

Peng, B., MacRae, G., Walpole, W., Moss, P., Dhakal R., and Clifton C. (2008). "Plastic hinge location in columns of steel frames subjected to seismic actions." *Bulletin-New Zealand Society for Earthquake Engineering*.

Popov, E., and Pinkney, B. (1969). “Cyclic yield reversal in steel buildings connections.” *Journal of the Structural Division*, ASCE, Vol. 95, No. ST3, 327-353.

Popov, E.P., Bertero, V.V., and Chandramoulli, S., (1975). “Hysteretic behavior of steel columns.” UCB/EERC 75-11, *Earthquake Engineering Research Center*, Richmond, USA.

Popov, E.P., Bertero, V.V., and Chandramouli, S. (1975). “Hysteretic behavior of steel columns.” *Earthquake Engineering Research Center*, University of California.

Popov, E.P. (1983). “Seismic moment connections for moment-resisting steel frames.” *Report No. UCB/EERC-83/02*, University of California, Berkeley, Berkeley, CA.

Salmon, C., and Johnson, J. (2009). *Steel structures: design and behavior, emphasizing load and resistance factor design*, Fourth Edition, HarperCollins Collage Publishers, New York, NY.

Seif, M., and Schafer, B.W. (2010). “Local buckling of structural steel shapes.” *Journal of Constructional Steel Research*, 66, 1232-1247.

Schneider, S.P., Roeder, C.W., Carpenter, J.E. (1993)., “Seismic behavior of moment-resisting steel frames: experimental study”, *Journal of Structural Engineering*, 119(6), 1885-1902.

Spoorenberg, R.C., Snijder, H.H., and Hoenderkamp, J.C.D. (2010). “Experimental investigation of residual stresses in roller bent wide flange steel sections.” *Journal of Constructional Steel Research*, 66, 737-747.

Spoorenberg, R.C., Snijder, H.H., Cajot, L.-G., and May, M.S. (2013). “Experimental investigation on residual stresses in heavy wide flange QST steel sections.” *Journal of Constructional Steel Research*, 89, 63-74.

Suzuki, Y., and Lignos, D.G., (2015). “Large scale collapse experiments of wide flange steel beam-columns.” *8th International Conference on Behavior of Steel Structures in Seismic Areas*, Shanghai, China.

Tebedge, N., Alpsten, G.A., and Tall, L. (1971). “Measurement of residual stresses- a study of methods.” *Report No. 337.8, Fritz Engineering Laboratory*, Lehigh University, Bethlehem, PA.

Tebedge, N., Alpsten, G., and Tall, L. (1973). “Residual-stress measurement by the sectioning method.” *Exp. Mech*, 13:88-96.

Timoshenko, S.P., and Gere, J.M. (1961). *Theory of elastic stability*, Dover Publications, Inc., Mineola, New York.

Uang, C.-M., Fan C.-C. (2001). “Cyclic stability criteria for steel moment connections with reduced beam section.” *Journal of Structural Engineering*, 127(9), 1021-1027.

Uang, C.-M., Ozkula, G., and Harris, J., (2015) “Observations from cyclic tests on deep slender wide-flange steel beam-column members”, *Structural Stability Research Council*, Nashville, Tennessee, USA, March 24-27, 2015.

Wang, Y.-B., Li, G.-Q., and Chen, S.-W. (2012). “Residual stresses in welded flame-cut high strength steel H-sections.” *Journal of Constructional Steel Research*, 79, 159-165.

Weng, C.C., Pekoz, T. (1990). “Residual stresses in cold-formed steel members.” *Journal of Structural Engineering*, ASCE, 116(1), 24-39.

White, M.W. (1956). “The lateral-torsional buckling of yielded structural steel members.” Fritz Engineering Lab., Rep. No. 205 E8, Lehigh University, Bethlehem, PA. `

Yu, Q. S., Gilton, C., and Uang, C.-M., (2000). “Cyclic response of RBS moment connections: loading sequence and lateral bracing effects.” *Report No. SAC/BD-00/22*.

Yura, J.A., Galambos, T.V., and Ravindra, M.S. (1978). “The bending resistance of steel beams.” *Journal of Structural Divisions*, ASCE, 104(9), 1355-1370.

Zeimian, R.D. (2010). *Stability design criteria for metal structures*, John Wiley & Sons, Inc. Hoboken, New Jersey.

APPENDIX A. EXPERIMENTAL TEST RESULTS

A.1 Phase 1: Global Responses and Axial Shortening of Tested Columns

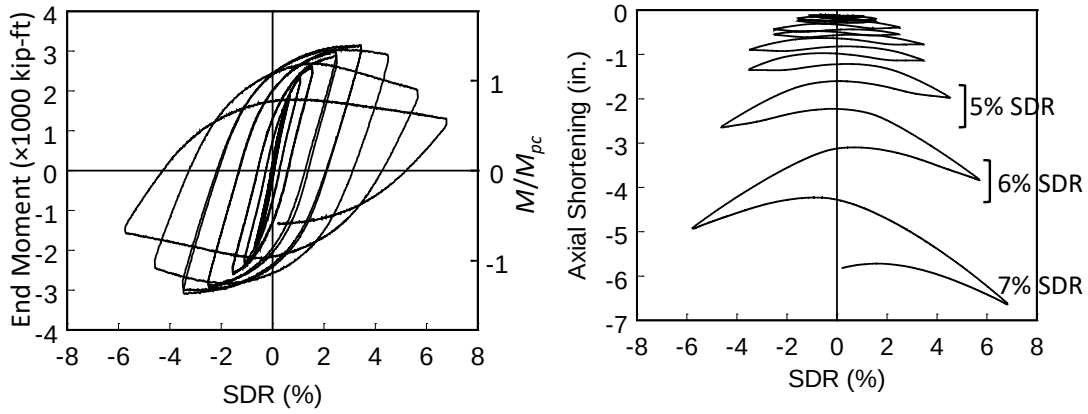

(a) Specimen 1L

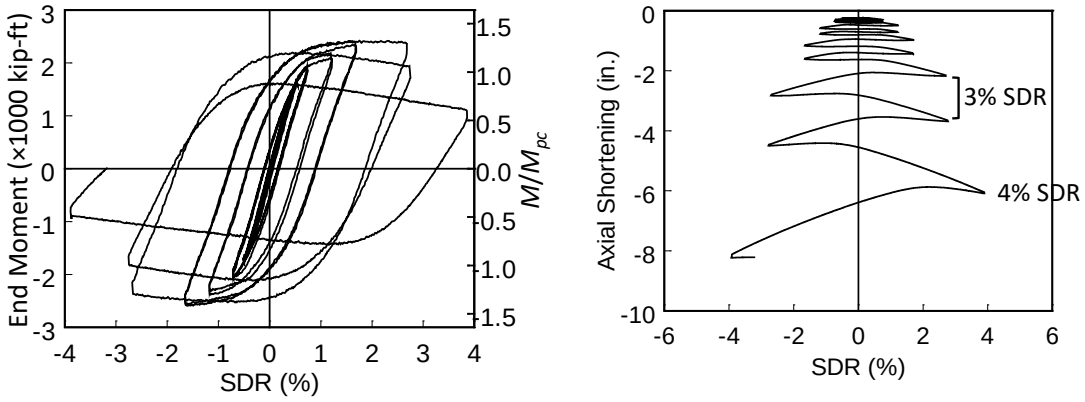

(b) Specimen 1M

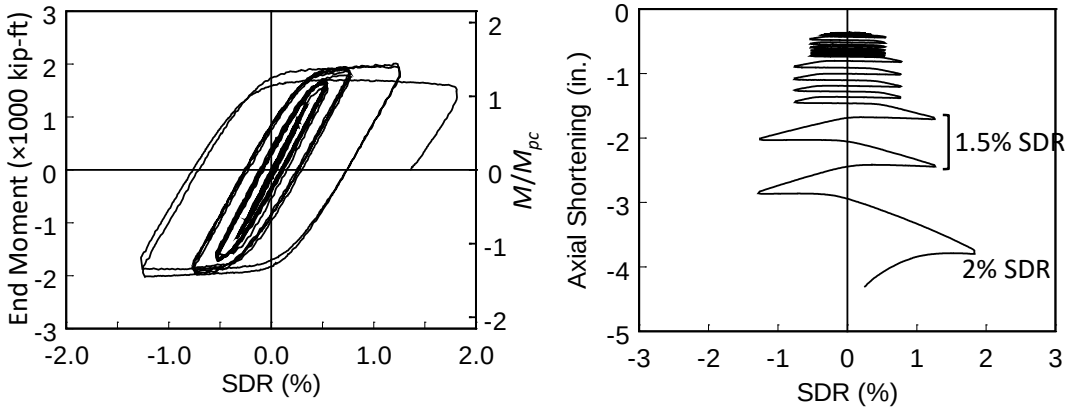

(c) Specimen 1H

Appendix A1 Group 1 Global Response (W24×176)

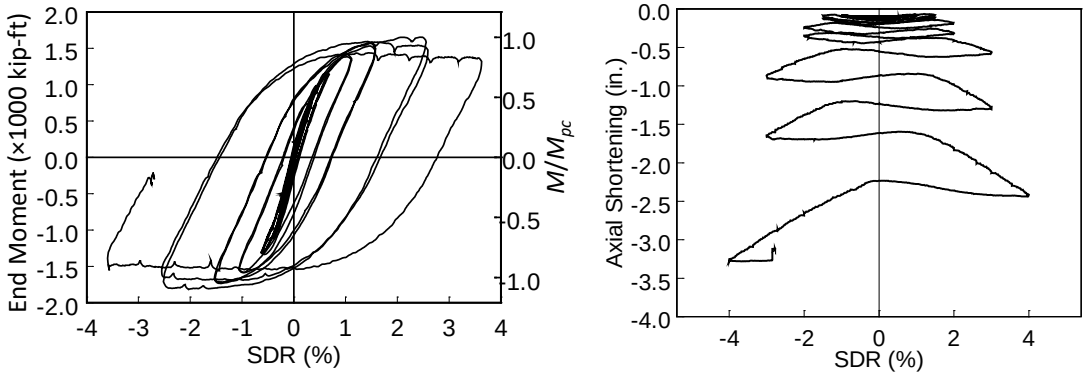

(a) Specimen 2L

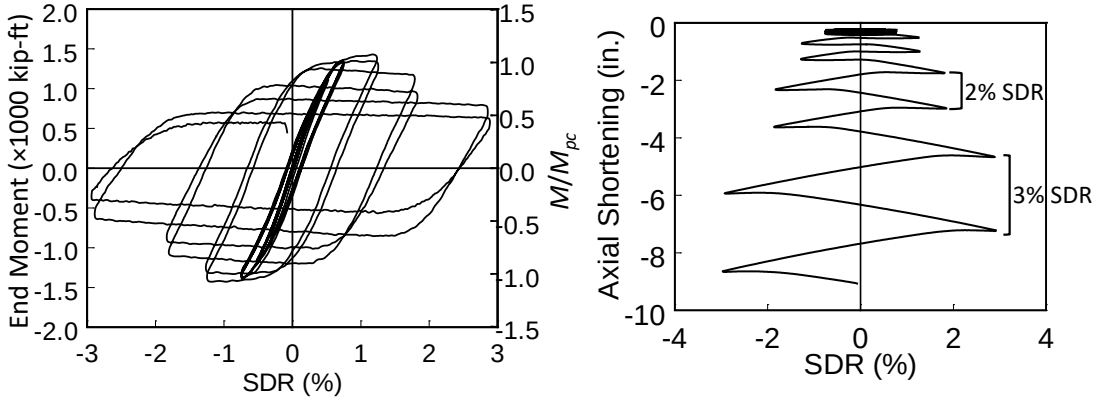

(b) Specimen 2M

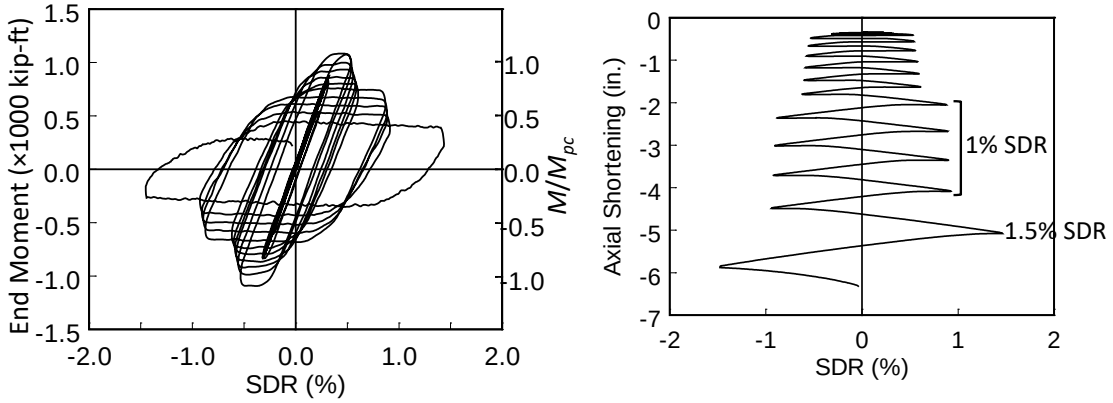

(c) Specimen 2H

Appendix A2 Group 2 Global Response (W24×131)

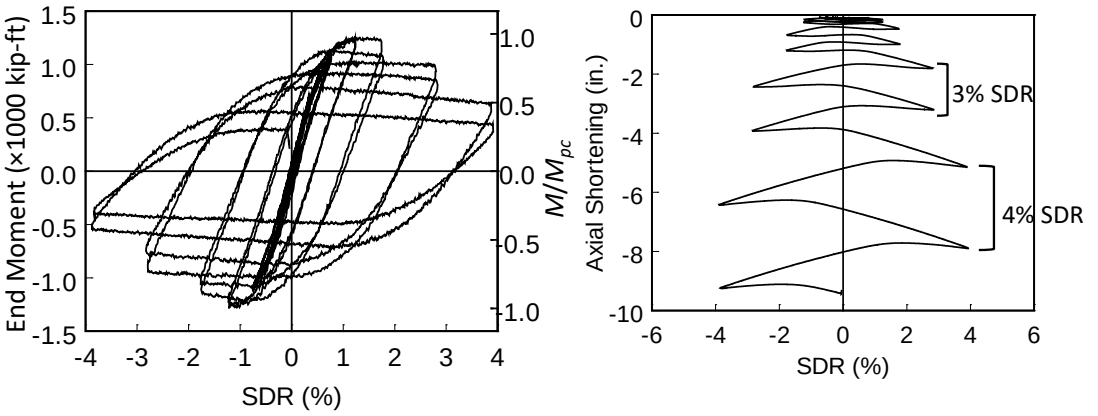

(a) Specimen 3L

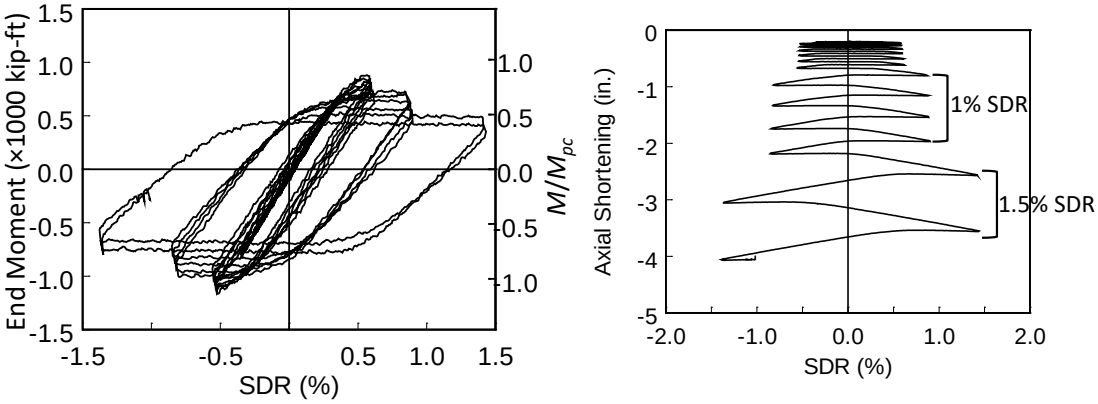

(b) Specimen 3M

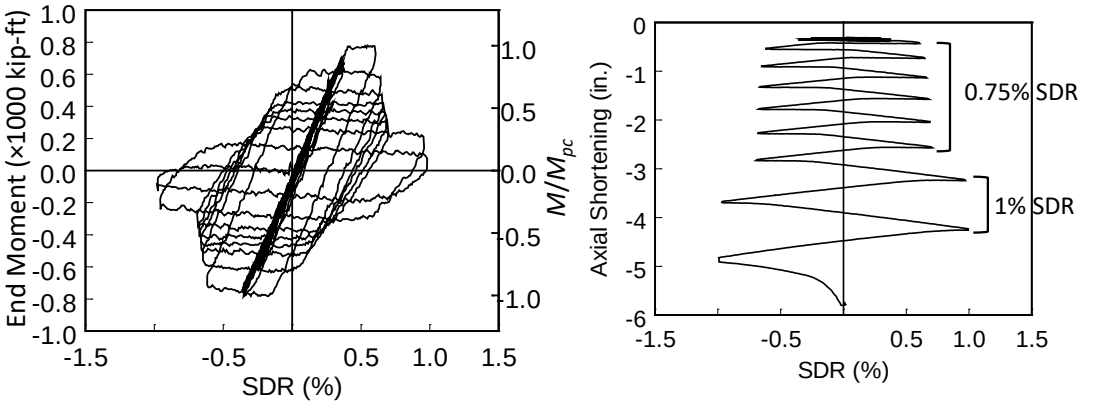

(c) Specimen 3H

Appendix A3 Group 3 Global Response (W24×104)

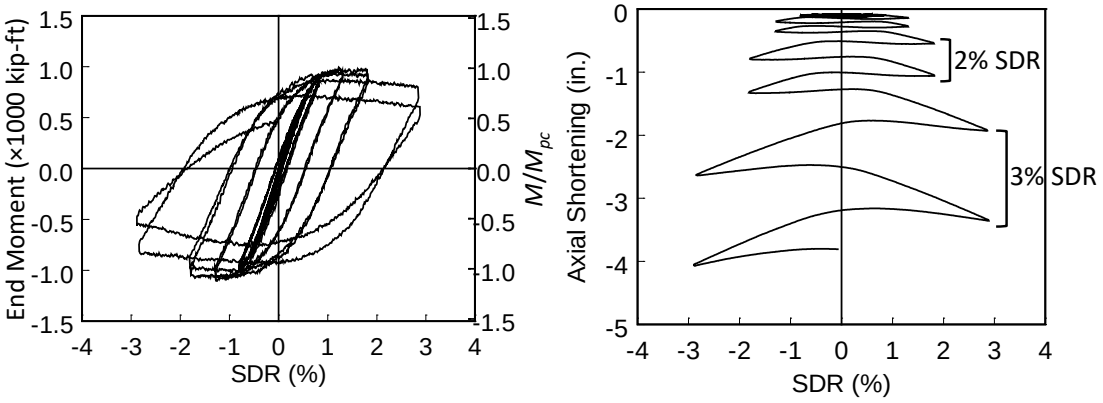

(a) Specimen 4L

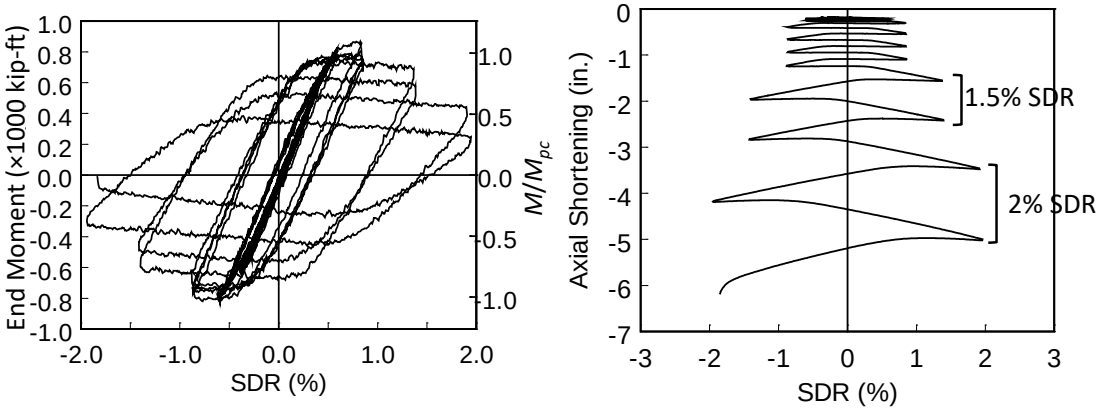

(b) Specimen 4M

Appendix A4 Group 4 Global Response (W24×84)

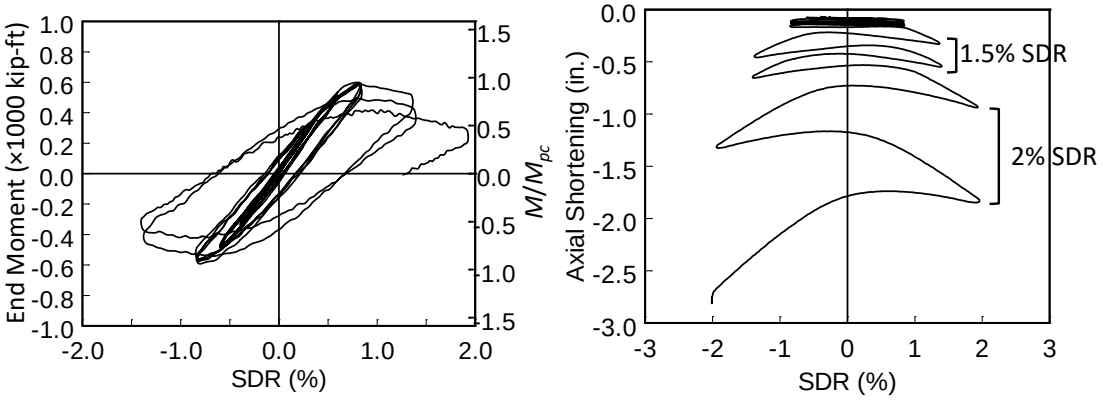

(a) Specimen 5L

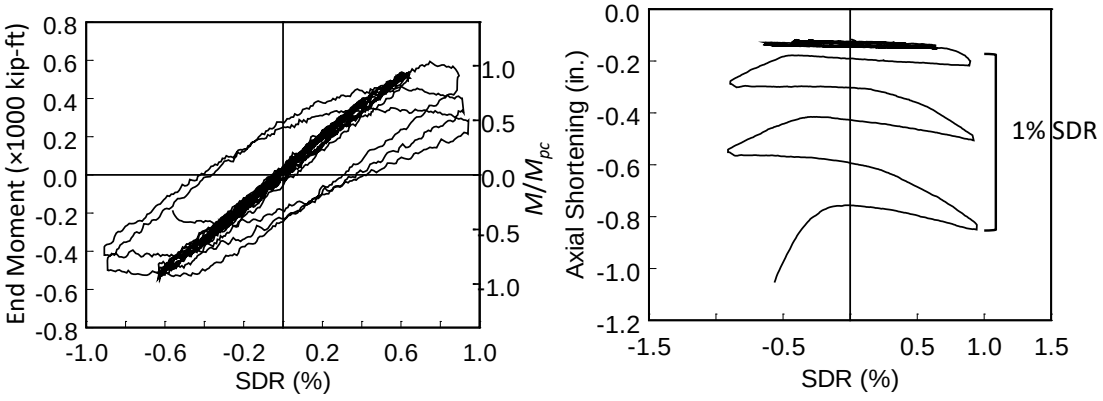

(b) Specimen 5LM

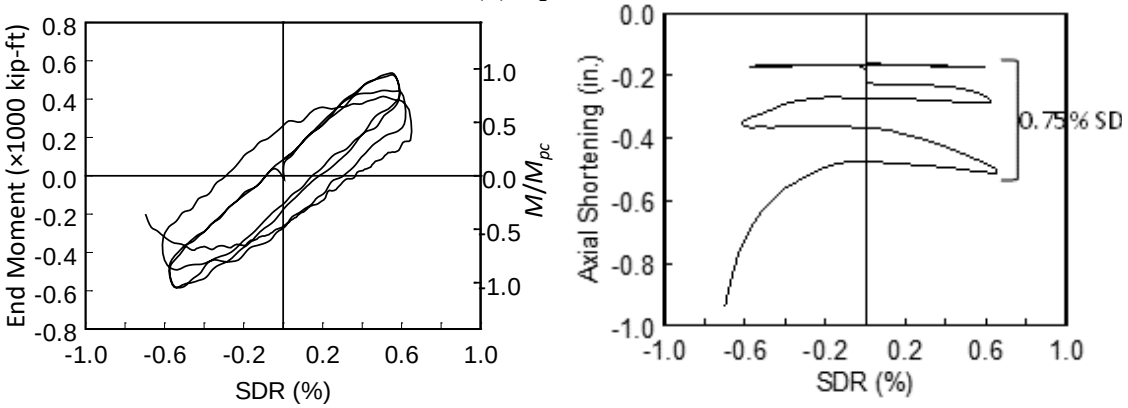

(c) Specimen 5M

Appendix A5 Group 5 Global Response and Axial Shortening (W24×55)

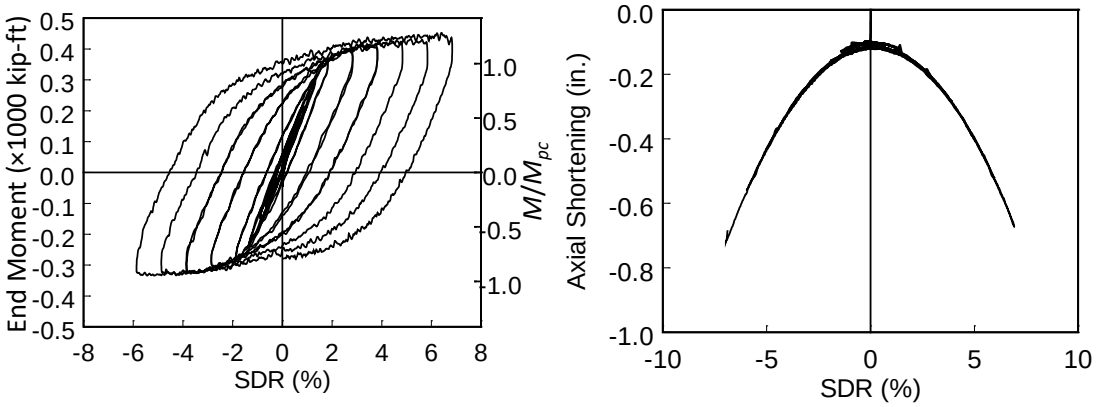

(a) Specimen 6L

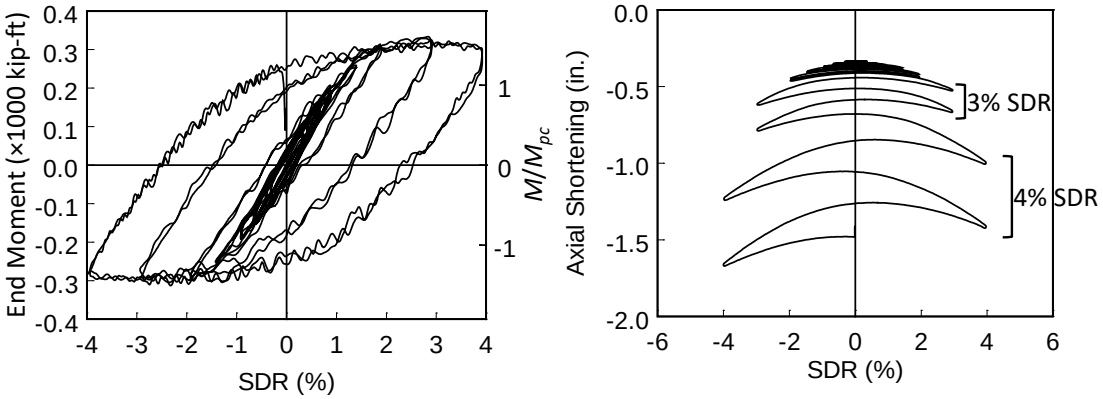

(b) Specimen 6H

Appendix A6 Group 6 Global Response and Axial Shortening (W24×131)

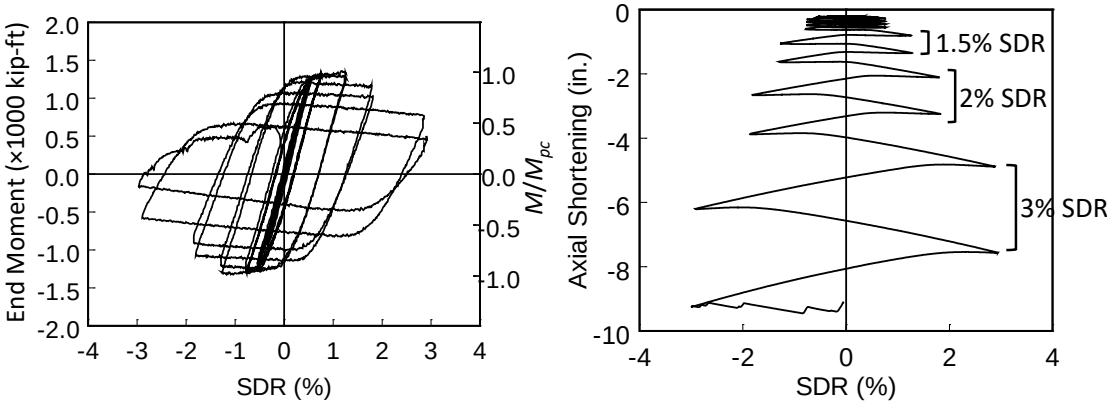

Appendix A7 Group 7 Global Response and Axial Shortening (W24×131)

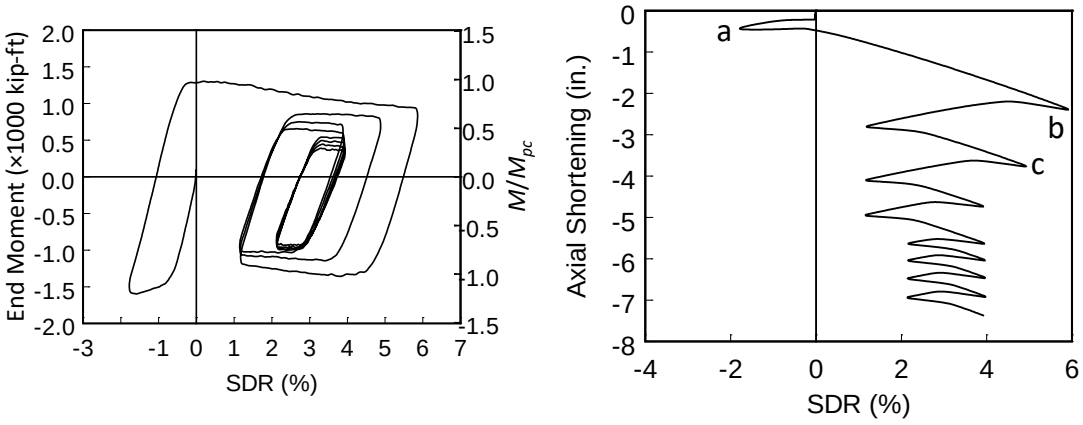

Appendix A8 Group 8 Global Response and Axial Shortening (W24×131)

A.2 Phase 2A: Global Responses and Axial Shortening of Tested Columns

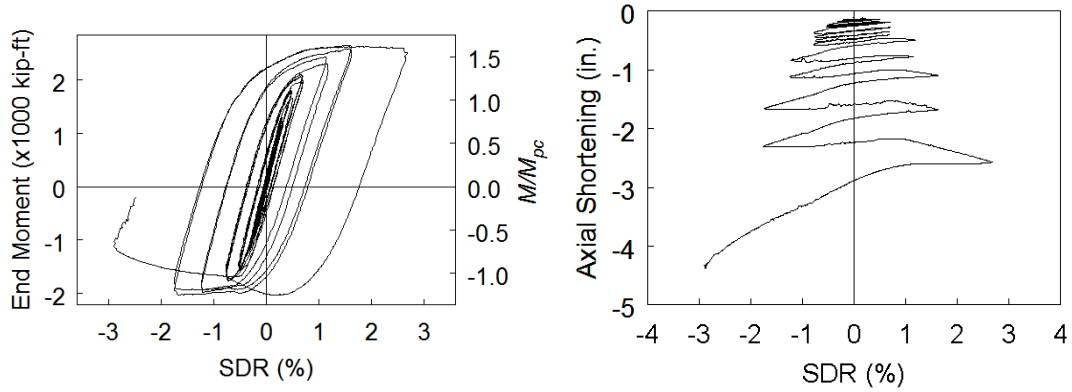

(a) Specimen 11H-VA

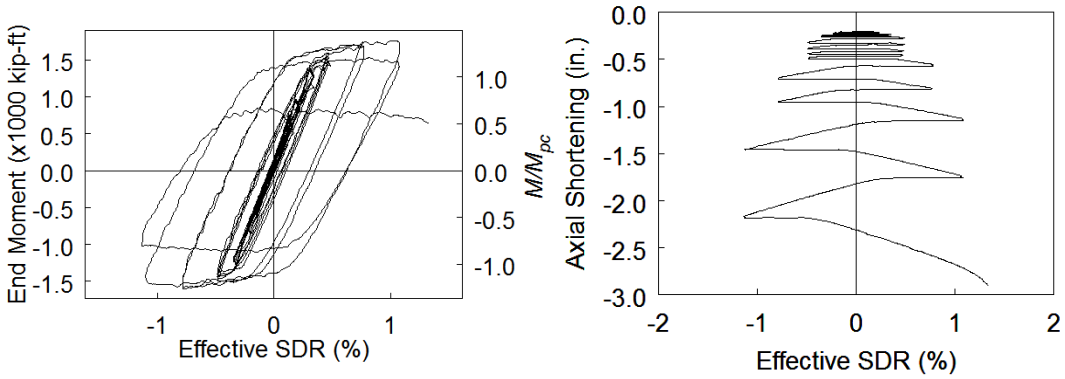

(b) Specimen 11H-BC

Appendix A9 Group 11 Global Response and Axial Shortening (W24×176)

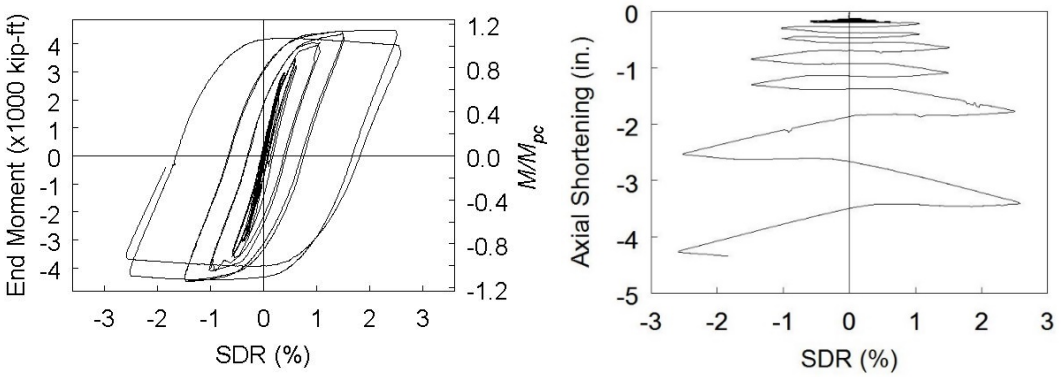

(a) Specimen 12LM

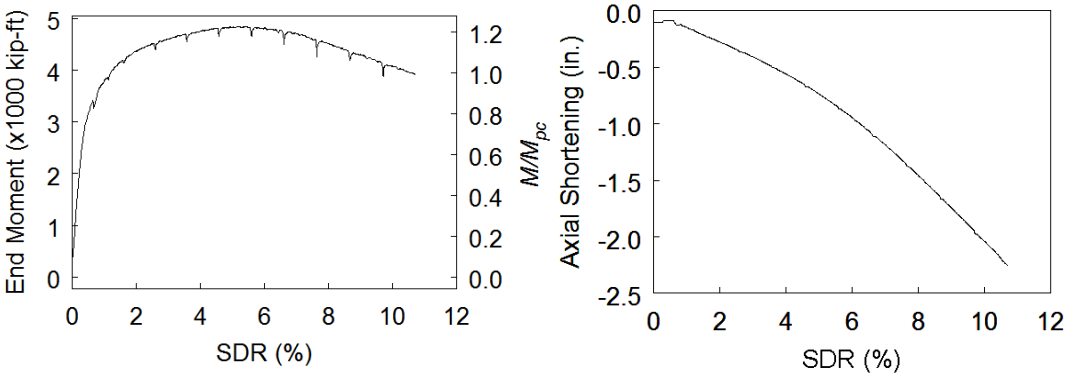

(b) Specimen 12LP

Appendix A10 Group 12 Global Response and Axial Shortening (W30×261)

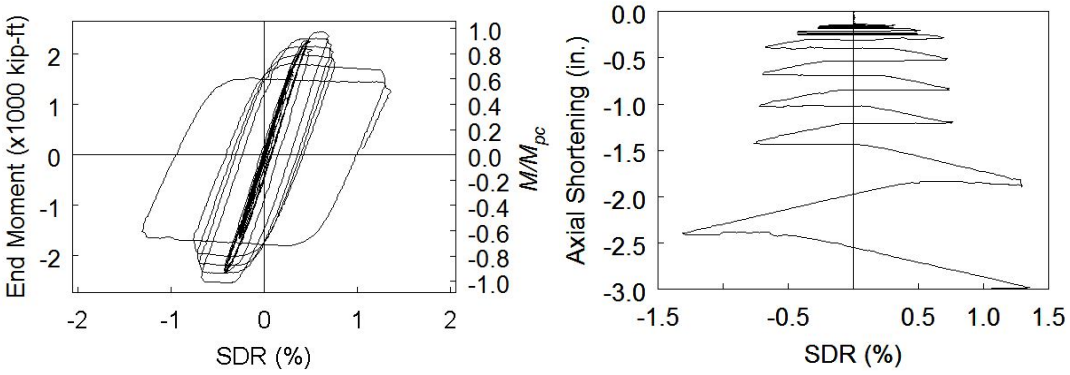

(a) Specimen 13M

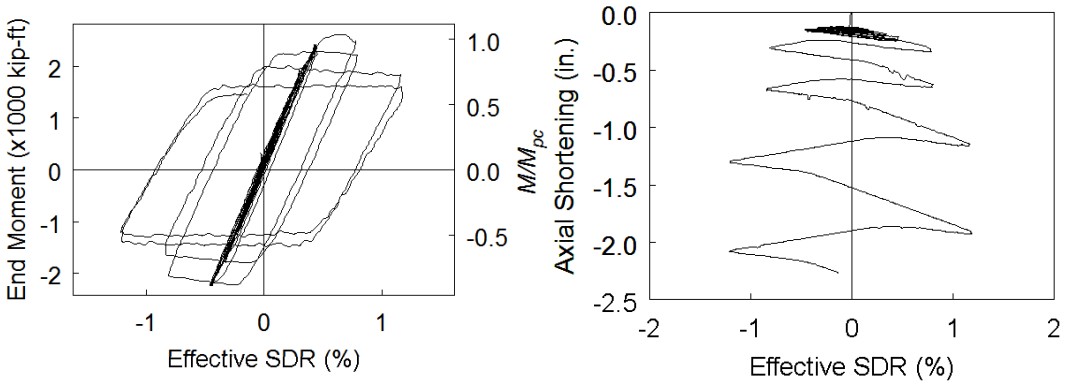

(b) Specimen 13M-BC

Appendix A11 Group 13 Global Response and Axial Shortening (W30×173)

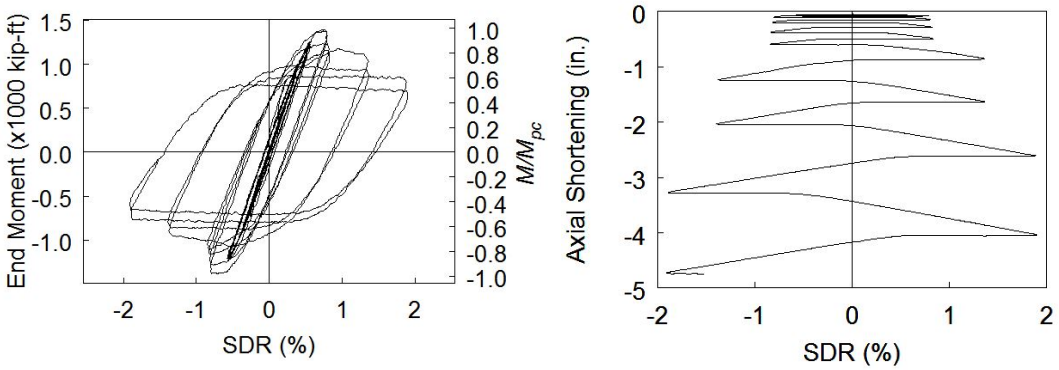

Appendix A12 Group 14 Global Response and Axial Shortening (W30×90)

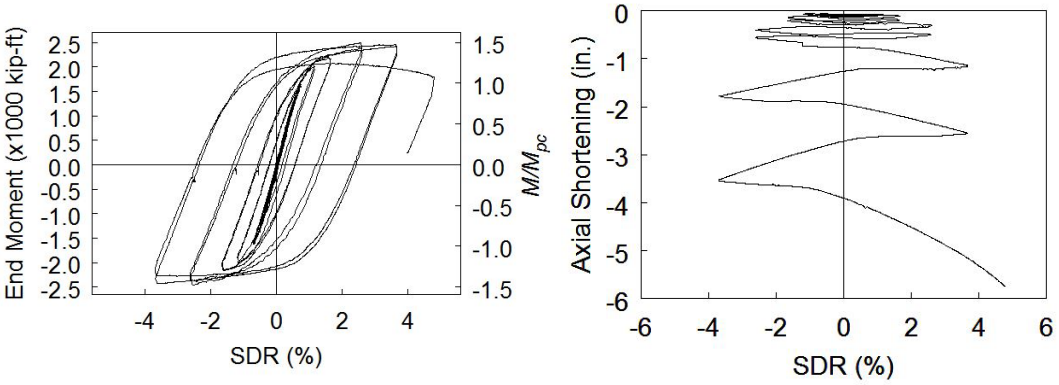

Appendix A13 Group 15 Global Response and Axial Shortening (W18×192)

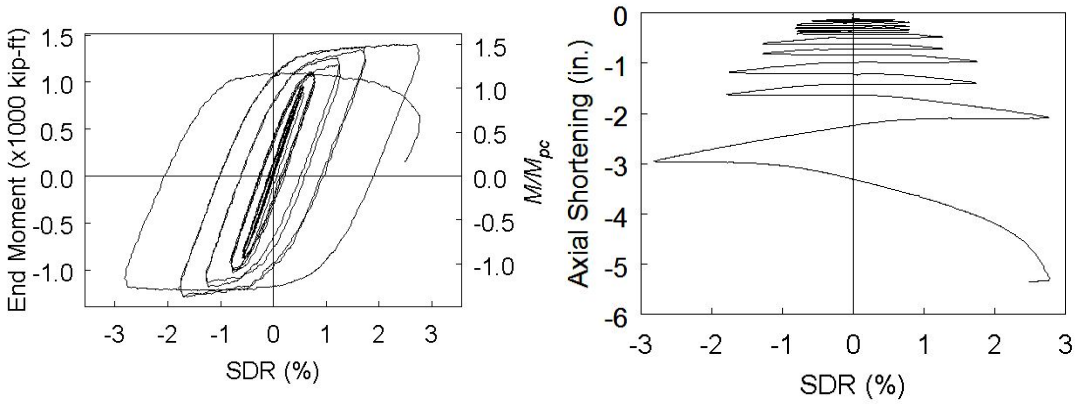

(a) Specimen 16M

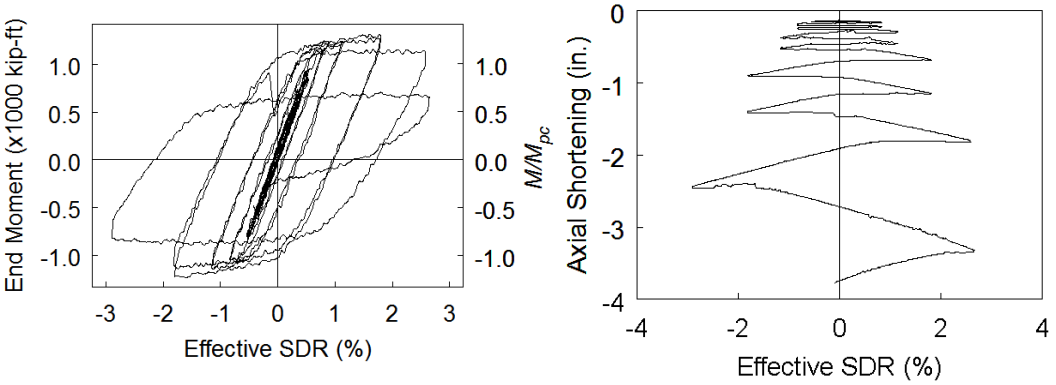

(b) Specimen 16M-BC

Appendix A14 Group 16 Global Response and Axial Shortening (W18×130)

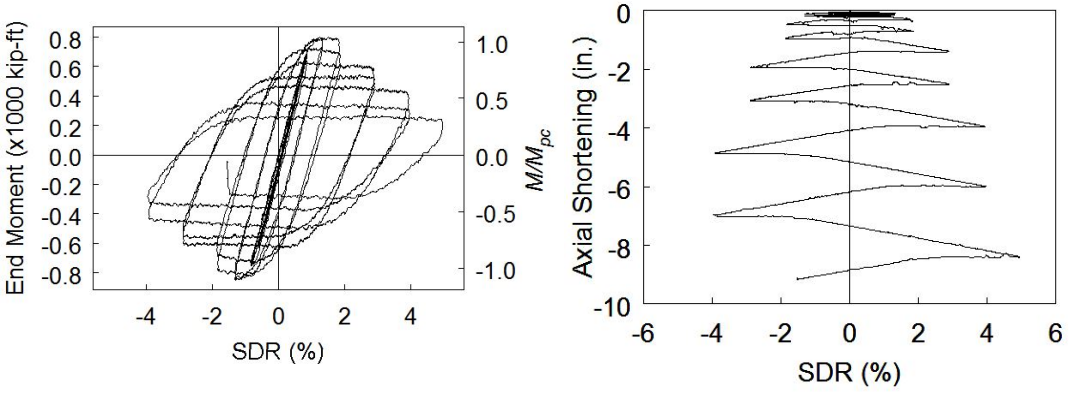

Appendix A15 Group 17 Global Response and Axial Shortening (W18×76)

A.3 Phase 1: Buckling Mode of Phase 1 Columns

(a) Specimen 1L

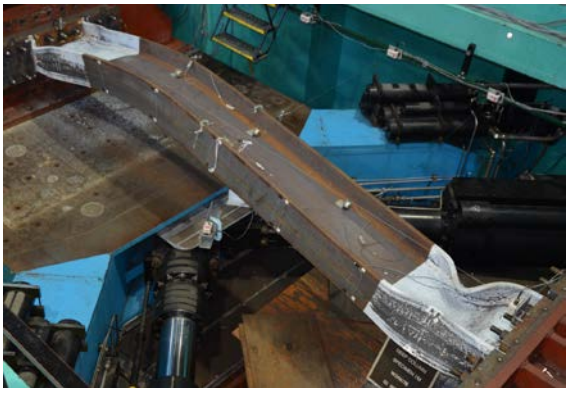

(b) Specimen 1M

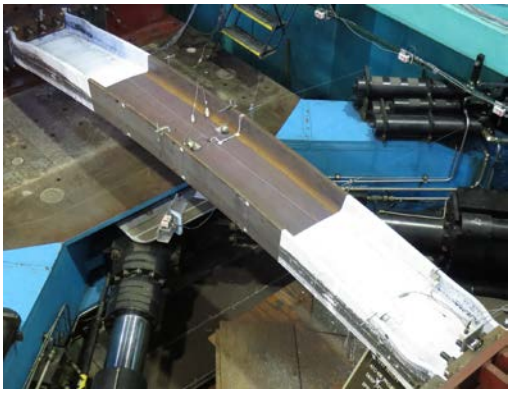

(c) Specimen 1H

Appendix A16 Group 1 Buckling Mode (W24×176)

(a) Specimen 2L

(b) Specimen 2M

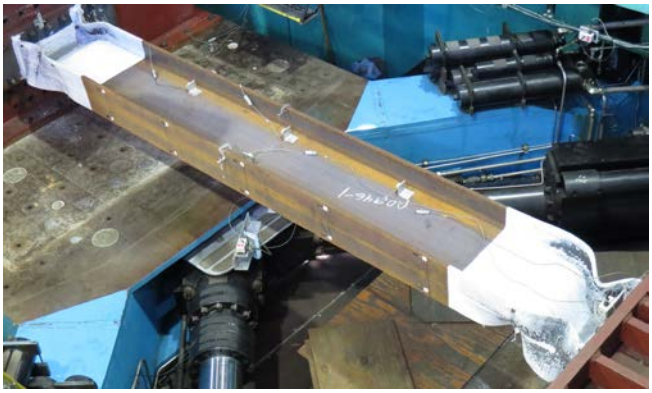

(c) Specimen 2H

Appendix A17 Group 2 Buckling Mode (W24×131)

(a) Specimen 3L

(b) Specimen 3M

(c) Specimen 3H

Appendix A18 Group 3 Buckling Mode (W24×104)

(a) Specimen 4L

(b) Specimen 4M

Appendix A19 Group 4 Buckling Mode (W24×84)

(a) Specimen 5L

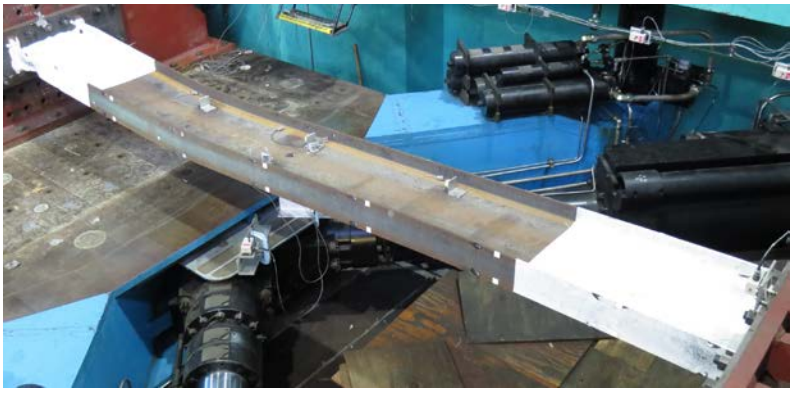

(b) Specimen 5LM

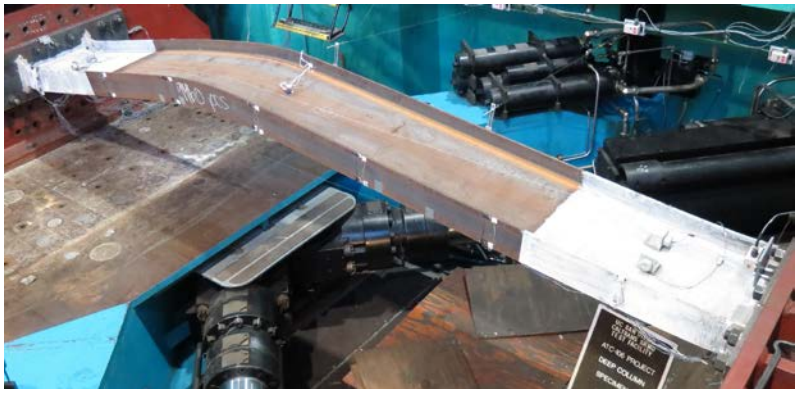

(c) Specimen 5M

Appendix A20 Group 5 Buckling Mode (W24×55)

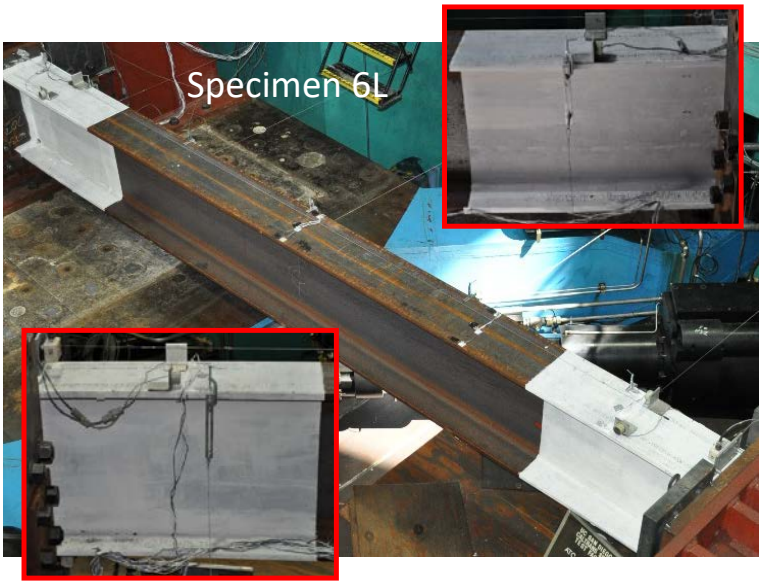

(a) Specimen 6L

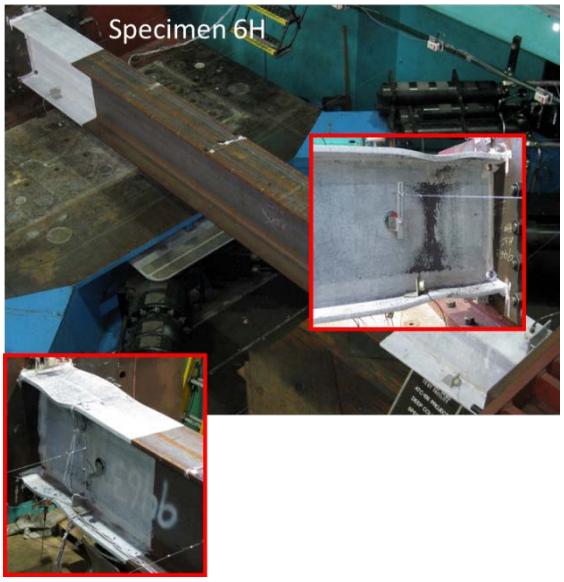

(b) Specimen 6H

Appendix A21 Group 6 Buckling Mode (W24×131)

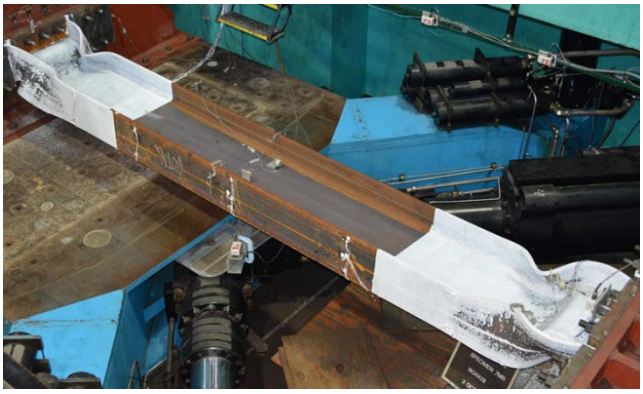

Appendix A22 Group 7 Buckling Mode (W24×131)

Appendix A23 Group 8 Buckling Mode (W24×131)

APPENDIX B. FINITE ELEMENT ANALYSIS RESULTS

B.1 Results of SFB Mode Sections

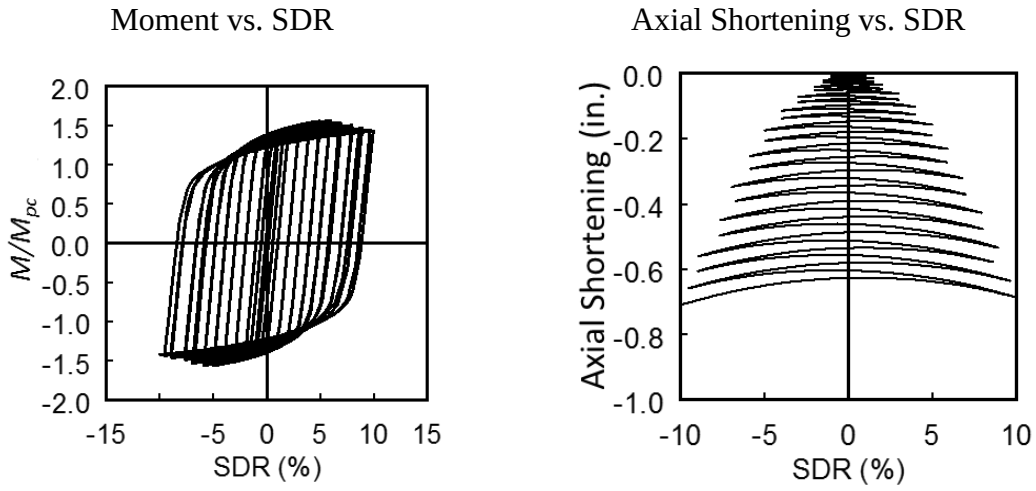

(a) W10×112

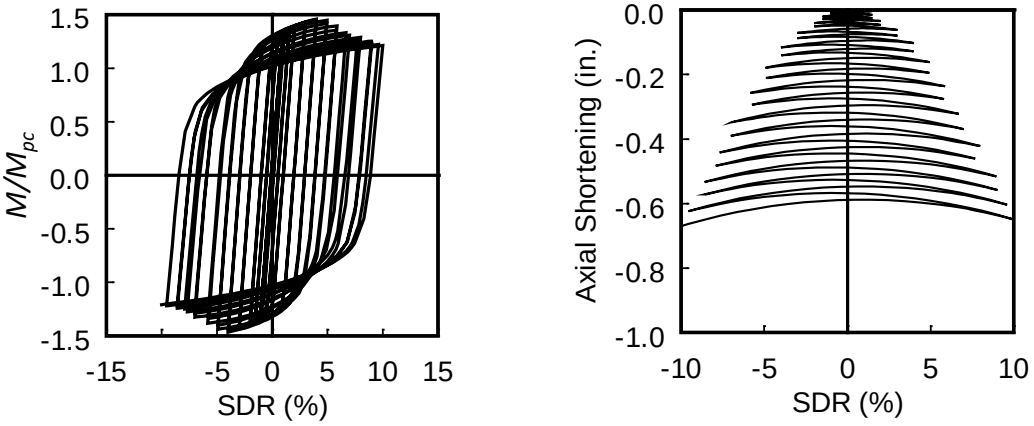

(b) W10×88

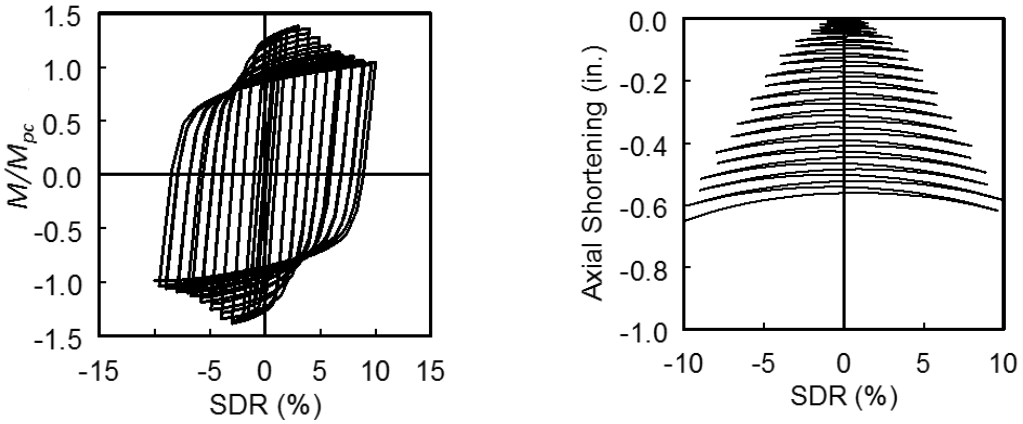

(c) W10×68

Appendix B 24 SFB Mode Global Response

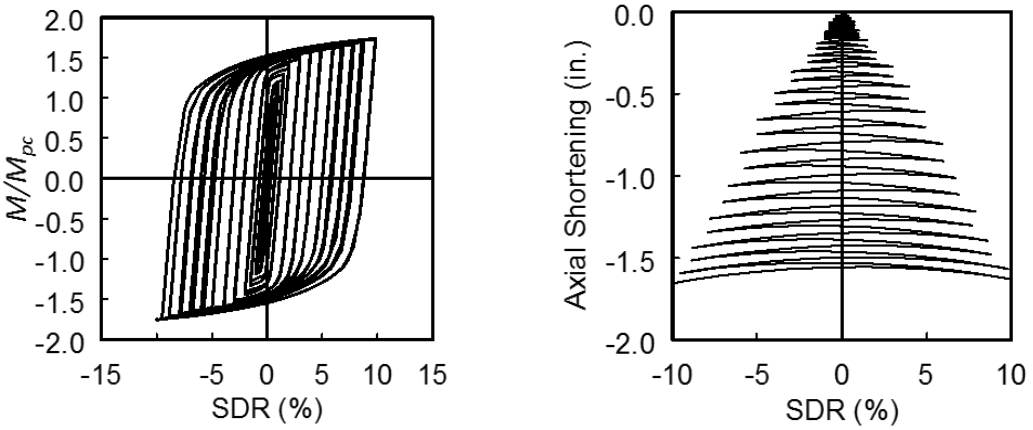

(d) W12×252

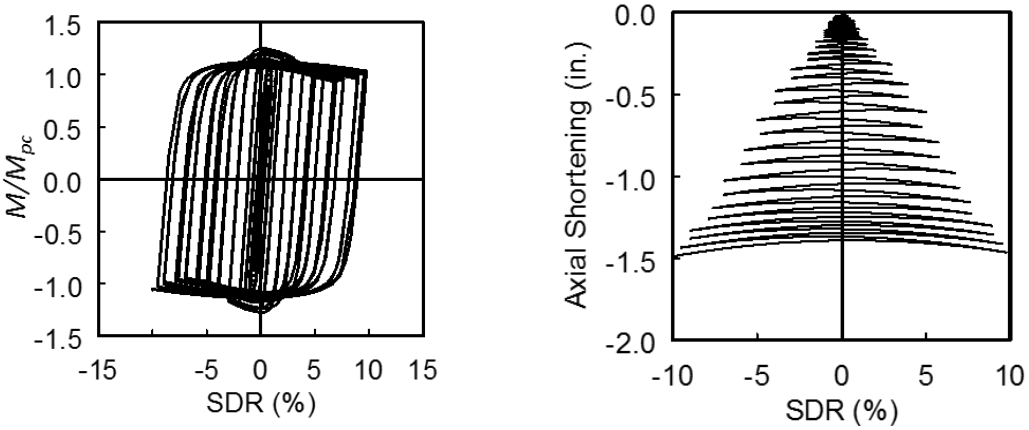

(e) W12×170

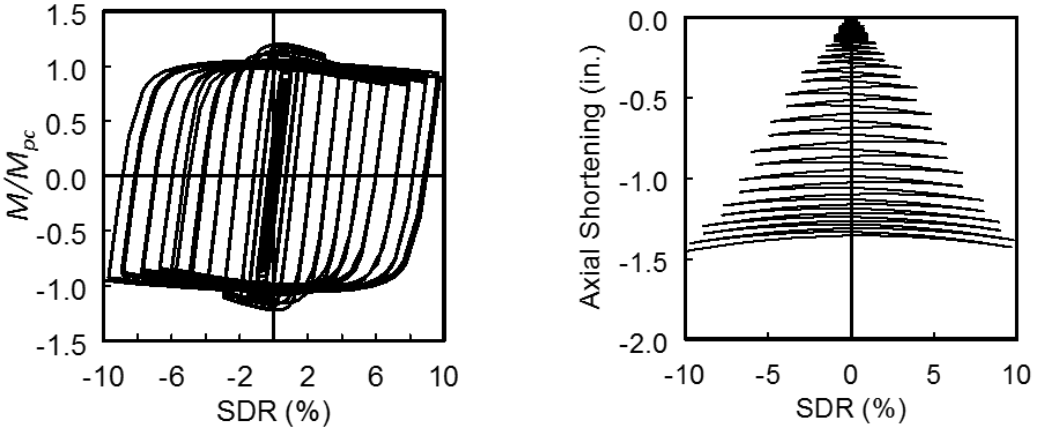

(f) W12×152

Appendix B 24 SFB Mode Global Response Cont.

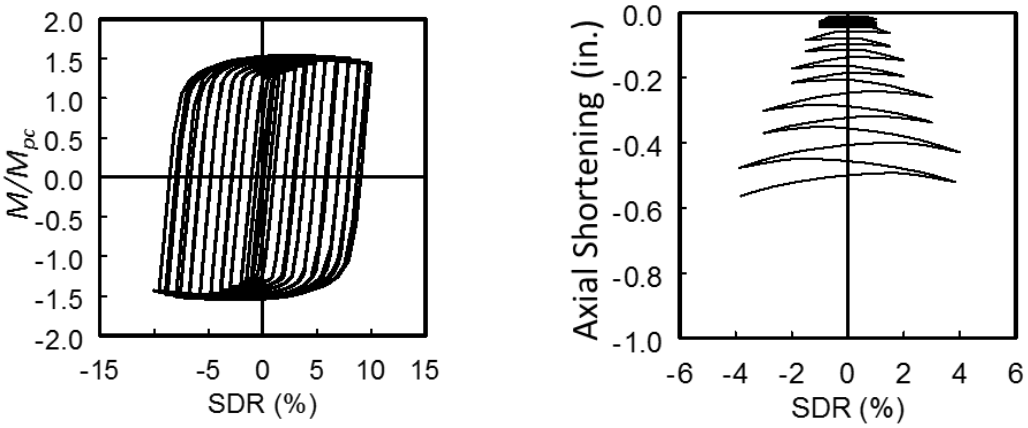

(g) W14×370

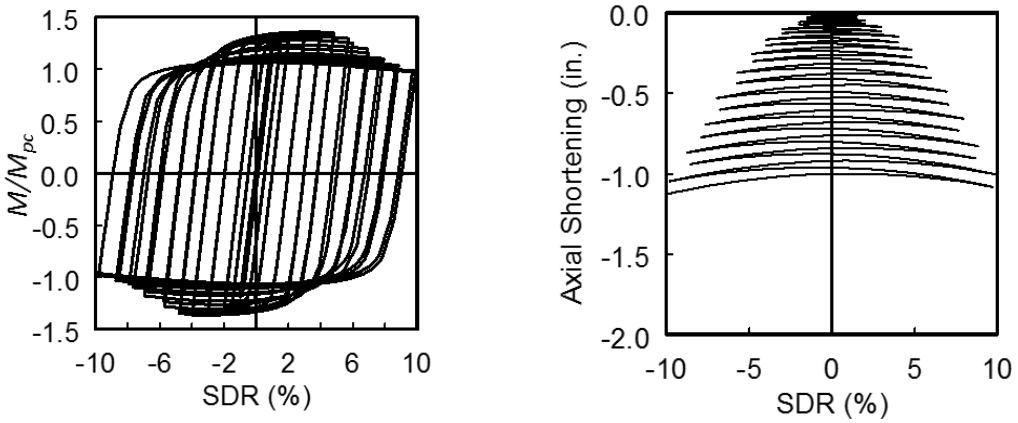

(h) W14×233

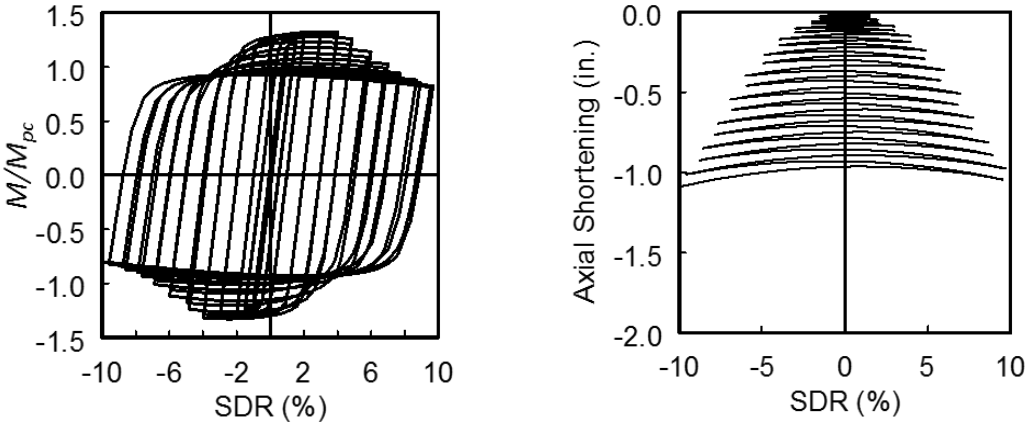

(i) W14×193

Appendix B 24 SFB Mode Global Response Cont.

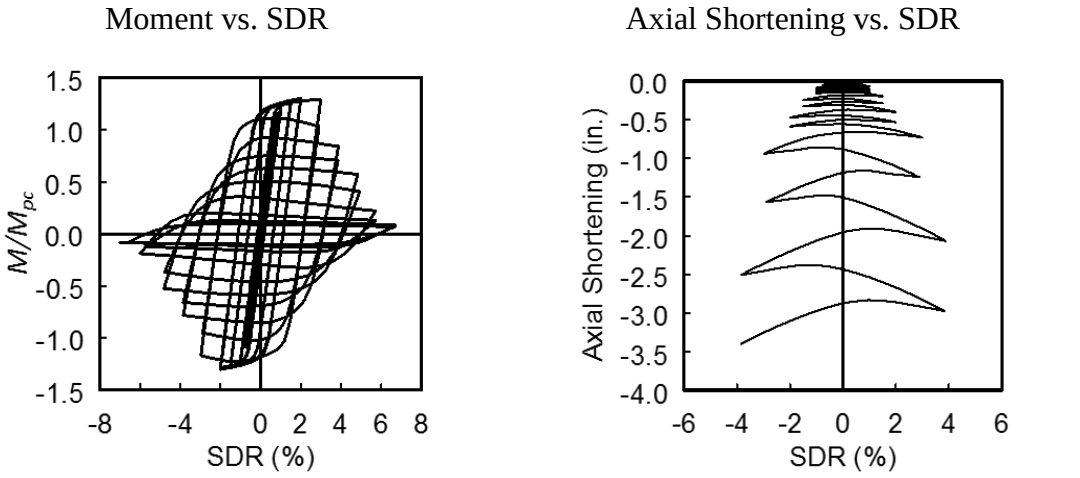

(a) W14×48

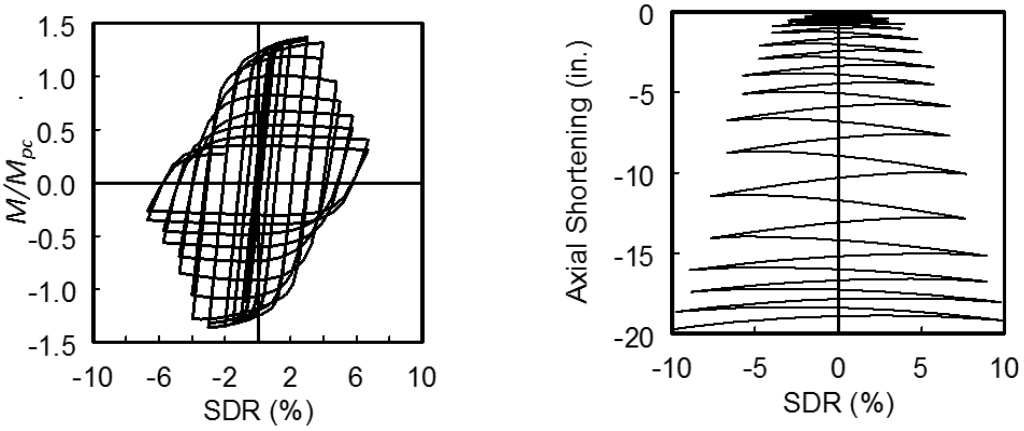

(b) W18×106

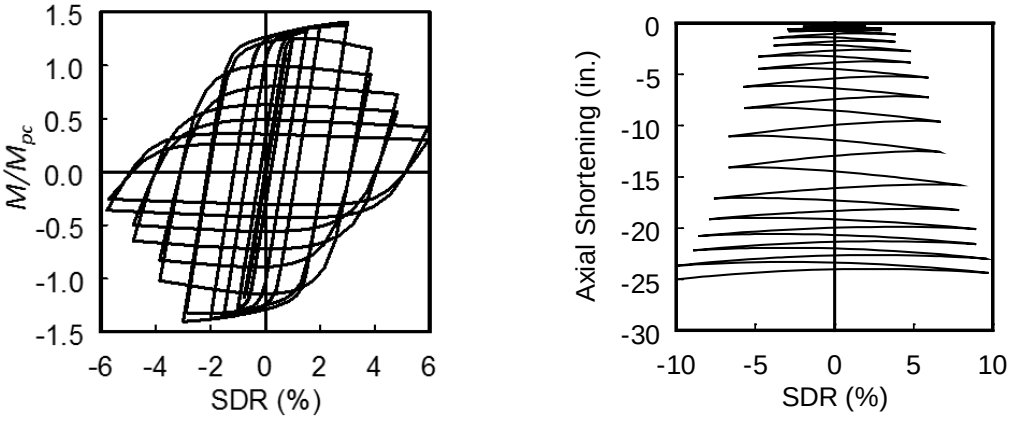

(c) W21×147

Appendix B 25 ALB Mode Global Response

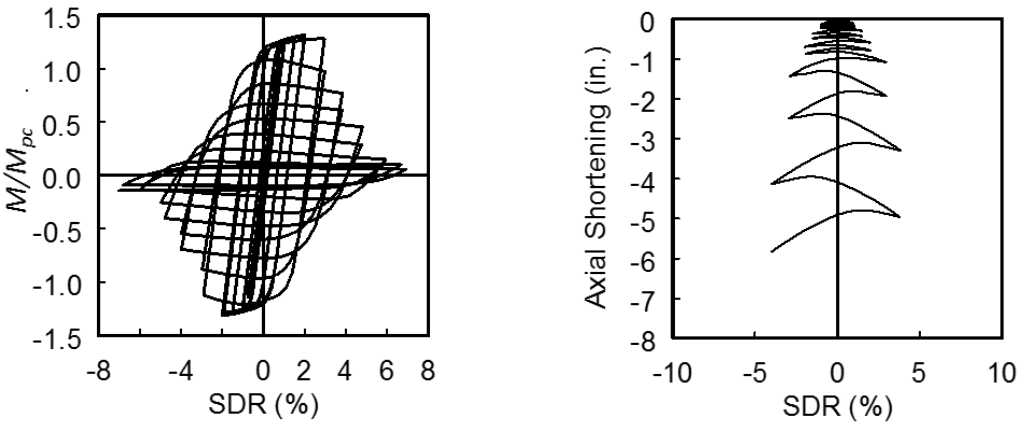

(d) W21×111

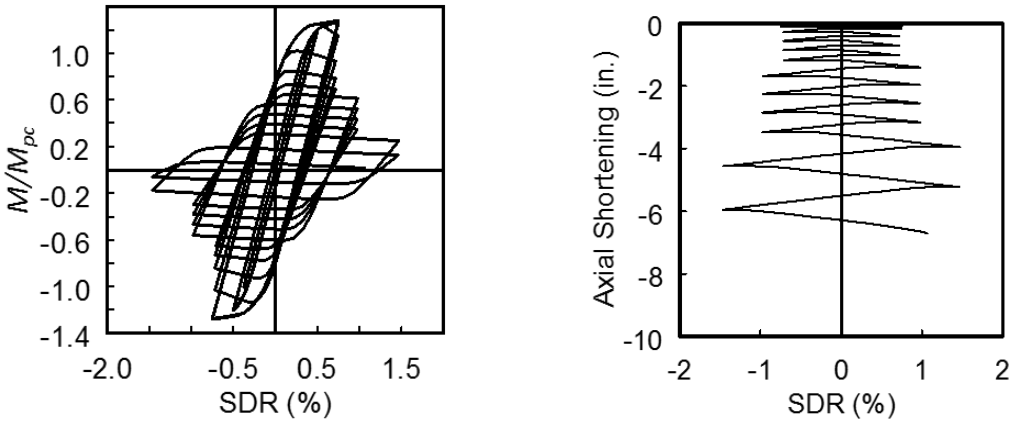

(e) W24×55

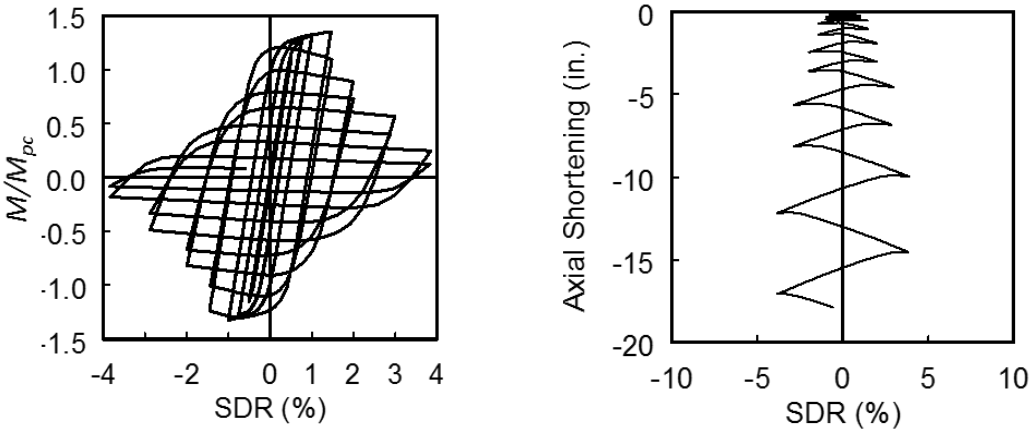

(f) W30×124

Appendix B 25 ALB Mode Global Response Cont.

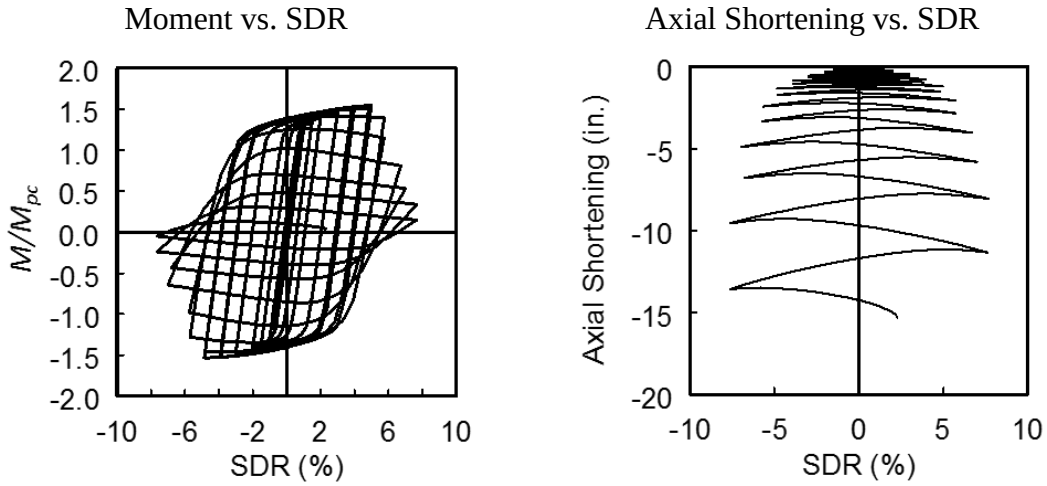

(a) W18×211

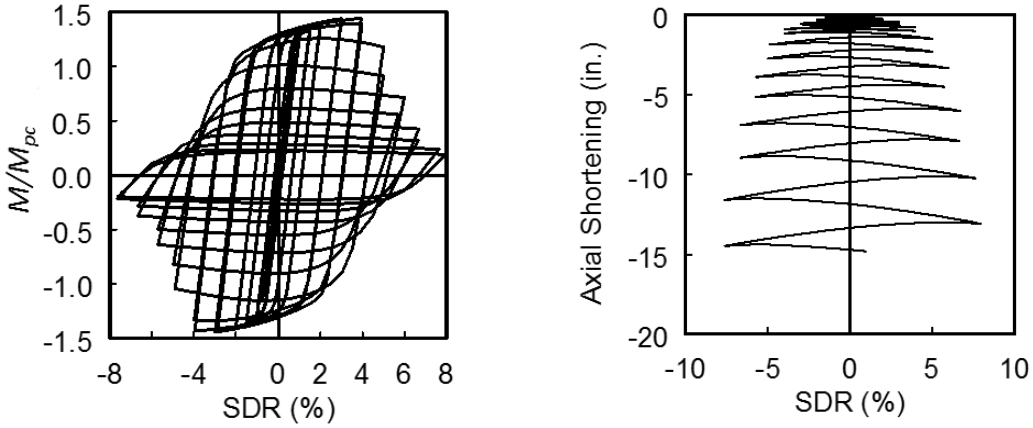

(b) W18×130

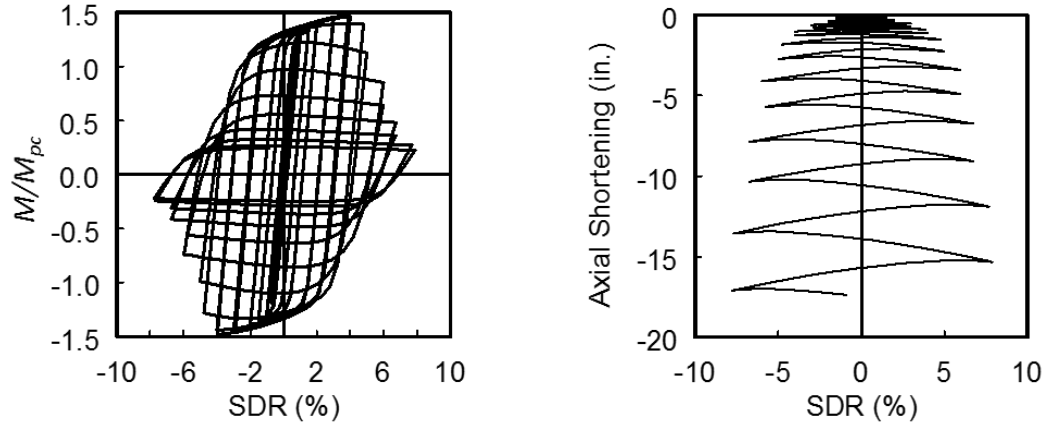

(c) W21×201

Appendix B 26 CB Mode Global Response

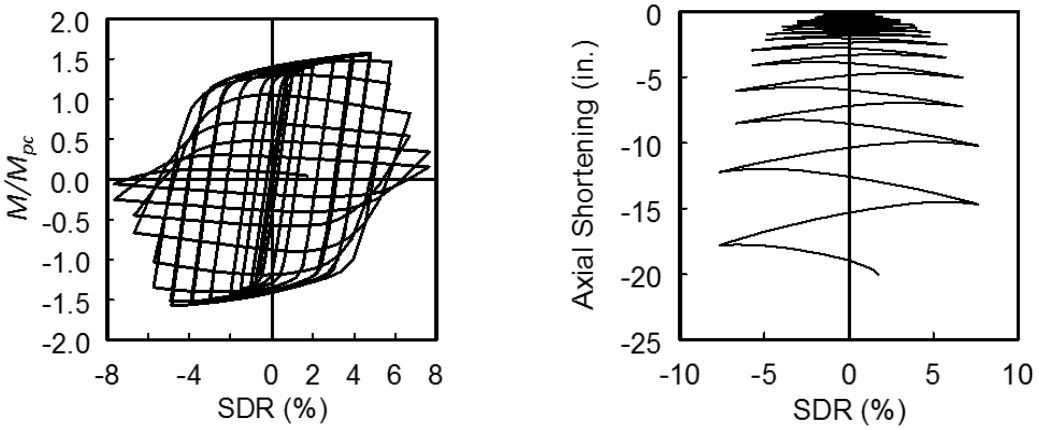

(d) W24×335

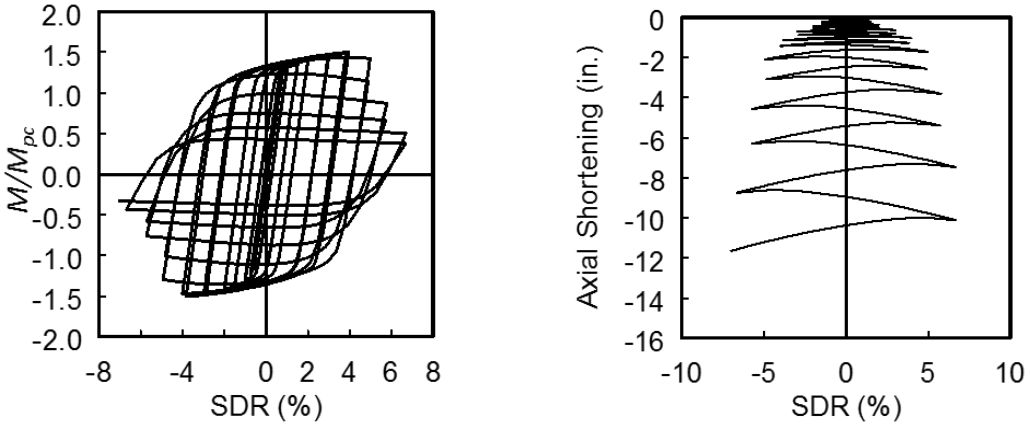

(e) W24×250

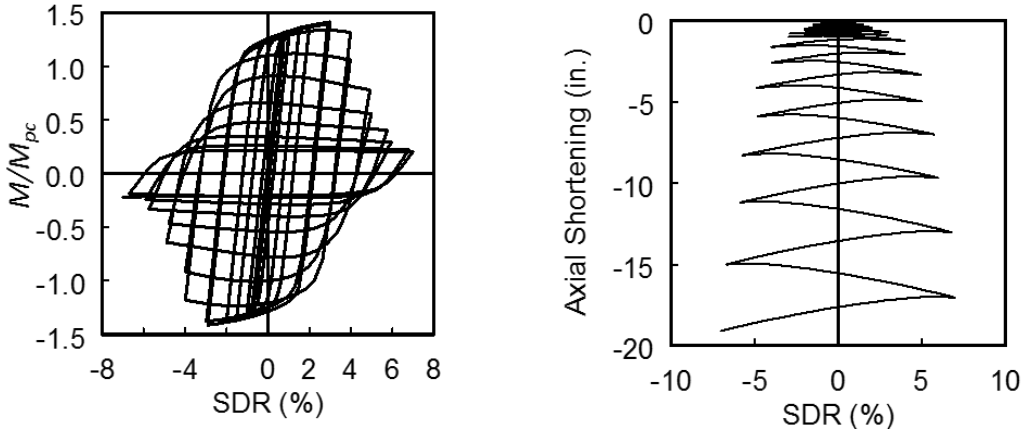

(f) W27×217

Appendix B 26 CB Mode Global Response Cont.

B.2 Buckling Patterns

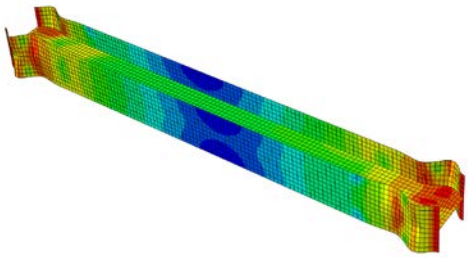

(a) W10×112

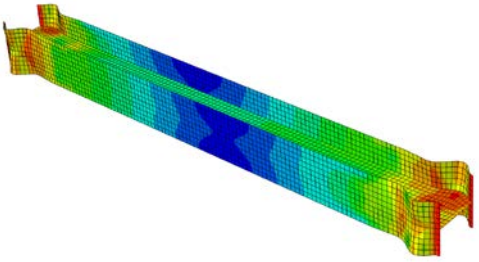

(b) W10×88

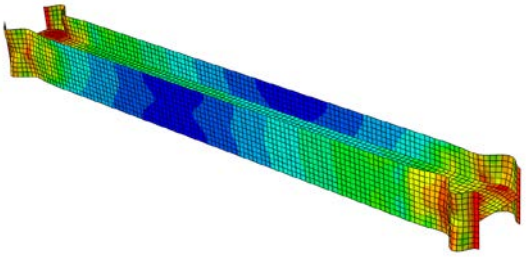

(c) W10×68

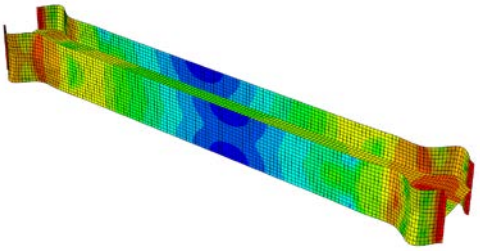

(d) W12×252

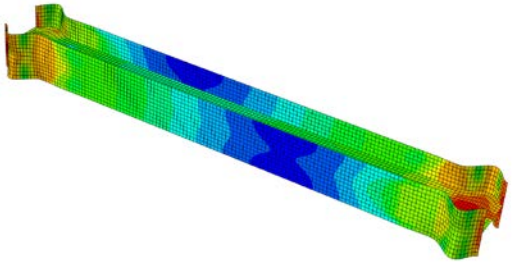

(e) W12×170

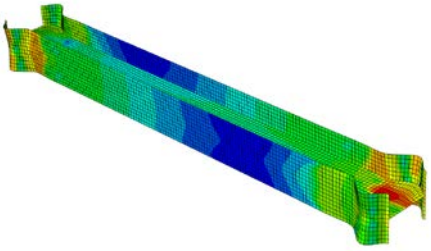

(f) W12×152

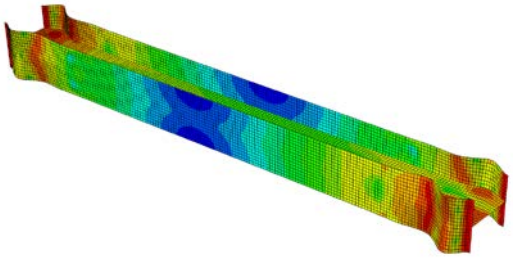

(g) W14×370

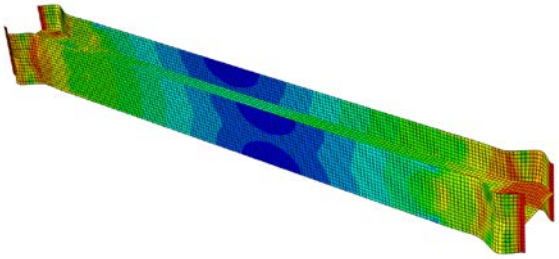

(h) W14×233

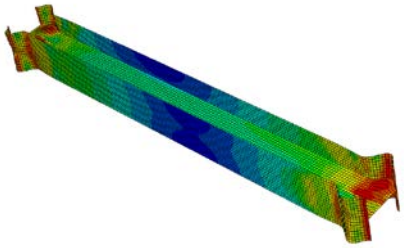

W14×193

Appendix B 27 SFB Mode Buckling Pattern

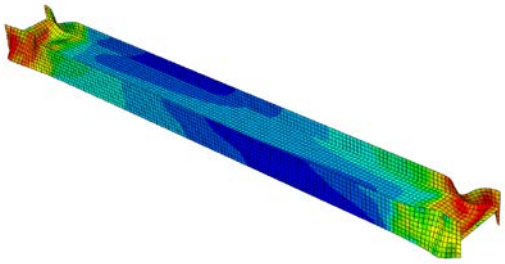

(a) W14×48

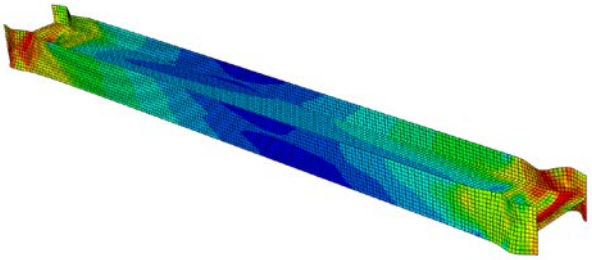

(b) W18×106

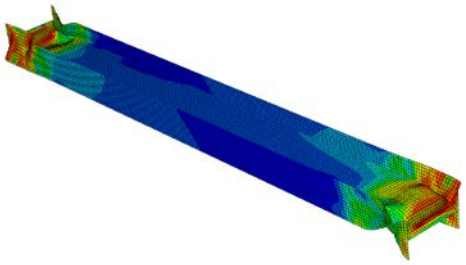

(c) W21×111

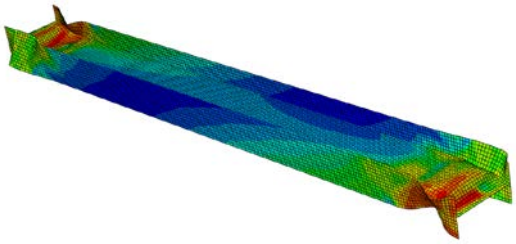

(d) W21×147

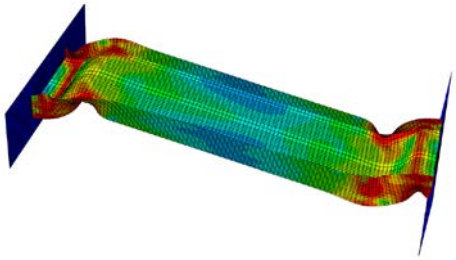

(e) W24×55

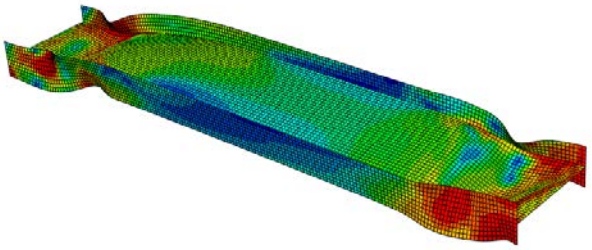

(f) W30×124

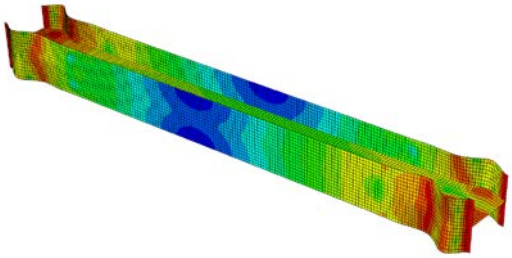

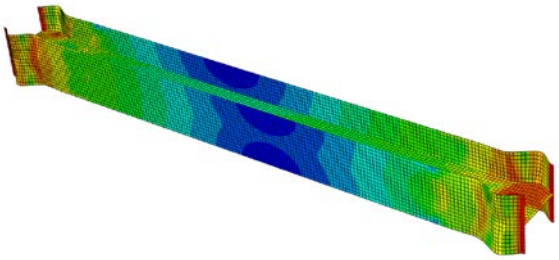

Appendix B 28 ALB Mode Buckling Pattern

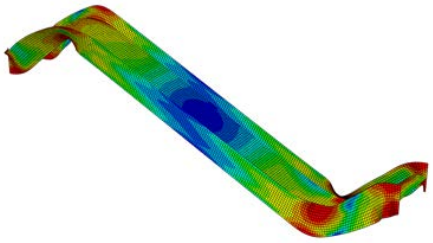

(a) W18×211

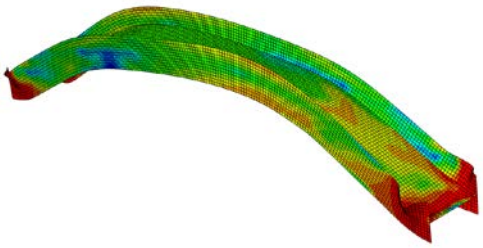

(b) W18×130

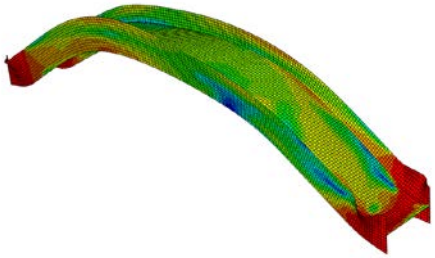

(c) W21×201

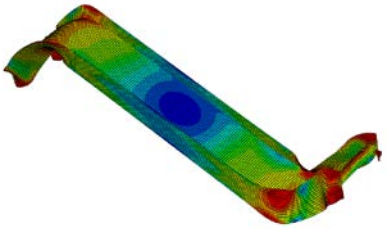

(d) W24×335

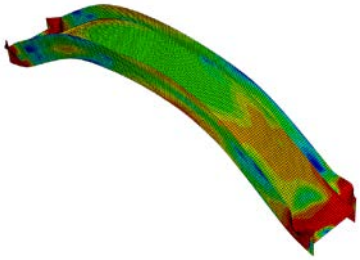

(e) W24×250

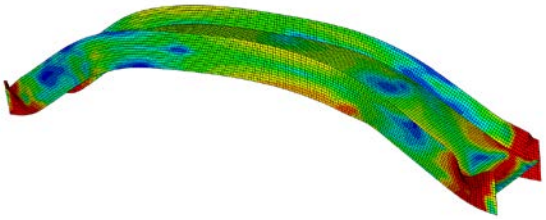

(f) W27×217

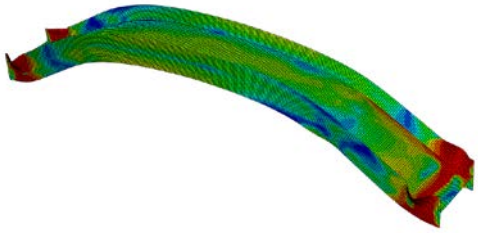

(g) W30×261

Appendix B 29 CB Mode Buckling Pattern